

**DEVELOPMENT OF A FLEXIBLE FORCING IMMERSED
BOUNDARY – LATTICE BOLTZMANN METHOD AND
ITS APPLICATIONS IN THERMAL AND PARTICULATE
FLOWS**

SUNIL MANOHAR DASH

(B.Tech. Mechanical Engineering, National Institute of Technology, Rourkela, India)

A THESIS SUBMITTED

FOR THE DEGREE OF DOCTOR OF PHILOSOPHY

DEPARTMENT OF MECHANICAL ENGINEERING


NATIONAL UNIVERSITY OF SINGAPORE

2014

Declaration

I hereby declare that this thesis is my original work and it has been written by me entirely. I have duly acknowledged all the sources of information which has been used in the thesis.

This thesis has also not been submitted for any degree in any university previously.


15/12/2014

Sunil Manohar Dash

Acknowledgements

First of all, I would like to express my sincere gratitude to my supervisor, *Associate Professor Thong See Lee* and my advisor, *Associate Professor Huang Haibo* (USTC, China) for their invaluable guidance, supervision, encouragement and support on my research and thesis work.

I am deeply grateful to my beloved late father for his confidence and love on me. I wish you are here to share this success with us. I am thankful to my mother and younger brother for being with me during these tough times and for their continuous encouragement and love.

In addition, I am sincerely thankful to *Professor Tee Tai Lim* for guiding me through the experimental studies and continuous motivation in these years. I am also thankful to *Professor Shu Chang* for his valuable clarifications on LBM concepts.

It won't be complete without acknowledging my colleagues, Dr. *Jiangyan Shao*, Dr. *Wang Liping*, Mrs. *Tanuja*, Mr. *Thirukumaran*, Mr. *Pardha*, Mr. *Ashoke*, Mr. *Vivek* and many others for their direct and indirect supports which pushed me through this phase of journey.

Finally, I am grateful to the *National University of Singapore* for granting the research scholarship and precious opportunity to pursue the Doctor of Philosophy degree.

Sunil Manohar Dash

Table of Contents

Declaration	i
Acknowledgements	ii
Table of Contents	iii
Summary	vii
List of Tables	x
List of Figures	xii
Nomenclatures	xviii
Chapter 1.....	1
Introduction and Literature Review	1
1.1 Background	1
1.2 Immersed boundary method.....	5
1.2.1 Defects in immersed boundary method	8
1.3 Lattice Boltzmann method	10
1.4 Thermal lattice Boltzmann method	13
1.5 Coupled immersed boundary – lattice Boltzmann method	15
1.6 Applications in thermal and moving boundary problems using immersed boundary – lattice Boltzmann method.....	17
1.6.1 Natural convection in a complex cavity.....	17
1.6.2 Particle sedimentation	20
1.7 Objective of the thesis	24
1.8 Outline of the thesis.....	26
Chapter 2.....	28
A 2D Flexible Forcing Immersed Boundary and Lattice Boltzmann Method.	28

2.1	Numerical methodology	29
2.1.1	Lattice Boltzmann method	29
2.1.2	Immersed Boundary method.....	34
2.1.3	Flexible forcing immersed boundary – lattice Boltzmann method	36
2.1.4	Kinematics of particulate flow	45
2.2	Accuracy test and Validations.....	48
2.2.1	Taylor – Green decaying vortex	48
2.2.2	Lid – driven cavity	51
2.2.3	Laminar flow past circular cylinder	54
2.2.4	A motion of the neutral buoyant particle in the linear shear flow	58
2.2.5	Single particle sedimentation	61
2.2.6	Two particles sedimentation	65
2.3	Concluding remarks	67
	Chapter 3.....	69
	Application of 2D Flexible Forcing IB –LBM for Particulate Flow in a Constricted Channel.....	69
3.1	Problem definition.....	70
3.2	Results and Discussion.....	73
3.2.1	Single particle sedimentation.....	73
3.2.2	Two particles sedimentation	83
3.3	Concluding remarks	90
	Chapter 4.....	92
	A 2D Flexible Forcing Immersed Boundary and Thermal Lattice Boltzmann Method	92
4.1	Numerical methodology	93
4.1.1	Thermal lattice Boltzmann method.....	93

4.1.2	Flexible forcing immersed boundary – thermal lattice Boltzmann method	99
4.2	Accuracy test and Validations.....	108
4.2.1	Natural convection in a square enclosure with a circular heat source	109
4.2.2	Forced convection from a square heat source.....	115
4.3	Concluding remarks	120
	Chapter 5.....	121
	Application of 2D Flexible Forcing IB–TLBM for Natural Convection in Complex Cavities.....	121
5.1	Problem definition.....	122
5.2	Results and Discussions	124
5.2.1	Case-1 Natural convection from an inclined square cylinder ..	124
5.2.2	Case-2 Natural convection from an eccentric square cylinder	136
5.3	Concluding remarks	150
	Chapter 6.....	152
	Extension of Flexible Forcing IB–LBM for 3D Flows around Stationary and Moving Boundary Problems	152
6.1	Flexible forcing IB-LBM scheme	153
6.1.1	Kinematics of the moving Sphere.....	161
6.2	Numerical validations	165
6.2.1	Flow past a stationary sphere	165
6.2.2	Single sphere sedimentation	170
6.2.3	Two sphere sedimentation	175
6.3	Concluding remarks	180
	Chapter 7.....	182
	Two Sphere Sedimentation Dynamics in a Viscous Liquid Column	182
7.1	Experimental setup and Procedure	183

7.2	Validation of the numerical solver	187
7.3	Results and Discussions	192
7.3.1	Problem setup descriptions	193
7.3.2	DKT and Inverse DKT.....	195
7.3.3	Forces acting on the settling spheres	198
7.3.4	Migration of the tumbling spheres	203
7.4	Concluding remarks	208
	Chapter 8.....	210
	Conclusions and Future Recommendations.....	210
8.1	Conclusions	210
8.2	Future recommendations	213
	References.....	215

Summary

The efficient and accurate numerical simulations of ubiquitously observed fluid – solid interactions have motivated the present thesis study and development of a hybrid numerical tool. The distinguish features of immersed boundary method (IBM) are adopted in this work, where the entire simulations is carried out on a Cartesian grid, which does not conform to the geometry of the immersed solid. Although the principles of IBM remove the burdens of body conformal meshing schemes such as grid transformations and time dependent mesh regeneration, but IBM suffers from certain numerical defects. One of such defects is improper/approximate satisfaction of the velocity/temperature boundary conditions, which leads to generation of non-physical streamline/isotherm penetration into the solid boundary. Looking into the literature, we observed that the ideas proposed to remove afore mentioned defects are either mathematically complex to implement or demands higher computational resources. Therefore, an attempt has been made here to formulate a simplified and efficient version of IBM, coupled together with lattice Boltzmann fluid solver.

At first, we have proposed a 2D version of flexible forcing immersed boundary – lattice Boltzmann method (IB – LBM), where an implicit formulation of velocity and body force correction is followed, that resolve the issues of improper satisfaction of boundary condition as seen in the conventional IB – LBM schemes. Here, use of a single Lagrangian velocity correction formulation simplifies the complex mathematics and reduces the computational memory and resource requirement. The numerical accuracy of

the proposed scheme has been evaluated by simulating several benchmark flow cases that involves stationary as well as moving solid boundaries, and the obtained results are validated by suitable comparisons with literatures.

We further studied the implementation of thermal boundary effects where an additional energy equation is solved for temperature evolution. In this case, the improper temperature boundary condition may leads to similar non-physical isotherm penetration into the solid boundary. Therefore, a single Lagrangian temperature correction is followed along with the previous velocity correction step for satisfying both temperature and velocity boundary conditions. Validation of the proposed scheme is done with natural and forced convection flow cases.

With suitable implications of flexible forcing IB – LBM in 2D cases, we have extended the studies to 3D and more practical flow scenarios. A modified version of coupled IB – LBM scheme is proposed here that accommodates 3D calculations in the basic frameworks of flexible forcing algorithm. Several benchmark flow simulations are performed to verify the accuracy and capabilities of the scheme, where the results are found to be in excellent agreement with the literature.

Now that we have gained confidence on the proposed IB – LBM scheme performance, we have tried to addresses some practical flow problems in relates to thermal and non-thermal conditions. In the present scope of study, only the applications involving natural convection flows and particulate flows are identified and assessed. Many significant findings are presented here with

different parametric studies. Also in case of particulate flows we have conducted in-house experiments to cross verify the numerical observations.

List of Tables

Table2.1	Comparison of CPU time and memory usage for lid-driven cavity flow at $Re = 100$ using two different IB-LBM schemes where the CC is 10^{-4}	53
Table 2.2	Comparison of force coefficients, recirculation length and Strouhal number for steady and unsteady flow past circular cylinder.....	56
Table 2.3	Variation of number of sub-iterations with CC and SRP for steady flow past circular cylinder.....	57
Table 2.4	Effects of CC variation for unsteady flow past cylinder ($Re=100$).....	57
Table 2.5	Variation of sub-iteration/number of forcing (NF) with respect to CC and SRP.....	64
Table 3.1	Grid independence test for particle sedimentation in the constricted passage.....	72
Table 3.2	Sedimentation time lag (in sec) between particle-2 and particle-1 for different constriction gap size and density of the particle.....	90
Table 4.1	Grid independence test by computing Nu_A on the hot circular cylinder at $Ra=10^5$	110
Table 4.2	Variation of number of forcing (NF) and CC while calculating Nu_A on the hot cylinder at $Ra=10^5$	113
Table 4.3	Comparisons of Nu_A on the hot circular cylinder at different Ra	114
Table 4.4	Grid independence test of flow past a square cylinder at $Re = 20$	117
Table 5.1	Nu_A on the enclosure surface as functions of Ra and θ	135
Table 6.1	Grid independence test of flow past a stationary sphere at $Re = 100$	166
Table 6.2	Comparison of drag coefficient (C_d) at $Re = 100, 200$	169
Table 6.3	Variation of number of forcing (NF) with CC and SRP at $Re = 100$	169

Table 6.4	Fluid properties used in the experiments by Ten Cate et al. (2002), and parameters used in the present simulations.....	171
Table 6.5	Grid independence test of single sphere sedimentation at $Re_T = 11.6$	172
Table 6.6	Parameters used in the present experimental studies along with the comparisons of data from experiments and flexible forcing IB-LBM scheme (U_T is terminal velocity, Re_T is corresponding Reynolds number).....	173
Table 6.7	Grid independence test of two equal spheres sedimentation case, by comparing the terminal velocity when only one sphere is released in the computational domain.....	176
Table 7.1	Parameters used in the present experiments (U_T is terminal velocity, $Re_T = \rho_f U_T d_p / \mu_f$ is the corresponding Reynolds number).....	187

List of Figures

Fig.1.1	Computational domain with (a) body fitted and (b) non-body fitted Cartesian mesh.....	2
Fig 2.1	D2Q9 lattice model with respective lattice velocity directions.....	33
Fig 2.2	A two dimensional domain Ω containing an immersed boundary Γ	36
Fig 2.3	Overall accuracy test of the proposed flexible forcing IB-LBM scheme using the Taylor–Green vortex.....	50
Fig 2.4	The schematic diagram of the lid-driven cavity in the computational domain and (b) the streamline plots inside the cavity at steady state condition for $Re = 100$, background colour code represent the pressure distribution....	52
Fig 2.5	The steady velocity components U_x/U and U_y/U along the centre lines (a) $y = x$ and (b) $y = -x$ respectively with different grid sizes.....	53
Fig 2.6	The streamlines and vorticity contours at (a) $Re=40$ and (b) $Re=100$	56
Fig 2.7	Schematic diagram of neutrally buoyant particle in the linear shear flow.....	59
Fig 2.8	Comparisons of lateral migration of the neutral buoyant particle.....	60
Fig 2.9	Comparison of the neutral buoyant particle translational velocities along X and Y directions.....	60
Fig 2.10	Instantaneous vorticity contours of single particle sedimentation at different time steps, where X and Y are in cms.....	62
Fig 2.11	Temporal evolution of (a) Y centre co-ordinate (Y_p), (b) Vertical velocity (V_p), (c) Reynolds number (Re_p) and (d) Translational kinetic energy of the particle (E_t), where the dimensional units of Y_p , V_p , E_t , and time are in CGS system.....	63
Fig 2.12	Instantaneous vorticity contours of two particles performing DKT phenomena where X and Y are in cms.....	66
Fig 2.13	Temporal evolution of (a) Y centre co-ordinate (b) Vertical velocity of the particle, where the dimensional units of Y_p , V_p and time are in CGS system.....	67

Fig 3.1	Schematic of particle sedimentation in a constricted channel where (a) single particle, (b) two particles and (c) division of the channel region, and (d) surrounding spatial domain near the particle.....	70
Fig 3.2	Study of the wall effects with increasing aspect ratio of the channel.....	72
Fig 3.3	Temporal evolution of (a) Y centre coordinate (b) Vertical velocity (c) Reynolds number (d) Translational kinetic energy of the particle with density 1.25 g/cm^3 and in the constriction gap size $1.25D$	75
Fig 3.4	Instantaneous pressure and vorticity contours at different time steps while the particle of density 1.25 g/cm^3 is travelling in Zone-1.....	75
Fig 3.5	Instantaneous pressure and vorticity contours at different time steps while the particle of density 1.25 g/cm^3 is travelling in Zone-2.....	77
Fig 3.6	Instantaneous pressure and vorticity contours at different time steps while the particle of density 1.25 g/cm^3 is travelling in Zone-3.....	78
Fig 3.7	Temporal evolution of (a) Y center co-ordinate (b) Vertical velocity (c) Reynolds number (d) Translational kinetic energy for different constriction gap size, where the settling particle has density 1.25 g/cm^3	79
Fig 3.8	Instantaneous pressure contours on the particle at the centreline of the constriction with gap size (a) $1.25D$, (b) $1.5D$, (c) $1.75D$ and (d) $2.0D$ and corresponding C_p distribution for particle density 1.25 g/cm^3	81
Fig 3.9	Comparisons of (a) maximum retardation velocity (V_R) and (b) sedimentation time for different constriction gap size and density of the particle.....	82
Fig 3.10	Temporal evolution of (a) Vertical velocity (b) Y center co-ordinate of the particles with density 1.5 g/cm^3 and the constriction gap size $1.75D$	84
Fig 3.11	Instantaneous pressure and vorticity contours at different time steps while the particles of density 1.25 g/cm^3 is travelling in Zone-1.....	84
Fig 3.12	Instantaneous pressure and vorticity contours at different time steps while the particles of density 1.25 g/cm^3 is travelling in Zone-2.....	87

Fig 3.13	Velocity vector plot at different time step for the particle of density 1.25 g/cm^3 near zone-2 where the constriction gap size is $1.75D$	88
Fig 3.14	Instantaneous pressure and vorticity contours at different time steps while the particles of density 1.25 g/cm^3 is travelling in Zone-3.....	88
Fig 3.15	Comparisons of maximum retardation velocity (V_R) for different constriction gap size and density of the particles; (a) Particle-2 (b) particle-1.....	89
Fig 4.1	A two dimensional domain Ω containing a heated immersed boundary Γ	101
Fig 4.2	Computational domain for Natural convection process from a hot circular cylinder; (b) additional circles at one and two mesh distance for calculation of normal direction gradient.....	110
Fig 4.3	Nu_L distribution along the enclosure walls at different Ra compared and with Kim, Lee et al. (2008).....	113
Fig 4.4	Isotherms (a-d) and Streamlines (e-h) for circular cylinder with increase in Ra $10^3, 10^4, 10^5$ and 10^6 (from left to right) (Contour of levels 1-10 is shown for Isotherm and Streamline respectively).....	115
Fig 4.5	Schematic diagram of computational domain for flow over the heated square cylinder.....	116
Fig 4.6	Isotherms (left) and Streamlines (right) around the square cylinder for different Re.....	119
Fig 4.7	Variation of drag coefficients with Re.....	119
Fig 5.1	Schematic of the computational domain for the proposed natural convection studies. 'S' is the direction used while calculating Nusselt number.....	124
Fig 5.2	Temporal evolution of Nu_A on the enclosure for different Ra, when the inclined square cylinder is at $\theta=30\text{deg}$	125
Fig 5.3	Isotherms (a-d) and Streamlines (e-h) for square cylinder at 0 deg inclination with increase in Ra value as $10^3, 10^4, 10^5$ and 10^6 (from left to right). (Dashed line represents opposite direction of circulation).....	131
Fig 5.4	Isotherms (a-d) and Streamlines (e-h) for square cylinder at 10 deg inclination with increase in Ra value as $10^3, 10^4, 10^5$ and 10^6 (from left to right). (Dashed line represents opposite direction of circulation).....	132
Fig 5.5	Isotherms (a-d) and Streamlines (e-h) for square cylinder at 20 deg inclination with increase in Ra value as $10^3, 10^4, 10^5$ and	

	10 ⁶ (from left to right). (Dashed line represents opposite direction of circulation).....	133
Fig 5.6	Isotherms (a-d) and Streamlines (e-h) for square cylinder at 30 deg inclination with increase in Ra value as 10 ³ , 10 ⁴ , 10 ⁵ and 10 ⁶ (from left to right). (Dashed line represents opposite direction of circulation).....	133
Fig 5.7	Isotherms (a-d) and Streamlines (e-h) for square cylinder at 45 deg inclination with increase in Ra value as 10 ³ , 10 ⁴ , 10 ⁵ and 10 ⁶ (from left to right). (Dashed line represents opposite direction of circulation).....	134
Fig 5.8	Nu_L and Nu_A distribution along the walls of the enclosure, at different Ra and inclination angles (a) $\theta = 0$ deg, (b) $\theta = 10$ deg, (c) $\theta = 20$ deg, (d) $\theta = 30$ deg, (e) $\theta = 45$ deg, (f) Nu_A vs Ra, where S is the direction used for calculation (ref. Fig.5.1)....	135
Fig 5.9	Isotherms (a-d) and streamlines (e-h) for square cylinder at $\chi=0$ with increasing Ra value as 10 ³ , 10 ⁴ , 10 ⁵ and 10 ⁶ (Contour levels of 1-9 and 1-14 are shown for isotherms and streamlines respectively).....	137
Fig 5.10	Isotherm and streamline plots at different displacement (χ) of inner cylinder for Ra=10 ³ (Contour levels of 1-10 and 1-12 are shown for isotherms and streamlines respectively).....	141
Fig 5.11	Isotherm and streamline plots at different displacement (χ) of inner cylinder for Ra=10 ⁴ (Contour levels of 1-10 and 1-12 are shown for isotherms and streamlines respectively).....	142
Fig 5.12	Isotherm and streamline plots at different displacement (χ) of inner cylinder for Ra=10 ⁵ (Contour levels of 1-10 and 1-12 are shown for isotherms and streamlines respectively).....	143
Fig 5.13	Isotherm and streamline plots at different displacement (χ) of inner cylinder for Ra=10 ⁶ (Contour levels of 1-10 and 1-12 are shown for isotherms and streamlines respectively).....	144
Fig 5.14	Nu_L distribution on the enclosure walls at different location of inner cylinder and for Ra equals to (a) 10 ³ (b) 10 ⁴ (c) 10 ⁵ and (d) 10 ⁶ . The direction used for 'S' can be referred from Fig.5.1.....	148
Fig 5.15	Surface average Nusselt Number on (a) top wall, (b) bottom wall, (c) side wall and (d) combined all walls of the enclosure vs χ at different Ra.....	151
Fig 6.1	Triangular surface elements used for discretising the sphere surface	158

Fig 6.2	Streamlines and velocity contours for the steady axis-symmetric flow past the sphere on XY plane at (a) $Re = 50$, (b) $Re = 150$	167
Fig 6.3	Recirculation region (L_s) behind the sphere at different Re ...	168
Fig 6.4	Streamlines and velocity contours for the steady non axis-symmetric flow past the sphere at $Re = 250$ on (a) XZ and (b) XY plane.....	170
Fig 6.5	Schematic diagram of the computational domain ($100 \times 160 \times 100 \text{ mm}^3$) followed for the single sphere sedimentation.....	171
Fig 6.6	Comparison of the settling spheres' (a) trajectories and (b) vertical velocities at different terminal Re , where H is the instantaneous vertical sphere centre height and d_p is the diameter of sphere.....	174
Fig 6.7	Experiment performed on single sphere sedimentation in glycerine-water mixture with the Derlin sphere of diameter, 12.7 mm and $Re_T = 50.25$. The instantaneous positions of falling sphere are shown.....	174
Fig 6.8	Experiments performed on two spheres sedimentation in glycerine-water mixture with the Derlin spheres of same diameter, 9.5 mm. The instantaneous positions of the falling spheres are shown while they exhibit Drafting – Kissing – Tumbling (DKT) phenomenon.....	178
Fig 6.9	Instantaneous positions of the spheres undergoing Drafting–Kissing–Tumbling (DKT) phenomenon as obtained from flexible forcing IB – LBM simulation.....	178
Fig 6.10	Schematic diagram of the computational domain ($10 \times 40 \times 10 \text{ mm}^3$) followed for the two sphere sedimentation mechanisms.....	179
Fig 6.11	Comparison of the two settling spheres trajectories along (a) X, (b) Z and (c) Y directions as well as their (d) vertical velocities.....	180
Fig 7.1	Schematic drawing of the experimental setup (a) Top view, (b) Side view and Real time image of the setup.....	186
Fig 7.2	Wall effects study by comparing the terminal velocity of the sphere ($d_p = 12.7 \text{ mm}$) with respect to varied aspect ratio (i.e. cross section width or depth of the computational domain to diameter of the sphere) of the fixed height computational domain.....	188
Fig 7.3	Experiments on single sphere sedimentation ($d_p = 12.7 \text{ mm}$).....	189

Fig 7.4	Single sphere sedimentation using flexible forcing IB – LBM for different diameters where (a) non-dimensional vertical centre trajectory and (b) non-dimensional vertical centre velocity of the spheres.....	190
Fig 7.5	Comparisons of the terminal velocity U_T as obtained from Experiments and IB – LBM observations.....	191
Fig 7.6	Two sphere sedimentation with their initial spacing $2d_p$. The box dimension is $(X, Z, Y) = (7.8d_p, 7.8d_p, 40d_p)$	194
Fig 7.7	Experimental visualization of two sphere sedimentation with (a) Drafting-Kissing-Tumbling and (b) Drafting – Kissing – Inverse Tumbling mechanism. ($d_p = 12.7$ mm).....	196
Fig 7.8	Numerical simulations on two sphere sedimentation using IB – LBM showing DKT and Inverse DKT. ($d_p = 12.7$ mm) where (a) Top view, (b) Front view of the 3D trajectory.....	197
Fig 7.9	The hydrodynamic force coefficients C_{dX} , C_{dY} and C_{dZ} on the (trailing) sphere-1 and (leading) sphere-2.....	200
Fig 7.10	The C_{dY} variation on the (trailing) sphere-1 and (leading) sphere-2 while performing drafting ($d_p = 12.7$ mm).....	200
Fig 7.11	Schematic of the hydrodynamic forces acting on the spheres to generate vertical and lateral migrations.....	201
Fig 7.12	The functions of maximum force coefficient C_{dX} , C_{dY} and C_{dZ} vs diameter of the spheres.....	202
Fig 7.13	Steady state alignment of the settling spheres after DKT and migration. The sphere sizes are, (a) $d_p = 12.7$ mm, (b) $d_p = 9.5$ mm and (c) $d_p = 7.9$ mm.....	203
Fig 7.14	Two spheres performing DKT mechanism with different diameters where Non-dimensional (a) X centre trajectories, (b) Z centre trajectories, (c) Y centre trajectory and (d) Vertical velocity of the spheres are shown.....	205
Fig 7.15	Y, X and Z centre migration of the two settling spheres with different diameter while undergoing DKT.....	206
Fig 7.16	Experimental and IB – LBM comparisons of the vertical migration of different diameter spheres during steady fall after DKT actions.....	207

Nomenclatures

Roman Letters

C_d	Drag coefficient
C_l	Lift coefficient
C_P	Coefficient of pressure
c_s	Sound speed
D	Spatial dimension
$\mathbf{e}_i, \mathbf{e}_\alpha$	Lattice velocity
\mathbf{f}, \mathbf{F}_B	Eulerian and Lagrangian body force density term
f_i, f_α	Density distribution function
f_i^{eq}, f_α^{eq}	Equilibrium density distribution function
f_q	Vortex shedding frequency
f_i^+	Post-collision density distribution function
g_i	Internal energy distribution function
g_i^{eq}	Equilibrium internal energy distribution function
h	Mesh spacing
L_w	Recirculation length

Nu	Nusselt number
P, p	Pressure
q, Q_B	Eulerian and Lagrangian heat source/sink density term
Pr	Prandtl number
R	Gas constant
Ra	Rayleigh number
Re	Reynolds number
St	Strouhal number
Δs	Arc length of Lagrangian boundary element
T, T_B	Eulerian and Lagrangian temperature
δt	Time step size
\mathbf{u}, \mathbf{U}_B	Eulerian and Lagrangian velocity
$\delta \mathbf{u}, \delta \mathbf{U}_B$	Eulerian and Lagrangian velocity correction
U_∞	Free stream velocity
W_i, W_α	Weighting coefficients
\mathbf{x}, \mathbf{X}_B	Eulerian and Lagrangian mesh coordinates
$\delta x, \delta y, \delta z$	Mesh size along X, Y and Z Cartesian coordinate direction

Greek Letters

α, β	Lattice velocity direction
δ	Dirac delta function
ε	Internal energy
η	Aspect ratio
θ	Rotational/Inclination angle
μ	Dynamic viscosity
ν	Kinematic viscosity
ξ	Fluid particle velocity
ρ	Macroscopic density
τ, τ_v, τ_c	Relaxation time
χ	Eccentricity
ω	Angular velocity
Γ	Lagrangian boundary curve
Ω	Computational domain

Abbreviations

2D	Two dimensional
3D	Three dimensional
BGK	Bhatnagar – Gross – Krook

CC	Convergence criterion
CCM	Cartesian/cut cell method
CFD	Computational fluid dynamics
DLM/FD	Distributed Lagrange multiplier/fictitious domain
DKT	Drafting – Kissing – Tumbling
FD/FDM	Finite difference/ Finite difference method
FE/FEM	Finite element/ Finite element method
FV/FMV	Finite volume/ Finite volume method
GFM	Ghost fluid method
IB/IBM	Immersed boundary/Immersed boundary method
IB – LBM	Immersed boundary – lattice Boltzmann method
IB – TLBM	Immersed boundary – thermal lattice Boltzmann method
IFEM	Immersed finite element method
IIM	Immersed interface method
ISLBM	Interpolation-supplemented LBM
LGCA	lattice gas cellular automata
LBE	Lattice Boltzmann equation
LB/LBM	Lattice Boltzmann/Lattice Boltzmann method

LILBM	Lagrangian interpolation based LBM
NF	Number of forcing/sub-iteration
NS	Navier-Stokes
RPKM	Reproducing Kernel Particle Method
SRP	Successive relaxation parameter
TLBM	Thermal lattice Boltzmann method
TLLBM	Taylor series expansion – and least square based LBM

Chapter 1

Introduction and Literature Review

1.1 Background

Numerical investigations of complex fluid flow problems using computational fluid dynamics (CFD) have become significantly important in both scientific researches and engineering applications. Although CFD simulations are considered as the cost-effective solutions over the experimental studies however, performing an accurate and efficient numerical analysis remains a primary issue in CFD.

A number of computational methods such as finite volume (FV), finite element (FE) and finite difference (FD) (Mavriplis (1997) and references therein) have been developed and deployed to understand the flow physics behind complex flow situations. These numerical schemes have advantages for direct implementation of the boundary conditions on a body-fitted mesh while their shortcomings are: 1) the grid transformations to generate the body-fitted meshing for realistic and complex geometries and 2) the time dependent re-meshing to solve the moving boundary problems. Although the modern

computational resources have evolved for high speed computation, but in these body fitted meshing schemes a significant amount of computational time is devoted in mesh constructions which subsequently enhances the overall simulation time by many folds. Therefore, it is necessary to look for an alternative in a non-body-fitted mesh technique where the complex boundary mesh is decoupled from the flow domain mesh.

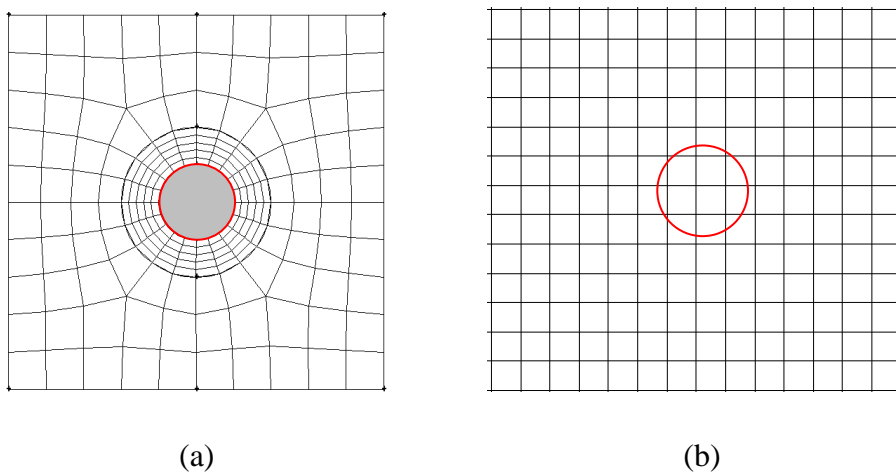


Fig.1.1. Computational domain with (a) body-fitted and (b) non-body-fitted Cartesian mesh.

As shown in Fig.1.1 to generate a body-fitted mesh, the boundary is defined at first then correspondingly the surface and volume mesh is generated in the computational domain whereas in case of a non-body-fitted mesh a simple Cartesian mesh is adhered in the computational domain and the effects of boundary is imposed in solution steps. In the decoupled/non-body-fitted mesh the flow field is solved on a fixed Cartesian/Eulerian mesh whereas the boundary evolution is solved in a moving Lagrangian mesh. Here, one may clearly identify the advantages of non-body-fitted meshing schemes for the moving boundary problems where the initially generated Cartesian mesh can

be used at all time steps unlike to the body-fitted meshing scheme, where the mesh is regenerated and the solution is projected onto the new mesh points (Tezduyar (2001)) at every time step.

The concept of non-body-fitted meshing schemes additionally requires an interface capturing technique as the boundary mesh may not coincide with the fluid domain mesh. Thus the non-body-fitted meshing schemes are subcategorised with the size of the captured interface thickness as 1) Sharp interface scheme and 2) Diffuse interface scheme.

In the case of sharp interface schemes, the thin/sharp boundary is traced by modifying the computational stencils around the boundary. The popular variants of the sharp interface schemes are, immersed interface method (IIM) (Leveque and Li (1997); Lee and Leveque (2003); Le et al. (2006); Shirokoff and Nave (2014)), ghost fluid method (GFM) (Fedkiw et al. (1999); Liu et al. (2000); Liu and Khoo (2007)), and Cartesian/cut cell method (CCM) (Udaykumar et al. (1997); Tucker and Pan (2000); Ingram et al. (2003)). The commonality between these variants is that the immersed solid boundary is cut out off the underlying Cartesian fluid mesh with negligible boundary thickness. The boundary conditions are then directly applied by incorporating the pressure and velocity jump conditions into the finite difference approximation of the governing equations near the boundary, or by using the reflection principles for the normal and tangential velocity components in the cut off portion of the Cartesian fluid cells. Also the sharp interface schemes require the reconstruction of the control volumes near the region of interface, where the integration of weak form governing equations are modified. One of

the severe limitations of the sharp interface schemes is the involved numerical instabilities while capturing the moving boundaries. In this case, the local stencil near the boundary changes too abruptly with minimal movement of the boundary which consequently generates substantial oscillations in the computed fluid force and may leads to a diverge solution (Kempe and Fröhlich (2012)).

On the other hand diffused interface schemes traces the boundary/interface with finite thickness which is smeared across some surrounding Cartesian mesh points. Here, the boundary conditions are easily implemented by introducing an additional body force density term into the governing equation, unlike to the tedious jump condition in the sharp interface schemes. The most common diffuse interface schemes are distributed Lagrange multiplier/fictitious domain algorithm (DLM/FD) (Glowinski et al. (1994); Glowinski et al. (1999); Glowinski et al. (2001)) and immersed boundary method (IBM) (Peskin (1977); Lai and Peskin (2000)). In the DLM/FD scheme a fictitious domain is utilised to represent the immersed solid boundary in a regular Cartesian grids. Using the distributed Lagrangian multiplier, the constraints of rigid body motion is imposed on the fictitious fluid inside the immersed solid boundary. But the form of Lagrange multiplier makes these schemes mathematically complex for practical implementations.

Alternatively, a simple non-Lagrangian multiplier based fictitious domain or immersed boundary method (IBM) is suggested. In the present study, the primary motivation is to develop an efficient IBM scheme to capture accurately different flow scenarios such as, athermal/thermal flows with

stationary/moving immersed solid objects. In the following, a brief literature review on existing IBM schemes and their defects are highlighted which will help to identify the scope and development for the present research work. In this study, we have used lattice Boltzmann method (LBM) to solve the flow field evolutions in various practical applications. Hence, corresponding literature reviews on LBM and selective applications are also outlined here.

1.2 Immersed boundary method

The pioneering work on IBM was proposed by Peskin (1977) to model the blood flow in the heart arteries. Such flow is regularised by the heart valves, which are moving boundaries in the fluid (blood) stream. In IBM, the flow field was discretised over a fixed Cartesian/Eulerian mesh whereas the boundaries are represented by a set of Lagrangian points that may be advected with the flow field interaction. The basic idea of IBM is that the boundary is considered to be deformable, but with high stiffness. The boundary deformation is thus model using elements with elastic (spring) links, where a restoring force as functions of deformation and elasticity is generated that revert back the deformed boundary to its original shape. Using Dirac delta functions the restoring force at the Lagrangian boundary points is distributed to the Eulerian fluid mesh and then the Navier-Stokes (NS) equations with added body force are solved in whole Eulerian domain to incorporate the effects of the solid boundary.

Hence, the imposition of solid boundary condition in IBM entirely depends on determination of the singular restoring force/body force term, which further

classifies IBM into two major groups 1) Continuous forcing and 2) Discrete forcing.

In the first method, the body force term is included in non-discretised form of NS equations and solved in the entire computational domain (solid + fluid). This is also called as continuous forcing IBM. A number of variants of continuous forcing IBM have been proposed in literature to simulate different flow scenarios. Peskin (1977) has used a feedback forcing principle to simulate the blood flow in an elastic heart valve where the boundary force was computed from Hooke's law with surface deformation and spring constant. Lai and Peskin (2000) applied the method for the rigid boundary problem such as flow past a circular cylinder with higher spring constant and stiffness. Goldstein et al. (1993) and Saiki and Biringen (1996) have developed a virtual boundary method that uses the feedback forcing in conjunction with the finite difference and spectral method. The virtual boundary method has two free parameters those need to be tuned according to the flow conditions. Zhu and Peskin (2003) have applied the continuous forcing IBM to simulate flapping filament in a flowing soap film.

Although the continuous forcing schemes are suitable for simulating interaction between the fluid flow and elastic immersed structures (Fauci and McDonald (1995); Zhu and Peskin (2002); Zhu and Peskin (2003)) but in case of a rigid body interaction this scheme poses severe numerical instabilities where one or more free parameters are involved. The improper selection of the free parameters (Goldstein et al. (1993); Mittal and Iaccarino (2005)) may leads to spurious elastic effects such as excessive deviation from the

equilibrium location. Again to derive an analytically integrable body force function that enforces a specific boundary condition is a tedious task and may not be always feasible for the NS equations.

In the second method, discrete forcing IBM, the governing equation is discretised on a Cartesian mesh without considering the presence of the immersed boundary. Then the cells near the immersed boundary are adjusted to account for its presence. This method differs from the continuous forcing scheme with respect to the introduction of the forcing function, where the body force term is incorporated after the NS equations are discretised. Hence, the followed spatial discretisation signifies the overall accuracy of the solution. Mohd-Yusof (1997) and Verzicci et al. (1998) have developed a direct forcing scheme where the forcing term is determined from the error between the calculated velocity and desired IB velocity. The direct forcing method does not depend on the free parameters and avoid the corresponding numerical instability issues. Fadlun et al. (2000) have applied the direct forcing method in the frame of FDM where the forcing point was located at the interior fluid node closest to the boundary. Kim et al. (2001) extended the direct forcing scheme for the FVM, where they have introduced a mass source/sink term to satisfy not only the no-slip condition but also the continuity for the cells encompassing the immersed boundary. Uhlmann (2005) had developed an improved direct forcing IBM using finite difference and fractional stepping to suppress the force oscillations in case of moving boundary problems such as particle sedimentation. Another variant of discrete forcing scheme was proposed by Niu et al. (2006), where the body force density on the Lagrangian points are calculated from Newton's second laws of

motion, i.e. the conservation of momentum. In this algorithm, by using simple momentum exchange the restoring force at the boundary point is computed and redistributed to Eulerian nodes.

In the context of applications, IBM have been well applied for diverse flow situations such as, compressible flow (De Palma et al. (2006); Ghias et al. (2007); Tran and Plourde (2014)), particulate flow (Feng and Michaelides (2004); Feng and Michaelides (2005); Uhlmann (2005); Kempe and Fröhlich (2012)), interaction of solid bodies (Fadlun et al. (2000); Gilmanov and Sotiropoulos (2005); Chen et al. (2007); Hu et al (2014)), multiphase flow (Li et al. (2012); Shao et al. (2013)), conjugate heat transfer (Jeong et al. (2010); Kang and Hassan (2011); Ren et al. (2012); Mark et al. (2013)), bio flow mechanics (Fauci and McDonald (1995); Tseng and Huang (2014)) etc. Although IBM has been promisingly implemented and many theoretical improvements have been suggested, still several issues are unaddressed.

1.2.1 Defects in immersed boundary method

In the conventional IBM, the body force is applied near the immersed boundary to enforce the no-slip condition that creates a discontinuity in the velocity gradient. This discontinuity reduces the local accuracy of the flow to first order. Suzuki and Inamuro (2013) have proposed a higher order IBM to smoothly expand the velocity field into the body domain across the boundary. The basic idea of this scheme is to keep the velocity discontinuity away from the boundary such that the velocity gradient is continuous near the boundary. Following this technique, the accuracy across the boundary is improved but

the velocity gradient discontinuity still prevails (rather shifted spatially) in the computational domain that reduces the overall order of accuracy of the scheme. Further, use of the lower order discrete delta function interpolation for Lagrangian, Eulerian velocity and body force transfer, the accuracy of the numerical scheme reduces. Wang and Liu (2004) have proposed an extended IBM namely immersed finite element method (IFEM). Here, both fluid and solid domain are modelled with FEM, where the boundary is detected by using Reproducing Kernel Particle Method (RPKM) with a higher order delta function. This enhances the order of accuracy of the numerical scheme.

Another defect of IBM is that the no-slip condition is only approximately satisfied at the converged solution state that may leads to non-physical streamline penetration into the immersed solid (Luo et al. (2007); Kang and Hassan (2011)). Shu et al. (2007) have suggested that the improper no-slip condition is formed because of the pre-calculated force density term. They have applied the fractional step technique to show that adding a body force density term into the governing equations in order to satisfy the no-slip condition is same as making a velocity correction. Therefore to enforce the no-slip boundary condition, the velocity correction is consider as unknown (implicit correction) and it would be determine such that the velocity at the boundary, interpolated from the corrected velocity field satisfies the accurate no-slip boundary condition. But the suggested implicit correction by Wu and Shu (Wu and Shu (2009); Wu and Shu (2010); Wu and Shu (2012), demands very complicated matrix operations along with significant computational memory usage and sequential coding pattern for the velocity correction coefficients. To avoid the complicated matrix operations an alternative multi-

direct-forcing scheme was proposed (Luo et al. (2007); Wang et al. (2008); Kang and Hassan (2011)), which uses iterative procedure to find out the body force density term. However, use of fixed number of iteration steps (Luo et al. (2007); Wang et al. (2008); Kang and Hassan (2011)) may not satisfy the no-slip condition accurately. In particular, for the unsteady and moving boundary flow cases the force and torque calculated with improper no-slip condition may produce significant error in the motion calculation of the moving objects. In addition, the sub iteration scheme enhances the computational time and cost.

To avoid the matrix calculation and reduce the iteration/computational cost, the present study is motivated for developing an efficient algorithm which satisfies the no-slip boundary condition and evaluates the accurate body force acting on the solid boundary at several flow situations.

1.3 Lattice Boltzmann method

In recent years, LBM has been a promising alternative over the traditional NS equations based fluid solvers and successfully applied to number of hydrodynamic problems. Unlike to the conventional CFD schemes that solves the macroscopic variables such as density, velocity and pressure using the Navier-Stokes equations, LBM solves the evolution of particle density distribution function with global streaming and local collision processes, using the microscopic kinetic equation (Boltzmann equation). The macroscopic fluid variables are then derived through moment integration of the distribution function at the lattice nodes. The kinetic nature of the LBM provides four

distinct advantageous over the traditional CFD schemes. First, the linear convection operator (or streaming process) of LBM in phase space (or velocity space) greatly reduces the computational effort compare to its nonlinear counterpart in NS equations. The simple linear convection in combination with a relaxation process (or collision process) recovers the nonlinear macroscopic advection through the multi-scale expansion. Second, in LBM the pressure is obtained from simple equation of states, whereas in the incompressible NS equations, pressure is derived using the Poisson equation with velocity strains which involves additional numerical difficulties and requires special treatment such as iterations or relaxation methods. Third, LBM follows minimum set of particle velocities in phase space in comparison to the traditional kinetic theory with the Maxwell equilibrium distribution, where the statistical averaging process requires information from the whole velocity phase space. Four, the algebraic form of the governing lattice Boltzmann equation (LBE) simplifies the computational effort in numerical code development and allows parallelisation for faster computation (Chen et al. (1996)).

The LBM was initially developed to address the drawbacks of the primitive gas kinetic scheme, lattice gas cellular automata (LGCA) (Frisch et al. (1986)), which suffers large statistical noise, non-Galilean invariance, unphysical velocity dependent pressure and large numerical viscosity. Unlike the Boolean particle variables in LGCA, a continuous single particle density distribution function with Maxwell Boltzmann equilibrium distribution function was proposed in LBM (McNamara and Zanetti (1988); Higuera and Jiménez (1989)), which neglects: the individual particle motion and particle-

particle correlation in the kinetic equations. This improved process removes the statistical noise and preserves the Galilean invariance. Later, Koelman (2007) and Qian et al. (1992), have also suggested that the particle distribution is close to the local equilibrium state and shifted by Bhatnagar-Gross-Krook (BGK) relaxation process. The linear collision BGK operator simplifies the computational process and enhances the numerical efficiency. Due to its simplicity, over the last few decades LBM has been widely applied to simulated incompressible flows (Succi et al. (1991); Hou et al. (1995); Mei et al. (2000); Wang et al. (2014)), compressible flows (Sun (2000); Hinton et al. (2001); Yan et al. (2006); Chen et al. (2014)), multi-component/multi-phase flows (He et al. (1999); Luo and Girimaji (2002); Lee and Lin (2005); Zheng et al. (2006); Huang et al. (2014)), particulate flows (Ladd (1993); Ladd (1994a); Ladd (1994b)), flows through porous media (Tölke et al. (2002); Pan et al. (2004); Ginzburg (2008); Taghilou and Rahimian (2014)), turbulent flows (Benzi and Succi (1990); Teixeira (1998); Yu et al. (2006); Touil and Ricot (2014)), electro-kinetic flows for colloids (Ladd and Verberg (2001); Cates et al. (2004); Adhikari et al. (2005)), magneto hydrodynamics (Chen and Shi (2005); Pattison et al. (2008)), viscoelastic flows (Boger (1987); Malaspinas et al. (2010)) and micro channel flows (Lim et al. (2002); Chen and Tian (2009); Verhaeghe et al. (2009); Shi and Tang (2014)).

In the standard LBM, the discretization of the phase space is coupled with the discretization of the momentum space, such that the minimal advection distance of the density distributions in the single time step must be equal to the minimal lattice separation. This limits LBM applicability to only uniform Cartesian mesh, which makes LBM not so efficient (in case of uniform fine

grid) or accurate (in case of uniform coarse grid) to attain the high resolution solutions. One of the alternatives for this defect is to decouple the computational mesh from the discretization of momentum space and use an interpolation-supplemented LBM (ISLBM) (He et al. (1996)) to determine the streaming of the density distribution in the new time level. Shu et al. (2003) have proposed an improved interpolation technique using Taylor series expansion in spatial direction with least square optimisation LBM (TLLBM). Although the expansion coefficients only depends on the mesh coordinates and lattice velocities, but the storage memory required is enhanced significantly in TLLBM. Recently, a second order accurate Lagrangian interpolation based LBM (LILBM) was introduced by Wu and Shu (2010) that simplifies the TLLBM interpolation technique to algebraic form and reduces the number of stored coefficient. We have followed LILBM in the present numerical simulations for the case of non-uniform meshed computational domain.

1.4 Thermal lattice Boltzmann method

Although LBM has been explicitly employed for number of isothermal fluid flow simulations but it has not gain similar attention in thermal flow cases. This is because, incorporating the temperature condition into the lattice equilibrium is not straightforward while using the standard lattice framework and simultaneously satisfying the multi scale moment integrals to recover the NS equations. At present, two distinct constructive approaches are available to model thermal lattice Boltzmann (LB) scheme. In the first approach, (also known as multispeed approach) (Chen et al. (1994); Watari and Tsutahara

(2004)) the local energy conservation and isotropy is satisfied together with higher number of discrete lattice velocities/off-lattice velocity sets and higher order velocity terms in the equilibrium distribution functions. The basic idea behind the multispeed thermal LB model is reasonably simple but it is onerous to define the parameters in the equilibrium distribution functions. Also the model experiences severe numerical instabilities and only suitable for low temperature range (McNamara et al. (1995); Pavlo et al. (1998)). In the second approach, (also known as double population approach) (He et al. (1998); Guo et al. (2002); Li et al. (2008)) instead of the original single particle distribution function that describes the evolution of the density, momentum and temperature field simultaneously, a separate distribution function is followed to describe the temperature/energy, which produces a better numerical stability. A sub-variant of the double population approach is passive scalar approach (Peng et al. (2003); Li et al. (2008)), where the temperature is governed by an advection-diffusion equation under the condition that both compression work and viscous heat dissipation are negligible. This assumption is only valid in the incompressible limit with low Prandtl/Eckert number. Among other thermal LB model, a thermal lattice Boltzmann flux solver (Wang et al. (2014)), a Taylor series expansion based thermal LBM (Shim and Gattignol (2011)) and a consistent energy conservation based LBM (Ansumali and Karlin (2005)) are proposed in recent years, but due to mathematical complexity these thermal LB schemes (Ansumali and Karlin (2005); Shim and Gattignol (2011); Wang et al. (2014)) are difficult to implement. In our present simulation studies we have utilised the modified double population based thermal LBM (Peng et al. (2003)).

1.5 Coupled immersed boundary – lattice Boltzmann method

The first coupled immersed boundary – lattice Boltzmann method (IB – LBM) was introduced by Feng and Michaelides (2004) to simulate the rigid particle motion. The profound key similarities between LBM and IBM have initiated this coupling process where instead of re-meshing the fluid domain, both the methods use a fixed Cartesian mesh. Here, the lattice grids represent the flow field and the boundary points represent particle surface. This IB – LBM scheme (Feng and Michaelides (2004)) is similar to the feedback forcing IBM (Lai and Peskin (2000)) where LB equations are solved instead of NS equations. Later, they have proposed an explicit diffuse interface scheme (Feng and Michaelides (2005)) to simulate 3D particulate flow. However, in their direct forcing IB – LBM, additional NS equations are solved for evaluation of the boundary forces. Dupuis et al. (2008) have proposed a pure direct forcing IB – LBM scheme where only LB equations are utilised to evaluate the boundary force density as well as to solve the fluid flow. To enhance the mesh resolution and numerical accuracy, a multi-block IB – LBM was developed by Peng et al. (2006) and Sui et al. (2007) and they have simulated the flow past aerofoil and deformable moving blood cells respectively. Niu et al. (2006) have proposed a momentum exchange based IB – LBM to simulate the incompressible flow where the body force is determined using Newton's laws of momentum conservation.

However, in the direct forcing IB – LBM (Feng and Michaelides (2005); Peng et al. (2006); Sui et al. (2007); Dupuis et al. (2008)) the kinetic nature of the LBM is neglected where the used lumped forcing LB equation does not recover the NS equation with second order accuracy. In contrast, the split forcing/implicit velocity correction based IB – LBM (Guo et al. (2002); Wu and Shu (2009); Kang and Hassan (2011)) removes the additional force divergence and time derivative terms and suitably recovers the NS equation with second order accuracy. But as discussed in section 1.2.1, the proposed implicit velocity correction IB – LBM (Wu and Shu (2009); Wu and Shu (2010); Wu and Shu (2012)) may demands for complex matrix operations that inhibits the computational performance and restrict the applicability to simple 2D problems, at the same time the alternative multi-direct forcing IBM (Luo et al. (2007); Wang et al. (2008)) requires higher computational resources and time. Therefore, in this study we focused on development of an efficient and accurate alternative IB – LBM approach.

In comparison to the athermal coupled IB – LBM schemes, very limited work is found in the literature for the thermal flow problems. Among these the notable ones are (Jeong et al. (2010); Kang and Hassan (2011); Seta (2013)). Similar to the introduction of the forcing term in the momentum equations, a heat source term is incorporated in the energy equation to satisfy the no-jump temperature boundary condition. The difference between the given temperature and the computed one at the Lagrangian boundary point is mapped back to the Eulerian mesh using the same idea as traditional feedback forcing IBM (Peskin (1977)). The explicit computation of the heat source term may create the similar defects as athermal IBM (see in section 1.2.1), where

the possibilities of non-physical solutions and isotherm penetration arose with unsatisfied boundary conditions. This further motivate us to propose an efficient implicit IB – LBM scheme for thermal flow problems such that both velocity and temperature boundary conditions are accurately satisfied.

1.6 Applications in thermal and moving boundary problems using immersed boundary – lattice Boltzmann method

1.6.1 Natural convection in a complex cavity

Natural convection has been a topic of research since the last century. The motivation of these researches was the desire and need to understand the fundamentals of physics and their wide industrial applications, such as in building insulation, cooling of electronic instruments, solar panel collector-receivers and cooling systems of nuclear reactors etc. The natural convection process can be broadly categorised into three major groups which are the convection processes from: 1) a heat source exposed to infinitely large cold surroundings (Alansary et al. (2012)), 2) differentially heated walls of an enclosed cavity (De Vahl Davis and Jones (1983); Raji et al. (2013)) and 3) a heat source in an enclosure (Deng (2008); Kalyana Raman et al. (2012)). In the present study, we have focused on the natural convection process in an enclosure with an eccentric discrete heat source where only limited works are available in the literature. This complex cavity situation has importance in engineering implications, particularly in the electronic PCB cooling and

microelectronic fabrication industries. The predominant factors driving this natural convection process are the Rayleigh number (Ra), Prandtl number (Pr) and aspect/blockage ratio (η) of the discrete heat source width to enclosure face length.

Kim et al. (2008) have investigated the natural convection from an eccentric hot circular cylinder placed inside a cold enclosure at different Ra. When the hot cylinder is displaced along the vertical centreline of the enclosure, the flow pattern and heat transfer rate is altered with formation of additional thermal cells. A similar study is performed by Hussain and Hussein (2010) for an eccentric circular cylinder with constant heat flux boundary condition and later Lee et al. (2010) have extended the work by reporting the thermal plumes and Nusselt number (Nu) variations for a horizontal and diagonal eccentric displacement of a hot circular cylinder. Among other studies Ghaddar (1992), Cesini et al. (1999) and Shu et al. (2001) have discussed the natural convection process in an air ($Pr = 0.71$) filled square enclosure with concentric/eccentric circular heat sources. In their studies, the qualitative/quantitative heat transfer rate and fluid flow pattern are depicted as functions of Ra (in the range $10^3 - 10^6$) and η (in the range $0.06 - 0.48$). But in practice, the discrete heat source may not be only limited to a circular shape. Recently, Bararnia et al. (2011) and Nabavizadeh et al. (2012) have extended the natural convection studies for elliptical ($\eta = 0.6$ and Ra between $10^3 - 10^6$) and sinusoidal ($\eta = 0.4$ and Ra between $10^3 - 10^6$) shaped heat sources. Alternatively, the heat source may have sharp edges with a square/rectangular shape. The geometrical difference between a circular and square-shaped heat

source alters the flow separation point (corners in the square shape), and hence a change of flow regime and heat transfer rate is expected.

Among the previous study reports on the square shaped heat source (or square cylinder), Asan (2000) has described the 2D natural convection process between two concentric isothermal square cylinders for $Pr = 0.7$ and Ra in the range $10^3 - 10^6$. Observed results in his study suggest that isotherms and flow patterns are greatly influenced by the dimensional ratio (η) of the square cylinders (1/5, 3/10 and 3/5) and Ra . Ha et al. (2002) studied the natural convective heat transfer from an adiabatic and isothermal square cylinder ($\eta = 1/\pi$). They performed steady and unsteady simulation for $Pr = 0.7$ and Ra in the range $10^3 - 10^6$. The flow pattern was observed to change from a steady symmetrical regime to an unsteady non-symmetrical regime with an increase in Ra . Mahapatra et al. (2013) have extended Ha et al. (2002) work, to determine the heat transfer enhancement and entropy generation in the enclosure with multiple square heat sources and Ra . Kumar De and Dalal (2006) have considered the natural convection around a hot tilted (inclination angle = 45 deg) square cylinder for Ra between $10^3 - 10^6$ and air ($Pr = 0.7$) as working fluid. The flow and heat transfer features for different enclosure aspect ratios (i.e. height/length between 0.5 – 2.0) and different boundary conditions on the hot square cylinder are presented in their study. They have shown that the uniform wall temperature is quantitatively different from the uniform heat flux condition.

Existing literature suggests that a systematic investigation of the natural convection process from an inclined or eccentric square heat source has not

made. These situations are of practical importance where the flow and heat transfer rates are expected to alter with Ra , inclination angle (θ) and eccentricity (χ). Therefore, in this study we have used the developed IB – LBM coupled scheme to characterise the natural convection process with above mentioned parameters in an enclosure that contains an inner square heat source.

1.6.2 Particle sedimentation

Fluid-particle interactions occur in many practical applications, such as chemical, environmental, geological, aerospace, nuclear, oil and gas engineering and biological science. Dispersion of pollutants in rivers, seas or in atmospheres, fluidized bed reactor, colloidal suspension, cell transport in arteries, processing mineral ores and transportation of settling slurries in a pipeline are few examples of this branch of physics. The inclusion of the solid particle suspension in the fluid domain is difficult to analyze in either theoretical or experimental techniques, where the hydrodynamic interactions of the fluid phase are complexly coupled with the Newtonian dynamics of the moving particle. One of the earliest theoretical works on the sedimentation behaviour of a pair of spherical particles through a viscous fluid was carried out by Smoluchowski (Smoluchowski (1911); Smoluchowski (1912)) for small Reynolds number and small ratio of the sphere radius to separation distance between their centres. The limitation of the theoretical analysis at high Reynolds number leads numerous researchers to conduct experimental and CFD investigations to better understand the sedimentation phenomena of the particles.

In recent years, experimental investigations on sedimentation of small clusters of spherical particles at low Re (10^{-4} to 10) were performed by Jayaweera et al. (1964). They found that as Re increases ($Re > 0.05$), the two spheres falling side by side may rotate inwards and separate. When the equal-sized spheres of $Re > 1$ fall vertically with one behind the other, the rear one accelerated into the wake of the leader, rotates around it and separates. Fortes et al. (1987) had extended the work for high Re ($Re > 500$) by conducting experiments on two spherical particles sedimentation in both two and three dimension fluidisation bed. They have characterised the non-linear wake interactions between the spherical particles as Drafting – Kissing – Tumbling (DKT) where the trailing sphere is “drag” into the wake of the leading sphere (also known as drafting) which subsequently leads to them touching momentarily (also known as kissing) before tumbling to break the unstable kissing equilibrium state and then separates away. This observation has raised two important questions: 1) *What are the driving hydrodynamic forces or couples that are responsible for the tumbling mechanism?* 2) *How do the separated settling spheres behave after the tumbling action?*

In an attempt to answer the first question, Hu et al. (1992) compared the tumbling mechanism of the spheres with that of settling of a long body in a Newtonian fluid. They reasoned that the fall of the long body experiences a turning couple induced by pressure distributions, stagnation and separation points, that puts its broad side perpendicularly to the stream, which and has close similarity to the tumbling of the kissing spheres. Although these two cases may qualitatively exhibit some degree of similarities, they differ in the magnitude of the forces and turning couple on the spheres due to the fact that

tumbled spheres may separate from each other, which is distinctly different from the fixed mass or geometry of the long body. In the later years, Joseph et al (Joseph et al. (1992); Joseph et al. (1994)) have attributed the tumbling action in Newtonian and viscoelastic fluids to the competition between inertia and normal stress terms that leads to the production of repulsive or attractive force among the spheres. They believed that the nature of this force, repulsive or otherwise, defines their tumbling action. To better understand how these forces are generated in Newtonian fluid, numerous researchers like Kim et al. (1993), Folkersma et al. (2000), Schouveiler et al. (2004) have performed numerical simulations on three dimensional flow past two identical stationary spheres held fixed relative to each other and with their connecting centre line normal to uniform stream. They observed that the wake structures for small centre spacing differ significantly from that for large centre spacing, and postulated that this generates lift, drag and moment that led to repulsion or attraction among the spheres. Although the study of fixed sphere wake interaction is useful in the characterisation of particle-laden flow, the analogy is incomplete without taking into consideration the additional inertia effects experienced by freely falling spheres. Moreover, the unsteady nature of the hydrodynamic forces during tumbling action may not be clearly identified by the simple flow past the tandem stationary spheres (Kim et al. (1993); Schouveiler et al. (2004)). We believe that a deeper of the understanding of DKT action can be made if we can identify temporal evolution of the unsteady hydrodynamic force on the settling spheres which motivated us to carry out the present study.

Another motivation is related to the second question regarding the behaviour of separated settling spheres after the tumbling action. Hu et al. (1992) have observed that tumbled spheres attain a steady equilibrium position when the trailing sphere locks itself in the wake of the leading one, and thereafter move together with certain centre alignment analogous to the flying bird flock. In a separate numerical study, Singh et al. (1989) have investigated the stable arrangement of two dimensional particles in periodic arrays subjected to a cross flow and noted that the arrays of the particles are stable only when they have equal centre spacing and arranging a line normal to the flow direction. They further identified that all other particle positions are prone to wake interactions and drafting. Although they qualitatively compare their two dimensional results with the three-dimensional regimes, we believe that the comparison may not reveal the whole story about three-dimensional spheres interaction. The desire to address this issue motivated us to conduct the present 3D studies.

Among numerical studies the fluid-particle interactions has been simulated using either finite volume method (FVM) or finite element method (FEM) (Hu (1996); Hu et al. (2001); Prosperetti and Oğuz (2001)) where the fluid phase is described by Navier-Stokes (NS) equations, while the description of the particle phase such as position and velocity are traced in Lagrangian frame. However, in generating geometrically adaptive mesh and projection of the fluid variables from the old to new mesh at every time step makes these methods computationally expensive. Alternatively, in LBM platform Ladd (1994a; 1994b), Behrend (1995), Aidun and Lu (1995), Qi (1999) have implemented the interactions between fluid and particle through momentum

exchange (bounce back rule). However, in the momentum exchange schemes the force curve as a function of time is not smooth and may oscillate dramatically. To overcome the drawbacks, the newly developed coupled IB – LBM scheme is utilised for the present 2D and 3D particle sedimentation studies.

1.7 Objective of the thesis

The primary objective of this thesis is to develop a new version of the IB – LBM scheme that overcomes the shortcomings of the existing/conventional IB – LBM solver to simulate the fluid flow problems including stationary and moving boundary problems. The work is also aimed to develop an efficient IB – LBM solver for thermal flow scenarios and later extension of the algorithm for studying 3D flow cases. The more specific aims are specified below.

- 1) To develop a novel flexible forcing IB – LBM scheme for fluid – solid interactions that avoids the numerical defects such as non-physical streamline penetrations into the solid boundary; improper hydrodynamic force and torque calculations. In contrast to the conventional IB – LBM scheme where the body force density term is explicitly defined, we proposed a simplified algorithm where the mathematical formulations keep the benefits of the implicit velocity corrections and avoid the complicated matrix operations.
- 2) To apply the developed flexible forcing IB – LBM scheme to investigate for the first time the single and two particle

sedimentation process in a constricted channel with semicircular constrictions. Further extensions of the parametric studies are performed by varying density of the solid particles, viscosity of the fluid, shape and size of the constriction.

- 3) To develop a new version of flexible forcing IB – thermal LBM scheme which uniquely combines the non-body-fitted IBM technique with the mesoscopic thermal LBM solver. While applying IBM to thermal flow case, apart from momentum equation an extra energy equation is solved where the improper temperature boundary condition may leads to non-physical isotherm penetration into the solid boundary. The proposed scheme accurately satisfies the temperature boundary condition with implicit definition of the heat source/sink density term.
- 4) To apply the developed flexible forcing IB – thermal LBM scheme to investigate the natural convection in complex cavities formed by an eccentric/inclined square heat source and a surrounding enclosure. Parametric studies are also performed for different Rayleigh number, eccentricity and inclination angle.
- 5) To apply the proposed flexible forcing IB – LBM for solving three dimensional flow cases and to study the stationary and moving boundary problems. After validating the solver, the classical physics relating the dynamics of two spheres settling in a viscous liquid column has been studied. To have concrete comparisons further experimental verifications are conducted.

1.8 Outline of the thesis

The organisation of the thesis is outlined below.

In Chapter 2, the standard LBM and IBM are introduced together with the coupled IB – LBM schemes for two dimensional flows. A novel flexible forcing IB – LBM scheme is presented to overcome the defects of the conventional IB – LBM scheme. The algorithm is developed to solve the stationary as well as moving boundary flow problem. The numerical accuracy of the proposed scheme is evaluated by performing test case simulations: 1) Taylor – Green decaying vortex and 2) Lid driven cavity. To further validate the present solver benchmark test cases such as, flow past circular cylinder, motion of a neutral buoyant particle in a linear shear flow and particle sedimentation are simulated.

In Chapter 3, the proposed flexible forcing IB – LBM scheme is extended to study the particulate flow in a constricted channel. In this numerical study, it is the first time we have characterized the sedimentation of single and two particles in a 2D channel with symmetric semicircular constriction walls. The effects of density of the solid particles, viscosity of the fluid, shape and size of the constriction are investigated and the observations and results are discussed in detail.

In Chapter 4, a novel flexible forcing IB – LBM scheme is proposed for modelling the fluid – structure interactions in the incompressible, viscous flow domain where the thermal effects are accounted. The detail description of the

numerical model is provided and the numerical accuracy/validations are checked by performing a number of benchmark flow case simulations.

In Chapter 5, the developed flexible forcing IB – thermal LBM is applied to study the natural convection process in complex cavity scenarios, where an eccentric or inclined square heat source and a surrounding enclosure together form the complex cavity. The flow pattern and heat transfer rate in the annulus of the enclosure are determined as functions of Rayleigh number (Ra), eccentricity and inclination angle of the inner square heat source and are discussed in details here.

In Chapter 6, the proposed flexible forcing IB – LBM scheme is extended for simulation of 3D flows. In particular stationary and moving boundary flow problems such as flow past a stationary sphere and sedimentation of single and two spheres are simulated and presented in this chapter. The obtained results are found in good agreement with the previous published data.

In Chapter 7, the 3D, IB – LBM code is applied to simulate the dynamics of two spherical particles sedimentation. In details, Drafting–Kissing–Tumbling (DKT) of the spheres and their trajectories are discussed. Experimental investigations are also performed to further validate the numerical observations.

In Chapter 8, we have concluded the present work with suggestions/recommendations for future extensions.

Chapter 2

A 2D Flexible Forcing Immersed Boundary and Lattice Boltzmann Method¹

In this chapter a two dimensional hybrid numerical scheme is introduced for modelling of fluid – solid interactions in an incompressible, viscous flow domain with stationary and moving solid boundaries. The developed scheme describes a unique way of coupling the immersed boundary (Peskin (1977)) concept in the framework of the lattice Boltzmann method (Succi et al. (1991)). As discussed in the previous Chapter 1, the conventional IB – LBM schemes often suffer from the numerical defects such as non-physical streamline penetration into the solid boundary; improper hydrodynamic force and torque calculations, where the body force density term is explicitly defined. In order to address these drawbacks Wu and Shu (2009) have discussed an implicit velocity correction based IB – LBM, where the mathematical formulation demands: a significant computational memory

¹ Part of this work has been published as:

Dash SM, Lee TS and Huang H. (2014). "A novel flexible forcing hybrid IB-LBM scheme to simulate flow past circular cylinder." International Journal of Modern Physics C **25**(01): 1340014.

usage and formation/inversion of a complex matrix. In contrast, our proposed flexible forcing algorithm simplifies the formulation while keeping the benefits of the implicit velocity corrections and at the same time avoids the complicated matrix operations. The detail mathematical formulations are outlined in the followings. The numerical accuracy and validation of the present scheme are checked by performing a number of benchmark flow case simulations.

2.1 Numerical methodology

2.1.1 Lattice Boltzmann method

As a successor of lattice gas cellular automata (LGCA), lattice Boltzmann method (LBM) retains the advantages of kinetic – based approach for the fluid flow simulations and removes the shortcomings of LGCA such as statistical noise and non-Galilean invariance. The LBM decomposes the continuum flow field into pockets of fluid particles which can only stay at rest or propagate to the neighbouring lattice sites in accordance with certain lattice velocity models and then exhibit local collision to conserve the mass, momentum and energy of the flow. To better understand LBM, at first we briefly introduced the continuous Boltzmann equation.

The Boltzmann equation is a well accepted mathematical model for describing the fluid in microscopic level. The evolution of single particle density distribution function $f(\mathbf{x}, \boldsymbol{\xi}, t)$ in the phase space $(\mathbf{x}, \boldsymbol{\xi})$ is governed by an integro – differential Boltzmann equation (ref. Eq.(2.1)).

$$\frac{\partial f}{\partial t} + \boldsymbol{\xi} \frac{\partial f}{\partial \mathbf{x}} + \mathbf{F} \frac{\partial f}{\partial \boldsymbol{\xi}} = Q(f), \quad (2.1)$$

where \mathbf{x} is the position, $\boldsymbol{\xi}$ is the particle velocity and \mathbf{F} is the body force. $Q(f)$ is the integral collision model as shown in Eq.(2.2), which describes the collision between two particles and the transformation of the incoming velocities $\boldsymbol{\xi}_1, \boldsymbol{\xi}_2$ to outgoing ones $\boldsymbol{\xi}'_1, \boldsymbol{\xi}'_2$ respectively.

$$Q(f(f_1, f_2)) = \int d\boldsymbol{\xi}_2 \int \sigma(\Omega) |\boldsymbol{\xi}_1 - \boldsymbol{\xi}_2| \left[f(\boldsymbol{\xi}'_1) f(\boldsymbol{\xi}'_2) - f(\boldsymbol{\xi}_1) f(\boldsymbol{\xi}_2) \right] d\Omega. \quad (2.2)$$

Due to the complex integral form of $Q(f)$, the collision operator is usually approximated by an alternate single relaxation time Bhatnagar–Gross–Krook (BGK) model (Bhatnagar et al. (1954); Qian et al. (1992); Koelman (2007)).

$$Q_{BGK}(f) = -\frac{f - f^{eq}}{\lambda}, \quad (2.3)$$

where λ is the relaxation time associated with collision relaxation period to attain a local equilibrium. The notion of local equilibrium is important for recovering the hydrodynamic behaviour from the continuous Boltzmann equation where the equilibrium distribution function follows the Maxwellian form,

$$f^{eq}(\mathbf{x}, \boldsymbol{\xi}, t) = \rho (2\pi RT)^{-D/2} \exp\left[-\frac{(\boldsymbol{\xi} - \mathbf{u})^2}{2RT}\right]. \quad (2.4)$$

R is the gas constant, T is the temperature, D is the spatial dimension. ρ and \mathbf{u} are the macroscopic density and velocity, respectively.

Now, if we discretise the continuous Boltzmann equation without the body force term (as in Eq.(2.1)) and with BGK approximation over a finite sets of lattice velocities \mathbf{e}_i , then Eq.(2.1) can be simplified to,

$$\frac{\partial f_i(\mathbf{x}, t)}{\partial t} + \mathbf{e}_i \frac{\partial f_i(\mathbf{x}, t)}{\partial \mathbf{x}} = -\frac{f_i(\mathbf{x}, t) - f_i^{eq}(\mathbf{x}, t)}{\lambda}, \quad (i=0,1,2,\dots,N), \quad (2.5)$$

where i represents the different lattice directions up to N , and the corresponding lattice velocities are \mathbf{e}_i . Integrating Eq.(2.5) from t to $t + \delta t$, with second order accuracy we get,

$$f_i(\mathbf{x} + \mathbf{e}_i \delta t, t + \delta t) = f_i(\mathbf{x}, t) - \frac{f_i(\mathbf{x}, t) - f_i^{eq}(\mathbf{x}, t)}{\tau}, \quad (i=0,1,2,\dots,N), \quad (2.6)$$

where $\tau = \lambda/\delta t$ is the non-dimensional relaxation parameter. The above equation is also referred as lattice Boltzmann equation (LBE). The equilibrium distribution function in LBE is obtained by expanding the Maxwell-Boltzmann distribution function (ref. Eq.(2.4)) using Taylor series expansion of \mathbf{u} up to second order accurate, as shown in the following.

$$\begin{aligned}
 f^{eq}(\mathbf{x}, \boldsymbol{\xi}, t) &= \rho(2\pi RT)^{-D/2} \exp\left[-\frac{(\boldsymbol{\xi} - \mathbf{u})^2}{2RT}\right] \\
 &= \rho(2\pi RT)^{-D/2} \exp\left[-\frac{\boldsymbol{\xi}^2}{2RT}\right] \exp\left[\frac{2\boldsymbol{\xi} \cdot \mathbf{u} - \mathbf{u}^2}{2RT}\right] \\
 &= \rho(2\pi RT)^{-D/2} \exp\left[-\frac{\boldsymbol{\xi}^2}{2RT}\right] \left(1 + \frac{\boldsymbol{\xi} \cdot \mathbf{u}}{RT} + \frac{(\boldsymbol{\xi} \cdot \mathbf{u})^2}{2(RT)^2} - \frac{\mathbf{u}^2}{2RT}\right) + o(\mathbf{u}^3).
 \end{aligned} \tag{2.7}$$

With the discrete lattice velocities \mathbf{e}_i and definition of sound speed as $c_s^2 = RT$, the Eq.(2.7) can be rewritten as,

$$f_i^{eq}(\mathbf{x}, \mathbf{e}_i, t) = W_i \rho \left(1 + \frac{\mathbf{e}_i \cdot \mathbf{u}}{c_s^2} + \frac{(\mathbf{e}_i \cdot \mathbf{u})^2}{2c_s^4} - \frac{\mathbf{u}^2}{2c_s^2}\right), \quad (i=0,1,2,\dots,N), \tag{2.8}$$

where $W_i = \rho(2\pi RT)^{-D/2} \exp\left[-\frac{\mathbf{e}_i^2}{2c_s^2}\right]$, is the weighting factor.

The discrete lattice velocity models are usually represented as $DnQm$, where n is the spatial dimension and m is the number of lattice directions/velocities. A square lattice D2Q9 model (Qian, D'Humières et al. (1992)) (ref.Fig.2.1) is utilised in the present study where the corresponding lattice velocities and weighting factors are shown in Eq.(2.9).

$$\mathbf{e}_i = c \begin{cases} (0,0), & i=0, \\ (\pm 1,0), (0,\pm 1), & i=1-4, \\ (\pm 1,\pm 1), & i=5-8. \end{cases} \quad W_i = \begin{cases} 4/9, & i=0, \\ 1/9, & i=1-4, \\ 1/36, & i=5-8. \end{cases} \tag{2.9}$$

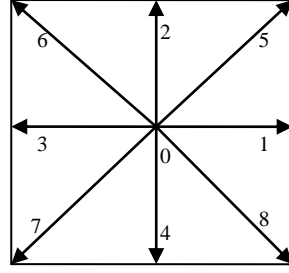


Fig.2.1. D2Q9 lattice model with respective lattice velocity directions.

The LBE recovers incompressible NS equation by multi-scale Chapman – Enskog expansion (Succi et al. (1991)) where the relaxation time is related with the kinematic viscosity as $\nu = (\tau - 0.5)c_s^2\delta t$. For evolution of the density distribution function f_i , the above LBE (Eq.(2.6)) can be implemented in two basic steps, *collision* and *streaming*.

$$f_i^{neq} = f_i(\mathbf{x}, t) - f_i^{eq}(\mathbf{x}, t), \quad (2.10)$$

$$f_i^+(\mathbf{x}, t) = f_i^{eq}(\mathbf{x}, t) + \left(1 - \frac{1}{\tau}\right) f_i^{neq}, \quad (2.11)$$

where f_i^{neq} is the non-equilibrium part of the density distribution function f_i and f_i^+ is the post-collision density distribution function. In the streaming step f_i^+ propagates to the neighbouring lattice node following the respective lattice velocity model.

$$f_i(\mathbf{x} + \mathbf{e}_i\delta t, t + \delta t) = f_i^+(\mathbf{x}, t). \quad (2.12)$$

After the collision and propagation steps the macroscopic density, momentum and pressure are calculated from the updated density distribution functions as shown below.

$$\rho = \sum_{i=0}^8 f_i, \quad \rho \mathbf{u} = \sum_{i=0}^8 \mathbf{e}_i f_i, \quad p = \rho c_s^2. \quad (2.13)$$

2.1.2 Immersed Boundary method

In the immersed boundary method (IBM) (Peskin (1977); Lai and Peskin (2000)), the solid boundary and fluid domain are independently discretised in a moving Lagrangian and a stationary Eulerian mesh respectively. In this decoupled mesh framework, the effects of the boundary are imposed in the fluid domain by a restoring force. The governing equations with such a force are solved in the whole computational domain. For a 2D, incompressible, viscous flow in the domain Ω which includes a closed loop immersed boundary Γ , (ref. Fig.2.2) the governing equations are,

$$\frac{\partial \rho}{\partial t} + \nabla \cdot \rho \mathbf{u} = 0, \quad (2.14)$$

$$\frac{\partial}{\partial t}(\rho \mathbf{u}) + \nabla \cdot (\rho \mathbf{u} \mathbf{u}) = -\nabla p + \nu \nabla \cdot \left[\rho \nabla \mathbf{u} + (\nabla \mathbf{u})^T \right] + \mathbf{f}, \quad (2.15)$$

$$\mathbf{f}(\mathbf{x}, t) = \int_{\Gamma} \mathbf{F}_B(s, t) \delta(\mathbf{x} - \mathbf{X}_B(s, t)) ds, \quad (2.16)$$

$$\frac{\partial \mathbf{X}_B(s, t)}{\partial t} = \mathbf{u}(\mathbf{X}_B(s, t), t) = \int_{\Omega} \mathbf{u}(\mathbf{x}, t) \delta(\mathbf{x} - \mathbf{X}_B(s, t)) d\mathbf{x}, \quad (2.17)$$

where the variables: ρ, \mathbf{u}, p, ν represent density, flow velocity, pressure and kinematic viscosity of the fluid respectively. \mathbf{x} and \mathbf{X}_B are Eulerian and Lagrangian mesh coordinates, \mathbf{f} and \mathbf{F}_B are the force density acting on the fluid and immersed boundary respectively. $\delta(\mathbf{x} - \mathbf{X}_B(s, t))$ is a Dirac delta

function. The above Eqs.(2.14) – (2.15) represent traditional NS equations with the force density \mathbf{f} that incorporates the solid boundary effects. Eq.(2.16) and (2.17) relates the immersed solid boundary Γ and fluid domain Ω by distributing the boundary force to the nearby fluid points and relating the boundary velocity with the fluid velocity. The boundary force $\mathbf{F}_B(s,t)$ on the segment $\mathbf{X}_B(s,t)$ is determined from the boundary configuration at time t as shown in Eq.(2.18), where \mathbf{S} satisfies the generalised Hooke's law.

$$\mathbf{F}_B(s,t) = \mathbf{S}(\mathbf{X}_B(s,t), t) \quad (2.18)$$

In summary the solution procedure of IBM can be realised as,

1. Use Eq.(2.18) to compute the Lagrangian boundary force density $\mathbf{F}_B(s,t)$.
2. Obtain the Eulerian force density \mathbf{f} using Eq.(2.16).
3. Solve Eqs.(2.14) – (2.15) with the force density \mathbf{f} to determine the updated Eulerian velocity field.
4. Using the Dirac delta function interpolation (Eq.(2.17)) transfer the Eulerian velocity to Lagrangian points.
5. Repeat the above steps (1) – (4) until the convergence achieved.

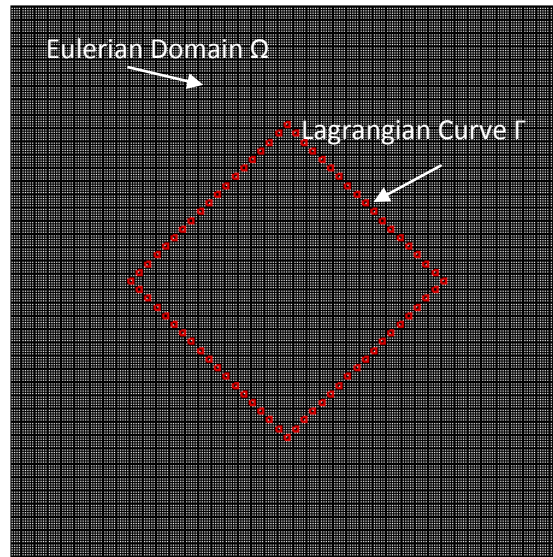


Fig.2.2. A two dimensional domain Ω containing an immersed boundary Γ .

2.1.3 Flexible forcing immersed boundary – lattice Boltzmann method

Due to similar computational implications of IBM and LBM with uniform Cartesian mesh in a flow domain, researchers have coupled these two methods together for solving fluid-structure interactions, and one of the earliest notable work in this direction is done by Feng and Michaelides (2004). When IBM is combined in the LBM framework, the governing Eqs.(2.14) – (2.15) change to Eq.(2.19).

$$f_i(\mathbf{x} + \mathbf{e}_i \delta t, t + \delta t) = f_i(\mathbf{x}, t) - \frac{1}{\tau} (f_i(\mathbf{x}, t) - f_i^{eq}(\mathbf{x}, t)) + F_i \delta t, \quad (i=0,1,2,\dots,8), \quad (2.19)$$

The above equation is a modified form of LBE (ref. Eq.2.6) where extra discrete body forces F_i are included along the lattice directions ‘ i ’

(ref.Fig.2.1), so as to incorporate the immersed boundary effect in the fluid domain.

To recover NS equation accurately, the correct definition of F_i is important. Various formulations of F_i was previously investigated by Huang et al. (2011) and Mohamad and Kuzmin (2010). They have showed that in case of single phase fluid problems the deviation of results was negligible with different formulation of F_i . In the present study, as we are only concerned about single phase fluid, hence a formula suggested by Guo et al. (2002) is adopted here. This definition retrieves the unsteady, second order NS equation accurately without any extra velocity – force divergence tensor terms (Kang and Hassan (2011)), when multi-scale Chapman – Enskog expansion is performed.

$$F_i = \left(1 - \frac{1}{2\tau}\right) W_i \left(\frac{\mathbf{e}_i - \mathbf{u}}{c_s^2} + \frac{\mathbf{e}_i \cdot \mathbf{u}}{c_s^4} \mathbf{e}_i \right) \cdot \mathbf{f}, \quad (2.20)$$

where \mathbf{f} in Eq.(2.20) is the force density at Eulerian fluid nodes, which is distributed from the force density of Lagrangian boundary points. This force density term can either be solved by an explicit or implicit time marching schemes. Ahlrichs and Dünweg (1999) and Nash et al. (2008) have followed the explicit computation to simulate the suspension of colloids. Also Kang and Hassan (2011) used the explicit approach to study flow past a circular cylinder. One of the drawbacks of the explicit time advancement scheme is that the boundary force density term is not explicitly involved in the actual calculation rather the velocity at the forcing node is directly replaced by the desired boundary velocity. As discussed in the previous section.1.2.1, this may

produce non-physical streamline penetration into the solid boundary with unsatisfied no-slip condition.

In contrast, in the implicit approach the force density term is calculated from the velocity correction in the predictor step and is later updated with the corrected velocity field such that the exact no-slip condition is satisfied. Therefore, in this study we have used the implicit approach where the descriptions are provided in the followings.

With the above definition of F_i in the Eq.(2.20), the macroscopic velocity field get shifted (Mohamad and Kuzmin (2010)) and is defined as,

$$\rho \mathbf{u} = \sum_{i=0}^8 \mathbf{e}_i f_i + \frac{1}{2} \mathbf{f} \delta t. \quad (2.21)$$

By defining, $\mathbf{u}^* = \sum_{i=0}^8 \mathbf{e}_i f_i / \rho$ an intermediate Eulerian velocity and

$\delta \mathbf{u} = (1/2\rho) \mathbf{f} \delta t$ an Eulerian velocity correction term; we can rewrite the

Eq.(2.21) as, $\mathbf{u} = \mathbf{u}^* + \delta \mathbf{u}$. Here, to perform implicit computation, the Eulerian velocity correction $\delta \mathbf{u}$ is kept unknown and is calculated such that the exact no-slip boundary condition is satisfied. Following the Dirac delta function interpolation the unknown Eulerian velocity correction $\delta \mathbf{u}$ can be derived from the unknown Lagrangian boundary velocity correction $\delta \mathbf{U}_B$ using Eq.(2.22).

$$\delta \mathbf{u}(\mathbf{x}, t) = \int_{\Gamma} \delta \mathbf{U}_B(\mathbf{X}_B, t) \delta(\mathbf{x} - \mathbf{X}_B) ds, \quad (2.22)$$

where the immersed boundary is represented using a set of Lagrangian coordinates $\mathbf{X}_B(s_k, t)$. s_k ($k=1,2,3,\dots,n$) are the positions of the Lagrangian co-ordinates. $\delta(\mathbf{x} - \mathbf{X}_B)$ is smoothly approximated by continuous Kernel distribution $D(\mathbf{x} - \mathbf{X}_B)$,

$$\delta(\mathbf{x} - \mathbf{X}_B^k) = D(\mathbf{x} - \mathbf{X}_B^k) = \frac{1}{h^2} \delta\left(\frac{x - X_B^k}{h}\right) \delta\left(\frac{y - Y_B^k}{h}\right), \quad (2.23)$$

where $\delta(r)$ is approximated using 2 point Dirac delta function (Peskin (1977)).

$$\delta(r) = \begin{cases} 1 - |r|, & |r| \leq 1, \\ 0, & |r| > 1. \end{cases} \quad (2.24)$$

Here, h is the Eulerian mesh spacing. Substituting the Eq.(2.23) into the Eq.(2.22), the velocity correction expression simplifies to an algebraic form,

$$\delta \mathbf{u}(\mathbf{x}, t) = \sum_k \delta \mathbf{U}_B^k(\mathbf{X}_B^k, t) D(\mathbf{x} - \mathbf{X}_B^k) \Delta s_k, \quad (2.25)$$

where Δs_k is the arc length of the Lagrangian boundary element.

In the view of mathematics, the no-slip boundary condition implies that the fluid velocity at the boundary point must be equal to the desired boundary velocity \mathbf{U}_B^{kd} at the same location. Using the concept of interpolation, the no-slip condition can be written as,

$$\mathbf{U}_B^{kd}(\mathbf{X}_B^k, t) = \sum_{x,y} \mathbf{u}(\mathbf{x}, t) D(\mathbf{x} - \mathbf{X}_B^k) \Delta x \Delta y, \quad (2.26)$$

where Δx and Δy are the mesh sizes in the horizontal and vertical direction of the computational domain. Substituting the intermediate velocity and Eulerian velocity correction in the Eq.(2.26) gives,

$$\begin{aligned} \mathbf{U}_B^{kd}(\mathbf{X}_B^k, t) = & \sum_{x,y} \mathbf{u}^*(\mathbf{x}, t) D(\mathbf{x} - \mathbf{X}_B^k) \Delta x \Delta y \\ & + \sum_{x,y} \sum_k \delta \mathbf{U}_B^k(\mathbf{X}_B^k, t) D(\mathbf{x} - \mathbf{X}_B^k) \Delta s_k D(\mathbf{x} - \mathbf{X}_B^k) \Delta x \Delta y. \end{aligned} \quad (2.27)$$

In the above equation, $\delta \mathbf{U}_B^k$ is kept unknown for an implicit forcing formulation and is obtained by solving Eq.(2.27). As we can see the evaluation of $\delta \mathbf{U}_B^k$ demands a formulation of coefficient matrix and its inversion (Wu and Shu (2009)). This requires a higher amount of memory usage as well as computational effort for sequential coding pattern. Further in case of moving boundary problems the formation/inversion of the coefficient matrix consumes a significant amount of computational time. These limitations make the scheme inefficient for 3D problems where the memory requirement and computational effort are enhanced by many fold.

To address the above issues, here we have proposed a simple solution for 2D flow case, whose extension to 3D domain will be discussed in the later chapter. If we analyse the Eq.(2.26), in most of the cases the desired boundary velocity \mathbf{U}_B^{kd} is known to us (i.e. equals to zero for stationary object or a value calculated using Newton's laws of motion for a moving object). Hence, the interpolated Eulerian velocity field (RHS of Eq.(2.26)) must match with \mathbf{U}_B^{kd} when the exact no-slip condition is satisfied. In case of IBM auto-satisfaction

of the no-slip condition is impractical, because the immersed boundary is defined on a moving Lagrangian mesh whereas the flow field is defined on a stationary Eulerian mesh, and the node points do not necessarily match. This creates a difference between LHS and RHS of Eq.(2.26), and the amount of deviation (otherwise called as velocity correction) must be accounted to satisfy the no-slip condition.

In the proposed flexible forcing algorithm a single Lagrangian velocity correction term $\delta\mathbf{U}_B^k(\mathbf{X}_B^k, t)^m$ is included in Eq.(2.26) to satisfy the desired velocity boundary condition (ref. Eq.(2.28)) where the amount of Lagrangian velocity correction required is given in Eq.(2.29).

$$\mathbf{U}_B^{kd}(\mathbf{X}_B^k, t) = \sum_{x,y} \mathbf{u}(\mathbf{x}, t) D(\mathbf{x} - \mathbf{X}_B^k) \Delta x \Delta y + \delta\mathbf{U}_B^k(\mathbf{X}_B^k, t)^m, \quad (2.28)$$

$$\delta\mathbf{U}_B^k(\mathbf{X}_B^k, t)^m = \mathbf{U}_B^{kd}(\mathbf{X}_B^k, t) - \sum_{x,y} \mathbf{u}(\mathbf{x}, t) D(\mathbf{x} - \mathbf{X}_B^k) \Delta x \Delta y, \quad (2.29)$$

This formulation retains the idea of implicit velocity correction (Wu and Shu (2009)) and is mathematically much simpler than Eq.(2.27), that reduces the computational efforts for the new code development and memory storage demand.

Following the above correction measures, one may not ensure the no-slip condition at all the boundary points in a single turn as the boundary velocity correction is linked with the Eulerian velocity correction (shown in Eq.(2.25)). Hence, an additional sub-iteration update scheme is imposed to satisfy the no-slip condition within a convergence limit. This further ensures that when

Eulerian velocities are interpolated back to the Lagrangian boundary nodes, they will satisfy the no-slip condition within a tolerance of the $O(\delta\mathbf{U}_B^k)$. The convergence criterion (CC) is set in Eq.(2.30), where m is the sub-iteration number until the CC is satisfied.

$$\left| \delta\mathbf{U}_B^k(\mathbf{X}_B^k, t)^m \right| \leq 10^{-6}. \quad (2.30)$$

It is worth to note that the CC is a case dependent term which can be adjusted to any higher/lower order tolerance based on complexity of the problem, required accuracy of the final result and available computational resources. This approach has certain similarities with the multiple forcing schemes (Luo et al. (2007); Wang et al. (2008); Kang and Hassan (2011)) where fixed number of sub-iterations is adopted. The differences in our scheme are: the sub-iteration depends on CC and its number can be varied till the exact no-slip boundary condition is satisfied. This makes the scheme flexible and computationally efficient by restricting the unnecessary sub-iteration. Again in the case of unsteady and moving boundary problems, use of the fixed sub-iteration may not yield the correct no-slip condition at each time step. Then the force and torque calculations are questionable. To overcome these defects, the proposed flexible sub-iteration scheme is a suitable alternative. This approach also reduces computational effort and storage demand by avoiding the matrix calculation and ensures the order of accuracy to $O(\delta\mathbf{U}_B^k)$.

We further tried to reduce the number of sub-iterations in the proposed flexible forcing scheme by introducing a successive relaxation parameter

(SRP), ‘ ε ’ as shown in Eq.(2.31). ε is set in the range of 0 – 1. The effects of SRP and CC selection will be discussed in the subsequent sections.

$$\left. \delta \mathbf{U}_B^k(\mathbf{X}_B^k, t) \right|^m = (1 - \varepsilon) \left. \delta \mathbf{U}_B^k(\mathbf{X}_B^k, t) \right|^{m-1} + \varepsilon \left. \delta \mathbf{U}_B^k(\mathbf{X}_B^k, t) \right|^m. \quad (2.31)$$

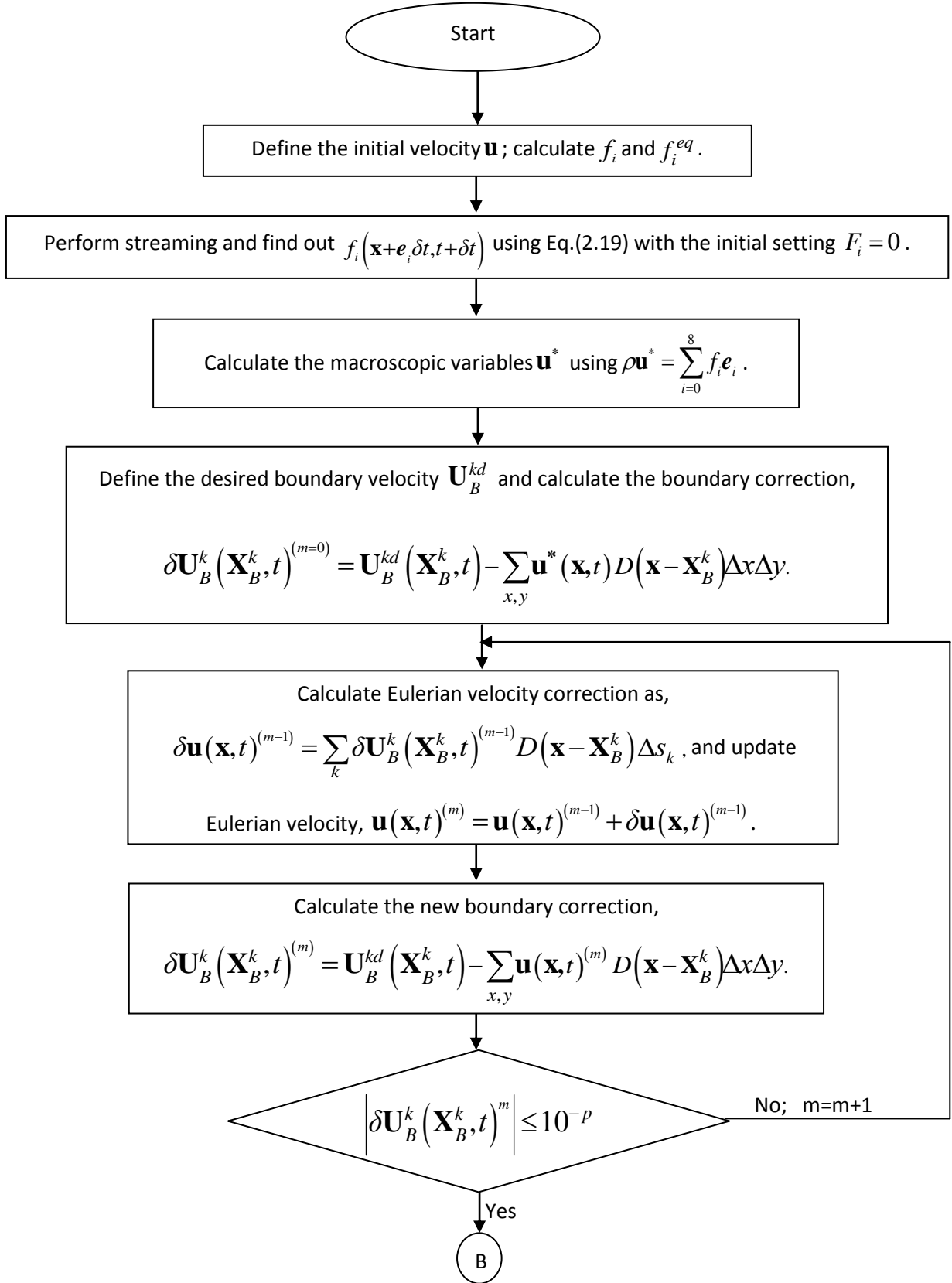
After calculating the velocity corrections, the force density at the Lagrangian and Eulerian grid points is derived using Eq.(2.32).

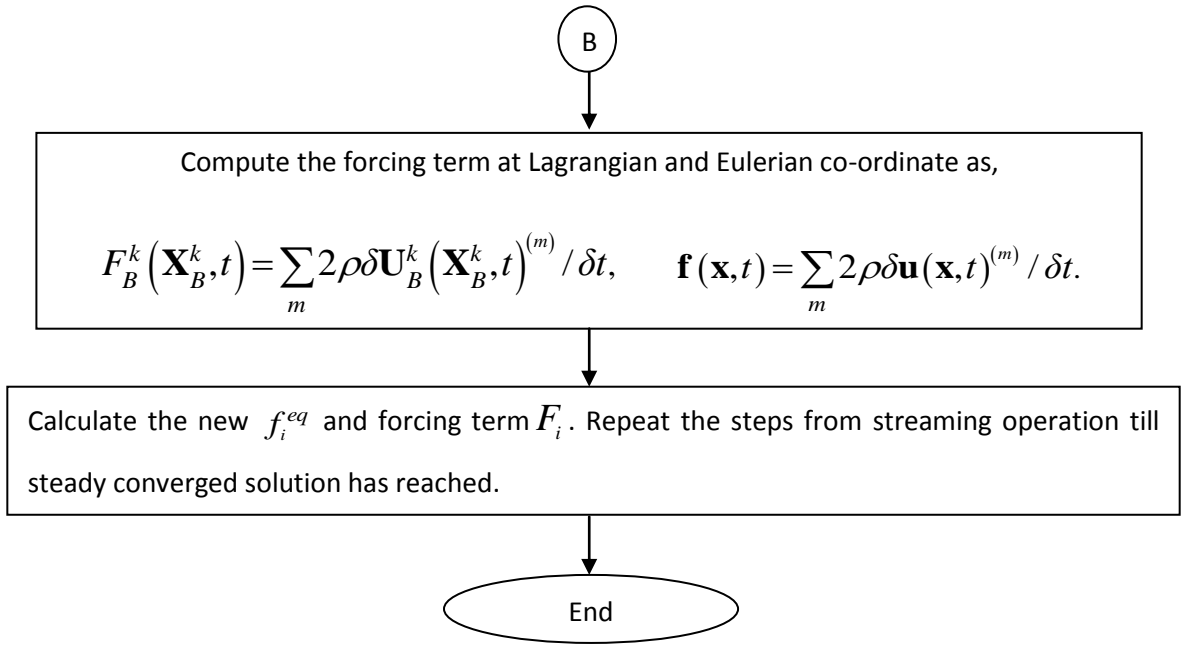
$$\mathbf{F}_B^k(\mathbf{X}_B^k, t) = \sum_m 2\rho \delta \mathbf{U}_B^k(\mathbf{X}_B^k, t)^m / \delta t, \quad \mathbf{f}(\mathbf{x}, t) = \sum_m 2\rho \delta \mathbf{u}(\mathbf{x}, t)^m / \delta t. \quad (2.32)$$

Other microscopic variables: density, pressure and kinematic viscosity are calculated using the following formula.

$$\rho = \sum_{i=0}^8 f_i, \quad p = \rho c_s^2, \quad \nu = \left(\tau - \frac{1}{2} \right) c_s^2 \delta t. \quad (2.33)$$

In summary, the numerical implementation steps of the proposed scheme are provided in the following flow chart.





2.1.4 Kinematics of particulate flow

To extend the applicability of the proposed flexible forcing IB – LBM scheme for the moving boundary flow problems, we have studied the particulate flow. In this flow problem, the translational and angular motion of the particles is governed by the active hydrodynamic forces and torques. From Newton’s laws of motion, the net force on the particle is calculated by combining the effects of the gravity, buoyancy, hydrodynamic and collision forces.

$$\mathbf{F}_l^{net} = \left(1 - \frac{\rho_f}{\rho_p}\right) M_l \mathbf{g} - \sum_k \mathbf{F}_B^k(\mathbf{X}_B^k) \Delta s_k + \mathbf{F}_l^{coll}, \quad (2.34)$$

where M_l is the mass of the particle, ρ_f and ρ_p are the densities of fluid and particle respectively. The hydrodynamic force $-\sum_k \mathbf{F}_B^k(\mathbf{X}_B^k) \Delta s_k$, is calculated using the Eq.(2.32) which can be considered as a reaction force.

Similarly, the torque acting on the particle can be computed as,

$$\mathbf{T}_l^{net} = -\sum_k (\mathbf{X}_B^k - \mathbf{X}_R) \times \mathbf{F}_B^k(\mathbf{X}_B^k, t) \Delta s_k, \quad (2.35)$$

where \mathbf{X}_R is the centre of mass of the particle.

To calculate the collision force between the particle-wall or particle-particle, a lubrication forcing mechanism is followed (Glowinski et al. (1999); Glowinski et al. (2001)). This force is repulsive in nature and acts only when the distance between the particle and nearest wall or another particle is less than λ . In our present study, we set $\lambda = 2\delta x$.

$$\mathbf{F}_i^{coll} = \begin{cases} 0 & d_{i,j} \geq R_i + R_j + \lambda, \\ \frac{1}{\varepsilon_p} (\mathbf{X}_i - \mathbf{X}_j) (R_i + R_j + \lambda - d_{i,j})^2 & d_{i,j} < R_i + R_j + \lambda, \end{cases} \quad (2.36)$$

where R_i and R_j are the radius of the colliding particles. In case of collision with a wall, this force calculation is done by assuming an imaginary particle of same size on the other side of wall. $d_{i,j}$ is the distance between centres of i^{th} and j^{th} particles with their corresponding centre location at \mathbf{X}_i and \mathbf{X}_j respectively. ε_p is a small positive stiffness parameter followed from the work of Glowinski et al. (1999).

In IBM simulation, the fluid phase is assumed to present at outside as well as inside of the solid boundary. This internal fluid does not affect the flow field and pressure outside the boundary once the no-slip condition is accurately

satisfied. However, a part of the body force term is utilized to move the internal fluids, therefore the net force and torque calculation on the particle is compromised. To include this internal loss effect we have followed Feng and Michaelides (2005) formulation for rigid body approximation. The corresponding translational velocity \mathbf{U}_R and angular velocity $\boldsymbol{\omega}$ calculation is done with added mass effect terms.

$$M_l \left. \frac{d\mathbf{U}_R}{dt} \right|^{n+1} = \mathbf{F}_l^{net} + \left(\frac{\rho_f}{\rho_p} \right) M_l \left. \frac{d\mathbf{U}_R}{dt} \right|^n, \quad (2.37)$$

$$\mathbf{I}_l \left. \frac{d\boldsymbol{\omega}}{dt} \right|^{n+1} = \mathbf{T}_l^{net} + \left(\frac{\rho_f}{\rho_p} \right) \mathbf{I}_l \left. \frac{d\boldsymbol{\omega}}{dt} \right|^n, \quad (2.38)$$

where \mathbf{I}_l is the moment of inertia tensor of the particle. ‘ n ’ is the time step.

In summary the solution procedures for the particulate flow using the proposed flexible forcing IB – LBM scheme are outlined below.

1. Set the initial flow field and calculate f_i and f_i^{eq} .
2. Perform streaming using Eq.(2.19) with initial setting $F_i, \delta\mathbf{u} = 0$ and

$$\text{calculate intermediate velocity } \mathbf{u}^* = \sum_{i=0}^8 \mathbf{e}_i f_i / \rho.$$

3. From the desired boundary velocity (follow Newton’s laws of motion

$$\text{and ref. Eq.(2.37)) calculate the velocity correction } \delta\mathbf{U}_B^k(\mathbf{X}_B^k, t) \Big|^{m=0}.$$

4. Update the Eulerian velocity \mathbf{u} with updated $\delta\mathbf{u}$ and calculate new $\delta\mathbf{U}_B^k(\mathbf{X}_B^k, t)$ using both the Eq.(2.29) and (2.31). Repeat this step with a sub-iteration loop until the CC in Eq.(2.30) is satisfied.
5. Calculate \mathbf{f} and f_i^{eq} using Eq.(2.8) and (2.32). Update the net force and torque on the particle and calculate its new position and velocity using Eqs.(2.34) – (2.38).
6. Repeat the above steps (2) – (5) for time evolution.

2.2 Accuracy test and Validations

The numerical accuracy of the proposed flexible forcing IB – LBM scheme was initially evaluated by performing two benchmark test case simulations: 1) Taylor Green decaying vortex and 2) Lid driven cavity. A set of two dimensional stationary (laminar flow past circular cylinder) and moving boundary (movement of neutral buoyant particle in linear shear flow, sedimentation of the single and two particles) flow problems are simulated to validate the present numerical algorithm.

2.2.1 Taylor – Green decaying vortex

To determine the numerical accuracy of the proposed flexible forcing IB – LBM scheme, at first the simulation of unsteady Taylor – Green vortex flow is carried out in a square box. This problem has analytical solutions for the velocity (u, v) and pressure (p) as shown in Eqs.(2.39) – (2.41). The test case environment is set similar to Chen et al. (2007), where a circle of radius $0.5L$

is embedded at the centre of the square box $[-L,L] \times [-L,L]$ with $L = 1.0$. The exact solution is used to provide the initial condition at $t = 0$ and the boundary condition on the outer boundary and on the surface of the immersed body.

$$u(x, y, t) = -u_0 \cos(x\pi / L) \sin(y\pi / L) e^{-\left(2\nu t \frac{\pi^2}{L^2}\right)}, \quad (2.39)$$

$$v(x, y, t) = u_0 \sin(x\pi / L) \cos(y\pi / L) e^{-\left(2\nu t \frac{\pi^2}{L^2}\right)}, \quad (2.40)$$

$$p(x, y, t) = p_0 - \frac{u_0^2}{4} [\cos(2x\pi / L) + \sin(2y\pi / L)] e^{-\left(4\nu t \frac{\pi^2}{L^2}\right)}, \quad (2.41)$$

The simulation is carried out using four sets of mesh resolutions: 21×21 , 41×41 , 81×81 and 161×161 , with ‘ h ’ as mesh step size. The Reynolds number is defined same as in Chen et al. (2007) with the free stream velocity u_0 , i.e. $Re = u_0 L / \nu = 10$ and the dimensionless relaxation time is set to $\tau = 0.65$. The solutions at time $t = 1.0$ are obtained, and the numerical error of the velocity is quantified using L_2 norm as defined in Eq.(2.42).

$$L_2 \text{ error} = \sqrt{\frac{\sum_N (u^{numerical} - u^{analytical})^2}{N_{mesh}}} \quad (2.42)$$

In Eq.(2.42), $u^{numerical}$ and $u^{analytical}$ are the numerical velocity and analytical solution respectively, N_{mesh} is the total number of Eulerian points in the computational domain. The L_2 error vs mesh spacing is plotted in log scale as shown in Fig.2.3. The slope of the plotted line is the measure of the

overall accuracy of the numerical of the scheme (Chen et al. (2007)), which is 1.85, slightly less than the second order accuracy.

LBM is known to be second-order accurate in space and time. However, the coupled IB – LBM scheme may produce slightly lower order overall accuracy. This is because, the Dirac delta function interpolation and the smoothing kernel needed to get the velocity correction at Eulerian and Lagrangian points has only first-order accuracy. Although it is only applicable in the region nearby the boundary, but it may have an effect on the global accuracy of solution in the whole domain. Therefore, the reduction of overall accuracy of the present scheme to 1.85 is attributed to the use of the first-order smoothing delta function interpolation.

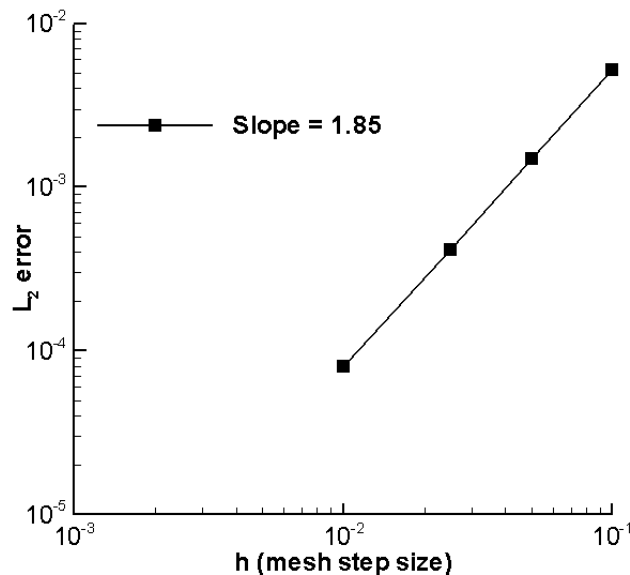


Fig.2.3. Overall accuracy test of the proposed flexible forcing IB-LBM scheme using the Taylor–Green vortex.

The stability of the proposed coupled IB – LBM scheme is found to have similar limits as that of the LBM scheme (Brownlee et al. (2007)), We have

simulated the Taylor – Green vortex problem for different dimensionless relaxation parameter (τ) and observe that the scheme is stable, if the incompressibility limit is valid i.e. Mach no < 0.15 and $\tau > 0.5$.

2.2.2 Lid – driven cavity

To further evaluate the numerical accuracy on a solid bounded flow domain, a lid driven cavity flow is simulated. The incompressible laminar flow in the square cavity is generated by supplying a uniform motion on the top wall of the square cavity. Fig.2.4(a) shows the schematic layout of the 45 deg inclined lid-driven cavity within a square domain $[-\sqrt{2}L, \sqrt{2}L] \times [-\sqrt{2}L, \sqrt{2}L]$, where L is the width and height of the inclined square cavity. To compare the accuracy, three different uniform Eulerian grids are followed ($N \times N$, $N = 121, 240, 480$) in discretising the computational domain, where the corresponding Lagrangian nodes are ($N_L = 4 \times 30, 4 \times 60, 4 \times 120$), respectively. We have set the Eulerian grid spacing as $\Delta x = \Delta y = 1/40$, Lagrangian node spacing $\Delta s = \sqrt{2} \Delta x$, the time step size as $\Delta t = \Delta x$ and Reynolds number as $Re = UL/\nu = 100$. The lid velocity U is defined such that the Mach number ($Ma = U/c_s < 0.2$) lies in the incompressible limit. Periodic boundary condition is prescribed on the external square boundary and proposed flexible forcing IB – LBM is adopted to define the no-slip and moving wall boundary condition on the internal cavity. The simulation is performed until the steady

convergence criterion is satisfied as shown in Eq.(2.43).

$$\sum_{i,j} \left\| \sqrt{\frac{(U_x^{n+1} - U_x^n)^2 + (U_y^{n+1} - U_y^n)^2}{(U_x^{n+1})^2 + (U_y^{n+1})^2}} \right\| \leq 10^{-6}. \quad (2.43)$$

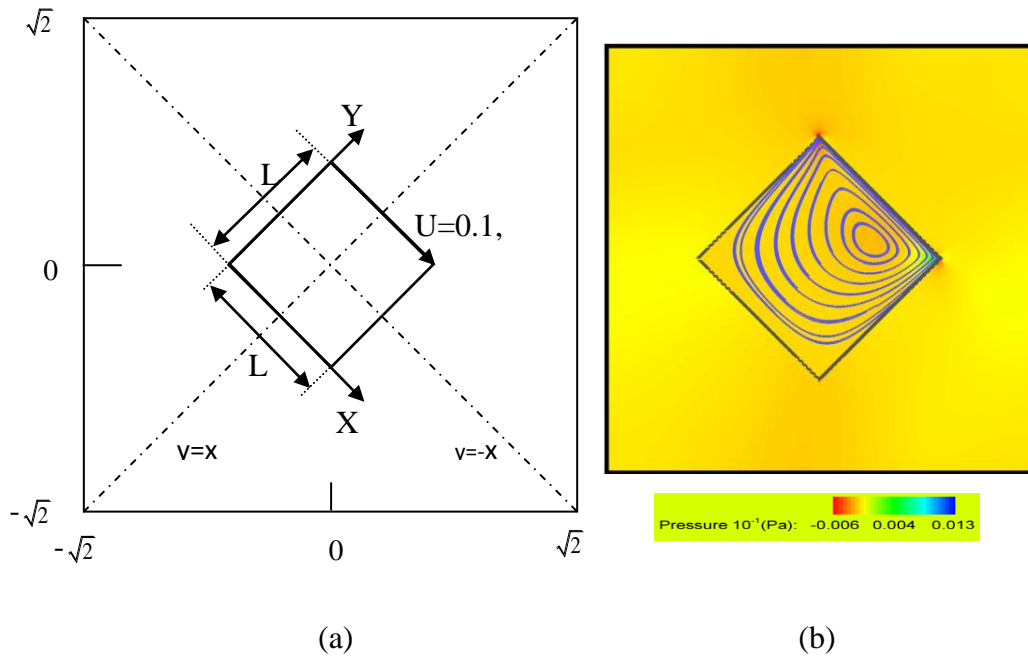


Fig.2.4(a). The schematic diagram of the lid driven cavity in the computational domain and (b) the streamline plots inside the cavity at steady state condition for $Re = 100$, background colour code represent the pressure distribution.

Fig.2.4(b) depicts the streamlines inside the cavity. Fig.2.5(a) and 2.5(b) show the normalised steady velocity component U_x/U and U_y/U inside the cavity along the line $y = x$ and $y = -x$ respectively, where the coordinates $Y = 0$ and $X = 0$, represent the point of intersection of the lines $y = x$ and $y = -x$ with respective edges of the cavity. We have compared our computed results with those of Ghia et al. (1982), and they are in good agreement, thus further validating the accuracy of our numerical scheme.

We have also checked the CPU time required for the converged steady state solution (ref. Eq.2.43) using the implicit matrix velocity correction (Wu and Shu (2009)) and the proposed flexible forcing IB-LBM schemes, and the comparisons are shown in Table 2.1.

Table 2.1 Comparison of CPU time and memory usage for lid-driven cavity flow at $Re = 100$ using two different IB-LBM schemes where the CC is 10^{-4} .

IB-LBM scheme	CPU Time	Max Memory
Wu and Shu (2009)	2575 sec	456 MB
Present	2526 sec	219 MB

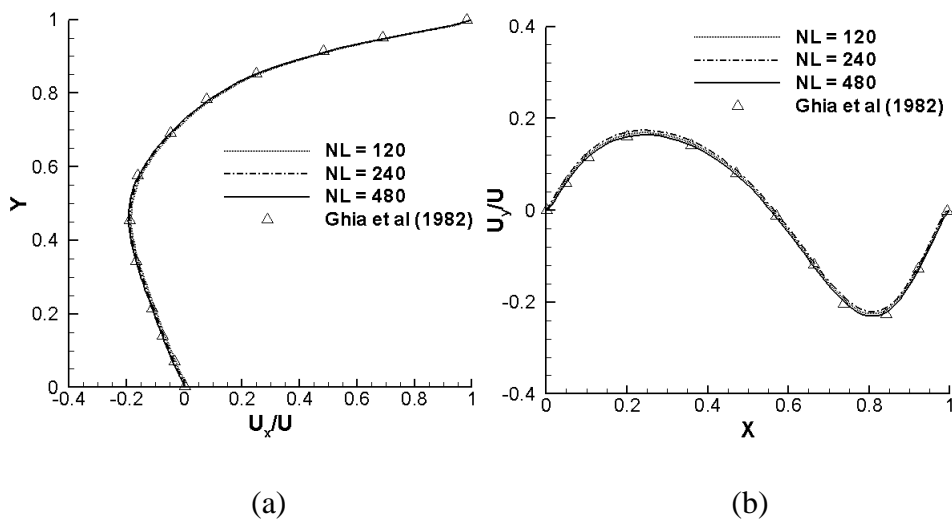


Fig.2.5. The steady velocity components U_x/U and U_y/U along the centre lines (a) $y = x$ and (b) $y = -x$ respectively with different grid sizes.

Although there is no significant computational time savings from our proposed numerical model for this particular 2D, stationary problem, the mathematical

simplicity of the flexible forcing algorithm has reduced the memory storage demand and computational effort for the code development.

2.2.3 Laminar flow past circular cylinder

To validate the proposed flexible forcing scheme on a stationary boundary flow domain, the laminar flow past a stationary circular cylinder is simulated. Extensive numerical, experimental and analytical studies on this benchmark flow problem have been reported in the literature (Dennis and Chang (1970); Fornberg (1980); Braza et al. (1986); Williamson (1996); Ding et al. (2004); Shukla et al. (2007)) where the flow behaviour is characterised with respect to the Reynolds number. The Re is defined as, $Re = U_{\infty}D/\nu$, where U_{∞} is the free stream velocity, D is the diameter of the cylinder and ν is the kinematic viscosity of the fluid.

At low Re ($Re_{critical} < 46$), the flow pattern remain steady where two recirculation vortices are developed behind the rear end of the cylinder. The recirculation vortices length is a function of Re and increases with the increase in Re (Dennis and Chang (1970); Fornberg (1980)). When the $Re > Re_{critical}$, the flow shifts to unsteady regime where the periodic Von-Karman vortex shedding is observed (Williamson (1996)).

To make a quantitative comparison of the performance of present scheme, the drag and lift force coefficients experienced on the cylinder are calculated which are defined in the following equations.

$$C_d = \frac{F_{drag}}{(1/2)\rho U_\infty^2 D}, \quad F_{drag} = -\sum_k \mathbf{F}_{BX}^k(\mathbf{X}_B^k, t) \Delta s_k, \quad (2.44)$$

$$C_l = \frac{F_{lift}}{(1/2)\rho U_\infty^2 D}, \quad F_{lift} = -\sum_k \mathbf{F}_{BY}^k(\mathbf{X}_B^k, t) \Delta s_k, \quad (2.45)$$

where $\mathbf{F}_{BX}^k(\mathbf{X}_B^k, t)$, $\mathbf{F}_{BY}^k(\mathbf{X}_B^k, t)$ are the X and Y components of the boundary force in the Eq.(2.32) and Δs_k is the arc length of the circular boundary element. It is worth to note that the cylinder will experience the lift force when the flow regime contains the alternate Von-Karman vortex sheet. We have represented the non-dimensional vortex shedding frequency with Strouhal number $St = f_q D / U_\infty$, where f_q is the vortex shedding frequency.

In the present study the fluid density and the free stream velocity are fixed as, $\rho = 1.0$, $U_\infty = 0.1$, respectively. To alter Re of the flow, the kinematic viscosity ν is modified and correspondingly the relaxation parameter τ is adjusted in LBM (ref. Eq.(2.33)).

A rectangular computational domain of size $40D \times 40D$ and $50D \times 40D$ is used for the steady and unsteady flow cases, with the mesh sizes: 401×401 and 501×401 , respectively. A non-uniform grid system with finer grids near the cylinder is adhered using the Lagrangian interpolation based LBM (LILBM) (Wu and Shu (2009)). The cylinder centre is located at $(20D, 20D)$ where the fine uniform mesh of size 97×97 is used near the region of the cylinder $1.2D \times 1.2D$. 120 Lagrangian marker points are utilised to represent the circumference of the cylinder.

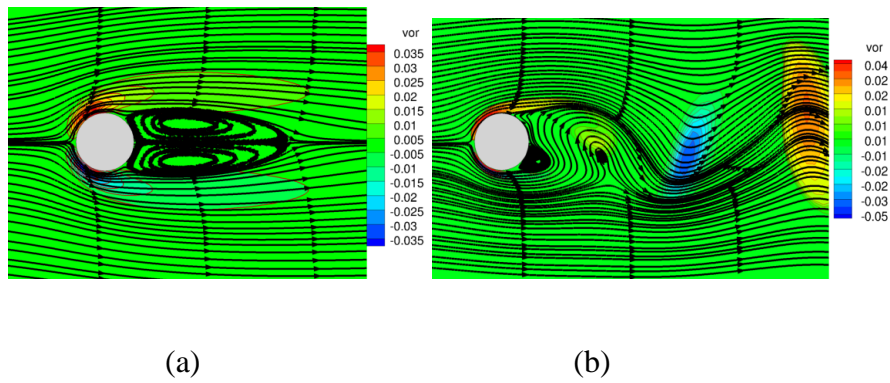


Fig.2.6. The streamlines and vorticity contours at (a) $Re= 40$ and (b) $Re= 100$.

Table 2.2 Comparison of force coefficients, recirculation length and Strouhal number for steady and unsteady flow past circular cylinder.

Reference	Re = 20		Re = 40		Re = 100		
	C_d	L_w	C_d	L_w	C_d	C_l	St
Kang and Hassan (2011)	2.075	0.95	1.555	2.34	1.368	0.346	0.163
Shu et al. (2007)	2.13	0.9	1.59	2.2	1.383	0.35	0.165
Wu and Shu (2009)	2.091	0.93	1.565	2.31	1.364	0.344	0.163
Present	2.119	0.937	1.586	2.32	1.362	0.341	0.162

In Fig.2.6, the streamlines and vorticity contours are shown for steady ($Re = 40$) and unsteady ($Re = 100$) flow where the no-slip condition is accurately satisfied without any streamline penetration. The C_d , C_l , St and the

recirculation wake length (L_w) are quantitatively compared with the literature as shown in Table 2.2. The results are found in excellent agreement.

Table 2.3 Variation of number of sub-iterations with CC and SRP for steady flow past circular cylinder.

CC	10^{-4}		10^{-5}		10^{-6}	
SRP	NF	C_d (Re=40)	NF	C_d (Re=40)	NF	C_d (Re=40)
0.2	15	1.5868	23	1.5866	32	1.5866
0.4	13	1.5867	21	1.5866	29	1.5865
0.6	6	1.5867	16	1.5866	24	1.5865
0.8	7	1.5866	18	1.5867	26	1.5865
1.0	11	1.5867	20	1.5867	28	1.5865

Table 2.4 Effects of CC variation for unsteady flow past cylinder (Re = 100).

CC	10^{-4}	10^{-5}	10^{-6}
C_d	1.369	1.362	1.361
C_d	0.349	0.341	0.341
St	0.164	0.162	0.162

As mentioned previously in our proposed scheme the CC and SRP are user dependent as shown in Eqs.(2.30) – (2.31), respectively. In Table 2.3, a comparison is made to find out the dependency of number of forcing/sub-

iteration on different CC and SRP. It is found that number of sub-iteration (NF) required for any CC strongly depends on SRP. For the present simulation ' ε ' in the range 0.6 – 0.7 gives least number of sub-iteration and hence correspondingly reduces the overall computation time and expenses. This makes our scheme comparatively faster than the other similar fixed iteration schemes (Luo et al. (2007); Wang et al. (2008); Kang and Hassan (2011)). In Table 2.4, effects of CC variation on C_d , C_l and St is shown for $Re = 100$. It is observed that with the decrease in CC or better approximation of the no-slip condition, enhances the accuracy of the final result. Again it is worth to note that higher accuracy demands higher number of forcing or sub-iteration.

2.2.4 A motion of the neutral buoyant particle in the linear shear flow

To investigate the capabilities of the proposed flexible forcing IB – LBM scheme in handling the moving boundary problems, the motion of the single neutral buoyant circular particle is simulated in a linear shear flow regime. The numerical study of the problem was previously reported in the literature using FEM Feng et al. (1994) and conventional IB – LBM (Feng and Michaelides (2004); Niu et al. (2006); Wu and Shu (2010)) schemes. They observed that the circular particle always transfers towards the centre of the channel irrespective of its initial position and release velocity.

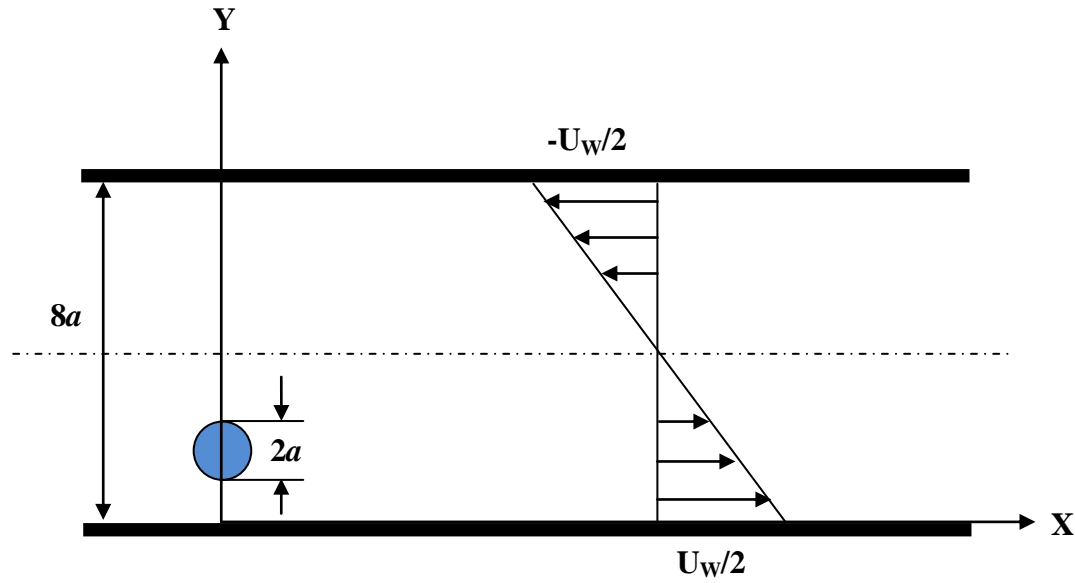


Fig.2.7. Schematic diagram of neutrally buoyant particle in the linear shear flow

The schematic diagram of the computational domain for this problem is shown in Fig.2.7. The other parameters used in our simulations are maintained as follows, the radius of the particle $a = 10$; the gap between the plates $H = 80$; the plate width $L = 2000$; the relaxation time $\tau = 0.6$ that makes the fluid kinematic viscosity in lattice units $\nu = 1/30$. A uniform mesh of size 2001×81 is followed in the domain. Periodic boundary condition is prescribed at the inlet and outlet of the channel.

Both the top and bottom plate of the channel moves with equal velocity $U_w/2 = 120$ in opposite directions which produce a shear rate of $\gamma = 1/4800$. The corresponding bulk Re of the flow is $Re = U_w H / \nu = 40$. The neutral buoyant particle was released at the position $Y_0 = 0.25H$ above the bottom plate (in the vertical halfway) towards the centre of the channel, with zero initial velocity.

This initial position results in a local slip velocity between the particle and fluid equals to $0.25U_w$, which induce the movement of the particle.

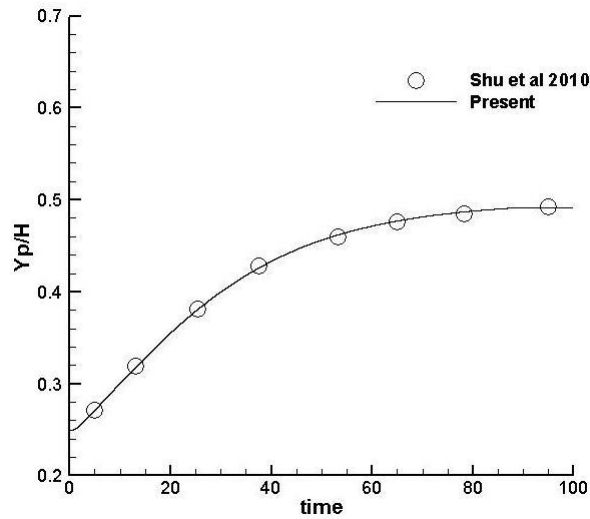


Fig.2.8. Comparisons of lateral migration of the neutral buoyant particle, where time is dimensionless.

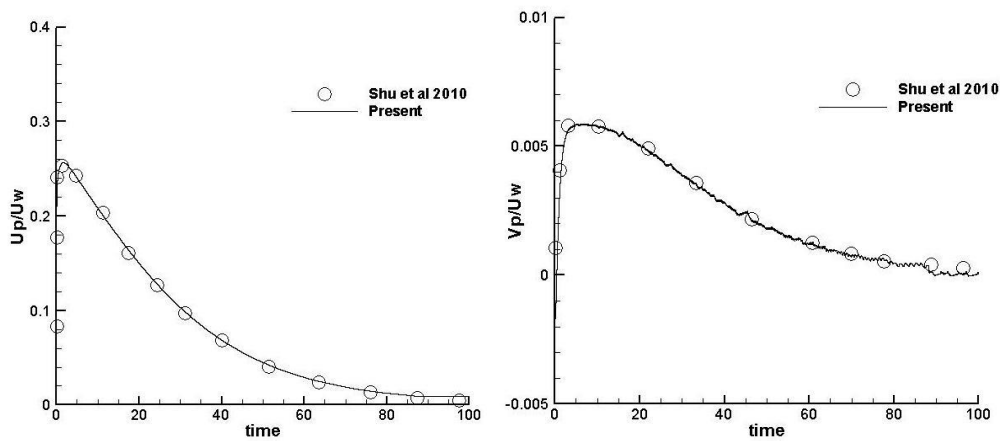


Fig.2.9. Comparison of the neutral buoyant particle translational velocities along X and Y directions, where time is dimensionless.

The vertical migration of the particle is shown in Fig.2.8 and compared with the results by Wu and Shu (2010). The particle has moved to the centre of the channel which is consistent with the previous observation (Feng et al. (1994); Niu et al. (2006); Wu and Shu (2010)). We have also calculate the translational velocities of the particle along X and Y directions as shown in Fig.2.9 and the magnitudes are in good agreement with the Wu and Shu (2010).

2.2.5 Single particle sedimentation

As another validation case we have simulated the single particle sedimentation problem, which has been extensively studied in the literature (Wan and Turek (2006); Wang, Fan et al. (2008); Wu and Shu (2010)). Here, an identical case as that in (Wan and Turek (2006); Wu and Shu (2010)) is simulated. A fluid filled two dimensional rectangular box of 2 cm wide and 6 cm high is selected. The fluid properties: density ρ_f and viscosity μ_f are set to 1.0 g/cm³ and 0.1 g/cm.s, respectively. A circular particle of diameter $d_p = 0.25$ cm and density $\rho_p = 1.25$ g/cm³ is initially kept in the rectangular box with its centre located at (1 cm, 4 cm). Initially both the fluid and particle are at rest. The computational domain is discretised with uniform Eulerian mesh of size 201×601, which is followed same as Wu and Shu (2010). To represent the surface of the circular particle, 50 Lagrangian mesh points are used.

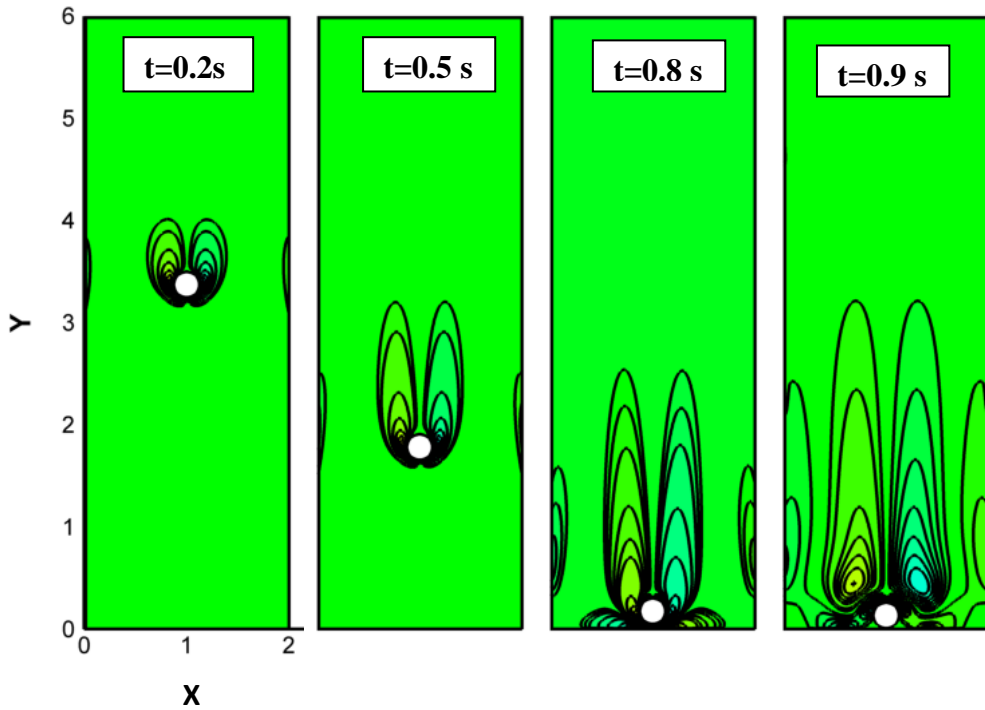


Fig.2.10. Instantaneous vorticity contours of single particle sedimentation at different time steps, where X and Y are in cms.

The particle starts falling under the effects of gravity once it is released from its initial position. The particle keeps accelerating until it reaches a steady/terminal velocity where the net upward force (drag + buoyancy) is balanced with the net downward force (weight). Thereafter, it settles with terminal velocity.

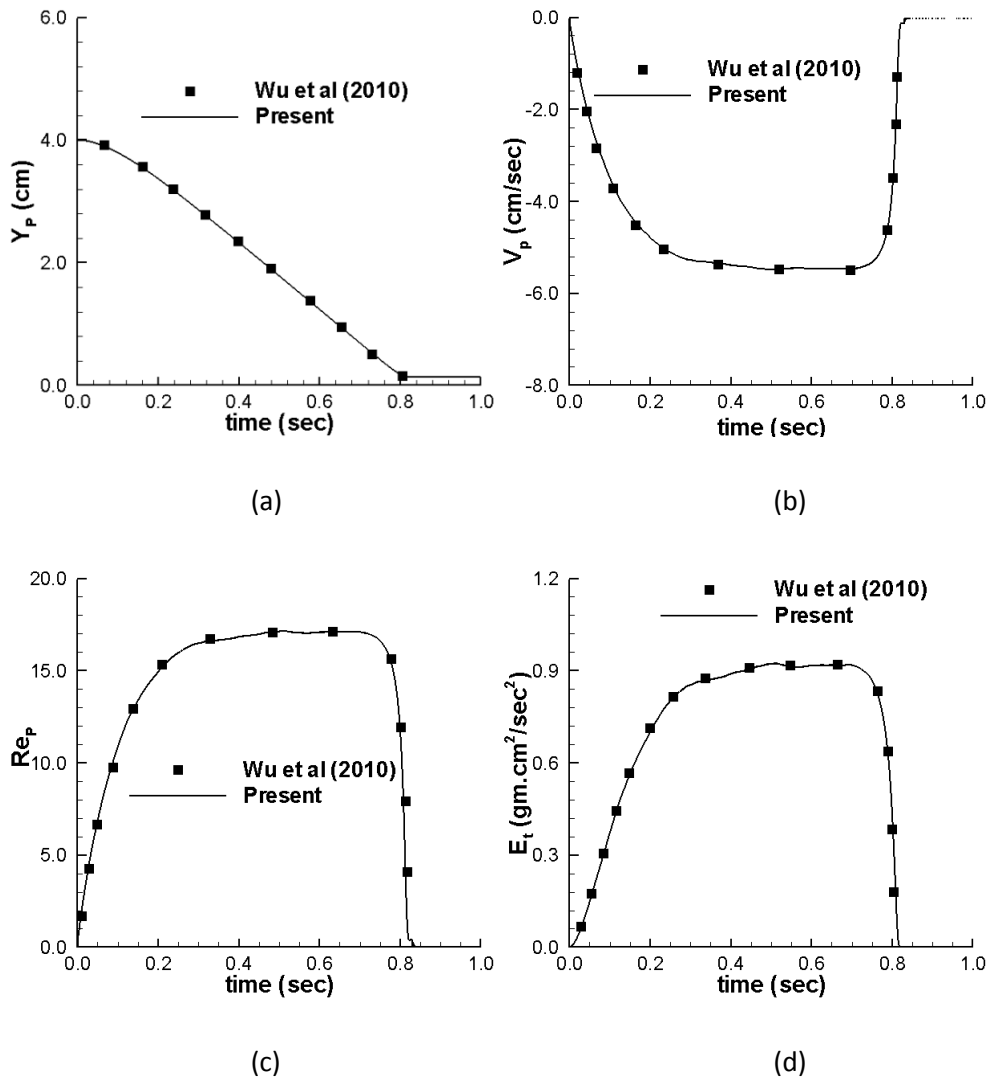


Fig.2.11. Temporal evolution of (a) Y centre co-ordinate (Y_p), (b) Vertical velocity (V_p), (c) Reynolds number (Re_p) and (d) Translational kinetic energy (E_t) for the single circular particle sedimentation.

The temporal evolution of the vorticity contours are shown in Fig.2.10, at different time steps. The longitudinal centre coordinate y_p , longitudinal velocity v_p , Reynolds number Re_p and translational kinetic energy E_t of the particle as functions of time are shown in Fig.2.11(a) – (d), respectively where the definition of Re_p and E_t are used as in Eqs.(2.46) – (2.47).

$$\text{Re}_p = \frac{\rho_p d_p \sqrt{u_p^2 + v_p^2}}{\mu_f}, \quad (2.46)$$

$$E_t = 0.5M(u_p^2 + v_p^2), \quad (2.47)$$

where M is the mass of the particle. The flow regimes and quantitative comparisons are found in good agreement with those in Wu and Shu (2010).

Table 2.5 Variation of sub-iteration/number of forcing (NF) with respect to CC and SRP

CC	10^{-4}		10^{-5}		10^{-6}	
SRP	NF	Re	NF	Re	NF	Re
0.2	8	17.17	11	17.11	17	17.08
0.4	6	17.16	8	17.11	15	17.07
0.6	4	17.15	6	17.10	10	17.07
0.8	4	17.15	6	17.10	10	17.07
1.0	5	17.16	7	17.10	12	17.07

The effects of CC and SRP in the simulations are also investigated. In Table 2.5, the variation of averaged forcing/sub-iteration numbers with change in CC and SRP are shown. As expected, with increase in accuracy or reduction in CC, the number of forcing/sub-iteration increases. We also observed that by suitably tuning SRP, overall computational time can be significantly reduced. If SRP is chosen in the range 0.6 – 0.8, the average forcing/sub-iteration number is almost reduced by half in comparison to other SRP values. Hence,

SPR plays an important role to improve the computational efficiency. It is also found that different CC (from 10^{-4} to 10^{-6}) has little effect on the maximum Reynolds number. The reason of this change is associated with the error allowed in the no-slip boundary convergence. When CC is set as 10^{-5} , the maximum Reynolds number 17.10 is comparable to that provided by Wu and Shu (2010), 17.08 and by Wan and Turek (2006), 17.15. Therefore, CC is followed as 10^{-5} for rest of our simulations.

2.2.6 Two particles sedimentation

To further validate the proposed algorithm, two particles sedimentation in a rectangular box is simulated. The working parameters are identical as those in (Wang et al. (2008)). Here the box dimension is selected as 2cm width and 6cm height. Same as Wang et al. (2008), a uniform mesh of size 201×601 is utilized to discretise the computational domain. Two circular particles of same diameter $d_p = 0.25$ cm and density $\rho_p = 1.5$ g/cm³, are kept in the rectangular box with their initial centre located at (1–0.001 cm, 4.5 cm) and (1+0.001 cm, 5.0 cm). Surface of the particles are represented by 50 Lagrangian points. The horizontal offset distance between the particles centres acts as a perturbation to breakdown the later equilibrium states as mentioned by Wang et al. (2008). It is expected that the particles will reproduce the Drafting – Kissing – Tumbling (DKT) phenomena Fortes et al. (1987). The fluid properties are set as: density $\rho_f = 1.0$ g/cm³ and viscosity $\mu_f = 0.01$ g/cm.s.

In Fig.2.12 the instantaneous vorticity contours of the settling particles are shown. Two particles are initially at rest and start to settle under the effects of gravity. During the fall, the leading particle (particle-2) leaves a low pressure wake behind where the trailing particle (particle-1) is caught. Due to the reduction in the drag force on the trailing particle, it settles faster than the leading one. With the increased speed of the trailing particle, it drafts towards the leading particle. Later the two particles momentarily contact each other, which is also referred as kissing. The kissing of particles is an unstable equilibrium state and with the supplied initial perturbation these particles get separated (also known as tumbling).

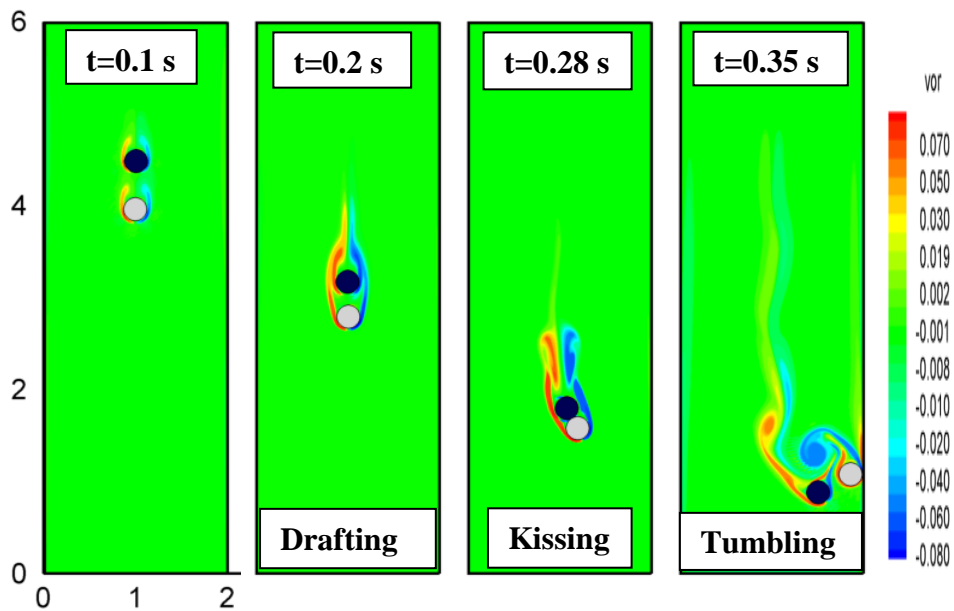


Fig.2.12. Instantaneous vorticity contours of two particles performing DKT phenomena where X and Y are in cms.

As mentioned by Fortes et al. (1987), the tumbling phenomena is breakdown of the unstable equilibrium state and with different numerical perturbation

schemes the results may differ after kissing. There are some discrepancies also observed in our comparisons.

Quantitative comparisons of the trajectory of the vertical centre co-ordinate Y_p and vertical velocity V_p of the particles as functions of time are made with those in (Wang et al. (2008)). Our results as plotted in Fig.2.13, are found highly consistent with those published data by Wang et al. (2008). These validation studies demonstrate the capabilities of the proposed scheme for accurate numerical simulation of the fluid-particle interactions.

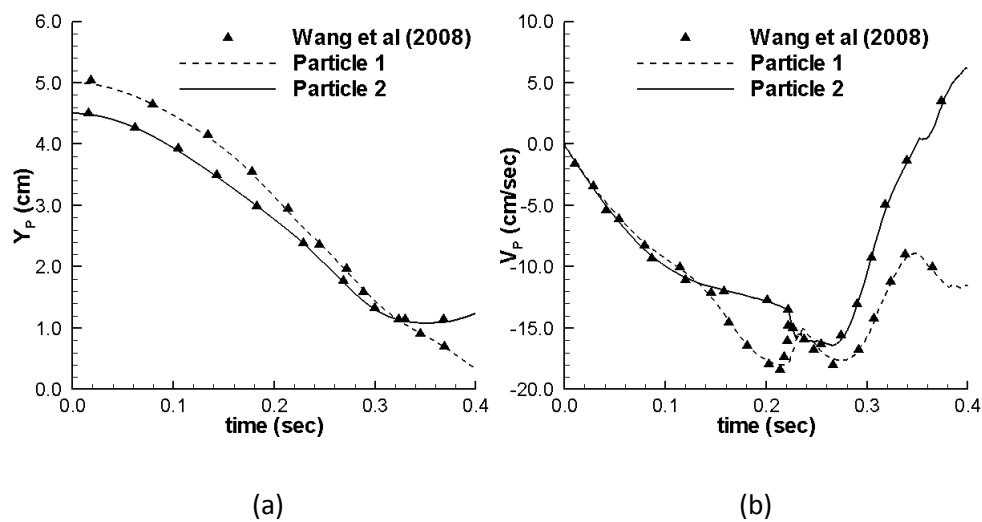


Fig.2.13. Temporal evolutions of (a) Y centre co-ordinate (b) Vertical velocity for two circular particles sedimentation.

2.3 Concluding remarks

In this chapter, we have discussed a novel flexible forcing hybrid IB – LBM scheme to simulate fluid flow problems that includes 2D stationary and moving solid boundary. Following the implicit type forcing term calculation,

an unknown single Lagrangian velocity correction is introduced for suitable satisfaction of the no-slip boundary condition within a convergence limit. Use of flexible forcing principle not only avoids the complex mathematics involved in matrix inversion but also satisfy the boundary condition consistently at every time step with same order of accuracy. This is advantageous for unsteady and moving boundary flow problems. Also the algorithm suggested here is simple for new computational code development.

The accuracy of the proposed numerical algorithm is tested by simulating 1) Taylor Green decaying vortex and 2) lid driven cavity. The overall accuracy is found to be 1.85, slightly less than the second order. Although the LBM is known to be second-order accurate in space and time, the coupled IB – LBM scheme may produce slightly lower order overall accuracy. This is because, the Dirac delta function interpolation and the smoothing kernel needed to get the velocity correction at Eulerian and Lagrangian points has only first-order accuracy. Further the solver validation is done by simulating a set of two dimensional stationary (laminar flow past circular cylinder) and moving boundary (movement of neutral buoyant particle in linear shear flow, sedimentation of the single and two particles) flow problems. The results are found to be in excellent agreement with previous published article.

Chapter 3

Application of 2D Flexible Forcing IB –LBM for Particulate Flow in a Constricted Channel²

In this chapter, the developed 2D moving boundary flexible forcing IB – LBM scheme is applied for the particulate flow in a constricted channel. The aim of the present study is to investigate the fluid – particle interactions where the surrounding wall effects are significant. In practice one may encounter a number of such flow situations and to name a few, sedimentation of the sand particles or rising of the bubbles in an hourglass, transport of the blood cells in an constricted arteries, granular flow in a hopper, multiphase mixed flow in a separator etc. Although several numerical and experimental studies (Fortes et al. (1987); Hu et al. (1992); Feng and Michaelides (2004); Feng and Michaelides (2005); Niu et al. (2006); Wang et al. (2008); Wu and Shu (2010)) on the particle sedimentation are reported in the literature where the

² Part of this work has been published as:

Dash SM, Lee TS and Huang H. (2014). "Particle sedimentation in a constricted passage using a novel flexible forcing IB-LBM scheme." International Journal of Computational Methods **11**(05): 1350095

wall effects are absent or minimal, the settling particles behaviour and the associate flow regime in a constricted channel are not yet addressed. To the best of our knowledge, it is the first time we have characterized the sedimentation of single and two particles in a 2D channel in presence of symmetric semicircular constriction walls. The effects of parameters such as, density of the solid particles, viscosity of the fluid, shape and size of the constriction are investigated in this chapter.

3.1 Problem definition

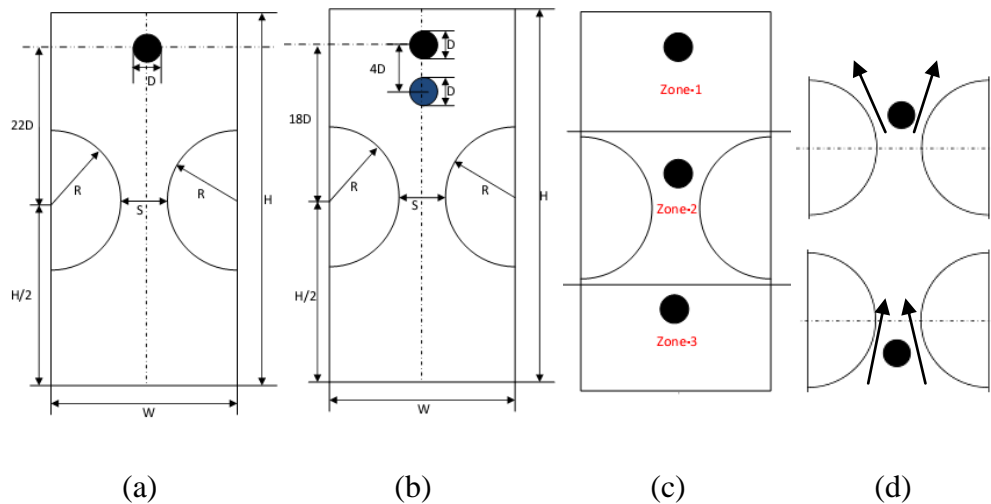


Fig.3.1. Schematic of particle sedimentation in a constricted channel where the sub-figures are, (a) single particle case, (b) two particle case, (c) divisions of the channel region, and (d) surrounding spatial domain near the particle.

A rectangular domain of width ‘W’ and height ‘H’ is selected to simulate the particle sedimentation in a constricted channel. Two symmetrical semicircular walls of radius ‘R’ are placed at the mid section of the domain to produce the constricted passage. The schematic of the problem is shown in Fig.3.1.

The radius of the semicircles can be adjusted to alter the constriction gap size. In the present study, the settling circular particle has diameter ‘D’ and density ρ_p . In case of two particles sedimentation, identical diameters and densities of the particles are selected. To make the results independent of the computational domain size, we have performed test case simulations by varying the aspect ratio (W/H) of the channel until the size/wall effects are minimized. We choose maximum retardation velocity (V_R) of the particle in the constriction zone as a parameter to check the size/wall effects. From the plot in Fig.3.2, the size/wall effects found reducing with the increase in aspect ratio. For our present study, we have chosen the aspect ratio of the channel as 1:9, where the other parameters used in the simulations are set as follows.

Width of the channel $W = 8D$

Height of the channel $H = 72D$

Constriction gap size $S = 1.25D - 2.0D$

Diameter of the particle $D = 0.0025 \text{ m}$

Density of the fluid $\rho_f = 1000.0 \text{ Kg/m}^3$

Viscosity of the fluid $\mu_f = 0.01 \text{ Kg/m.sec}$

Density of the particle $\rho_p = 1250 - 2000 \text{ Kg/m}^3$

Grid independence test is also performed to confirm that the results are invariable with grid resolutions. Table 3.1 shows the change in maximum retardation velocity (V_R) with different grid size for a constant particle density

and constriction gap size. From the grid independence results we have selected uniform grid of size 201×1801 to discretise the computational domain. 50 Lagrangian node points are used to represent the surface of the particle. In the present simulation, IBM is also employed to satisfy the no-slip boundary condition on the stationary semicircular constriction walls. The number of Lagrangian forcing points on the surface of semicircular constriction is uniformly distributed with their spacing $\Delta s_k = 1.4\Delta x$.

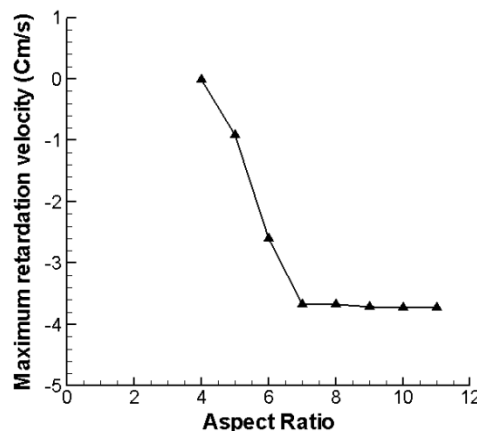


Fig.3.2. Study of the wall effects with increasing aspect ratio of the channel.

Table 3.1 Grid independence test of the particle sedimentation in the
constricted channel.

Mesh size	V_R	% Error =
		$\left \frac{V_R^{Newgrid} - V_R^{Oldgrid}}{V_R^{Oldgrid}} \right \times 100$
100×900	3.75	--
150×1350	3.72	0.8
200×1800	3.714	0.16
250×2250	3.708	0.16

3.2 Results and Discussion

The results presented in the following section correspond to the observed flow regimes for single and two particles sedimentation cases, as functions of particle density and constriction gap size.

3.2.1 Single particle sedimentation

For simulation of single particle sedimentation, the circular particle is kept at initial height of $22D$ from centre of the semicircular constriction and along the vertical centreline of the rectangular box. The density of the particle is varied between $1.25 - 2.0 \text{ gm/cm}^3$ to achieve different Reynolds number of the flow. Also to find the effects of different constriction gap size the radius of semicircular constrictions is adjusted. We restrict our focus to the constriction gap size in the range of $1.25D - 2.0D$.

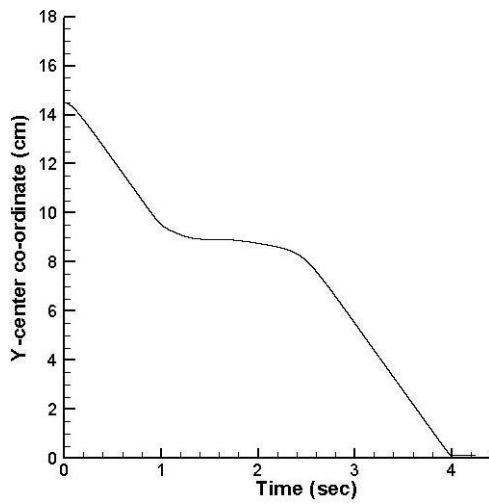
3.2.1.1 Flow regime

To better illustrate the obtained results, we have divided the whole computational domain into three different zones as shown in Fig.3.1(c).

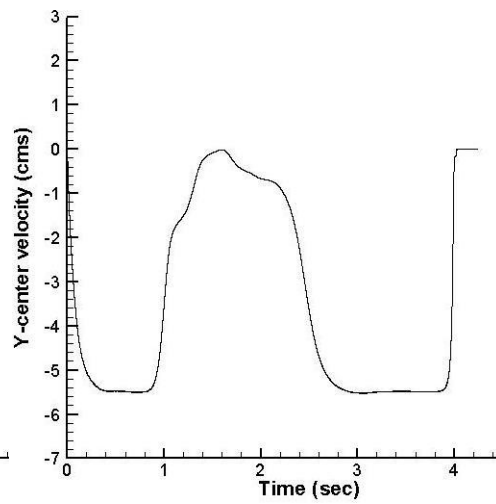
Zone-1

This zone corresponds to the region of the box above the constriction walls. Initially the particle is at rest. With time the particle starts to accelerate by gravity force. From Fig.3.3(b), it can be observed that the velocity magnitude increases until the particle attains a steady state/constant terminal velocity condition (– ve because of sign convention). At this moment, the net upward

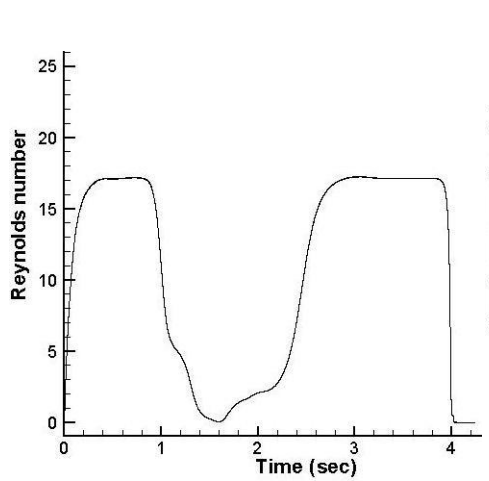
force (drag and buoyancy forces) on the particle gets balanced with the net downward force (weight of the particle). Corresponding to the velocity plot, similar behaviour is observed for Reynolds number Re and translational kinetic energy E_t of the particle. The definition of Re and E_t are followed from Eqs.(2.46) – (2.47). Once the particle attains the constant terminal velocity, it continues to move with that magnitude till it encounters the constrictions or zone-2.



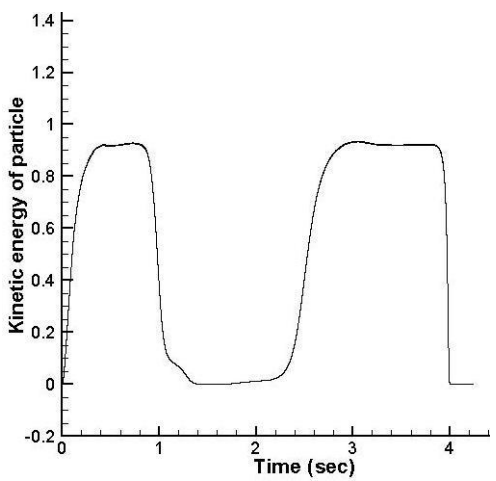
(a)



(b)



(c)



(d)

(Continued....)

Fig.3.3. Temporal evolution of (a) Y centre coordinate (b) Vertical velocity (c) Reynolds number (d) Translational kinetic energy of the settling particle of density 1.25 g/cm^3 where the constriction gap size $1.25D$.

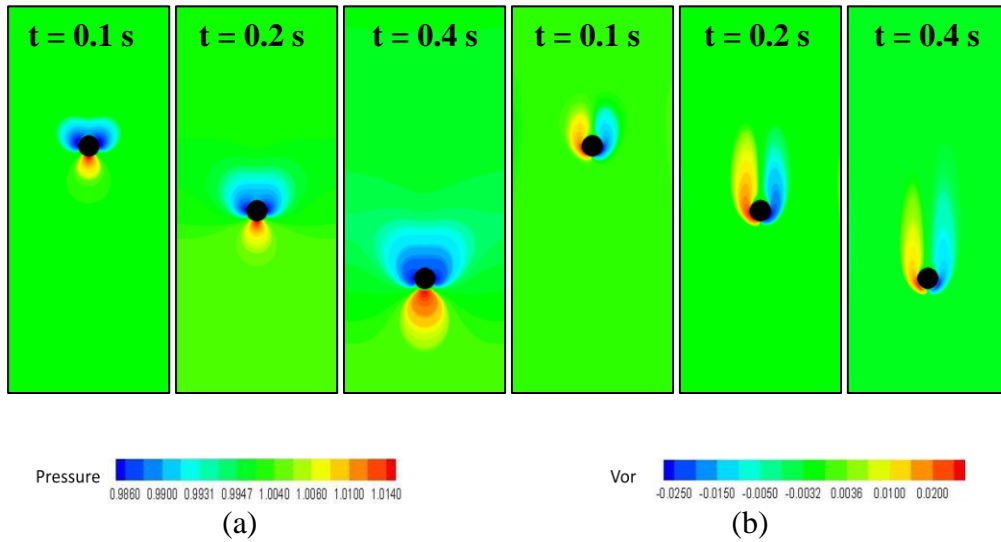


Fig.3.4. Instantaneous pressure and vorticity contours at different time steps of the settling particle of density 1.25 g/cm^3 , while travelling in Zone-1.

In Fig.3.4(a), the pressure contours around the particle are shown where the reference pressure is $\rho_0 c_s^2$. We can observe that the pressure distributions below and above the particle are different. The pressure near the front face of the particle is comparatively higher than the rear end of the particle. This is because the fluid encounters the particle at the front face first and hence leads to formation of the stagnation point or the maximum positive pressure zone. While at the rear end of the particle, there is development of wake separation which leads to low pressure. The rear end pressure contours spread over time that implies increase in the wake length. This growth of the wake region is also observed in the vorticity contour plot, as shown in Fig.3.4(b). The

vorticity growth is associated with the continuous transfer of kinetic energy from the moving particle to the fluid (Ten Cate et al. (2002)).

Zone-2

This is the region of the channel that contains the constriction walls. The particle has attained the terminal velocity in zone-1 before moving to zone-2. At the entrance of zone-2, the velocity plot in Fig.3.3(b), suggests that the particle starts to decelerate with reduction in its velocity magnitude as well as Re and E_t values. In the zone-2, presence of the constriction walls significantly reduces the available space for the particle movement. In literatures (Ten Cate et al. (2002); Feng and Michaelides (2004); Wang et al. (2013)), it was reported that the drag force exerted on the moving particle is a complex inverse function of the channel size. In our present study the channel width in zone-2 is less than other zones. Hence, the drag force on the particle due to the small gap will be higher in zone-2.

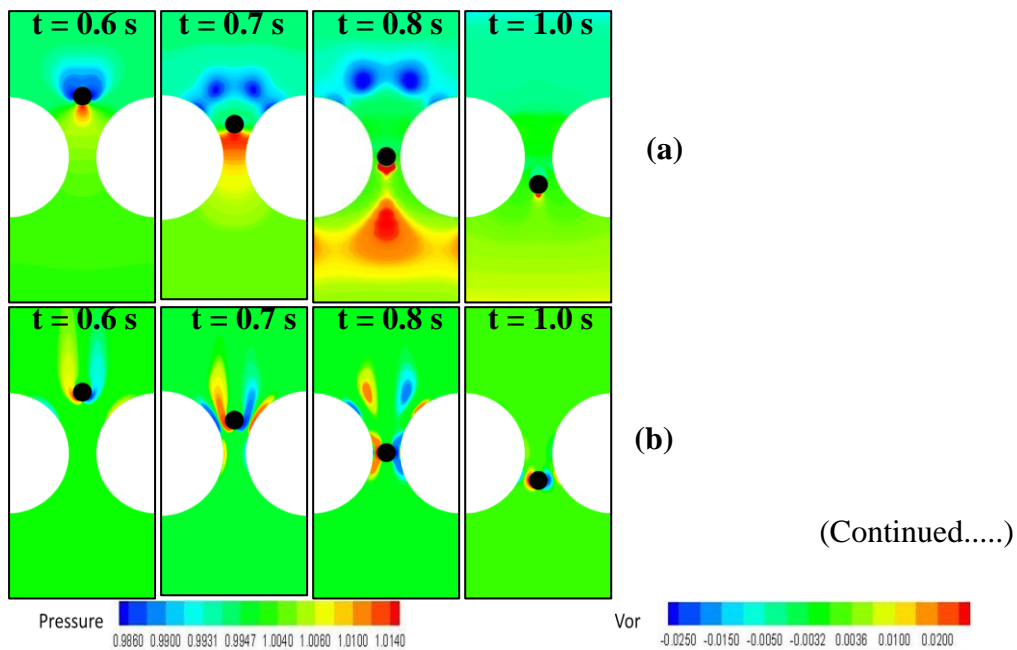


Fig.3.5. Instantaneous pressure and vorticity contours at different time steps while the particle of density 1.25 g/cm^3 is travelling in Zone-2.

In Fig.3.5(a) – (b), the pressure and vorticity contours are plotted, while the particle is settling in zone-2, respectively. In this zone, lateral pressure contours are present due to the constriction walls. While the particle tries to move further down in the constricted section, it squeezes out the surrounding fluid along the sides of the constriction walls. The followed semicircular/convex shaped constriction creates an adverse pressure gradient for this squeezed flow field, which leads to a boundary layer separation as shown in Fig.3.5(b) ($t = 0.7 \text{ s}$). This separated flow field forms two recirculation vortices above the constriction walls. At $t = 0.7 \text{ s}$, there is a low pressure band formed above the constriction walls that includes the two attached vortices on the particle. In the view of flow physics, the low pressure band will attracts the surrounding fluid and spreads its area of influence. Hence, the circulation of the vortices increases as shown in Fig.3.5(b) ($t = 0.8 \text{ s}$). When the attached vortices on the particle are sufficiently large in size, they will shed from the particle. As the particle further settles, the drag force on the particle keeps increasing in the converging section of the constriction gap. Hence, the minimum particle velocity will be noticed at the narrowest gap, which is referred as the maximum retarding velocity (V_R). Beyond the narrowest gap, in the diverging profile of the constriction, the particle again starts accelerating as shown in Fig.3.3(b). It is worth to mention that the retarding and accelerating part of the velocity plot in the constriction zone are not symmetric, which may be due to the presence of lateral pressure contours

in the convergence section and change of the available spatial gap in the divergence section as shown in Fig.3.1(d).

Zone-3

After leaving zone-2, the particle enters to zone-3 which is the bottom section of the channel. The particle keeps accelerating similar to the zone-1 till the steady state/terminal velocity condition is attained. Thereafter particle continues to move with the constant terminal velocity until it settles on the bottom of the channel. As the particle approaches the channel bottom, the kinetic energy of the particle decays and it starts decelerating by squeezing out the fluid between the particle and the bottom wall. This also generates outward flow as shown in the vorticity plot Fig.3.6(b) ($t = 4.0$ s).

In Fig.3.6(a) – (b), the pressure and vorticity contours are plotted while the particle is travelling in zone-3. The plots are similar to that of the zone-1. To realize the collision between the particle and the bottom wall, the lubrication force (Glowinski et al. (2001)) as described in Eq.(2.36) is followed.

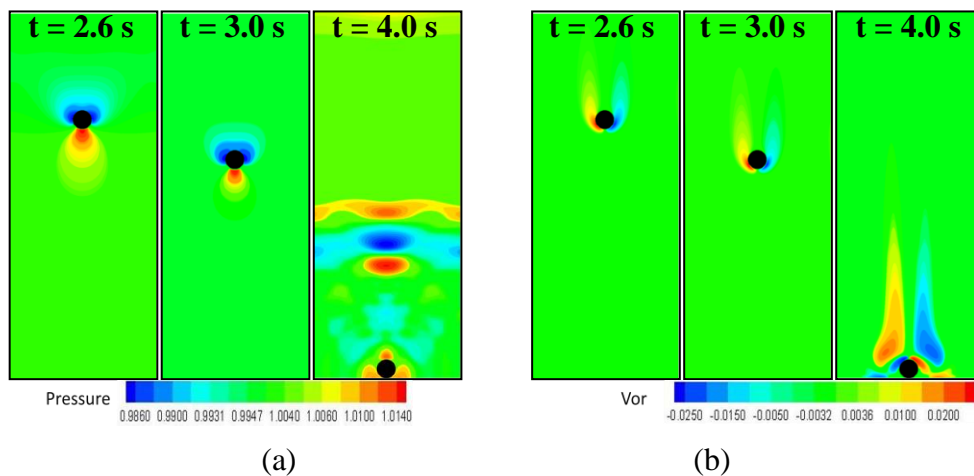


Fig.3.6. Instantaneous pressure and vorticity contours at different time steps while the particle of density 1.25 g/cm^3 is travelling in Zone-3.

3.2.1.2 Effects of constriction gap size

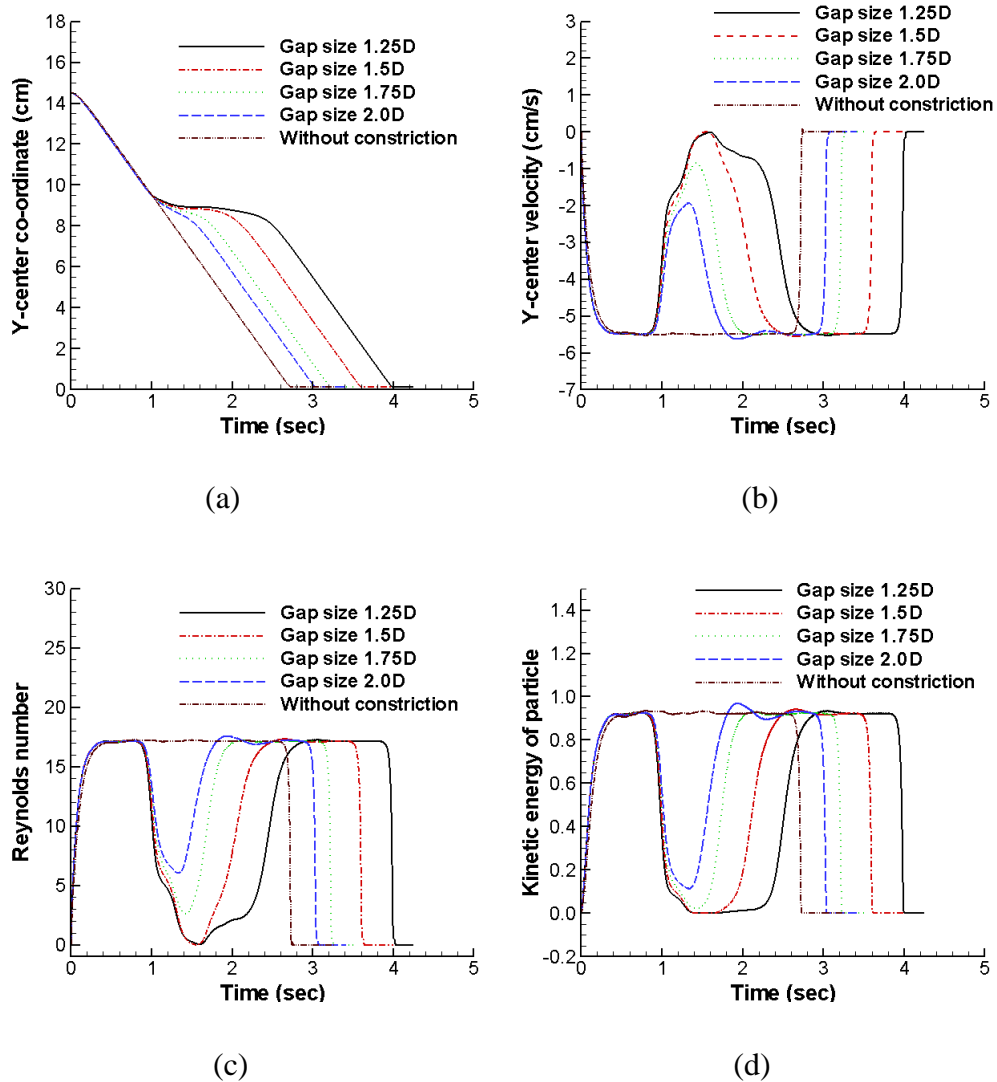
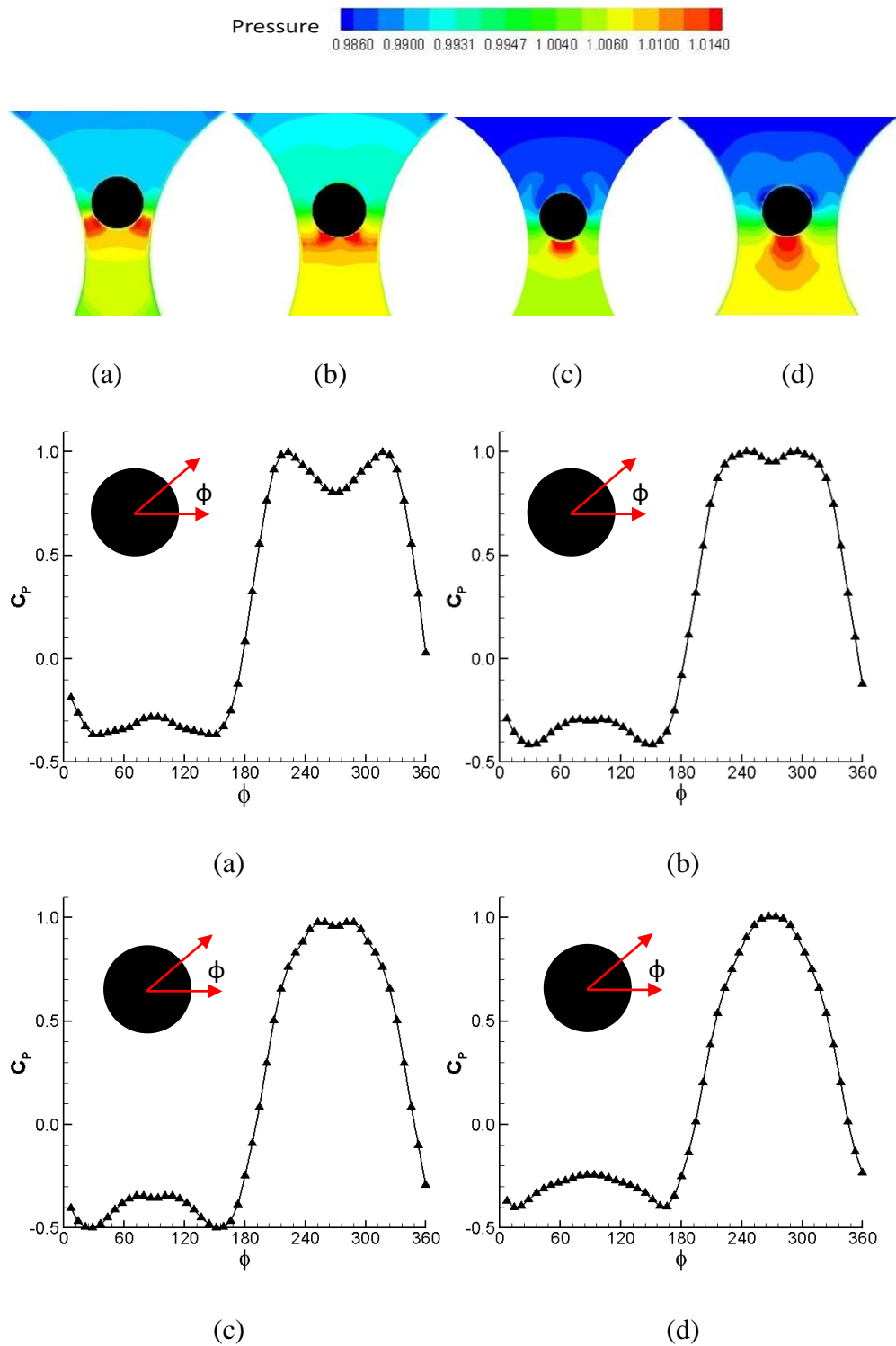


Fig.3.7. Temporal evolution of (a) Y centre co-ordinate (b) Vertical velocity (c) Reynolds number (d) Translational kinetic energy for different constriction gap size, where the settling particle has density 1.25 g/cm^3 .

In order to find out the effects of the constriction gap size, the radius of the semicircular constriction walls are varied. In the present study, we focused the gap size in the range of $1.25D - 2.0D$, between the two constriction walls

along the horizontal centreline. In Fig.3.7 vertical velocity, trajectory, Re and E_t of the particle are plotted for various constriction gaps.



(Continued...)

Fig.3.8. Instantaneous pressure contours on the particle at the centreline of the constriction with gap size (a) 1.25D, (b) 1.5D, (c) 1.75D and (d) 2.0D and corresponding C_p distribution for particle density 1.25 g/cm^3 .

It is found that with the decrease in the constriction gap size the maximum retardation velocity (V_R) increases and corresponding changes in Re and E_t are also produced. This behaviour is associated with the drag force in the narrow gap. In Fig.3.8, the pressure contours and the instantaneous coefficient of pressure (C_p) are shown for different constriction gap sizes, when the particle reaches the centreline of the constriction. In the lower array of Fig.3.8, the distribution of C_p as a function of Φ is shown. For the cases of gap size 1.25D and 1.5D, there are two stagnation points. But for the larger constriction gap there is only one stagnation point. With increase in number of stagnation points, the pressure recovery for the gap size 1.25D is less than that of 2.0D. Hence, the drag force on the particle will be higher in case of gap size 1.25D.

3.2.1.3 Effects of density of the particle

Density of the particle is varied to generate different Reynolds number. For higher density, particle's terminal velocity increases. As the drag force on the particle is an inverse function of the flow velocity, therefore the drag force on the denser particle will be less compare to the lighter particle for a constant constriction gap size. Hence, the magnitude of V_R increases with decrease of particle density. In Fig.3.9(a), V_R as a function of density of the particle is plotted for various channel gaps. It is also found that for a particular particle density, magnitude of V_R decreases with the increase in constriction gap.

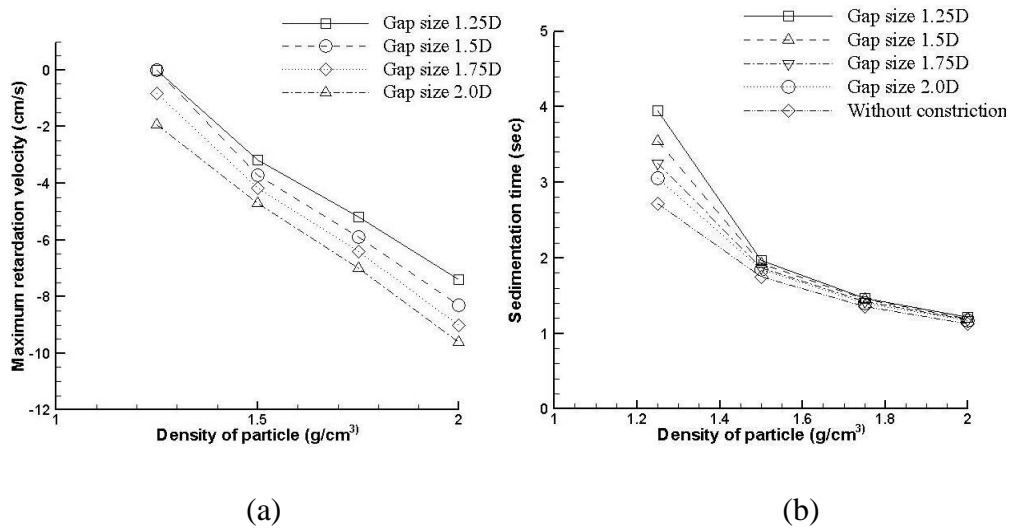


Fig.3.9. Comparisons of (a) maximum retardation velocity (V_R) and (b) sedimentation time for different constriction gap size and density of the particle.

As we know, with increase in the particle density the velocity of the particle increases and thus the sedimentation time gets reduced to reach the channel bottom. The variation in sedimentation time with different constriction gap sizes and densities of the particle are plotted in Fig.3.9(b). It is also observed that with the increase in particle density, the constriction wall effects become insignificant and variation of the sedimentation time is negligible.

Another interesting finding in the constricted passage sedimentation problem is that there may be formation of a ‘*virtual stationary state*’. The particle attains this state with both near zero kinetic energy and slope of the particle trajectory as shown in Fig.3.3(a) – (d). This occurs for certain combination of the particle density and the constriction gap size.

3.2.2 Two particles sedimentation

Two circular particles of same density and diameter are used to study the present sedimentation problem. We named the particles as per their initial order of arrangement: particle-2 and particle-1 for the leading and trailing particles respectively. The initial gap between two particles is $6D$. The initial positions of the particles are $18D$ and $12D$ for particle-2 and particle-1 respectively, which is measured above the center of the semicircular constriction and along the vertical centerline of the channel. In the following, the effects of different constriction gap size ($1.25D - 2.0D$) and different particle density ($1.25 - 2.0 \text{ g/cm}^3$) on the flow regime will be analyzed.

3.2.2.1 Flow regime

Zone-1

This is the region above the constriction walls of the channel. At time $t = 0$, both the particles are at rest and start to fall with gravity effect. In Fig.3.10, velocity and trajectory of the particles is plotted. During the accelerating stage the velocity increases over time and the particle-2 follows the trend of the particle-1 during the initial time steps. But deviation is noticed at the later time steps, which may be due to the interaction between the trailing particle with the wake of the leading one.

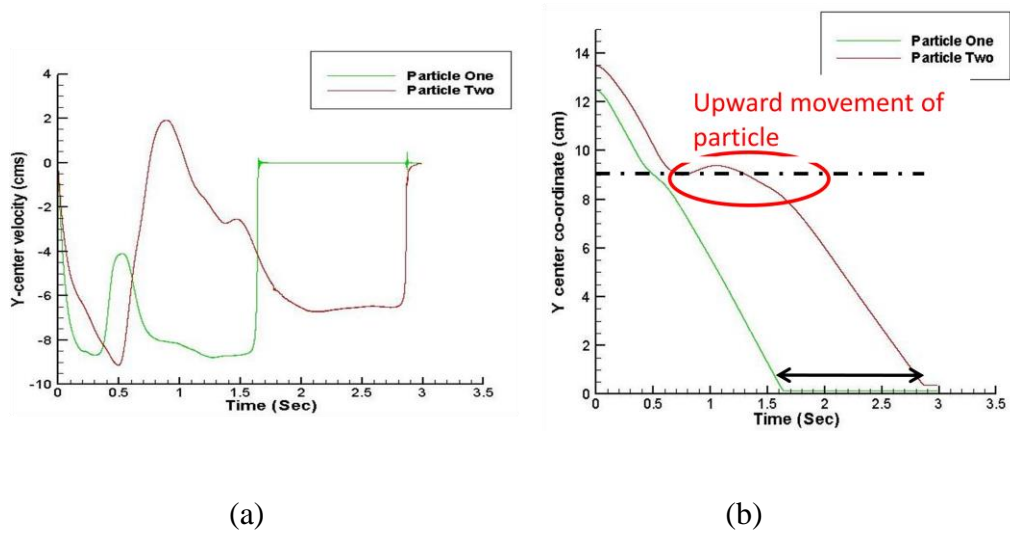


Fig.3.10. Temporal evolution of (a) Vertical velocity (b) Y centre co-ordinate of the particles with density 1.25 g/cm^3 and the constriction gap size $1.5D$.

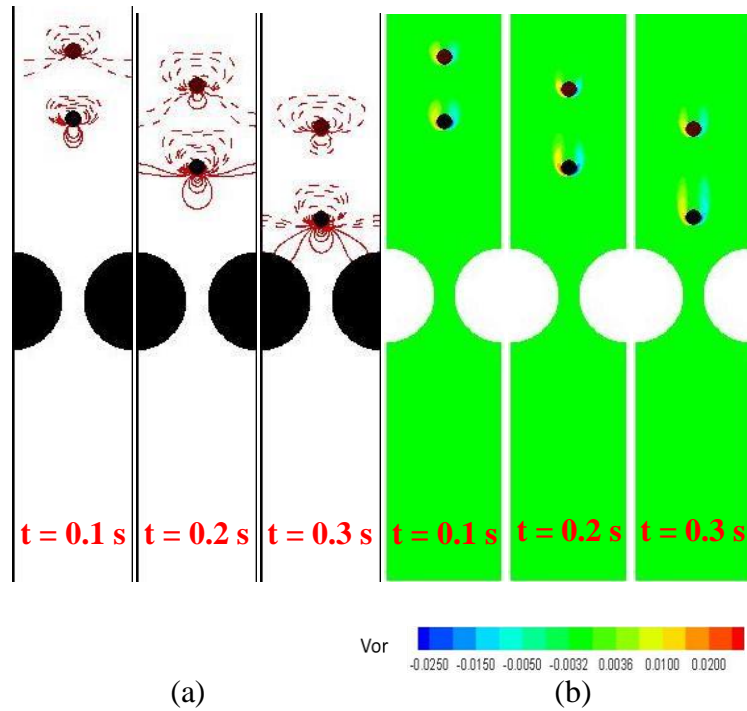


Fig.3.11. Instantaneous pressure and vorticity contours at different time steps while the particles of density 1.25 g/cm^3 is travelling in Zone-1.

At the initial time step the two particles sedimentation resembles closely as an impulsively started flow over tandem circular cylinders. As shown by Sumner, Price et al. (1999) the temporal development of the flow regime is dependent on the cylinders' centre distance. For the centre distance less than $2D$, separated shear layers from the upstream cylinder reattach on the surface of the downstream cylinder. But for the higher centre distance this reattachment is avoided. In the present simulation, we set the initial gap as $4D$ and as the initial Re of the flow is low, which also avoids the streamline reattachment. This can be verified from the vorticity plot in Fig.3.11(b) where the vortices of the two particles do not interact. Again from the pressure contours as shown in Fig.3.11(a), the force exerted on two particles will be different that produce different settling velocities.

Zone-2

This is the region of the channel that contains the constriction walls. For two particles sedimentation, it is found that while particle-2 is travelling in zone-1, particle-1 has already entered zone-2. The behaviour of the particle-1 is similar to that discussed in single particle sedimentation section 3.2.1. Here only the behaviour of the particle-2 will be discussed.

As previously reported a low pressure band will be formed above the constriction wall, once the particle-1 cross zone-2. When the particle-2 enters this low pressure zone with lesser drag force, it accelerates faster and attains higher velocity magnitude than the particle-1 as shown in Fig.3.10(a). With further settling of the particle-2, it encounters narrowing portion of the

constriction zone and the particle-2 starts decelerating due to increase of drag force. From Fig.3.10(a), it is found that the velocity of the particle-2 may reduce to zero and reverse its direction. This means, the particle-2 may have moved upward in zone-2 for certain time before it again starts falling.

The interesting upward movement may be due to the wake region of the particle-1. When the particle-1 crosses the centreline of the constriction it starts accelerating, while from Fig.3.12 we can see that the particle-2 is still decelerating. With forward movements of the particle-1 in the diverging part of the constriction, squeezes out the surrounding fluid through its converging part. This squeezed fluid moves in the opposite direction relative to the motion of the particle-2 thus helping in its velocity deceleration. With the combined effects of the upward drag force and the oppositely moving squeezed fluid may be sufficient to balance the weight of the particle and makes the particle move upward. Using the vector plots (Fig.3.13) of the fluid velocity this motion can be verified. To further verify this flow regime, pressure contours are plotted. It is noticed that there is a critical point in the wake of the particle-1 where streamlines are discontinuous. From the definition of Perry and Chong (1987), this discontinuity is associated with formation of a 'node/critical point'. Again the critical point is linked with a pressure gradient (Perry and Chong (1987)) and hence leads to a force generation. We noticed that the pressure gradient reduces with further downward movement of the particle-1. With the reduction in drag force and under the effects of gravity, the particle-2 again starts falling downward and reaches the zone-3. The corresponding vorticity plots are shown in Fig.3.12(b).

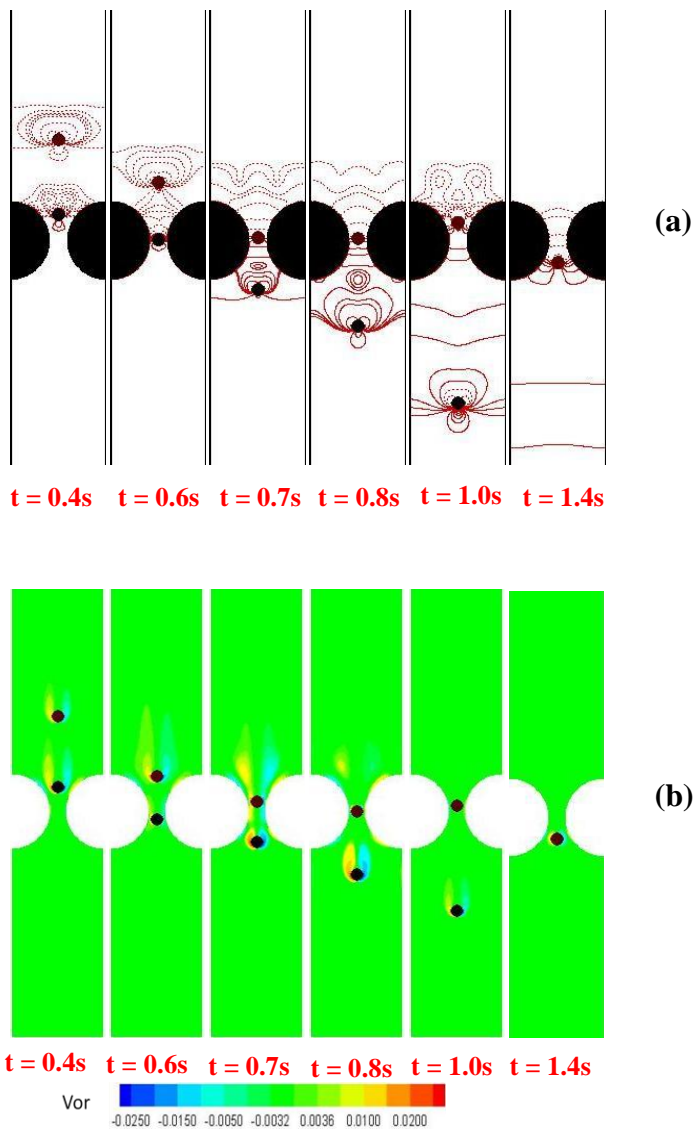


Fig.3.12. Instantaneous pressure and vorticity contours at different time steps while the particles of density 1.25 g/cm^3 is travelling in Zone-2.

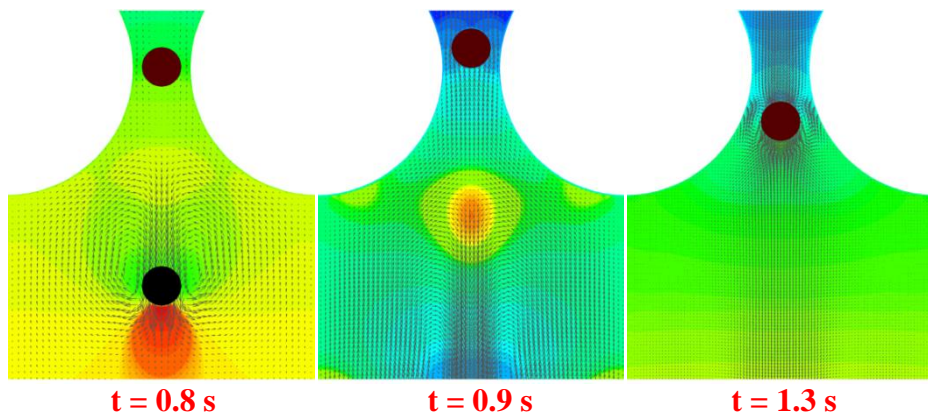


Fig.3.13. Velocity vector plot at different time step for the particle of density 1.25 g/cm^3 near zone-2 where the constriction gap size is $1.75D$.

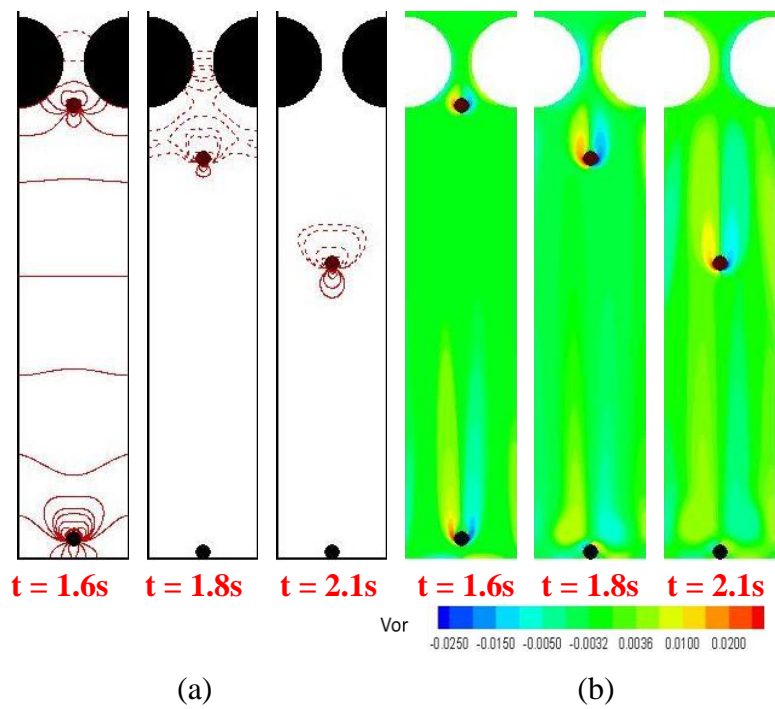


Fig.3.14. Instantaneous pressure and vorticity contours at different time steps while the particles of density 1.25 g/cm^3 is travelling in Zone-3.

Zone-3

This is the region of the channel below the constriction walls. The flow regimes behind the particles are much similar to the zone-3 of the single particle sedimentation case. The particles attain the terminal velocity before resting on the channel base. Here one thing should be noticed that the terminal velocity of the particle-2 is less than the terminal velocity of the particle-1. This is because with movement of the particle-1, the fluid in its wake gains kinetic energy and as mentioned by ten Cate, Nieuwstad et al. (2002), the momentum diffusive time scale of the fluid is larger than the particle advection time scale. Therefore, when the particle-2 moves in the wakes of the particle-1 the surrounding flow field still retains certain relative velocity. Thus the terminal velocity is smaller for the particle-2. The pressure and vorticity plots for this zone are shown in Fig.3.14(a) – (b).

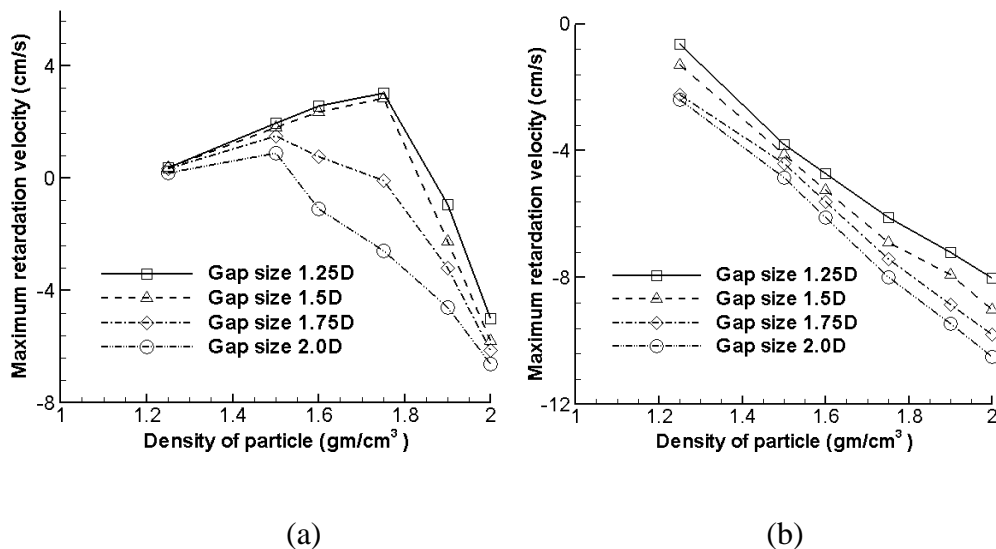


Fig.3.15. Comparisons of maximum retardation velocity (V_R) for different constriction gap size and density of the particles; (a) Particle-2 (b) particle-1.

3.2.2.2 *Effects of constriction gap*

Constriction gap effects are studied by comparing the maximum retarding velocities (V_R) of the particles. With the decrease of the constriction gap, the retardation velocity increases for a constant particle density. Again by increasing the density of the particle, the retardation velocity is found decreasing. A comparison plot is shown in Fig.3.15 for particle-1 and particle-2. We have also compared the sedimentation time lag between two particles as shown in Table 3.2. It is found that with reduction in the constriction gap size, the time lag increases significantly. Also with the increase in particle density, the time lag decreases.

Table 3.2 Sedimentation time lag (in sec) between particle-2 and particle-1 for different constriction gap size and density of the particle.

Density (g/cm^3)	Gap size = 1.25D	Gap size = 1.5D	Gap size = 1.75D	Gap size = 2.0D
1.25	3.0	2.4	1.6	1.5
1.5	1.8	1.2	1.1	0.98
1.75	1.3	1.0	0.7	0.5
2.0	0.3	0.2	0.15	0.1

3.3 Concluding remarks

In this chapter, we have utilized the developed 2D flexible forcing hybrid IB – LBM scheme to simulate the particulate flow in presence of surrounding wall effects where minimal study reports are available in literature. Therefore, in

this numerical study, it is the first time we have characterized the sedimentation of single and two particles in a 2D channel with two symmetric semicircular constriction walls. The effects of density of the solid particles, viscosity of the fluid, shape and size of the constriction are investigated separately for single and two particle sedimentation cases. In this study only the circular shaped constrictions are used where other shapes (like rectangular or triangular) are under the scope of future investigation.

Chapter 4

A 2D Flexible Forcing Immersed Boundary and Thermal Lattice Boltzmann Method³

In this chapter a two dimensional hybrid numerical scheme is introduced for modelling fluid – solid interactions in an incompressible, viscous flow domain where the thermal effects are accounted. As discussed previously, IBM have been extensively utilised to simulate various fluid – solid coupled problems without thermal effects (Peskin (1977); Lai and Peskin (2000); Zhu and Peskin (2002); Feng and Michaelides (2004); Feng and Michaelides (2005); Wu and Shu (2009); Wu and Shu (2010); Wu and Shu (2010)) whereas only limited works were reported for thermal flow cases (Pacheco et al. (2005); Wang et al.

³ Part of this work has been published as:

Dash SM, Lee TS and Huang H. (2013). "Natural Convection from an Eccentric Square Cylinder Using a Novel Flexible Forcing IB-LBM Method." Numerical Heat Transfer, Part A: Applications **65**(6): 531-555

Dash SM and Lee TS (2014). "Natural Convection from Inclined Square Cylinder Using Novel Flexible Forcing IB-LBM Approach." Engineering Applications of Computational Fluid Mechanics **8**(1): 91-103

Dash SM, Lee TS and Huang H. (2013). "A Novel Flexible Forcing Hybrid Ib-Thermal Lb Model for Natural Convection from a Circular Cylinder." International Journal of Dynamics of Fluids **9**(1): 1-15

(2009); Jeong et al. (2010); Ren et al. (2012)). In the conventional IBM, the unsatisfied velocity boundary condition may produce non-physical streamline penetration into the solid boundary. While applying IBM to the thermal flow case, apart from momentum equation an extra energy equation is solved where the improper temperature boundary condition may leads to similar non-physical isotherm penetration into the solid boundary. In Chapter 2, we have discussed a flexible forcing IB – LBM model for isothermal flow case that removes these defects, at the same time the simplified mathematical formulation lessen the computational effort and resource requirement. Here, the developed scheme has uniquely combined the non-body-fitted IBM techniques with the mesoscopic thermal LBM solver. The details of the mathematical formulations are outlined in the followings. The numerical accuracy and validation of the present scheme are checked by performing a number of benchmark flow case simulations.

4.1 Numerical methodology

4.1.1 Thermal lattice Boltzmann method

The thermal lattice Boltzmann model (TLBM) are presently categorised into three major groups: 1) Multispeed approach, 2) Passive scalar approach and 3) Thermal energy distribution approach (also referred as double density population approach). We have highlighted the shortcomings such as numerical instabilities and restriction on Prandtl number (Pr) selection, of the multispeed model (Chen et al. (1994); Watari and Tsutahara (2004)) and

passive scalar model (Li et al. (2008)) in previous introduction section (ref. Chapter 1). Alternatively, He et al. (1998) have proposed a thermal energy distribution/double population TLBM, that uses two distinct density distribution functions for evolution of the momentum and temperature field. Although this model is able to solve complex thermal problems, but the drawbacks like complicated gradient term and involvement of viscosity in the momentum as well as energy equations raises numerical difficulty for practical implementation and produces inconsistency while applying the boundary condition. Peng et al. (2003) have suggested a simplified model where the viscosity definition is consistent in both the evolution LBEs and removed the complicated gradient term by omitting the viscous heat dissipation and compression work due to the pressure. In the present study, we have followed this modified double distribution function model (DDF) (Peng et al. (2003)) to describe the temperature field evolution. The relevant derivations of DDF model are provided in the followings.

From the kinetic theory, the evolution of the single particle density distribution function obeys continuous Boltzmann equation.

$$\partial_t f + (\mathbf{e} \cdot \nabla) f = \Omega(f) + F_f \quad (4.1)$$

where f is the single particle density distribution function, \mathbf{e} is the microscopic particle velocity, $\Omega(f) = -\frac{f - f^{eq}}{\tau_v}$ is the collision operator,

f^{eq} is the equilibrium distribution function and τ_v is the relaxation time.

$F_f = \mathbf{G} \cdot \nabla_e f$ is a term due to the external force \mathbf{G} that acts on per unit fluid mass.

Here, the fluid variables i.e. density ρ , velocity \mathbf{u} and temperature T can be defined as the moments of f in D dimensional space.

$$\begin{pmatrix} \rho \\ \rho \mathbf{u} \\ \frac{D\rho RT}{2} \end{pmatrix} = \begin{pmatrix} \int f d\mathbf{e} \\ \int \mathbf{e} f d\mathbf{e} \\ \int \frac{(\mathbf{e} - \mathbf{u})^2}{2} f d\mathbf{e} \end{pmatrix}. \quad (4.2)$$

In the above although the BGK model retains the main features of the original Boltzmann collision operator, it limits the applicability to a fixed Pr (Jehring (1992). To avoid this defect He et al. (1998) have introduced another relaxation time into the non-equilibrium distribution function after noticing that the momentum and energy should have different transport time scale during the collision process. They have defined a new variable as, an internal energy distribution function which is shown in Eq.(4.3),

$$g = \frac{(\mathbf{e} - \mathbf{u})^2}{2} f. \quad (4.3)$$

A BGK type kinetic equation for g can be constructed based on the Boltzmann equation (Eq.(4.1)), which allows for the internal energy having a relaxation time scale different from that of the momentum transport.

$$\partial_t g + (\mathbf{e} \cdot \nabla) g = \frac{(\mathbf{e} - \mathbf{u})^2}{2} \Omega(f) - f (\mathbf{e} - \mathbf{u}) \cdot [\partial_t \mathbf{u} + (\mathbf{e} \cdot \nabla) \mathbf{u}]. \quad (4.4)$$

We can simplify the Eq.(4.4) to Eq.(4.5) by defining

$$\frac{(\mathbf{e}-\mathbf{u})^2}{2}\Omega(f) = -\frac{g-g^{eq}}{\tau_c},$$

$$\partial_t g + (\mathbf{e}\cdot\nabla)g = -\frac{g-g^{eq}}{\tau_c} - f(\mathbf{e}-\mathbf{u})\cdot[\partial_t\mathbf{u} + (\mathbf{e}\cdot\nabla)\mathbf{u}], \quad (4.5)$$

where

$$g^{eq} = \frac{(\mathbf{e}-\mathbf{u})^2}{2} f^{eq} = \frac{(\mathbf{e}-\mathbf{u})^2}{2} \rho (2\pi RT)^{-D/2} \exp\left[-\frac{(\mathbf{e}-\mathbf{u})^2}{2RT}\right]. \quad (4.6)$$

With above modifications, the macroscopic density and velocity are still determine from the moments of the density distribution function f as presented in Eq.(4.2), but the internal energy $\epsilon = DRT/2$ is now defined with the new internal energy distribution function g .

$$\rho\epsilon = \int g d\mathbf{e} \quad (4.7)$$

The above continuous Boltzmann evolution equations (Eq.(4.1) and Eq.(4.5)) should be discretised in the temporal, spatial and velocity (phase) space so as to recover the correct macroscopic equations. In isothermal LBM, this is done by integrating the Eq.(4.1) using the first order scheme, where the second-order truncation error is absorbed into the physical viscous term. The effect is that the viscosity value changes from $\tau_v RT$ to $(\tau_v - 0.5)RT\delta t$. However, in the thermal models, the viscosity is not only involved in the momentum equations but also in the energy equation. As shown by He et al. (1998), the

second order term is no longer trivial, and the viscous heat dissipation term comes from the non-equilibrium part of the density distribution function. This term is not affected by the second order truncation error and only arises from the second order Chapman – Enskog expansion. Hence, the viscosity in the viscous heat dissipation can retain the value $\tau_v RT$. To eliminate the above identified inconsistency, we have followed Peng et al. (2003) second order discretisation process neglecting the viscous heat dissipation and compression work by pressure where the discretised governing equations for the simplified thermal energy distribution model are,

$$f_i(\mathbf{x} + \mathbf{e}_i \delta t, t + \delta t) = f_i(\mathbf{x}, t) - \frac{f_i(\mathbf{x}, t) - f_i^{eq}(\mathbf{x}, t)}{\tau_v} + \delta t F_i, \quad (i=0,1,2,\dots,N), \quad (4.8)$$

$$g_i(\mathbf{x} + \mathbf{e}_i \delta t, t + \delta t) = g_i(\mathbf{x}, t) - \frac{g_i(\mathbf{x}, t) - g_i^{eq}(\mathbf{x}, t)}{\tau_c}, \quad (i=0,1,2,\dots,N), \quad (4.9)$$

When D2Q9 lattice model is employed, the lattice velocities \mathbf{e}_i and weighting coefficients W_i are defined as,

$$\mathbf{e}_i = c \begin{cases} (0,0), & i=0, \\ (\pm 1,0), (0,\pm 1), & i=1-4, \\ (\pm 1,\pm 1), & i=5-8. \end{cases} \quad W_i = \begin{cases} 4/9, & i=0, \\ 1/9, & i=1-4, \\ 1/36, & i=5-8. \end{cases} \quad (4.10)$$

For this lattice model, the equilibrium density distribution functions of momentum and thermal energy (f_i^{eq}, g_i^{eq}) are defined as,

$$f_i^{eq}(\mathbf{x}, \mathbf{e}_i, t) = W_i \rho \left(1 + \frac{\mathbf{e}_i \cdot \mathbf{u}}{c_s^2} + \frac{(\mathbf{e}_i \cdot \mathbf{u})^2}{2c_s^4} - \frac{\mathbf{u}^2}{2c_s^2} \right), \quad (i=0,1,2,\dots,8), \quad (4.11)$$

$$g_0^{eq}(\mathbf{x}, \mathbf{e}_i, t) = -\frac{2\rho\epsilon}{3} \frac{|\mathbf{u}|^2}{c^2}, \quad (4.12)$$

$$g_{1,2,3,4}^{eq}(\mathbf{x}, \mathbf{e}_i, t) = \frac{\rho\epsilon}{9} \left[\frac{3}{2} + \frac{3\mathbf{e}_i \cdot \mathbf{u}}{2c^2} + \frac{9(\mathbf{e}_i \cdot \mathbf{u})^2}{2c^4} - \frac{3|\mathbf{u}|^2}{2c^2} \right], \quad (4.13)$$

$$g_{5,6,7,8}^{eq}(\mathbf{x}, \mathbf{e}_i, t) = \frac{\rho\epsilon}{36} \left[3 + 6\frac{\mathbf{e}_i \cdot \mathbf{u}}{c^2} + \frac{9(\mathbf{e}_i \cdot \mathbf{u})^2}{c^4} - \frac{3|\mathbf{u}|^2}{2c^2} \right]. \quad (4.14)$$

The macroscopic density, velocity and temperature are then calculated as:

$$\rho = \sum_{i=0}^8 f_i, \quad \rho \mathbf{u} = \sum_{i=0}^8 \mathbf{e}_i f_i, \quad \rho \epsilon = \sum_{i=0}^8 g_i. \quad (4.15)$$

When Chapman – Enskog expansion is performed, Eq.(4.8) will recover the continuity and momentum equations (Eq.(2.14) – (2.15)) where the viscosity ν is defined as $(\tau_v - 0.5)RT\delta t$. Similarly, Eq.(4.9) will recover the energy equation (Eq.(4.16)) where the thermal diffusivity ψ is defined as $2(\tau_c - 0.5)RT\delta t$ (Peng, Shu et al. (2003)).

$$\partial_t(\rho\epsilon) + \nabla \cdot (\rho \mathbf{u} \epsilon) = \psi \nabla^2(\rho\epsilon) \quad (4.16)$$

4.1.2 Flexible forcing immersed boundary – thermal lattice Boltzmann method

To formulate this coupled scheme, let us consider an incompressible viscous thermal flow of Newtonian fluid in a two-dimensional domain Ω , which contain a heated closed immersed boundary curve Γ as shown in Fig.4.1. By extending the original idea of Peskin (1977), the heated boundary condition on Γ can be modelled as a set of heat sources at each of the boundary segments (represented with Lagrangian Marker points). Hence, the effects of the immersed boundary Γ can be realised on the surrounding fluid domain Ω by introducing the forcing term into the momentum equations and incorporating the heat source/sink term in the energy equation. The modified governing equations in primitive variable form are:

$$\frac{\partial \rho}{\partial t} + \nabla \cdot \rho \mathbf{u} = 0, \quad (4.17)$$

$$\frac{\partial}{\partial t}(\rho \mathbf{u}) + \nabla \cdot (\rho \mathbf{u} \mathbf{u}) = -\nabla p + \nu \nabla \cdot [\rho \nabla \mathbf{u} + (\nabla \mathbf{u})^T] + \mathbf{f}, \quad (4.18a)$$

$$\frac{\partial}{\partial t}(\rho \mathbf{u}) + \nabla \cdot (\rho \mathbf{u} \mathbf{u}) = -\nabla p + \nu \nabla \cdot [\rho \nabla \mathbf{u} + (\nabla \mathbf{u})^T] + \rho g (1 - \beta(T - T_{mean})) \vec{j} + \mathbf{f}, \quad (4.18b)$$

$$\rho C_P \left(\frac{\partial T}{\partial t} + \nabla \cdot (T \mathbf{u}) \right) = k \nabla^2 T + q, \quad (4.19)$$

$$\mathbf{f}(\mathbf{x}, t) = \int_{\Gamma} \mathbf{F}_B(s, t) \delta(\mathbf{x} - \mathbf{X}_B(s, t)) ds, \quad (4.20)$$

$$q(\mathbf{x}, t) = \int_{\Gamma} Q_B(s, t) \delta(\mathbf{x} - \mathbf{X}_B(s, t)) ds, \quad (4.21)$$

together with the boundary conditions Eqs.(4.22) – (4.23) on Γ .

$$\mathbf{U}_B(\mathbf{X}_B(s, t), t) = \mathbf{u}(\mathbf{X}_B(s, t), t) = \int_{\Omega} \mathbf{u}(\mathbf{x}, t) \delta(\mathbf{x} - \mathbf{X}_B(s, t)) d\mathbf{x}, \quad (4.22)$$

$$T_B(\mathbf{X}_B(s, t), t) = T(\mathbf{X}_B(s, t), t) = \int_{\Omega} T(\mathbf{x}, t) \delta(\mathbf{x} - \mathbf{X}_B(s, t)) d\mathbf{x}, \quad (4.23)$$

where the variables: $\rho, \mathbf{u}, p, \nu, T, k, C_p$ represent density, flow velocity, pressure, kinematic viscosity, temperature, thermal conductivity and constant pressure specific heat of the working fluid respectively. \mathbf{x} and \mathbf{X}_B are Eulerian and Lagrangian mesh co-ordinates, \mathbf{f} and \mathbf{F}_B are the force density acting on the fluid and immersed boundary respectively. q and Q_B are the heat source/sink density acting on the fluid and immersed boundary respectively.

$\delta(\mathbf{x} - \mathbf{X}_B(s, t))$ is the Dirac delta function. \vec{j} is the unit vector in positive Y direction. The above Eq.(4.17) is the continuity equation which together will be solved with momentum equations (Eq.(4.18a) for forced convection and Eq.(4.18b) for natural convection). Eqs.(4.20) – (4.21) relates the immersed solid boundary Γ and fluid domain Ω by distributing the boundary force to the nearby fluid points and relating the boundary velocity/temperature with the fluid velocity/temperature.

The above flow governing equations (Eqs.(4.17) – (4.19)), are solved using the developed flexible forcing IB – TLBM scheme, where the corresponding lattice Boltzmann equations (LBEs) are:

$$f_i(\mathbf{x}+\mathbf{e}_i\delta t, t+\delta t) = f_i(\mathbf{x}, t) - \frac{1}{\tau_v} \left(f_i(\mathbf{x}, t) - f_i^{eq}(\mathbf{x}, t) \right) + F_i\delta t + F_i^T\delta t, \quad (4.24)$$

$$g_i(\mathbf{x}+\mathbf{e}_i\delta t, t+\delta t) = g_i(\mathbf{x}, t) - \frac{1}{\tau_c} \left(g_i(\mathbf{x}, t) - g_i^{eq}(\mathbf{x}, t) \right) + Q_i\delta t. \quad (4.25)$$

Here, f_i and g_i are the density distribution functions for fluid flow and internal energy respectively, along the discrete lattice direction i . f_i^{eq} and g_i^{eq} are the corresponding equilibrium distribution function which are derived from Taylor series expansion of Maxwell Boltzmann distribution as shown in Eqs.(4.11) – (4.14). τ_v and τ_c are the non-dimensional relaxation parameters in the BGK approximation.

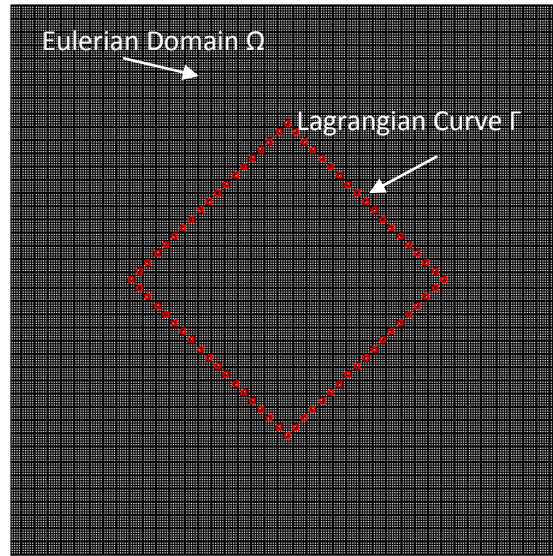


Fig.4.1. A two dimensional domain Ω containing a heated immersed boundary Γ .

In IBM with decoupled fluid and solid mesh additional body force/heat source density terms, \mathbf{f}, q are included in the flow equations to satisfy the no-slip

velocity/no-jump temperature boundary conditions on the immersed cylinder.

In LBM framework these source terms, F_i , Q_i are represented in the discrete lattice directions as (Guo et al. (2002)),

$$F_i = \left(1 - \frac{1}{2\tau_v}\right) W_i \left(\frac{\mathbf{e}_i - \mathbf{u}}{c_s^2} + \frac{\mathbf{e}_i \cdot \mathbf{u}}{c_s^4} \mathbf{e}_i \right) \cdot \mathbf{f}, \quad (4.26)$$

$$Q_i = W_i q. \quad (4.27)$$

To simulate the natural convection where buoyancy is the only source of flow generation, we have followed Boussinesq approximation of a temperature dependent density term \mathbf{G} and correspondingly additional discrete forcing F_i^T (Luo (1998)) is included in LBE Eq.(4.24).

$$\rho \mathbf{G} = \rho \beta g (T - T_{mean}) \vec{j}, \quad (4.28)$$

$$F_i^T = \frac{\mathbf{G} \cdot (\mathbf{e}_i - \mathbf{u})}{RT} f_i^{eq}, \quad (4.29)$$

where g is the acceleration due to gravity along the vertical direction \vec{j} (unit vector). With above definitions, the macroscopic velocity and temperature are calculated as (Guo et al. (2002)),

$$\rho \mathbf{u} = \sum_i \mathbf{e}_i f_i + \frac{1}{2} \mathbf{f} \delta t, \quad (4.30)$$

$$\rho \epsilon = \sum_i g_i + \frac{1}{2} q \delta t. \quad (4.31)$$

Now defining, $\mathbf{u}^* = \sum_{i=0}^8 \mathbf{e}_i f_i / \rho$, $T^* = \sum_{i=0}^8 g_i / R\rho$ intermediate Eulerian velocity and temperature; $\delta\mathbf{u} = (1/2\rho)\mathbf{f}\delta t$, $\delta T = (1/2R\rho)q\delta t$ Eulerian velocity and temperature correction term respectively, we can rewrite the Eqs.(4.30) – (4.31) as, $\mathbf{u} = \mathbf{u}^* + \delta\mathbf{u}$, $T = T^* + \delta T$. Here, to perform implicit computation, the Eulerian velocity and temperature correction ($\delta\mathbf{u}$, δT) are kept unknown and are calculated such that the exact no-slip velocity and no-jump temperature boundary conditions are satisfied. Following the Dirac delta function interpolation the unknown Eulerian velocity and temperature correction can be derived from the unknown Lagrangian boundary velocity and temperature correction ($\delta\mathbf{U}_B$ and δT_B).

$$\delta\mathbf{u}(\mathbf{x}, t) = \int_{\Gamma} \delta\mathbf{U}_B(\mathbf{X}_B, t) \delta(\mathbf{x} - \mathbf{X}_B) ds, \quad (4.32)$$

$$\delta T(\mathbf{x}, t) = \int_{\Gamma} \delta T_B(\mathbf{X}_B, t) \delta(\mathbf{x} - \mathbf{X}_B) ds, \quad (4.33)$$

where the immerse boundary is represented using a set of Lagrangian coordinates $\mathbf{X}_B(s_k, t)$. s_k ($k=1,2,3\dots n$) is the position in the Lagrangian coordinates. $\delta(\mathbf{x} - \mathbf{X}_B)$ is smoothly approximated by continuous Kernel distribution $D(\mathbf{x} - \mathbf{X}_B)$,

$$\delta(\mathbf{x} - \mathbf{X}_B^k) = D(\mathbf{x} - \mathbf{X}_B^k) = \frac{1}{h^2} \delta\left(\frac{x - X_B^k}{h}\right) \delta\left(\frac{y - Y_B^k}{h}\right), \quad (4.34)$$

where $\delta(r)$ is approximated using 2 point Dirac delta function

$$\delta(r) = \begin{cases} 1-|r|, & |r| \leq 1, \\ 0, & |r| > 1. \end{cases} \quad (4.35)$$

Here, h is the Eulerian mesh spacing. Substituting the Eq.(4.34) into the Eqs.(4.32) – (4.33), the velocity and temperature correction expressions can be simplified to algebraic forms,

$$\delta \mathbf{u}(\mathbf{x}, t) = \sum_k \delta \mathbf{U}_B^k(\mathbf{X}_B^k, t) D(\mathbf{x} - \mathbf{X}_B^k) \Delta s_k, \quad (4.36)$$

$$\delta T(\mathbf{x}, t) = \sum_k \delta T_B^k(\mathbf{X}_B^k, t) D(\mathbf{x} - \mathbf{X}_B^k) \Delta s_k, \quad (4.37)$$

where Δs_k is the arc length of the Lagrangian boundary element.

The next task is to calculate the no-slip velocity/no-jump temperature boundary conditions. Mathematically, these boundary conditions imply that the fluid velocity/temperature at the boundary point must be equal to the desired boundary velocity/temperature $(\mathbf{U}_B^{kd}, T_B^{kd})$ at the same position.

These can be expressed as,

$$\mathbf{U}_B^{kd}(\mathbf{X}_B^k, t) = \sum_{x,y} \mathbf{u}(\mathbf{x}, t) D(\mathbf{x} - \mathbf{X}_B^k) \Delta x \Delta y, \quad (4.38)$$

$$T_B^{kd}(\mathbf{X}_B^k, t) = \sum_{x,y} T(\mathbf{x}, t) D(\mathbf{x} - \mathbf{X}_B^k) \Delta x \Delta y, \quad (4.39)$$

where Δx and Δy are the mesh sizes in horizontal and vertical direction.

Substituting the intermediate velocity/temperature and Eulerian velocity/temperature correction in the Eqs.(4.38) – (4.39) we get,

$$\begin{aligned} \mathbf{U}_B^{kd}(\mathbf{X}_B^k, t) &= \sum_{x,y} \mathbf{u}^*(\mathbf{x}, t) D(\mathbf{x} - \mathbf{X}_B^k) \Delta x \Delta y \\ &+ \sum_{x,y} \sum_k \delta \mathbf{U}_B^k(\mathbf{X}_B^k, t) D(\mathbf{x} - \mathbf{X}_B^k) \Delta s_k D(\mathbf{x} - \mathbf{X}_B^k) \Delta x \Delta y. \end{aligned} \quad (4.40)$$

$$\begin{aligned} T_B^{kd}(\mathbf{X}_B^k, t) &= \sum_{x,y} T^*(\mathbf{x}, t) D(\mathbf{x} - \mathbf{X}_B^k) \Delta x \Delta y \\ &+ \sum_{x,y} \sum_k \delta T_B^k(\mathbf{X}_B^k, t) D(\mathbf{x} - \mathbf{X}_B^k) \Delta s_k D(\mathbf{x} - \mathbf{X}_B^k) \Delta x \Delta y. \end{aligned} \quad (4.41)$$

The implicit computation involves the unknowns $\delta \mathbf{U}_B^k$ and δT_B^k . To evaluate these correction terms complex matrices inversion are required. For the flow problems with larger Lagrangian boundary points such as, 3D or complex geometries, inversion of matrix is computationally tedious and expensive. Also the coefficients of $\delta \mathbf{U}_B^k$ and δT_B^k in Eqs.(4.40) – (4.41) need a sequential computational code, which also demands higher memory usage even for a simple 2D problem. To avoid these difficulties a simple modification is proposed here. In RHS of Eqs.(4.40) – (4.41), the second term is responsible for making the form of equation complex. Instead of above formulation single Lagrangian velocity/temperature correction is followed as shown in Eqs.(4.42) – (4.43), that makes the corrected boundary velocity/temperature equals to the desired boundary velocity/temperature (\mathbf{U}_B^k or T_B^k).

$$\mathbf{U}_B^{kd}(\mathbf{X}_B^k, t) = \sum_{x,y} \mathbf{u}(\mathbf{x}, t) D(\mathbf{x} - \mathbf{X}_B^k) \Delta x \Delta y + \delta \mathbf{U}_B^k(\mathbf{X}_B^k, t)^m, \quad (4.42)$$

$$T_B^{kd}(\mathbf{X}_B^k, t) = \sum_{x,y} T(\mathbf{x}, t) D(\mathbf{x} - \mathbf{X}_B^k) \Delta x \Delta y + \delta T_B^k(\mathbf{X}_B^k, t)^m, \quad (4.43)$$

$$\delta \mathbf{U}_B^k(\mathbf{X}_B^k, t)^m = \mathbf{U}_B^{kd}(\mathbf{X}_B^k, t) - \sum_{x,y} \mathbf{u}(\mathbf{x}, t) D(\mathbf{x} - \mathbf{X}_B^k) \Delta x \Delta y, \quad (4.44)$$

$$\delta T_B^k(\mathbf{X}_B^k, t)^m = T_B^{kd}(\mathbf{X}_B^k, t) - \sum_{x,y} T(\mathbf{x}, t) D(\mathbf{x} - \mathbf{X}_B^k) \Delta x \Delta y, \quad (4.45)$$

where the amount of boundary velocity/temperature correction ($\delta \mathbf{U}_B^k$ or δT_B^k), can be obtained using Eqs.(4.44) – (4.45). The above correction principle may not ensure the exact boundary conditions at all the boundary points in single turn as the boundary velocity/temperature correction are linked with the Eulerian velocity/temperature correction (Eq.(4.36) – (4.37)). Hence, an additional sub-iteration update scheme is imposed to satisfy the boundary conditions within a convergence limit. The convergence criteria (CC) are set in Eqs.(4.46) – (4.47), where m is the sub-iteration number until CC is satisfied.

$$\left| \delta \mathbf{U}_B^k(\mathbf{X}_B^k, t)^m \right| \leq 10^{-p}. \quad (4.46)$$

$$\left| \delta T_B^k(\mathbf{X}_B^k, t)^m \right| \leq 10^{-p}. \quad (4.47)$$

It is worth to mention here, the CC is a case dependent term, which allows flexibility to the user in selection of ‘ p ’ values. With available computational resources and required accuracy of the final results, ‘ p ’ value can be suitably chosen.

We have tried to reduce the number of sub-iterations in the proposed flexible forcing scheme by introducing a successive relaxation parameter (SRP), ‘ ε ’ as shown in Eqs.(4.48) – (4.49). ε is set in the range of 0 – 1. The effects of SRP and CC selection will be discussed in the subsequent sections.

$$\delta \mathbf{U}_B^k(\mathbf{X}_B^k, t) \Big| \Big|^m = (1 - \varepsilon) \delta \mathbf{U}_B^k(\mathbf{X}_B^k, t) \Big| \Big|^{m-1} + \varepsilon \delta \mathbf{U}_B^k(\mathbf{X}_B^k, t) \Big| \Big|^m. \quad (4.48)$$

$$\delta T_B^k(\mathbf{X}_B^k, t) \Big| \Big|^m = (1 - \varepsilon) \delta T_B^k(\mathbf{X}_B^k, t) \Big| \Big|^{m-1} + \varepsilon \delta T_B^k(\mathbf{X}_B^k, t) \Big| \Big|^m. \quad (4.49)$$

After calculating the velocity and temperature corrections, the force/heat source density at the Lagrangian and Eulerian grid points are derived using Eqs.(4.50) – (4.51).

$$\mathbf{F}_B^k(\mathbf{X}_B^k, t) = \sum_m 2\rho \delta \mathbf{U}_B^k(\mathbf{X}_B^k, t) \Big| \Big|^m / \delta t,$$

$$\mathbf{f}(\mathbf{x}, t) = \sum_m 2\rho \delta \mathbf{u}(\mathbf{x}, t) \Big| \Big|^m / \delta t. \quad (4.50)$$

$$Q_B^k(\mathbf{X}_B^k, t) = \sum_m 2\rho c_s^2 \delta T_B^k(\mathbf{X}_B^k, t) \Big| \Big|^m / \delta t T_{mean},$$

$$q(\mathbf{x}, t) = \sum_m 2\rho c_s^2 \delta T(\mathbf{x}, t) \Big| \Big|^m / \delta t T_{mean}. \quad (4.51)$$

Other microscopic variables: density, pressure and kinematic viscosity and thermal diffusivity are calculated using the following formula.

$$\rho = \sum_{i=0}^8 f_i, \quad p = \rho c_s^2, \quad \nu = \left(\tau_v - \frac{1}{2} \right) c_s^2 \delta t, \quad \psi = 2 \left(\tau_c - \frac{1}{2} \right) c_s^2 \delta t. \quad (4.52)$$

In summary, the solution procedure for the proposed algorithm is outlined below:

1. Set the initial flow field and calculate f_i, g_i, f_i^{eq} and g_i^{eq} .
2. Perform streaming using Eqs.(4.24) – (4.25) with initial setting $F_i, F_i^T, Q_i = 0$ and calculate the intermediate velocity and temperature
$$\mathbf{u}^* = \sum_{i=0}^8 \mathbf{e}_i f_i / \rho, T^* = \sum_{i=0}^8 g_i / R\rho.$$
3. From the desired boundary velocity/temperature, calculate the velocity/temperature correction $\delta \mathbf{U}_B^k(\mathbf{X}_B^k, t) \Big|^{m=0}, \delta T_B^k(\mathbf{X}_B^k, t) \Big|^{m=0}$ using Eqs.(4.44) – (4.45).
4. Update the Eulerian velocity and temperature, with the updated $\delta \mathbf{u}$ and δT . Calculate new $\delta \mathbf{U}_B^k(\mathbf{X}_B^k, t) \Big|^m, \delta T_B^k(\mathbf{X}_B^k, t) \Big|^m$ using Eqs.(4.44) – (4.45). Repeat this step with sub-iteration loops until the CC in Eqs.(4.46) – (4.47) are satisfied.
5. Calculate \mathbf{f}, q, f_i^{eq} and g_i^{eq} using Eqs.(4.50), (4.51), (4.11) – (4.14) respectively.
6. Repeat the steps (2) – (5) above until the converged solution has reached.

4.2 Accuracy test and Validations

The numerical accuracy of the proposed flexible forcing IB – TLBM scheme was evaluated by performing benchmark test case simulations: natural

convection in a square enclosure with a circular heat source at different Ra (10^3 - 10^6). To further validate the proposed scheme, we have simulated the forced convection flow over a square heat source (cylinder).

4.2.1 Natural convection in a square enclosure with a circular heat source

At first to check the accuracy of the proposed algorithm we have simulated the natural convection process. A schematic diagram of the computational domain in 2D plane is shown in Fig.4.2(a). The system consists of a square enclosure with side of length L and a stationary circular cylinder of diameter $D = 0.4L$, which is located at the centre of the enclosure ($x = 0, y = 0$). The walls of the enclosure were kept at a constant lower temperature $T_C = 0.0$, whereas the cylinder surface is maintained at a constant higher temperature $T_H = 1.0$. All the fluid properties are assumed to be constant, except for the density in the buoyancy term, which follows the Boussinesq approximation (ref. Eqs.(4.28) – (4.29)). The gravitational force acts along the negative Y direction. The grid independence test is performed as shown in Table 4.1. A uniform grid of size 201×201 is found sufficient to determine the accurate solution where the circumference of the cylinder is discretised with 240 Lagrangian marker points.

Ra and Pr are two significant parameters that describe the mode and heat transfer rate. From theory (Kang and Hassan (2011)) Ra and Pr can be defined as,

$$Ra = \frac{g\beta\Delta TL^3}{\nu\alpha}, \quad Pr = \frac{\nu}{\alpha}. \quad (4.53)$$

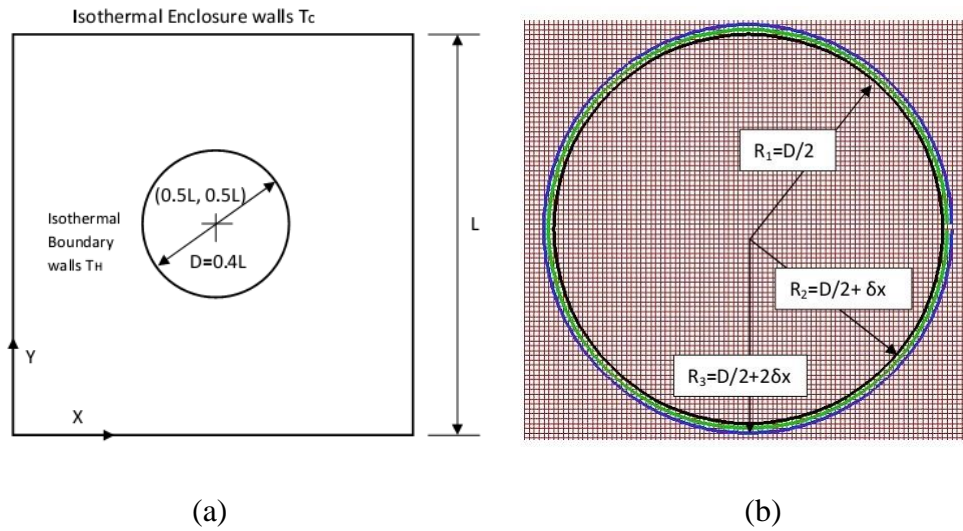


Fig.4.2 Computational domain for Natural convection process from a hot circular cylinder; (b) additional circles at one and two mesh distance for calculation of normal direction gradient.

Table 4.1 Grid independence test by computing Nu_A on the hot circular cylinder at $Ra = 10^5$.

Mesh size	Nu_A	% Error = $\left \frac{Nu_A^{Newmesh} - Nu_A^{Oldmesh}}{Nu_A^{Oldmesh}} \right \times 100$
101×101	7.81	--
151×151	7.78	0.38
201×201	7.77	0.12
251×251	7.76	0.12

Using the relation of Ra and Pr, the relaxation coefficients (τ_v, τ_c), non-dimensional viscosity (ν) and thermal diffusivity (α) are expressed as,

$$\nu = \sqrt{\frac{\text{Pr}}{\text{Ra}}} U_c, \quad \alpha = U_c L / \sqrt{\text{RaPr}}, \quad \tau_v = 3\sqrt{\frac{\text{Pr}}{\text{Ra}}} U_c L + \frac{1}{2},$$

$$\tau_c = \frac{3}{2} \frac{U_c L}{\sqrt{\text{RaPr}}} + \frac{1}{2}, \quad (4.54)$$

where U_c is the characteristics velocity and defined as, $U_c = \sqrt{g\beta\Delta TL}$. The value U_c should be chosen to ensure the incompressible limit of the flow. Here, U_c is specified as 0.1.

The temperature and velocity boundary condition on the immersed cylinder is satisfied using proposed flexible forcing IB – TLBM scheme. Non-equilibrium density distribution function bounce back scheme (Peng et al. (2003)) is used on the enclosure walls for no-slip velocity/no-jump temperature boundary condition, as shown in Eq.(4.55).

$$f_\alpha^{neq} = f_\beta^{neq}, \quad g_\alpha^{neq} = -g_\beta^{neq}, \quad (4.55)$$

where f_α^{neq} and g_α^{neq} are the non-equilibrium parts of density distribution functions f_α and g_α respectively. α and β are the lattice directions opposite to each other. Pr is set as 0.71. The simulations are performed till the steady state is achieved where the convergence criteria are followed from the previous works (Peng et al. (2003); Kang and Hassan (2011)),

$$\max \left(\left| \sqrt{(u^{n+1})^2 + (v^{n+1})^2} - \sqrt{(u^n)^2 + (v^n)^2} \right| \right) \leq 10^{-6}, \quad (4.56)$$

$$\max \left(|T^{n+1} - T^n| \right) \leq 10^{-7}. \quad (4.57)$$

Here, $n+1$ and n represents the current and previous time step values respectively.

To perform quantitative comparisons we have calculated local (Nu_L) and average Nusselt number (Nu_A), which are defined in the following,

$$Nu_L = \left(\frac{\partial T'}{\partial n'} \right)_{wall}, \quad Nu_A = \frac{1}{W} \int_0^W Nu_L ds, \quad (4.58)$$

where n' is the normal direction with respect to the wall and W is the average surface area of the wall where the temperature is non-dimensionalised as, $T' = (T - T_C) / (T_H - T_C)$. For calculation of Nu_L on the hot cylinder surface special treatment is done. Additional two circular cylinders with respective diameters ' $0.4L + 2\delta x$ ' and ' $0.4L + 4\delta x$ ' are considered, as shown in Fig.4.2(b). The Lagrangian nodes on these two cylinders are kept same to ensure the normal direction. The temperature gradient is then calculated using the second order forward difference scheme, as shown in Eq.(4.59).

$$\left. \frac{\partial T}{\partial n} \right|_{i,1} = \frac{-4T_{i,2} + T_{i,3} + T_{i,1}}{2\delta x}, \quad (4.59)$$

where 1, 2 and 3 are the circles' in order, and i , is Lagrangian node point. As mentioned before, in our proposed scheme number of sub-iteration is variable

and depends on the CC. In Table 4.2, a comparison is made to check this dependency. We have simulated the natural convection flow for $Ra = 10^5$. It is found that the number of sub-iteration required, is strongly dependent on the CC. This means the overall computational time dependence on the CC and by removing the unnecessary sub-iteration loops the computational cost can be significantly saved.

Table 4.2 Variation of number of forcing (NF) and CC while calculating Nu_A on the hot cylinder at $Ra = 10^5$.

CC	NF	Nu_A
10^{-4}	11	7.771
10^{-5}	20	7.770
10^{-6}	31	7.769

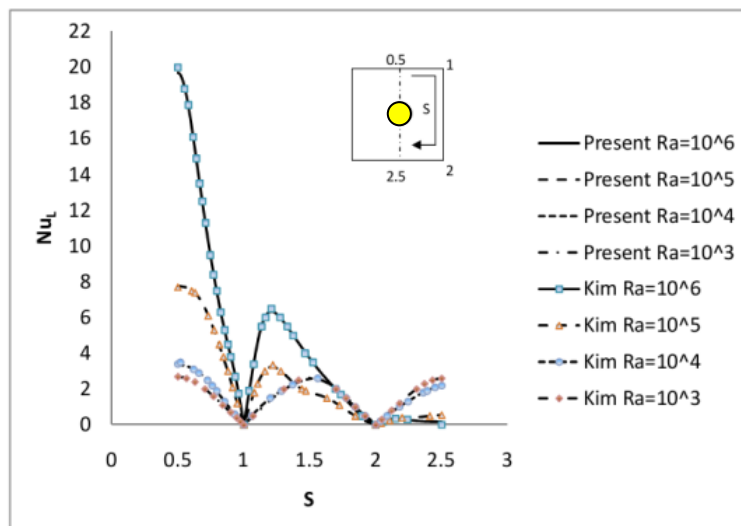


Fig.4.3. Nu_L distribution along the enclosure walls at different Ra compared and with Kim et al. (2008).

Table 4.3 Comparisons of Nu_A on the hot circular cylinder at different Ra.

Case	Reference	Nu_A
Ra= 10^3	Lee et al. (2010)	5.107
	Kim et al. (2008)	5.093
	Present	5.065
Ra= 10^4	Lee et al. (2010)	5.109
	Kim et al. (2008)	5.108
	Present	5.112
Ra= 10^5	Lee et al. (2010)	7.761
	Kim et al. (2008)	7.767
	Present	7.771
Ra= 10^6	Lee et al. (2010)	14.064
	Kim et al. (2008)	14.11
	Present	14.086

The distribution of Nu_L on the enclosure boundary wall as a function of Ra, are compared with the results obtained by Kim et al. (2008) and plotted in Fig.4.3. Further Nu_A on the hot cylinder surface is compared in Table 4.3. The observed results from the proposed numerical scheme are found in excellent agreement with the literature.

The streamline and isotherm contours are plotted for various Ra in Fig.4.4. At low Ra = $10^3 - 10^4$, isotherms are symmetrical and regularly distributed. Streamlines at this Ra contains two primary and secondary vortices in the annulus of the enclosure. With increase in Ra to $10^5 - 10^6$ merging of vortices are noticed and flow regime changes from bi-cellular mode to single cellular

mode. Thermal plumes are also visible at these Ra. The observed streamlines and isotherms are in well match with literature.

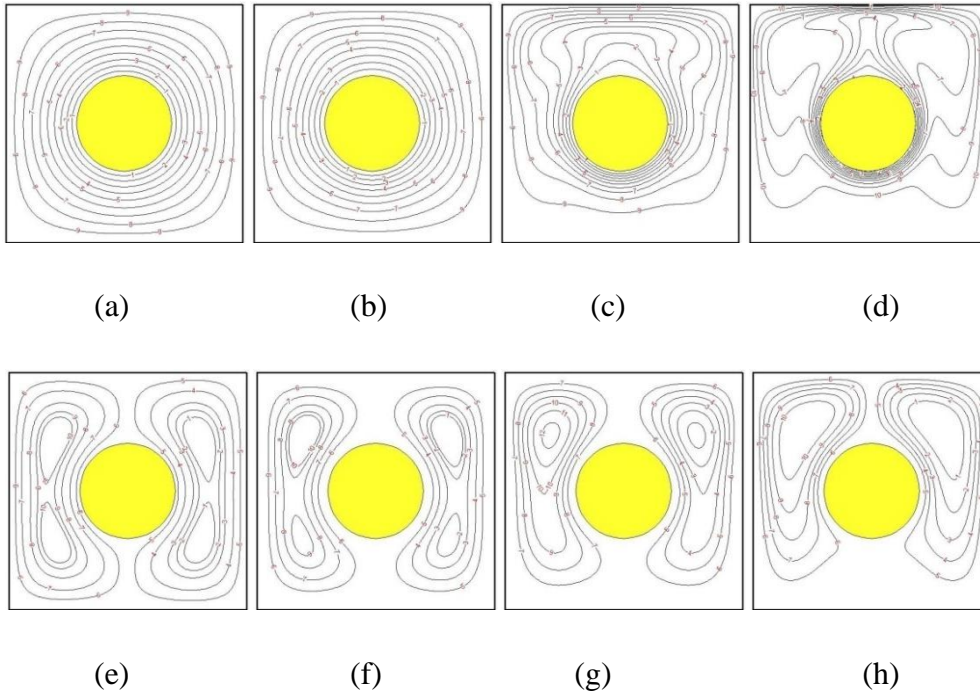


Fig.4.4. Isotherms (a-d) and Streamlines (e-h) for circular cylinder with increase in Ra 10^3 , 10^4 , 10^5 and 10^6 (from left to right) (Contour of levels 1-10 is shown for Isotherm and Streamline respectively).

4.2.2 Forced convection from a square heat source

The coupled fluid flow and heat transfer over bluff cylinder have been studied over last few decades and are considered to be benchmark test problem for the numerical schemes. To further validate our proposed IB – TLBM algorithm, we have simulated forced convection from a hot square cylinder subjected to an external flow of Re varying in the range 10 – 40. For this Re, flow and thermal fields are found to be steady and separated without the superimposed thermal buoyancy (i.e. for pure forced convection). It is worth to mention here

that the flow patterns and wake structures for the case of flow over square cylinder are considerably different than a circular cylinder, because unlike the circular cylinder the square counterpart tends to fix the separation point, causing differences in the critical flow regimes. Also, the separation mechanisms and the aerodynamic forces differ significantly for these two geometries.

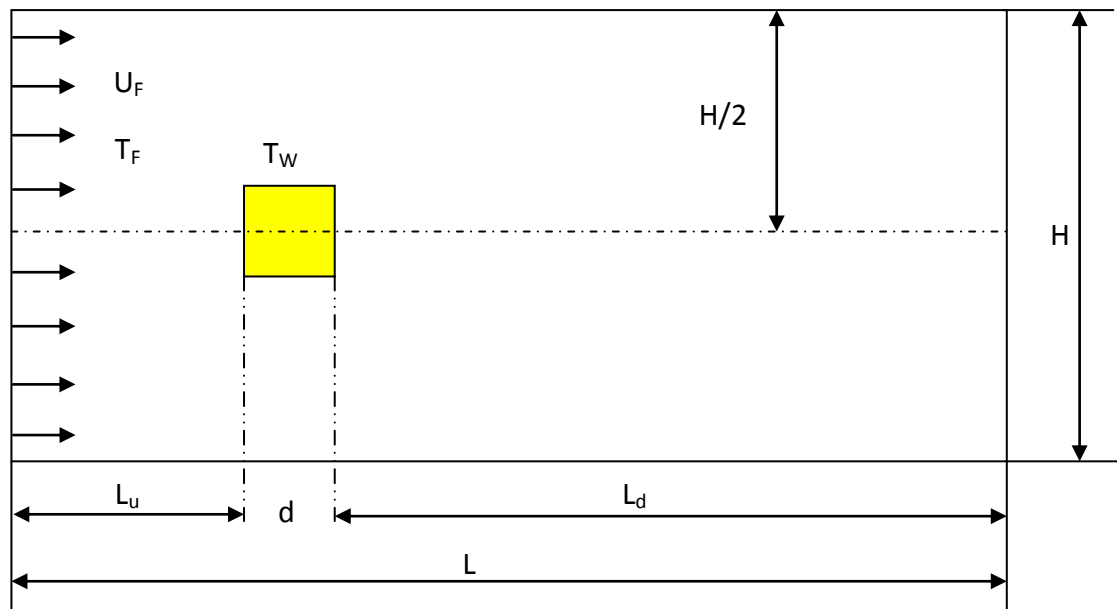


Fig.4.5. Schematic diagram of computational domain for flow over the heated square cylinder.

The selected flow configuration is shown in Fig.4.5. A stationary 2D square cylinder with sides d , heated to a temperature T_w is exposed to a free stream velocity U_F and temperature $T_F (< T_w)$. The computational domain is selected in such a way that the blockage effects are minimal (Sohankar, Norberg et al. (1998)). Here, the upstream and downstream of the computational domain is fixed at $L_u = 15d$ and $L_d = 30d$ respectively. Similarly, the far field boundary

are selected as $H/2 = 15d$. Re of the flow is defined using side length of the square. Pr is set as 0.71. Using the definition in Eq.(4.54), the flow governing equations (Eq.(4.17),(4.18a) and (4.19)) are solved with proposed IB – TLBM scheme. The uniform flow condition is specified at the inlet and far field boundaries and outflow boundary condition is specified at the exit of the domain.

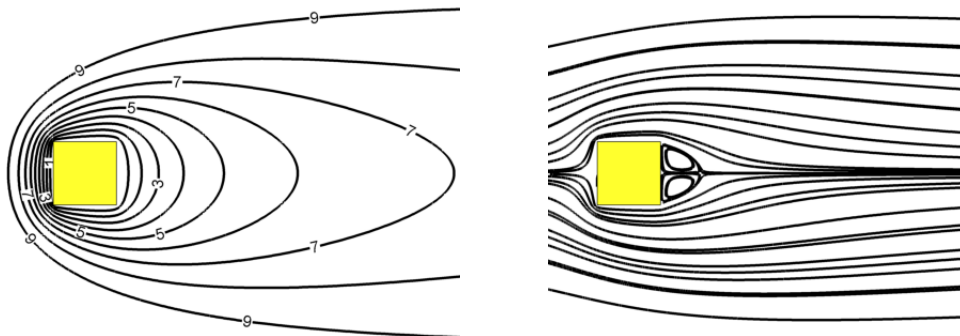
A non-uniform mesh system is followed where finer mesh is specified near the square cylinder and coarser mesh otherwise in the domain. A Lagrangian interpolation based LBM (Wu and Shu (2009)) is utilised to solve the flow field evolution in the non-uniform mesh.

We have also performed grid independence study as shown in Table 4.4. From the observations in the Table 4.4, a total mesh size of 820×560 with fine mesh 200×200 near the square cylinder is followed for the present simulation study. Here, the square cylinder surface is discretised with 128 Lagrangian points.

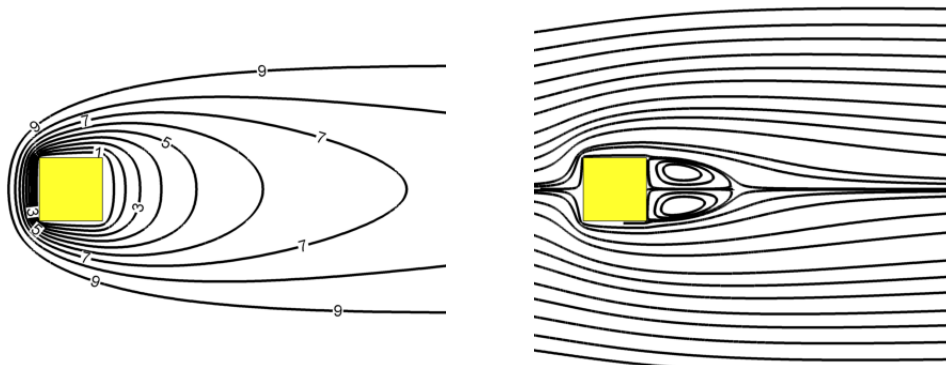
Table 4.4 Grid independence test of flow past a square cylinder at $Re = 20$.

Mesh size	C_d	% Error = $\left \frac{C_d^{\text{Newgrid}} - C_d^{\text{Oldgrid}}}{C_d^{\text{Oldgrid}}} \right \times 100$
574×392	2.395	--
697×476	2.391	0.16
820×560	2.388	0.12
1025×700	2.386	0.10

The streamline and isotherm contours are plotted in Fig.4.6. At low Re , the flow separates from the upstream corners of the square cylinder and forms a steady recirculation zone behind the trailing edge. The length of the recirculation zone found increasing with the increase in Re . The observed contours from our proposed scheme are found to be in excellent agreement with previous published results by Chatterjee and Mondal (2011) and Sharma and Eswaran (2004). We have also compared the drag coefficients on the square cylinder using the C_d definition as in Eq.(2.44). The results are plotted in Fig.4.7 for different Re , which are in good match with Chatterjee and Mondal (2011).

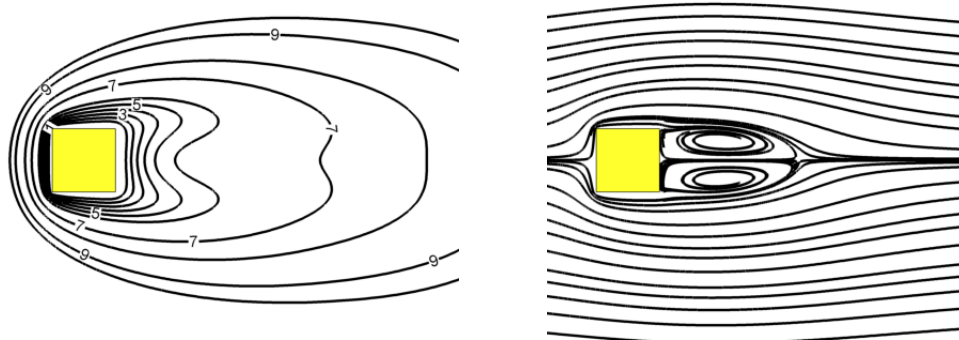


(a) $Re=10$



(b) $Re=20$

(Continued.....)



(c) $Re=40$

Fig.4.6. Isotherms (left) and Streamlines (right) around the square cylinder for different Re .

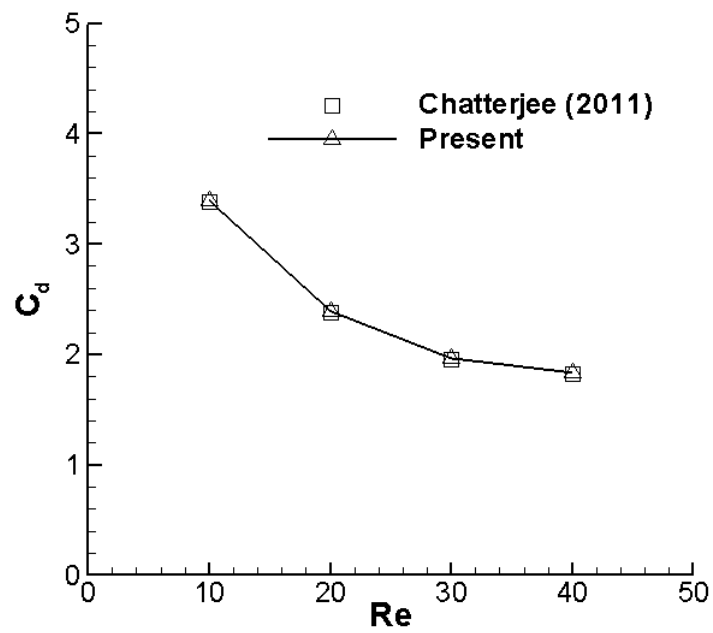


Fig.4.7. Variation of drag coefficients with Re .

4.3 Concluding remarks

In this chapter, we have discussed a novel flexible forcing hybrid IB – thermal LBM scheme to simulate 2D thermal fluid flow problems with an immersed solid boundary. Following the implicit type forcing term calculation, unknown single Lagrangian velocity/temperature corrections are introduced for suitable satisfaction of the no-slip velocity boundary condition and no-jump temperature boundary condition within a convergence limit. Use of flexible forcing principle not only avoids the complex mathematics involved in matrix inversion but also satisfy the boundary condition consistently at every time step with same order of accuracy. Also the algorithm suggested here is simple for new computational code development.

Validation of the developed solver is done by simulating a set of two dimensional flow problems: natural convection past circular cylinder and forced convection over a square cylinder. The results are found to be in excellent agreement with previous published articles.

Chapter 5

Application of 2D Flexible Forcing IB–TLBM for Natural Convection in Complex Cavities⁴

In this chapter, the developed 2D flexible forcing IB – TLBM scheme is applied for the natural convection process in complex cavity situations. Natural convection plays an important role in diverse engineering applications starting from, building insulation, electronic cooling, solar panel heating, furnace design to nuclear reactor where the convection process can be broadly categorised into three groups: the convection processes from (i) a heat source exposed to infinitely large cold surroundings, (ii) differentially heated walls of an enclosed cavity and (iii) a heat source in an enclosure. In the present study,

⁴ Part of this work has been published as:

Dash SM, Lee TS and Huang H. (2013). "Natural Convection from an Eccentric Square Cylinder Using a Novel Flexible Forcing IB-LBM Method." Numerical Heat Transfer, Part A: Applications **65**(6): 531-555

Dash SM and Lee TS (2014). "Natural Convection from Inclined Square Cylinder Using Novel Flexible Forcing IB-LBM Approach." Engineering Applications of Computational Fluid Mechanics **8**(1): 91-103

Dash SM, Lee TS and Huang H. (2013). "A Novel Flexible Forcing Hybrid Ib-Thermal Lb Model for Natural Convection from a Circular Cylinder." International Journal of Dynamics of Fluids **9**(1): 1-15

we have focused on the natural convection in the complex cavities that consists of an enclosure and an eccentric/inclined square heat source. This convective heat transfer process is analogous to many practical situations such as, electronic chips in CPU or TV cabinet, microelectronic fabrication. Existing literature suggests (ref. Chapter 1) that most of the previous studies on the natural convection in an enclosure are limited to circular or elliptical shaped inner heat source whereas the natural convection process from an eccentric/inclined square shaped heat source in an enclosure is not yet addressed. The objective of the present study is to determine the flow pattern and heat transfer rate in the annulus of the enclosure, as functions of Ra, eccentricity and inclination of the inner square cylinder (heat source). That may find useful in the industrial applications and future studies.

5.1 Problem definition

The schematic diagrams of the computational domain are shown in Fig.5.1. An outer square enclosure with side length L and an inner square cylinder with side length $0.4L$ together define the computational domain. Isothermal boundary conditions are adopted on the enclosure and inner cylinder walls where the maintained temperatures are, $T_C = 0$ (cold) and $T_H = 1$ (hot) respectively. We have considered two complex cavity scenarios with, 1) an inclined square heat source and 2) an eccentric square heat source as shown in Fig.5.1. In the first case the inclination of angle of the inner square is varied between $0 < \theta < 45$ deg. In the second case the inner square cylinder is displaced along the vertical centreline of the enclosure in a range, $0.25L \leq \chi$

$\leq -0.25L$ at a spatial interval of $0.05L$. All the fluid properties are assumed constant, except for the density associated with the buoyancy term that follows the Boussinesq approximation.

To make the numerical results independent of grid resolution, uniform Cartesian mesh of sizes 101×101 , 151×151 , 201×201 , and 251×251 were tested. It was found that the mesh size 201×201 is sufficient to produce the accurate result. This mesh size is followed for rest of the simulations in the present study. The definition of Ra and Pr are followed from Eq.(4.53). For both the cases simulations are performed for Ra in the range $10^3 - 10^6$, and $Pr = 0.71$. The no-slip velocity and no-jump temperature boundary conditions are satisfied on the enclosure walls and on the inner square cylinder surface by bounce back scheme (Peng et al. (2003)) and proposed flexible forcing IB-TLBM, respectively. The rate of heat transfer is calculated by measuring the local and average Nusselt number (Nu_L, Nu_A) where the definitions are given in Eq.(4.58). The simulations are performed till steady converged criteria (Eqs.(4.56) – (4.57)) are satisfied. Here, we have selected the steady state solver after noticing that the flow pattern and heat transfer eventually reaches to a time independent solution irrespective selected Ra ($10^3 - 10^6$). Sample transient studies of Nu_A variations for different Ra are shown in Fig.5.2 that further supports the steady state condition.

The followed IB-Thermal LBM numerical scheme is well validated in the previous chapter; hence in the following section only the results will be discussed for the considered natural convection problem and some

comparisons are highlighted wherever similar observations are made in the literature.

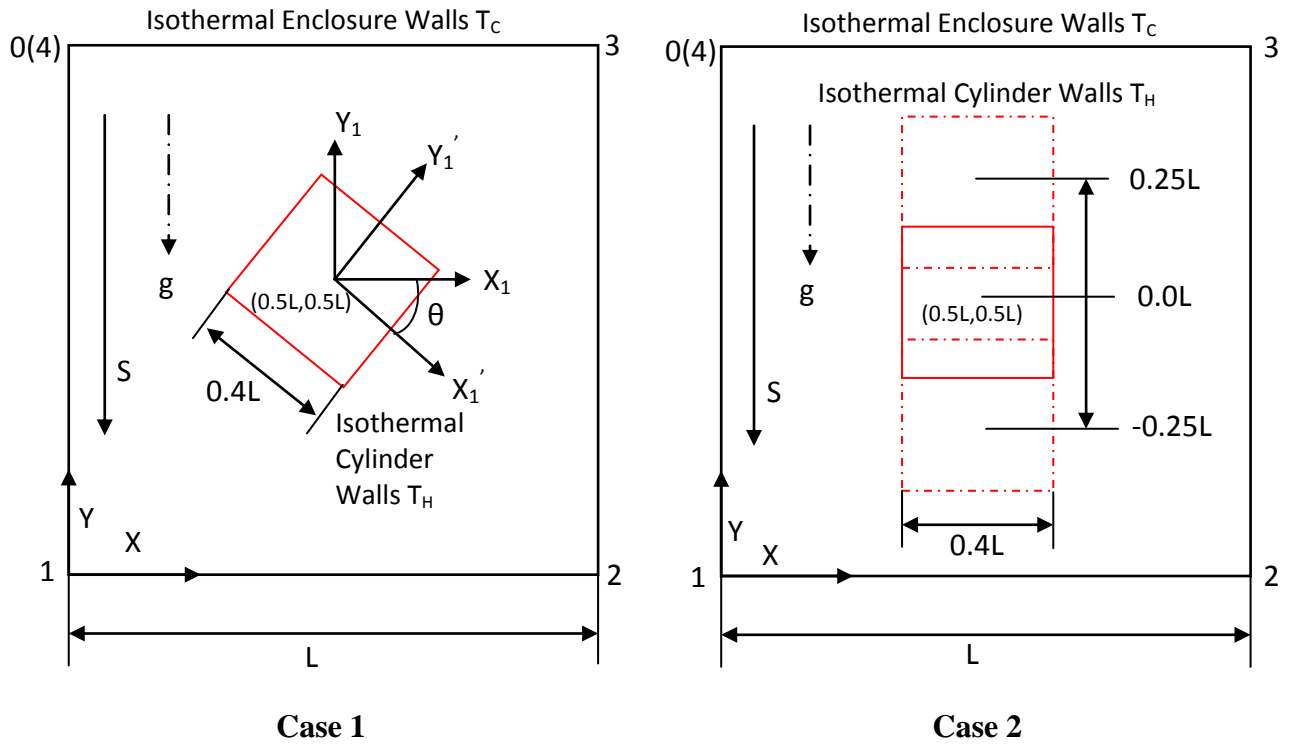


Fig.5.1. Schematic of the computational domain for the proposed natural convection studies. ‘S’ is the direction used while calculating Nusselt number.

5.2 Results and Discussions

The results presented in this section correspond to the observed flow regime and heat transfer as functions of inclination angle, eccentricity, Ra. Two cases as shown in Fig.5.1 are separately discussed in the followings.

5.2.1 Case-1 Natural convection from an inclined square cylinder

In this section, a complex cavity thermal flow problem is addressed, in which the orientation (inclination angle) of the hot square cylinder has significant effects. Alteration of the inclination angle (θ) not only changes the annular space, but also affects the flow and heat transfer rate in the enclosure. For better interpretation of the observed results, the inclination of the hot cylinder is studied at three different angle ranges: *small* ($0 < \theta < 20$ deg), *intermediate* ($20 < \theta < 30$ deg) and *high* ($30 < \theta < 45$ deg).

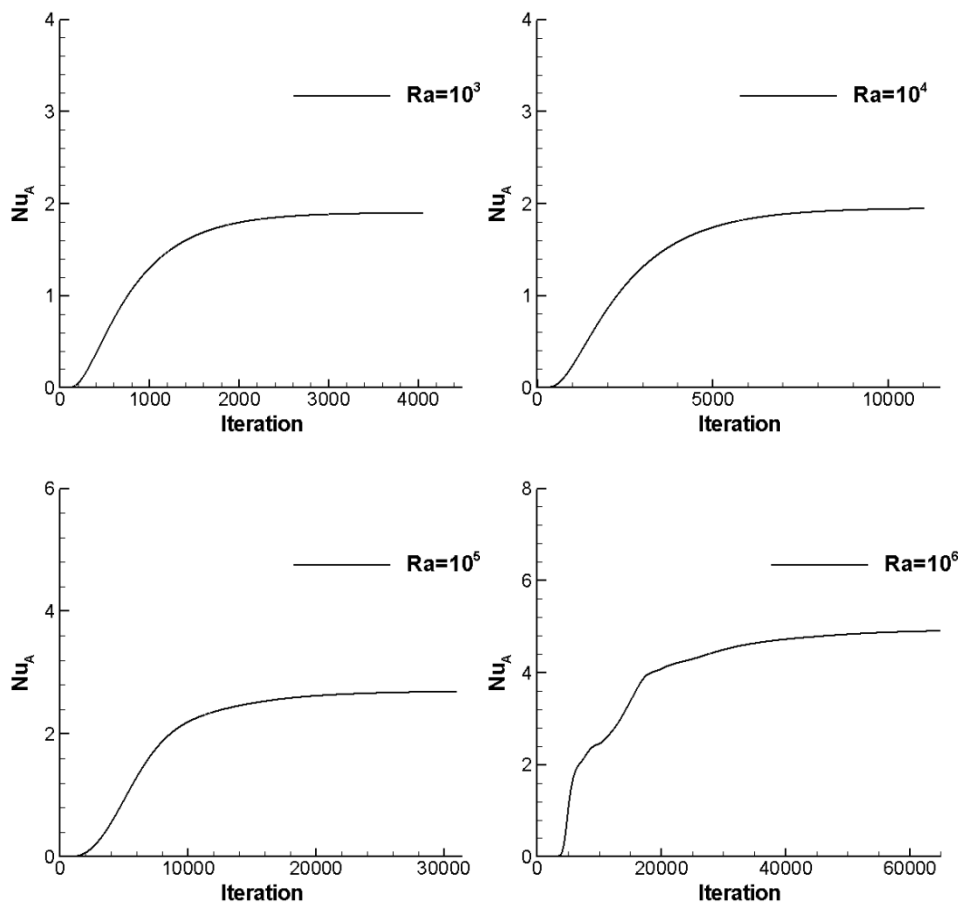


Fig.5.2. Temporal evolution of Nu_A on the enclosure for different Ra , when the inclined square cylinder is at $\theta=30$ deg.

The natural convection process in the present problem involves the uplift of the lighter fluid along the hot surface of the inner square cylinder. The hot

fluid continues to move upward until it encounters the cold enclosure walls. In contact with the cold walls, the fluid gets cooler and denser and starts to descend. The denser fluid when reaches the bottom of the enclosure, it may have lost all its kinetic energy, and forms a stagnant stratified zone. This cycle of natural convection is influenced by the square cylinder inclination angle and Ra.

5.2.1.1 Streamlines and Isotherms

$$\underline{Ra = 10^3}$$

At $Ra = 10^3$, the conductive mode of heat transfer is pronounced in the annulus, with smooth and regular isotherm distributions. The isotherm pattern is found to be similar for all the inclination angles, as shown in Fig.5.3(a) – 5.7(a), while changes in the fluid flow pattern is observed (Fig.5.3(e) – 5.7(e)). At small inclination angles, when $\theta = 0$ deg, two counter rotating primary vortices are noticed, with their vortex eyes at the mid-plane of the enclosure, as shown in Fig.5.3(e). When θ is increased further, asymmetry in the orientation of the cylinder initiates the formation of secondary vortices and modifies the circulation pattern from single vortex to double vortex mode (Fig.5.4(e)). For intermediate and high inclination angles, the double vortex mode prevails and the size of the secondary vortex increases. This growth of the secondary vortex is because of spatial alterations of the annular space in the enclosure. At $\theta = 45$ deg, the square cylinder attains another symmetric orientation, and therefore both the primary and secondary vortex are of equal strength and size (Fig.5.7(e)).

$Ra = 10^4$

As Ra increases to 10^4 , the convective heat transfer mode appears. The isotherms and streamlines at small inclination angles are similar to $Ra = 10^3$, but with careful observation it can be noticed that, as shown in (Fig.5.3(f)), the primary vortex eyes have moved above the mid-plane of the enclosure. The convective flow at the upper region produces this shift. Distorted isotherms are also visible at intermediate and high inclination angles.

$Ra = 10^5$

A further increase in Ra to 10^5 augments the convective heat transfer. At $Ra = 10^5$, isotherms are closer near the inner cylinder walls and thermal plumes are developed. The closer isotherms indicate the presence of a thermal boundary layer that gets separated from the upper corners of the inner square cylinder. This boundary layer separation forms a thermal plume. At small inclinations, three distinct plumes are noticed. When $\theta = 0$ deg, two symmetrical upwelling plumes rise from the upper corners of the inner cylinder. A third downwelling plume appears with thermal inversion. These multiple thermal plumes change the flow field by forming additional tertiary vortices on the upper surface of the inner cylinder, as shown in Fig.5.3(g). A similar phenomenon was also noticed by Asan (2000). With the increase in inclination angle and change in the annular space, the shapes and sizes of the two tertiary vortices differs from each other (Fig.5.4(g)). When θ is further increased to the intermediate range, geometrical asymmetry shifts the thermal boundary layer separation points. The shift of the separation points can be qualitatively seen, and compared, in

Fig.5.4(c) – 5.5(c). Thus the combined effects of the shift of the separation points and the change in annular space may lead to different isotherm distribution, which further avoids the formation of the multiple plumes and tertiary vortices. When θ is changed to a high inclination range, only one thermal plume is formed (Fig.5.6(g) – 5.7(g)) without any tertiary vortices. Also we have observed distant isotherm contours near the bottom of the enclosure for all θ , which implies presence of a colder fluid regime.

$$\underline{Ra = 10^6}$$

The heat transfer is primarily governed by the convective mode at $Ra = 10^6$. The thermal boundary layer separates from the upper corners of the inner cylinder, which results in strong thermal plumes. For θ in the range of small and intermediate angles, upwelling thermal plumes strongly impinge on the cold top wall of the enclosure, forming a thinner thermal boundary layer near the impinged region. The subsequent thermal inversion forms a downwelling plume, which leads to formation of the tertiary vortices as shown in Fig.(5.3(h) – 5.4(h)). The strength of these tertiary vortices is comparatively (compared with circulation contour levels) higher than $Ra = 10^5$. At the intermediate inclination angle apart from the tertiary vortices, tiny secondary vortices are formed. A further increase in θ to high inclination range shifts the thermal boundary layer separation point, and single upwelling thermal plume is observed. Because of higher convection current at the upper portion of the enclosure, the isotherms are highly distorted, while a stagnant stratified fluid zone is noticed at the bottom portion of the enclosure for all inclination angles.

5.2.1.2 Local Nusselt number (Nu_L)

Small Inclination Angle (0 – 20 deg)

Nu_L distributions along the enclosure walls are computed using Eq.(4.58). The plot of the Nu_L distribution as a function of Ra is shown in Fig.5.8(a) – (b), for $\theta = 0$ and 10 deg. At low Rayleigh numbers ($10^3 - 10^4$), the heat transfer is governed by conduction. Smooth and regular distributions of isotherms in the conduction mode produce systematic Nu_L distribution along the enclosure walls. With reference to Fig.5.8(a), when moved from corner point 0 in the direction of the arrow head (as in Fig.5.1), Nu_L increases to a local maximum near the midpoint of the wall 01, and then decreases to a local minimum at corner 1. Similar Nu_L distribution may be observed on the other walls of the enclosure. As asymmetry increases with θ , secondary vortices are initiated. This shifts the local maxima from the midpoints, as shown in Fig.5.8(b).

When Ra is increased to a higher range ($10^5 - 10^6$), enhanced convection rate and the presence of tertiary vortices alters the Nu_L distribution. Local maxima are moved nearer to corners 0 and 3 for the walls 01 and 23. Again, formation of upwelling and downwelling plumes leads to double peak Nu_L distribution on the wall 34. With an increase in θ , the shape and strength of the plumes are changed, which in turn changes the peak values, as shown in Fig.5.8(b). Due to presence of flow stratification and stagnation, Nu_L variation on the bottom edge 12 is negligible.

Intermediate Inclination Angle (20 – 30 deg)

The distribution of Nu_L is similar to the small inclination range, with the presence of local maxima and minima at low Ra ($10^3 - 10^4$). But the position of the local maxima is shifted from the mid-point of the wall with increased geometrical asymmetry, as shown in Fig.5.8(c). When $Ra = 10^5$, the local maxima of Nu_L is increased with a higher convection rate. At this Ra , Nu_L distribution on the wall 34 is different from the small angle case, where double peaks are absent. With further increase in Ra to 10^6 , distinct upwelling and downwelling plumes are formed, which reverts the double peak type Nu_L distribution on the top wall 34. On the side walls 01 and 23, Nu_L varies with formation of local maxima and minima. Again, flow stagnation at the lower portion of the enclosure brings the heat transfer rate close to zero.

High Inclination Angle (30 – 45 deg)

Nu_L distributions on the enclosure walls are plotted in Fig.5.8(d) – (e) for $\theta = 30$ and 45 deg. At lower Ra ($10^3 - 10^4$), Nu_L variation is very similar to the previous two ranges. With an increase in Ra to 10^5 or 10^6 , the local maxima value is increased and the highest peak is observed on the top wall 34. As shown in Fig.5.6(c) – (d) and Fig.5.7(c) – (d), isotherms contain only one upwelling plume, and therefore the Nu_L variation on the top wall contains a single peak. When the inclination angle is increased to 45 deg, the variation of Nu_L on the top wall 34 is symmetrical with the local maxima exactly at the midpoint of the wall. With the flow stratification, the Nu_L on the bottom wall is found close to zero.

5.2.1.3 Average Nusselt number (Nu_A)

In Fig.5.8.(f), the Nu_A on the enclosure walls is plotted as functions of Ra and θ . It is found that with an increase in Ra, the convective heat transfer rate increases, which in turn increases the Nu_A . As can be seen in Fig.5.8(a) – (e), the Nu_L distribution varies with different θ , but the overall variation of the Nu_A is negligible at any particular Ra. Again, from Table 5.1, it can be concluded that the inclination angle has the least effect on the Nu_A variation.

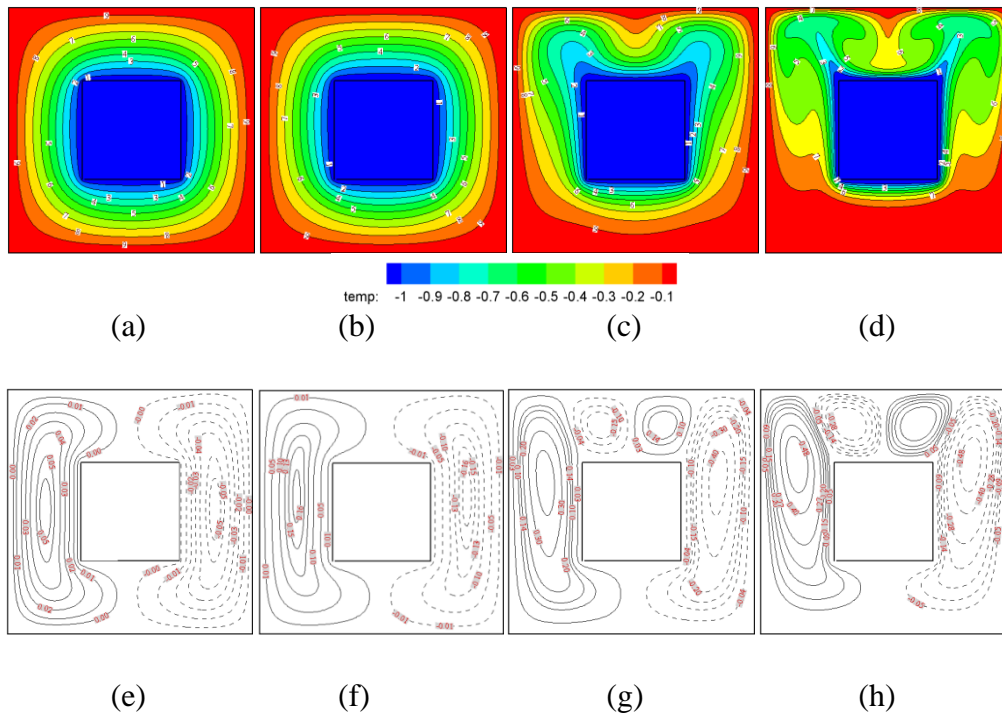


Fig.5.3. Isotherms (a-d) and Streamlines (e-h) for square cylinder at 0 deg inclination with increase in Ra value as 10^3 , 10^4 , 10^5 and 10^6 (from left to right). (Dashed line represents opposite direction of circulation).

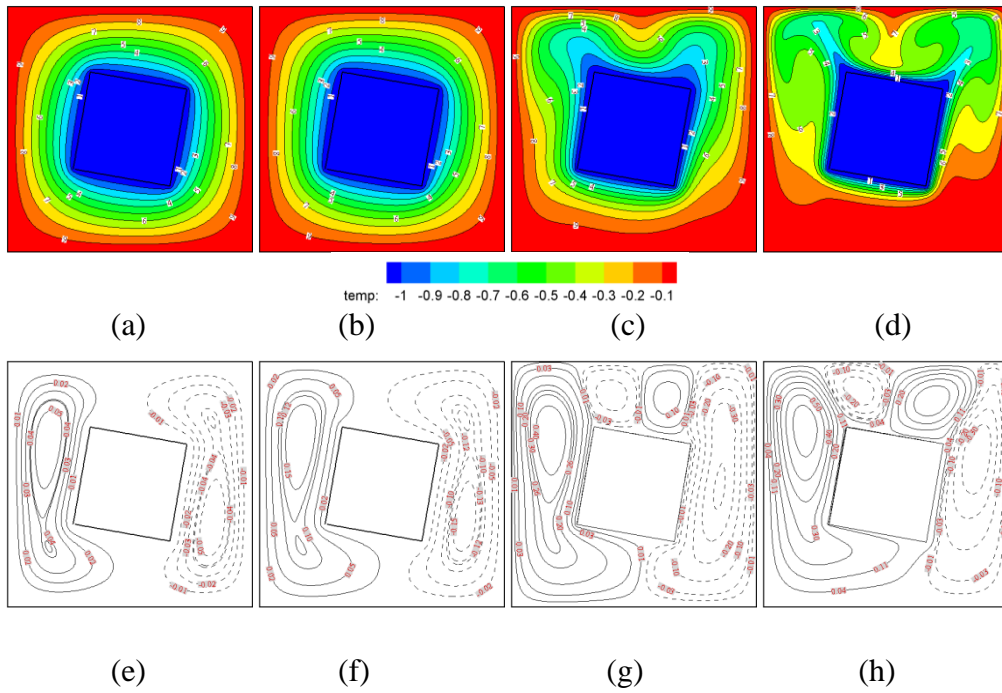
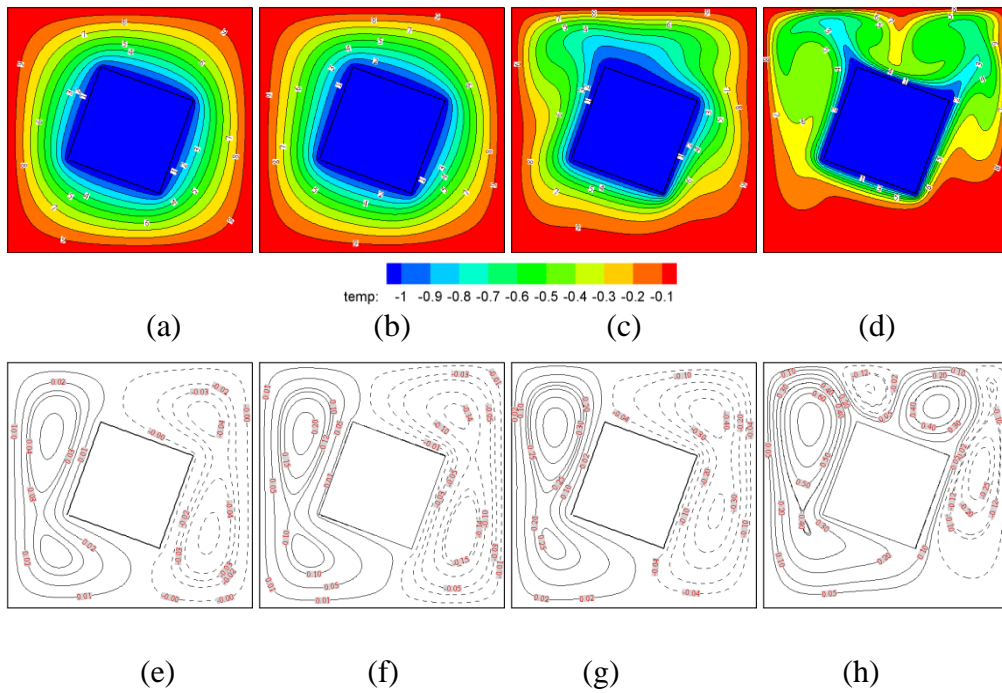


Fig.5.4. Isotherms (a-d) and Streamlines (e-h) for square cylinder at 10 deg inclination with increase in Ra value as 10^3 , 10^4 , 10^5 and 10^6 (from left to right). (Dashed line represents opposite direction of circulation).



(Continued...)

Fig.5.5. Isotherms (a-d) and Streamlines (e-h) for square cylinder at 20 deg inclination with increase in Ra value as 10^3 , 10^4 , 10^5 and 10^6 (from left to right). (Dashed line represents opposite direction of circulation).

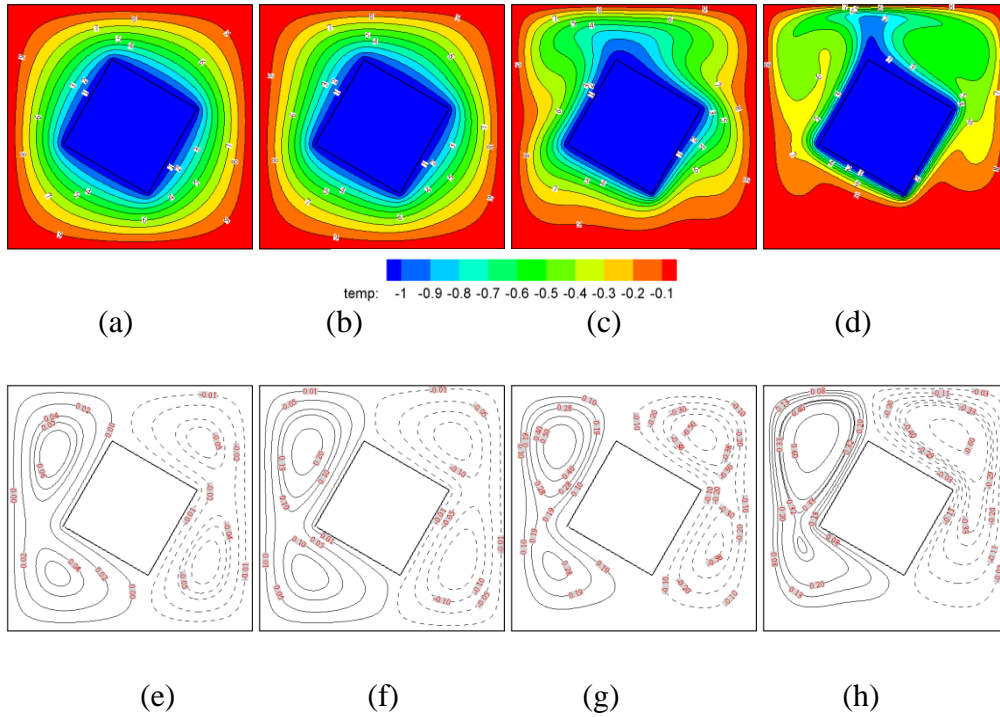
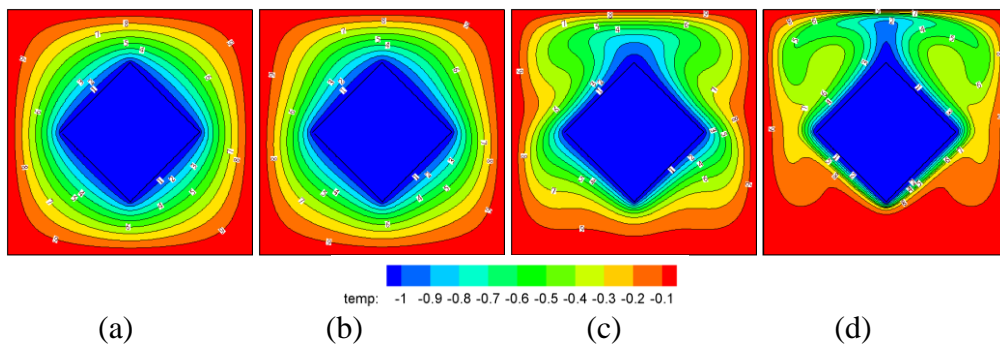


Fig.5.6. Isotherms (a-d) and Streamlines (e-h) for square cylinder at 30 deg inclination with increase in Ra value as 10^3 , 10^4 , 10^5 and 10^6 (from left to right). (Dashed line represents opposite direction of circulation).



(Continued....)

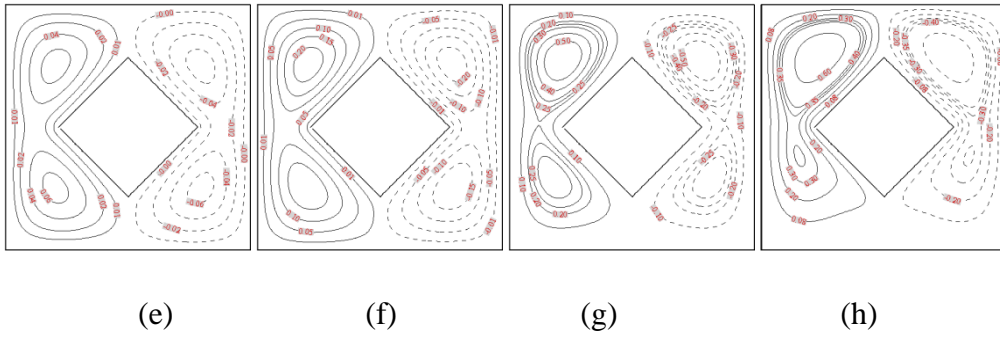
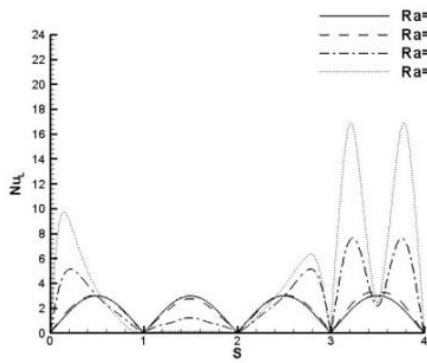
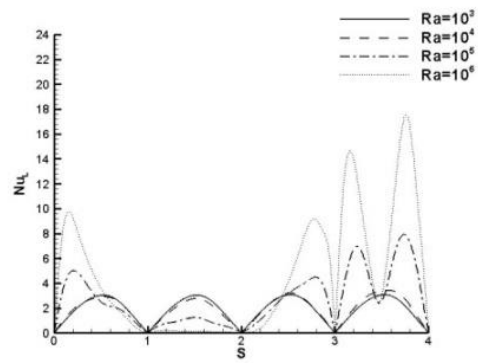


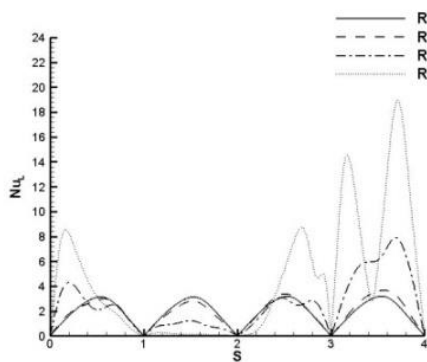
Fig.5.7. Isotherms (a-d) and Streamlines (e-h) for square cylinder at 45 deg inclination with increase in Ra value as 10^3 , 10^4 , 10^5 and 10^6 (from left to right). (Dashed line represents opposite direction of circulation).



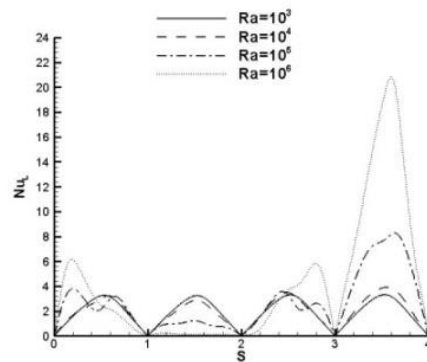
(a)



(b)



(c)



(d)

(Continued.....)

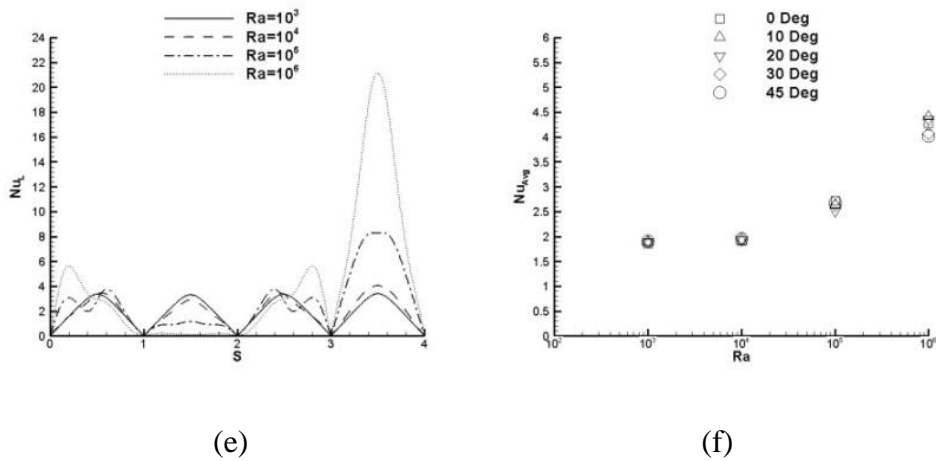


Fig.5.8. Nu_L and Nu_A distribution along the walls of the enclosure, at different Ra and inclination angles (a) $\theta = 0$ deg, (b) $\theta = 10$ deg, (c) $\theta = 20$ deg, (d) $\theta = 30$ deg, (e) $\theta = 45$ deg, (f) Nu_A vs Ra, where S is the direction used for calculation (ref. Fig.5.1).

Table 5.1 Nu_A on the enclosure surface as functions of Ra and θ .

$\theta \backslash Ra$	10^3	10^4	10^5	10^6
0 deg	1.860	1.910	2.715	4.281
10 deg	1.885	1.925	2.648	4.415
20 deg	1.891	1.935	2.515	4.352
30 deg	1.901	1.953	2.618	4.072
45 deg	1.903	1.959	2.679	4.027

5.2.2 Case-2 Natural convection from an eccentric square cylinder

In this section, a complex cavity thermal flow problem is addressed, in which the vertical eccentricity (χ) of the hot square cylinder has significant effects. Alteration of the eccentricity not only changes the annular space, but also affects the flow and heat transfer rate in the enclosure.

5.2.2.1 Streamlines and Isotherms when $\chi = 0$

In the following, the natural convection process is discussed when the inner cylinder is at centre of the enclosure ($\chi = 0$).

At $Ra = 10^3$, conduction is the dominant mode of heat transfer where isotherms and streamlines are symmetrically distributed as shown in Fig.5.9(a),(e). Two counter rotating primary vortices (or primary cells) are found in the flow field. Increase of Ra to 10^4 , the isotherms on the cylinder surface get closer with inception of the thermal boundary layer.

At $Ra = 10^5$, the convective heat transfer becomes significant, that forms distinct thermal plumes. The two upwelling plumes that are developed from the upper corners of the hot cylinder impinge on the enclosure top wall. Subsequently, thermal inversion forms a down welling plume as shown in Fig.5.9(c). These thermal plumes alter the flow pattern by forming the additional cells (tertiary cells) in the annulus (Here, it is advised to take a note on the nomenclature, that we have defined tertiary cells first instead of

secondary cells). Near the bottom of the enclosure isotherms are found distant which further suggests a stratified flow regime.

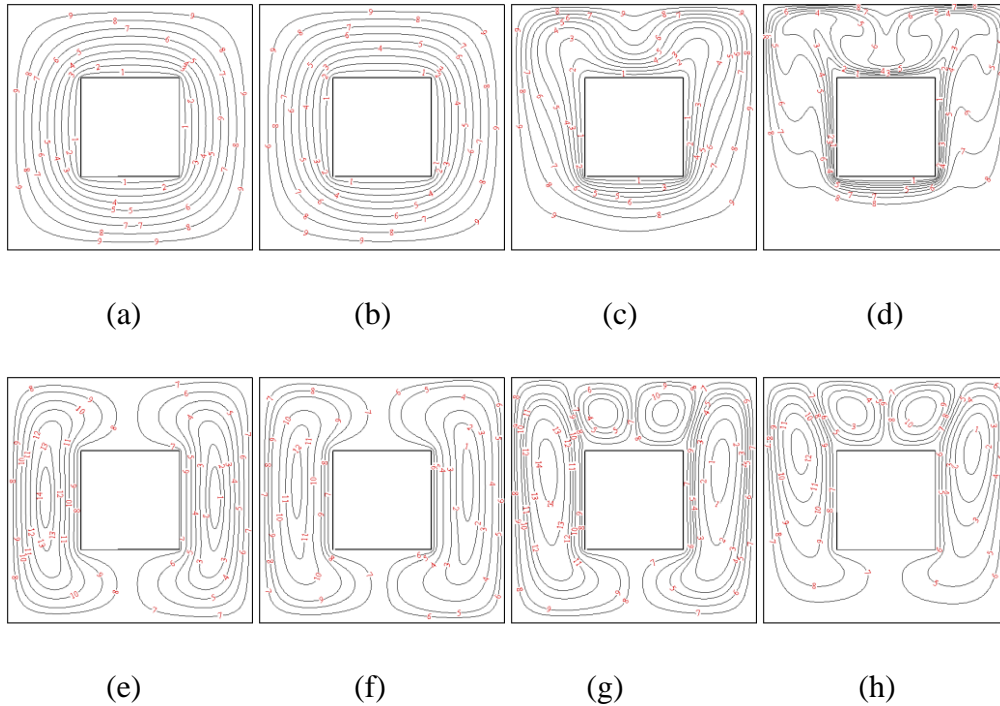


Fig.5.9. Isotherms (a-d) and streamlines (e-h) for square cylinder at $\chi=0$ with increasing Ra value as 10^3 , 10^4 , 10^5 and 10^6 (Contour levels of 1-9 and 1-14 are shown for isotherms and streamlines respectively).

At $Ra = 10^6$, the heat transfer is primarily governed by convection mode. Distorted mushroom shaped isotherms are observed in the annulus as shown in Fig.5.9(d). Similar to $Ra = 10^5$, two upwelling and one downwelling thermal plumes along with tertiary cells are formed in the flow field.

5.2.2.2 Streamlines and Isotherms when $\chi \neq 0$

In the following, the flow structure and heat transfer in the enclosure are discussed for the eccentric ($\chi \neq 0$) inner cylinder as a function of Ra.

$$\underline{Ra = 10^3}$$

In Fig.5.10(a) – (j), the distribution of streamlines and isotherms are showed at different χ s. When the inner cylinder is moved in downward direction at $\chi = -0.05$, the flow field is found uni-cellular in presence of the primary cells. Further increase of the eccentricity initiates the flow bifurcation, and the flow field changes to bi-cellular with formation of the secondary cells. When $\chi = -0.2$ or -0.25 , the flow field turns to uni-cellular, while the secondary cells merge with the primary ones.

When the inner cylinder is moved in upward direction at $\chi = 0.05$, the flow field is found uni-cellular type. The flow field is altered to bi-cellular at higher χ s. Increased gap between the inner cylinder and bottom wall of the enclosure allows merging of the primary and secondary cells, which reverts the flow field to unicellular type at $\chi = 0.25$.

As conduction is the dominant mode of heat transfer at this Ra, the isotherms are primarily regular shaped and symmetrically distributed about the vertical centreline of the enclosure. The isotherm distribution changes with the eccentricity. Denser isotherms are found in the region where the proximity between the inner cylinder and enclosure wall (either top or bottom wall) is small, while distant isotherms are observed on the opposite side of the inner cylinder.

$$\underline{Ra = 10^4}$$

In Fig.5.11(a) – (j), the distribution of streamlines and isotherms are showed at different χ s. With the increase in Ra to 10^4 , the convective mode of heat

transfer is initiated. When the inner cylinder is moved downward, the flow field remains unicellular at all χ s. When the inner cylinder is moved upward, the flow field is unicellular at $\chi = 0.05$. Further increase in the eccentricity alters the flow field to bi-cellular type with formation of the secondary cells.

The isotherms are found similar to that of $Ra = 10^3$, except for the case of $\chi = -0.20$ or -0.25 , where upwelling thermal plumes are observed.

$Ra = 10^5$

In Fig.5.12(a) – (j), the distribution of streamlines and isotherms are showed at different χ s. At this Ra , the convection heat transfer is augmented and multiple thermal plumes are developed in the annulus. For downward movement of the inner cylinder till $\chi = -0.15$, three distinct plumes (two upwelling and one down welling) are formed. The flow field also contains tertiary cells. When the inner cylinder is further displaced down, with the increased spatial gap and dominant convective flow in the upper region of the enclosure, the direction and the number of thermal plumes are altered. Instead of three plumes only a single upwelling plume is observed as shown in Fig.5.12(i) – (j), which also changed the flow field to uni-cellular type. When the inner cylinder is moved upward, tertiary cells are formed and the size of the cells are decreased till the $\chi = 0.15$. With further increase in the eccentricity, conduction becomes locally dominant, that makes isotherms regularized/straight and avoids tertiary cells formation in the annulus as shown in Fig.5.12(d) – (e).

$$\underline{Ra = 10^6}$$

In Fig.5.13(a) – (j), the distribution of streamlines and isotherms are showed at different χ s. As the convection is primary mode of heat transfer at this Ra, higher thermal gradient forms distorted mushroom shaped isotherms. The thermal boundary layer on the inner cylinder surface becomes thinner. When the inner cylinder is moved downward, two upwelling thermal plumes are raised from the upper corners of the cylinder, which forms a third downwelling plume with a subsequent thermal inversion. The isotherms are strongly distorted in presence of mushroom shaped contours. When the eccentricity is further increased, two small vortices are noticed near the upper corners of the enclosure. These vortices are formed because the thermal plumes impinge on the cold side walls, that subsequently leads to the boundary layer separation and give rises to the recirculation regime. Also the sizes of tertiary vortices grow with the increase in eccentricity.

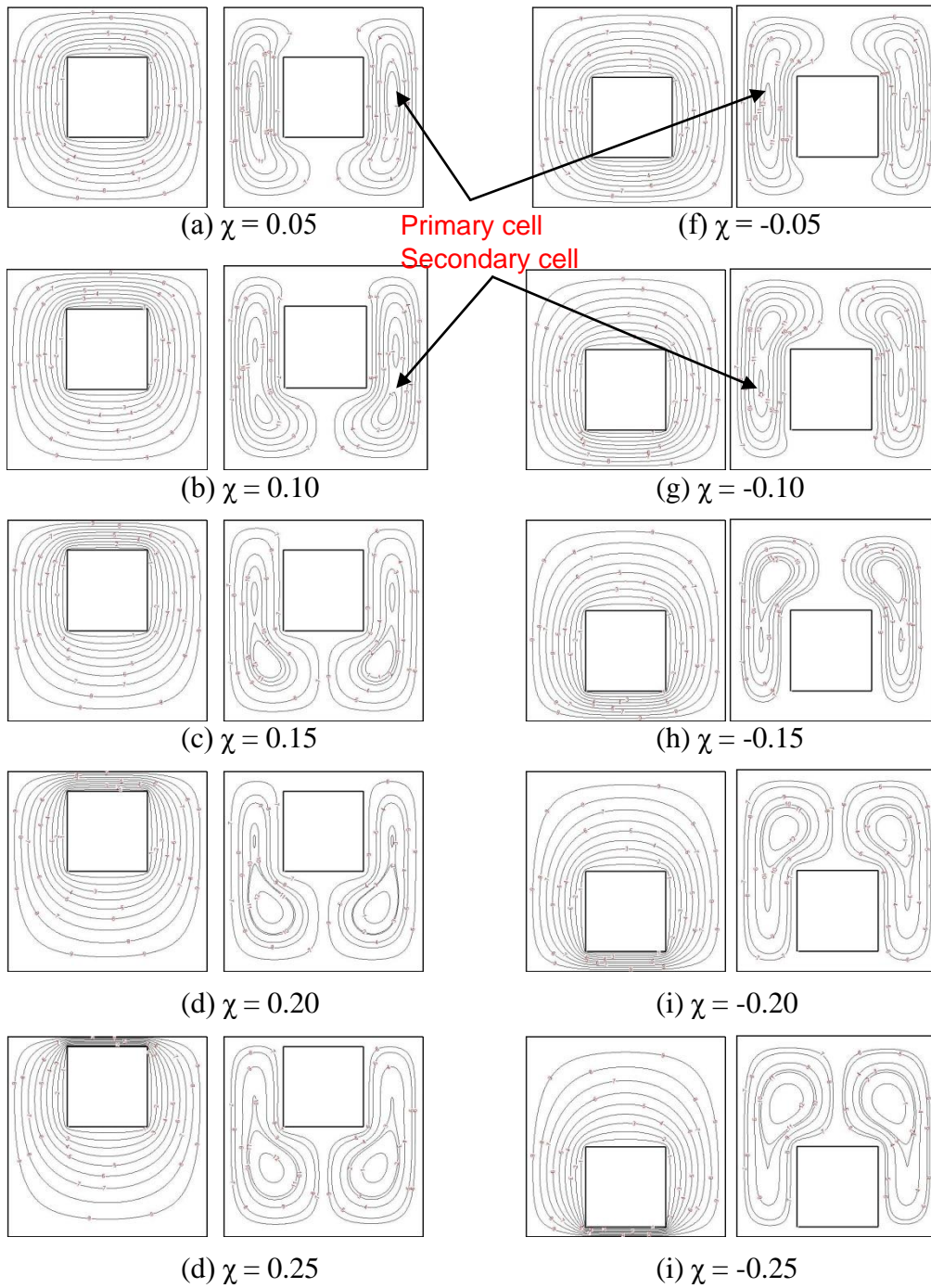


Fig.5.10. Isotherm and streamline plots at different displacement (χ) of inner cylinder for $Ra=10^3$ (Contour levels of 1-10 and 1-12 are shown for isotherms and streamlines respectively).

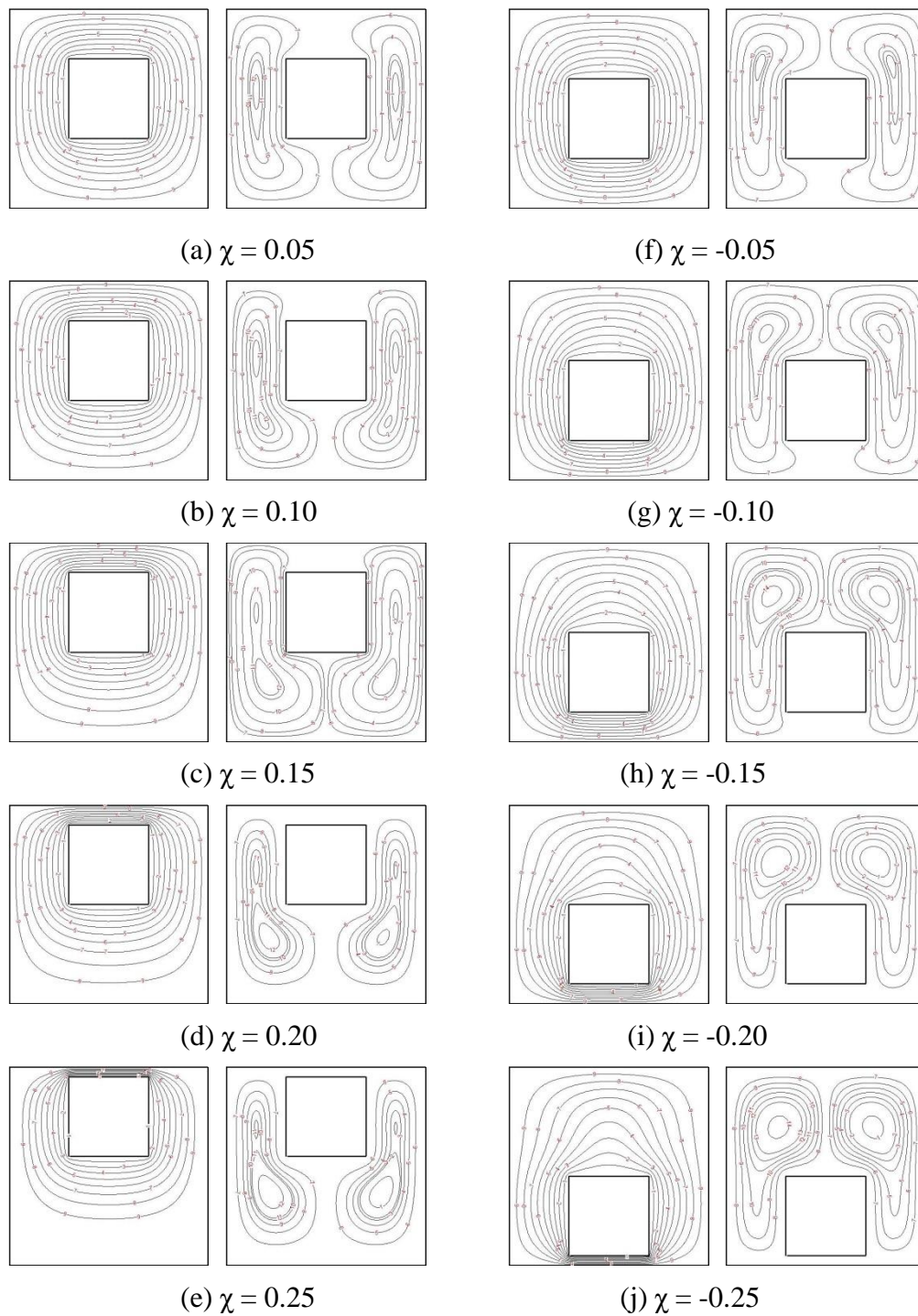


Fig.5.11. Isotherm and streamline plots at different displacement (χ) of inner cylinder for $Ra=10^4$ (Contour levels of 1-10 and 1-12 are shown for isotherms and streamlines respectively).

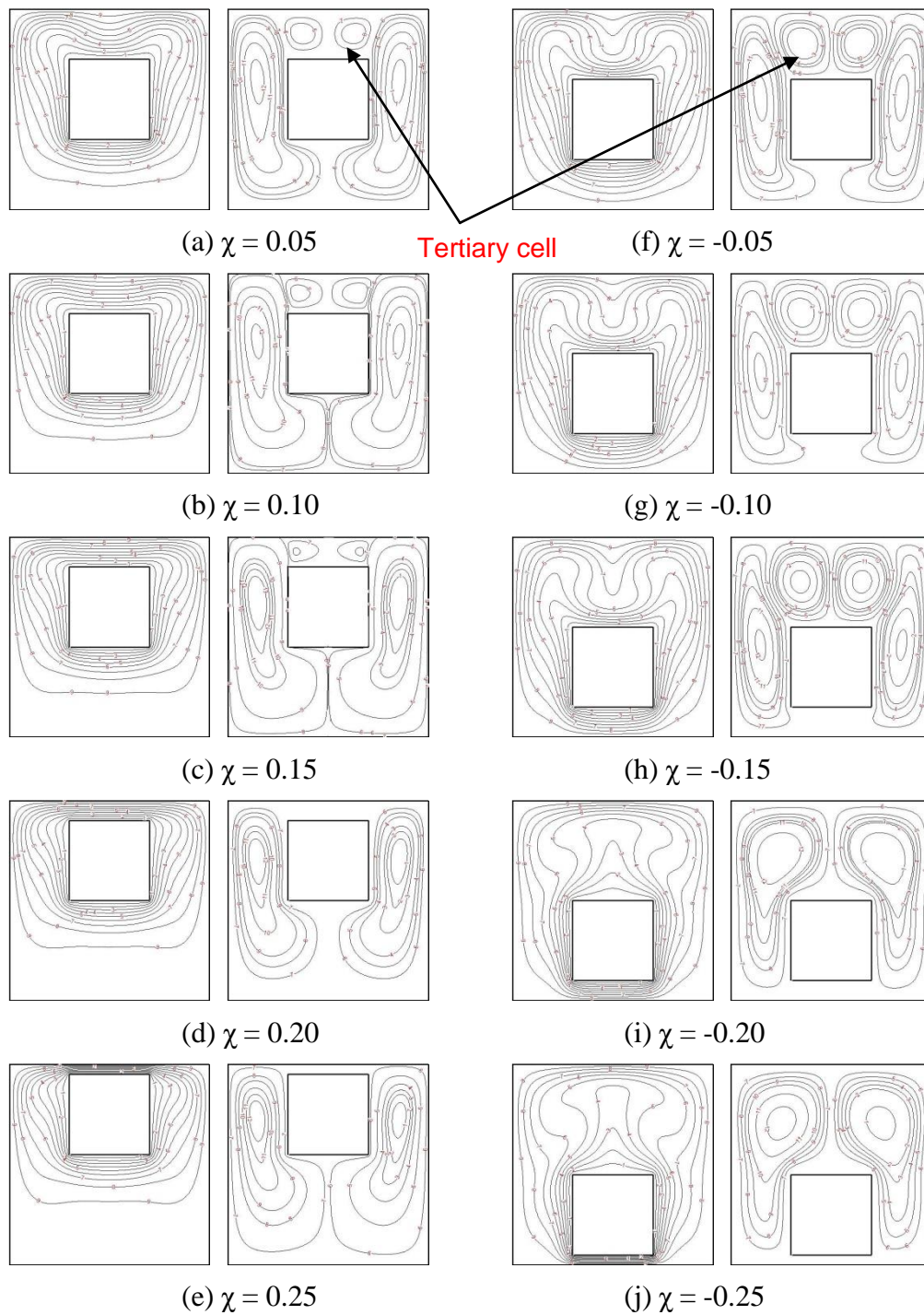


Fig.5.12. Isotherm and streamline plots at different displacement (χ) of inner cylinder for $Ra=10^5$ (Contour levels of 1-10 and 1-12 are shown for isotherms and streamlines respectively).

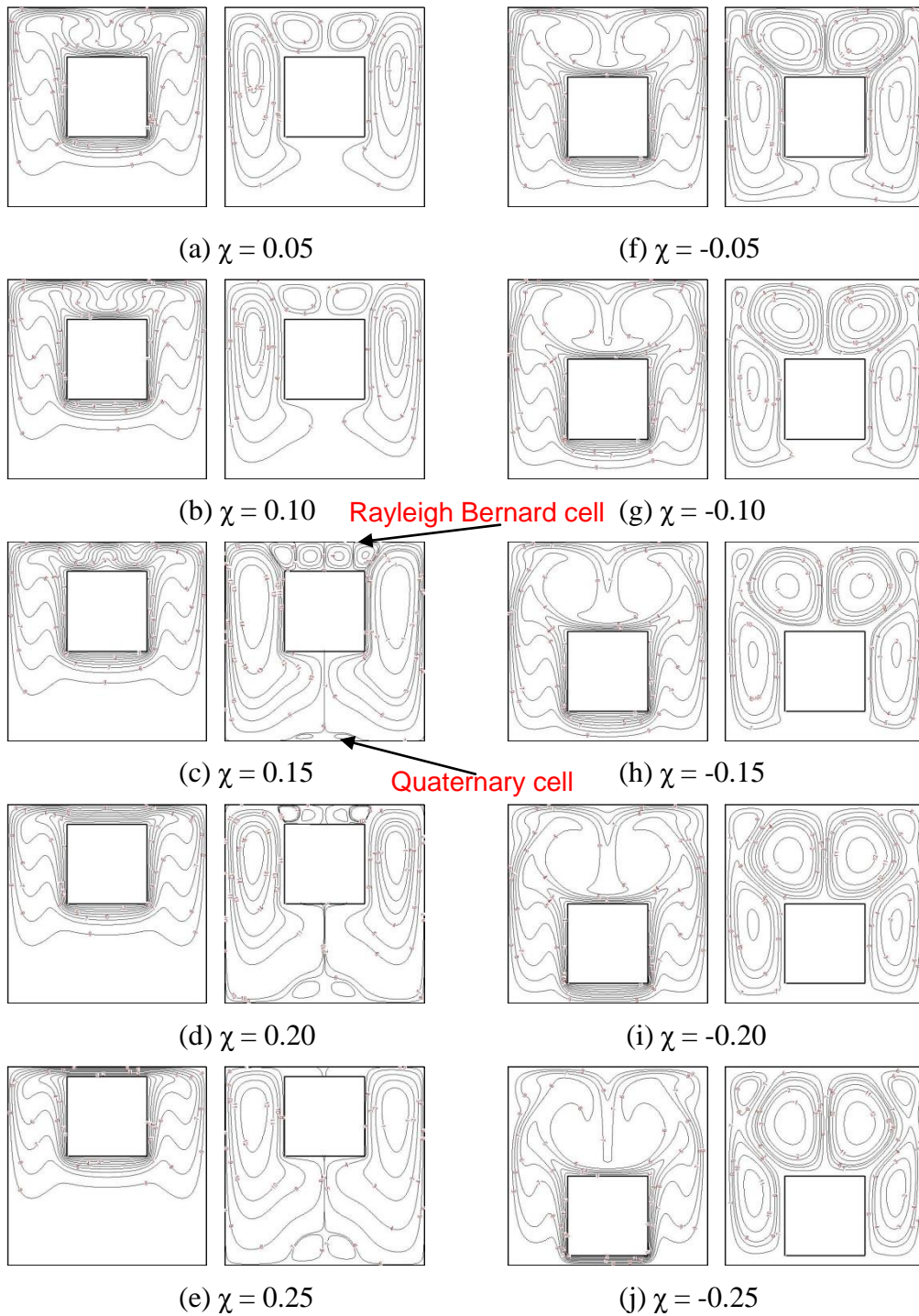


Fig.5.13. Isotherm and streamline plots at different displacement (χ) of inner cylinder for $Ra=10^6$ (Contour levels of 1-10 and 1-12 are shown for isotherms and streamlines respectively).

When the inner cylinder is moved upward, the produced flow pattern is similar to the downward movement case. The flow field contains tertiary cells and thermal plumes. With further increase in the eccentricity at $\chi = 0.15$, multiple thermal plumes are formed that leads to formation of Rayleigh Bernard (RB) cells. Also two additional circulations (Quaternary cells) are formed near the bottom of the enclosure as shown in Fig.5.13(c). The formation of the quaternary cells is associated with loss of the kinetic energy of the moving fluid. As the uprising hot fluid strikes the cold walls of the enclosure, it loses heat and becomes denser and colder, and gradually reaches to the bottom wall of the enclosure. By this time the fluid has almost lost its kinetic energy. Hence, the flow gets separated near the vertical mid-plane of the enclosure with formation of quaternary cells. When χ is increased to 0.2, the size of RB cells are reduced due to local dominance of conduction and lesser annular gap. When $\chi = 0.25$, RB cells disappear and quaternary cells grow in size. The isotherms as shown in Fig.5.13(e), are mostly concentrated in the upper half of the enclosure, and are coarser and distant in the bottom half (implying the stratified fluid zone).

5.2.2.3 Local Nusselt number (Nu_L)

$$\underline{Ra = 10^3}$$

At $Ra = 10^3$, conduction is the mode of heat transfer. Therefore, isotherms are symmetrically distributed at $\chi = 0.0$. This further produces similar Nu_L profile on all the walls of the enclosure, as shown in Fig.5.14(a). The vertical movements of the inner cylinder change the distribution of Nu_L . If the inner

cylinder approaches bottom (12) or top (34) wall of the enclosure, corresponding increase in the thermal gradient near the wall enhances the heat transfer and Nu_L . Shift in Nu_L on the enclosure side walls (01 or 23) are also noticed with the change in eccentricity.

$Ra = 10^4$

At $Ra = 10^4$, the heat transfer mode is still consider to be conduction dominance with regular isotherm distribution, as shown in Fig.5.11(a) – (j). Therefore, Nu_L variation is qualitatively found similar to $Ra = 10^3$, but comparatively higher values. Again initiation of the convection, makes the distribution of Nu_L asymmetric on the enclosure wall, unlike at $Ra = 10^3$. The change in the eccentricity of the inner cylinder also shifts Nu_L distribution.

$Ra=10^5$

At $Ra = 10^5$, convective heat transfer is stronger than $Ra = 10^3$ and 10^4 . Hence, increase in Nu_L is observed. As the convective flow is primarily occupied in the upper region of the enclosure, therefore irrespective of the inner cylinder movements, local maxima always stays near the upper corners for the side walls (01 and 23).

When the inner cylinder is moved downward, Nu_L distribution on the bottom wall (12) of the enclosure increases and attains maximum at $\chi = -0.25$. Nu_L is varied with multiple peaks on the upper wall (34) till $\chi = -0.15$, beyond which single peak Nu_L variation is observed. The change of the flow regime with eccentricity may have produced this change in Nu_L distribution.

When the inner cylinder is moved upward, Nu_L distribution on the upper wall (34) of the enclosure increases and attains maximum at $\chi = 0.25$. Also Nu_L distribution has shown multiple peaks, when $\chi < 0.15$. Further increase in χ , forms concentrated isotherms with the local dominance of conduction. This avoids the formation of multiple peaks in Nu_L distribution on the wall 34, and enhances the local heat transfer rate as shown in Fig.5.14(c).

$$\underline{Ra = 10^6}$$

When the inner cylinder is moved downward, Nu_L distribution on the bottom wall (12) is increased. On the side walls (01 and 23), Nu_L distribution contains two peaks with different maximum. This can be correlated to the formation of tiny vortices near the upper corners of the enclosure as shown in Fig.5.13(g) – (j). In presence of both upwelling and down welling plumes, multiple peaks type Nu_L distribution is found on the upper wall (34).

When the inner cylinder is moved upward, Nu_L distribution is altered with the eccentricity. At $\chi < 0.15$, Nu_L is distributed with two peaks and a valley on the upper wall (34). When χ is increased further, additional peaks and valleys are found in Nu_L distribution with the formation of RB cells. At $\chi = 0.25$, due to local dominance of conduction the distribution of Nu_L on the wall 34 changes to single peak type.

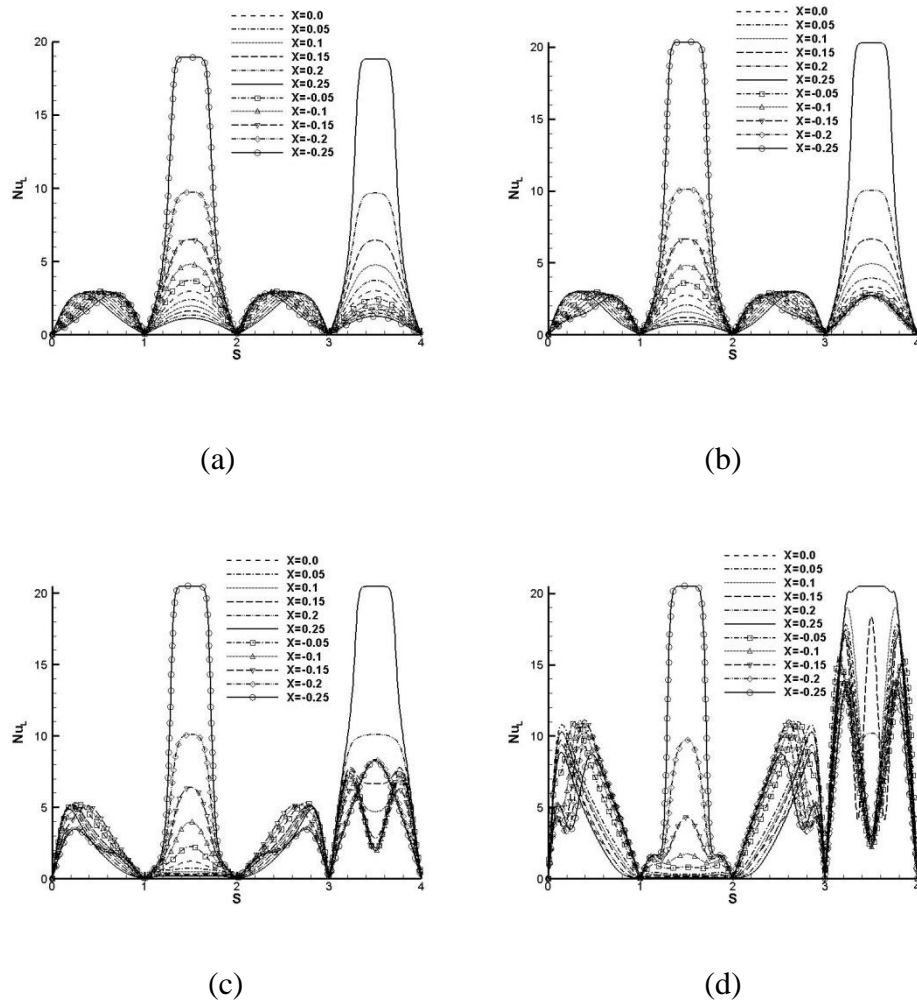


Fig.5.14. Nu_L distribution on the enclosure walls at different location of inner cylinder and for Ra equals to (a) 10^3 (b) 10^4 (c) 10^5 and (d) 10^6 . The direction used for ‘S’ can be referred from Fig.5.1.

5.2.2.4 Surface average Nusselt number (Nu_A)

In Fig.5.15(a), Nu_A on the top wall of the enclosure is plotted with χ for Ra in the range $10^3 - 10^6$. At Ra = 10^3 , Nu_{AT} increases with the increase in χ . The rate of increase of Nu_{AT} is slow at $\chi < 0$, but when $\chi > 0$, rapid increment is noticed. This may be linked with the proximity difference between enclosure top wall and the inner cylinder. The variation of Nu_{AT} at Ra = 10^4 , is similar to

the case of $Ra = 10^3$. At $Ra = 10^5$, the trend of Nu_{AT} is different because of the increased convection rate. When $\chi < -0.15$, Nu_{AT} shows increasing trend but a sudden fall is noticed at $\chi = -0.15$. The change in the flow pattern as shown in Fig.5.12(h) – (i), may be responsible for this fall. With further increase in χ , Nu_{AT} increases and reaches to maximum at $\chi = 0.25$. The variation of Nu_{AT} at $Ra = 10^6$, also shows continuous increase. When $\chi = 0.1$, the formation of RB cells reduces the heat transfer and hence, Nu_{AT} shows a decreasing slope for $0.1 < \chi < 0.2$. Again with the disappearance of RB cells, increase in Nu_{AT} is observed for $\chi > 0.2$.

In Fig.5.15(b), Nu_A variation on the bottom wall of the enclosure is shown. Almost similar trend of variation is observed for all Ra . Maximum Nu_{AB} is found while the inner cylinder is at $\chi = -0.25$. When the inner cylinder moves upward, the proximity between the inner cylinder and bottom wall of the enclosure increases, which reduces the thermal gradient near the bottom wall. Thus, decrease in Nu_{AB} is noticed.

In Fig.5.15(c), Nu_A on the side wall of the enclosure is shown. The variation of Nu_{AS} is comparatively less than other walls of the enclosure. At $Ra = 10^3$ and 10^4 , Nu_{AS} has shown negligible variation with χ . At higher Ra or higher convection rate, Nu_{AS} values are enhanced.

In Fig.5.15(d), Nu_{Aen} is plotted as a function of χ at different Ra . At $Ra = 10^3$ or 10^4 , Nu_{Aen} variation shows a parabolic profile with maximum at the extreme eccentricity of the inner cylinder, i.e. $\chi = -0.25$ and 0.25 , and minimum when the cylinder is at the centre, i.e. $\chi = 0.0$. At $Ra = 10^5$, the symmetric

distribution of Nu_{Aen} is broken. Minimum location of Nu_{Aen} is shifted to $\chi = 0.1$, in presence of the secondary cells. When Ra increases to 10^6 , Nu_{Aen} starts from a maximum and shows a decreasing trend. At $\chi = 0.2$, concentrated isotherms and without RB cells, enhancement in the heat transfer is observed that rises Nu_{Aen} distribution.

5.3 Concluding remarks

In this chapter, we have utilized the developed 2D flexible forcing hybrid IB – thermal LBM scheme to study the complex cavity natural convection flow with 1) an inclined and 2) a vertical eccentric square heat source (cylinder). Although these flow conditions have many practical implications but they are not thoroughly analysed in the literature. Here, we have made an attempt to study the flow regime and heat transfer pattern by looking into the detail distributions of streamlines and isotherms contours at different Ra, in the range $10^3 - 10^6$. Further investigations on local Nusselt number and surface average Nusselt number on different walls of the enclosure are made by varying Ra, eccentricity and inclination angle.

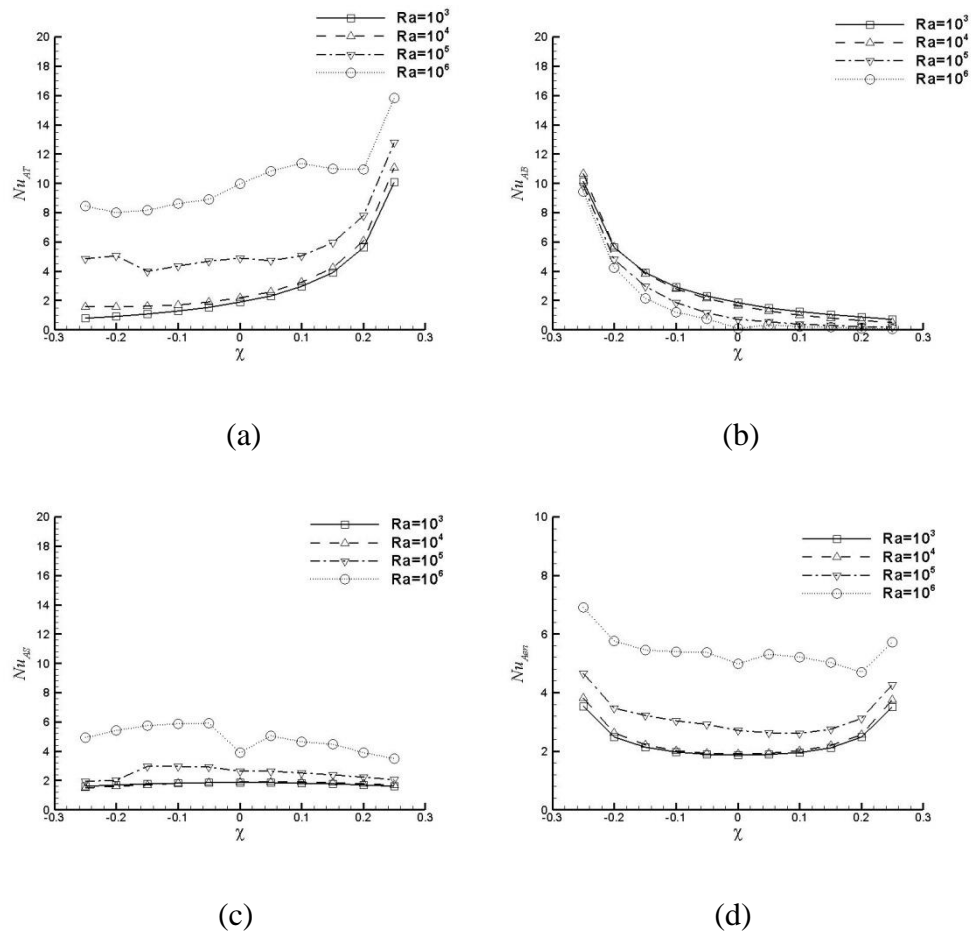


Fig.5.15. Surface average Nusselt Number on (a) top wall, (b) bottom wall, (c) side wall and (d) combined all walls of the enclosure vs χ at different Ra .

Chapter 6

Extension of Flexible Forcing IB– LBM for 3D Flows around Stationary and Moving Boundary Problems⁵

In the previous chapters 2, 3, 4 and 5 a flexible forcing IB – LBM scheme is introduced that have been successfully implemented for 2D flow scenarios with or without thermal effects. In this chapter we have extended the proposed numerical model to simulate 3D flows that contain stationary as well as moving immersed solid boundaries. The proposed new version of IB – LBM model is validated with three-dimension flow past stationary and moving spheres, and the results are found in excellent agreement with the data obtained from previous literatures. The detail mathematical formulations are

⁵ Part of this work has been published as:

Dash SM, Lee TS, Lim TT and Huang H. (2014). "A flexible forcing three dimensional IB-LBM scheme for flow past stationary and moving sphere." *Computers and Fluids* **95**(0): 159-170
Dash SM, Lim TT and Lee TS. (2014). "Two spheres sedimentation dynamics in a viscous liquid column." *Physics of Fluids*: (Under Review)

outlined in the followings. We have also validated the 3D numerical scheme by simulating many benchmark flow cases.

6.1 Flexible forcing IB-LBM scheme

In this section, we will briefly describe the extension of the flexible forcing IB – LBM scheme for 3D implementation. The governing equations of a three dimensional, incompressible, unsteady flow with an immersed boundary are (Wu and Shu (2010)),

$$\frac{\partial \rho}{\partial t} + \nabla \cdot \rho \mathbf{u} = 0, \quad (6.1)$$

$$\frac{\partial}{\partial t}(\rho \mathbf{u}) + \nabla \cdot (\rho \mathbf{u} \mathbf{u}) = -\nabla P + \nu \nabla \cdot \left[\rho \nabla \mathbf{u} + (\nabla \mathbf{u})^T \right] + \mathbf{f}, \quad (6.2)$$

$$\mathbf{f}(\mathbf{x}, t) = \int_{\Gamma} \mathbf{F}_B(s, t) \delta(\mathbf{x} - \mathbf{X}_B(s, t)) ds, \quad (6.3)$$

$$\frac{\partial \mathbf{X}_B(s, t)}{\partial t} = \mathbf{u}(\mathbf{X}_B(s, t), t) = \int_{\Omega} \mathbf{u}(\mathbf{x}, t) \delta(\mathbf{x} - \mathbf{X}_B(s, t)) d\mathbf{x}. \quad (6.4)$$

where the variables: ρ, \mathbf{u}, P, ν represent density, flow velocity, pressure, and kinematic viscosity of the fluid, respectively. \mathbf{x} and \mathbf{X}_B are Eulerian and Lagrangian mesh co-ordinates, \mathbf{f} and \mathbf{F}_B are the force density acting on the fluid and immersed boundary, respectively. $\delta(\mathbf{x} - \mathbf{X}_B(s, t))$ is Dirac delta function.

In the above, Eqs.(6.1) – (6.2) represent the traditional NS equations with the force density \mathbf{f} . Eqs.(6.3) – (6.4) relate the immersed solid boundary (Γ) and fluid domain (Ω) by distributing the boundary force to nearby fluid points and computing the boundary velocity from the fluid velocity.

From the multi-scale Chapman-Enskog expansion, the lattice Boltzmann equations (LBE) (Wu and Shu (2010)) with discrete body force term F_α , that recovers Eqs.(6.1) – (6.2) can be written as,

$$f_\alpha(\mathbf{x}+\mathbf{e}_\alpha\delta t,t+\delta t) = f_\alpha(\mathbf{x},t) - \frac{1}{\tau}\left(f_\alpha(\mathbf{x},t)-f_\alpha^{eq}(\mathbf{x},t)\right) + F_\alpha\delta t, \quad (6.5)$$

$$F_\alpha = \left(1 - \frac{1}{2\tau}\right) W_\alpha \left(\frac{\mathbf{e}_\alpha \cdot \mathbf{u}}{c_s^2} + \frac{\mathbf{e}_\alpha \cdot \mathbf{u}}{c_s^4} \mathbf{e}_\alpha \right) \cdot \mathbf{f}, \quad (6.6)$$

$$\rho\mathbf{u} = \sum_\alpha \mathbf{e}_\alpha f_\alpha + \frac{1}{2}\mathbf{f}\delta t. \quad (6.7)$$

$f_\alpha(\mathbf{x},t)$ and $f_\alpha^{eq}(\mathbf{x},t)$ are the density distribution functions and its corresponding equilibrium part along the discrete lattice directions α . τ is a non-dimensional relaxation parameter in the BGK approximation. The discrete lattice velocities \mathbf{e}_α are selected such that their directions match with a standard D3Q15, three dimensional lattice model (Wu and Shu (2010)). Here, D3Q15 model is chosen to achieve faster computation rate (Usman (2009)) compare to other three dimensional lattice models D3Q19 and D3Q27. Although D3Q15 model is least isotropic (Mei et al. (2000)) but for low Re flow the model is not prone to numerical instabilities, which have been

verified for stationary and moving boundary flow scenarios (Feng and Michaelides (2005); Wu and Shu (2010); Wu and Shu (2012)).

$f_\alpha^{eq}(\mathbf{x}, t)$ in Eq.(6.5) is obtained from Taylor series expansion of Maxwell

Boltzmann distribution function where W_α is the weighting coefficient.

$$f_\alpha^{eq}(\mathbf{x}, t) = \rho W_\alpha \left[1 + \frac{\mathbf{e}_\alpha \cdot \mathbf{u}}{c_s^2} + \frac{(\mathbf{e}_\alpha \cdot \mathbf{u})^2 - (c_s |\mathbf{u}|)^2}{2c_s^4} \right], \quad (6.8)$$

$$\mathbf{e}_\alpha = c \begin{cases} (0,0,0), & \alpha = 0, \\ (\pm 1, 0, 0), (0, \pm 1, 0), (0, 0, \pm 1), & \alpha = 1-6, \\ (\pm 1, \pm 1, \pm 1), & \alpha = 7-14. \end{cases} \quad (6.9)$$

$$W_\alpha = \begin{cases} 2/9, & \alpha = 0, \\ 1/9, & \alpha = 1-6, \\ 1/72, & \alpha = 7-14. \end{cases} \quad (6.10)$$

The sound speed is defined as, $c_s = c / \sqrt{3}$, where $c = \delta x / \delta t$, is the lattice speed. δx and δt are the mesh and time step size, respectively.

In Eq.(6.7) the macroscopic velocity \mathbf{u} is derived from the density distribution and the force density. If we define an intermediate velocity $\mathbf{u}^* = \sum_\alpha \mathbf{e}_\alpha f_\alpha / \rho$,

and a velocity correction $\delta \mathbf{u} = (1/2\rho) \mathbf{f} \delta t$, then Eq.(6.7) can be rewritten as,

$$\mathbf{u} = \mathbf{u}^* + \delta \mathbf{u}. \quad (6.11)$$

In the IBM, Eulerian velocity correction $\delta \mathbf{u}$ is usually distributed from Lagrangian boundary velocity correction $\delta \mathbf{U}_B$ as shown in Eq.(6.12) (Wu and Shu (2010)).

$$\delta \mathbf{u}(\mathbf{x}, t) = \int_{\Gamma} \delta \mathbf{U}_B(\mathbf{X}_B, t) \delta(\mathbf{x} - \mathbf{X}_B) ds, \quad (6.12)$$

where the immerse boundary is represented using a set of Lagrangian co-ordinates $\mathbf{X}_B(s_p, t)$. s_p ($p=1,2,3\dots n$) are the co-ordinates. $\delta(\mathbf{x} - \mathbf{X}_B)$ is smoothly approximated with continuous Kernel distribution $D(\mathbf{x} - \mathbf{X}_B^p)$ (Peskin (1977)) using 4 point discrete delta function.

$$\delta(r) = \begin{cases} \frac{1}{4} \left(1 + \cos\left(\frac{\pi|r|}{2}\right) \right), & |r| \leq 2, \\ 0, & |r| > 2. \end{cases} \quad (6.13)$$

$$D(\mathbf{x} - \mathbf{X}_B^p) = \frac{1}{h^3} \delta\left(\frac{x - X_B^p}{h}\right) \delta\left(\frac{y - Y_B^p}{h}\right) \delta\left(\frac{z - Z_B^p}{h}\right), \quad (6.14)$$

where h is the Eulerian mesh size. Using Eqs.(6.13) – (6.14), we can simplify Eq.(6.12) to an algebraic equation (Eq.(6.15)).

$$\delta \mathbf{u}(\mathbf{x}, t) = \sum_p \delta \mathbf{U}_B^p(\mathbf{X}_B^p, t) D(\mathbf{x} - \mathbf{X}_B^p) \Delta s_p, \quad (6.15)$$

where Δs_p is area of the boundary element. In the present 3D simulations, the sphere surface is discretized with triangular boundary elements as shown in Fig.6.1. Once Eulerian velocity correction is obtained, the corrected Eulerian velocity can be computed using Eq.(6.11).

Now, the next step is to satisfy the no-slip boundary condition on the immersed sphere. From mathematics, the no-slip condition implies that the fluid velocity at the boundary point must be equal to the boundary velocity at the same position. Using the concept of interpolation, we can write the no-slip condition equation as,

$$\mathbf{U}_B^p(\mathbf{X}_B^p, t) = \sum_{i,j,k} \mathbf{u}(\mathbf{x}, t) D(\mathbf{x} - \mathbf{X}_B^p) \Delta x \Delta y \Delta z, \quad (6.16)$$

where Δx , Δy and Δz are Eulerian mesh sizes along Cartesian coordinate directions. Substituting Eqs.(6.11) and (6.15) in Eq.(6.16) gives rise to a complex equation (Eq.(6.17)),

$$\begin{aligned} \mathbf{U}_B^p(\mathbf{X}_B^p, t) = & \sum_{i,j,k} \mathbf{u}^*(\mathbf{x}, t) D(\mathbf{x} - \mathbf{X}_B^p) \Delta x \Delta y \Delta z \\ & + \sum_{i,j,k} \sum_p \delta \mathbf{U}_B^p(\mathbf{X}_B^p, t) D(\mathbf{x} - \mathbf{X}_B^p) \Delta s_p D(\mathbf{x} - \mathbf{X}_B^p) \Delta x \Delta y \Delta z, \end{aligned} \quad (6.17)$$

which demands a matrix inversion (Wu and Shu (2010)) to obtain the boundary velocity correction $\delta \mathbf{U}_B^p$. In the case of moving boundary problem, repeating the matrix inversion consumes a significant computational time. Again, the proposed scheme (Wu and Shu (2010)) requires higher computational memory space in the case of a three dimensional problem, along with trouble of the sequential code generation for the coefficient of $\delta \mathbf{U}_B^p$.

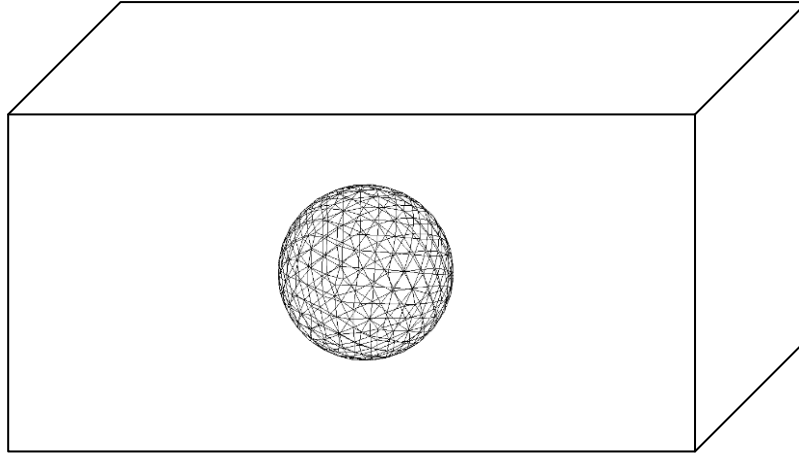


Fig.6.1 Triangular surface elements used for discretising the sphere surface.

To address the above issues, we have proposed a simple solution for two dimensional flow cases in Chapter 2. Here, the extension of the work is made to three dimensional problems. If we analyse the Eq.(6.16), the desired boundary velocity \mathbf{U}_B^p in most of the cases is known to us (i.e. equals to zero for stationary sphere or calculated using Newton's laws of motion for a moving sphere). Hence, the interpolated Eulerian velocity field (RHS of Eq.(6.16)) must match with \mathbf{U}_B^p when the no-slip condition is satisfied. In case of IBM auto-satisfaction of the no-slip condition is impractical, because the immersed boundary is defined on a Lagrangian frame whereas the flow field is defined on an Eulerian frame, and the node points do not necessarily matches. This creates a difference between LHS and RHS of Eq.(6.16), and the amount of deviation (otherwise called as velocity correction) must be accounted to satisfy the exact no-slip condition.

Therefore, in our previously proposed two dimensional model (ref. Chapter 2), this velocity correction is accounted for in the Lagrangian frame and can also be applied in three dimensional case as shown in Eq.(6.18).

$$\mathbf{U}_B^{pd}(\mathbf{X}_B^p, t) = \sum_{i,j,k} \mathbf{u}(\mathbf{x}, t) D(\mathbf{x} - \mathbf{X}_B^p) \Delta x \Delta y \Delta z + \delta \mathbf{U}_B^p(\mathbf{X}_B^p, t)^m, \quad (6.18)$$

$$\delta \mathbf{U}_B^p(\mathbf{X}_B^p, t)^m = \sum_{i,j,k} \mathbf{u}(\mathbf{x}, t) D(\mathbf{x} - \mathbf{X}_B^p) \Delta x \Delta y \Delta z - \mathbf{U}_B^{pd}(\mathbf{X}_B^p, t), \quad (6.19)$$

where \mathbf{U}_B^{pd} is the desired boundary velocity and $\delta \mathbf{U}_B^p$ is the amount of boundary velocity correction. Following the above correction measures, one may not ensure the no-slip condition at all the boundary points in single turn as the boundary velocity correction is linked with the Eulerian velocity correction (shown in Eq.(6.15)). Hence, an additional sub-iteration update scheme is imposed to satisfy the no-slip condition within a convergence limit. This further ensures that when Eulerian velocities are interpolated back to the Lagrangian boundary nodes, they will satisfy the no-slip condition with an accuracy of the order $\delta \mathbf{U}_B^p$. The convergence criterion (CC) is set in Eq.(6.20), where m is the sub-iteration number until the CC is satisfied.

$$\left| \delta \mathbf{U}_B^p(\mathbf{X}_B^p, t)^m \right| \leq 10^{-6}. \quad (6.20)$$

This formulation retains the basic idea of implicit velocity correction (Wu and Shu (2010)) and mathematically much simpler as it reduces the computational efforts and storage demands. It is worth mentioning that the CC is a case dependent term, which may be adjusted to a higher/lower order tolerance

depending on complexity of the problem with required accuracy of the final result and available computational resources. Compare to the multiple direct forcing schemes (Wang et al. (2008); Kang and Hassan (2011)) where fixed number of sub-iterations is adopted, our present proposed scheme is advantageous. As in case of unsteady and moving boundary problems, use of fixed forcing/sub-iteration scheme (Wang et al. (2008); Kang and Hassan (2011)) may not yield the correct no-slip condition at each time step. The force and torque calculations then become questionable. To overcome these defects, the proposed flexible sub-iteration scheme is a suitable alternative.

Further, the proposed scheme is computationally efficient because the defined convergence criterion in Eq.(6.20) discards all the unnecessary sub-iterations in the single time-step marching once the no-slip condition is accurately satisfied. This saves significant computational time unlike the fixed forcing scheme (Wang et al. (2008); Kang and Hassan (2011)).

Again, to minimise the number of sub-iteration in the proposed scheme, a successive relaxation parameter (SRP), ε is prescribed to update the velocity correction. By suitably selecting the ε between 0 – 1, the computational time can be significantly reduced.

$$\delta\mathbf{U}_B^p(\mathbf{X}_B^p, t)^m = (1 - \varepsilon)\delta\mathbf{U}_B^p(\mathbf{X}_B^p, t)^{m-1} + \varepsilon\delta\mathbf{U}_B^p(\mathbf{X}_B^p, t)^m. \quad (6.21)$$

The effects of SRP and CC selection will be discussed in the following section.

After calculating the velocity corrections, the force density at the Lagrangian and Eulerian grid points is derived using Eq.(6.22).

$$\mathbf{F}_B^p(\mathbf{X}_B^p, t) = \sum_m 2\rho\delta\mathbf{U}_B^p(\mathbf{X}_B^p, t)^{(m)} / \delta t,$$

$$\mathbf{f}(\mathbf{x}, t) = \sum_m 2\rho\delta\mathbf{u}(\mathbf{x}, t)^{(m)} / \delta t. \quad (6.22)$$

6.1.1 Kinematics of the moving Sphere

Using Newton's laws of motion, net force \mathbf{F}_i^{net} on the moving sphere can be calculated as the combined effects of the gravity, buoyancy, hydrodynamic and collision forces.

$$\mathbf{F}_i^{net} = \left(1 - \frac{\rho_f}{\rho_p}\right) M_i \mathbf{g} - \sum_p \mathbf{F}_B^p(\mathbf{X}_B^p) \Delta s_p + \mathbf{F}_i^{coll}, \quad (6.23)$$

where M_i is the mass of the sphere, ρ_f and ρ_p are densities of the fluid and solid sphere, respectively. To calculate the collision force \mathbf{F}_i^{coll} between sphere-wall/sphere-sphere, a lubrication forcing mechanism is followed (Singh et al. (2000)). This force is repulsive in nature and acts only when the distance between the sphere and nearest wall or another sphere is less than λ . In our present study, we set $\lambda = 2\delta x$.

$$\mathbf{F}_i^{coll} = \begin{cases} 0 & d_{i,j} \geq R_i + R_j + \lambda, \\ \frac{1}{\epsilon_p} (\mathbf{X}_{Ri} - \mathbf{X}_{Rj}) (R_i + R_j + \lambda - d_{i,j})^2 & d_{i,j} < R_i + R_j + \lambda, \end{cases} \quad (6.24)$$

where R_i and R_j are the radius of the colliding spheres. In case of collision with a wall, this force calculation is done by assuming an imaginary sphere of same size on the other side of wall. $d_{i,j}$ is the distance between the centre of i^{th} and j^{th} spheres' with their corresponding centre location at \mathbf{X}_{Ri} and \mathbf{X}_{Rj} respectively. ε_p is a small positive stiffness parameter followed from Singh et al. (2000).

Similarly, from the hydrodynamic force, the torque \mathbf{T}_i^{net} acting on the moving sphere can be computed as,

$$\mathbf{T}_i^{net} = -\sum_p (\mathbf{X}_B^p - \mathbf{X}_R) \times \mathbf{F}_B^p(\mathbf{X}_B^p, t) \Delta s_p, \quad (6.25)$$

where \mathbf{X}_R is the centre of mass of the sphere. Using the concept of the conservation of translational $\mathbf{L}_T(t)$ and angular momentum $\mathbf{L}_A(t)$ we can write,

$$\frac{\partial \mathbf{L}_T(t)}{\partial t} = \frac{\partial M_i \mathbf{v}(t)}{\partial t} = \mathbf{F}_i^{net}, \quad (6.26)$$

$$\frac{\partial \mathbf{L}_A(t)}{\partial t} = \frac{\partial \mathbf{I}(t) \boldsymbol{\omega}(t)}{\partial t} = \mathbf{T}_i^{net}, \quad (6.27)$$

where $\mathbf{v}(t)$ and $\boldsymbol{\omega}(t)$ are the linear and angular velocities of the moving sphere. $\mathbf{I}(t)$ is the inertia tensor at the current coordinate system. For a symmetrical object like sphere, $\mathbf{I}(t)$ is independent of rotation and coordinate system (Glowinski et al. (2001)). Hence, we have used a constant moment of

inertia $I(t) = I_0 = (2/5)M_i R_i^2$ for the moving sphere. To represent the displacement of any surface point $\mathbf{X}_B^p(t)$ on the sphere at time t , Eq.(6.28) can be used,

$$\mathbf{X}_B^p(t) = \mathbf{X}_R(t) + R_c(t) \mathbf{X}_B^p(0), \quad (6.28)$$

where $R_c(t)$ is a 3×3 rotational matrix that describes the rotation/orientation of the sphere about its centre of mass $\mathbf{X}_R(t)$. The $\mathbf{X}_R(t)$ and $R_c(t)$ in Eq.(6.28) are time updated using the following equations.

$$\frac{\partial \mathbf{X}_R(t)}{\partial t} = \mathbf{v}(t), \quad (6.29)$$

$$\frac{\partial R_c(t)}{\partial t} = \boldsymbol{\omega}(t) \times R_c(t) = \begin{vmatrix} 0 & -\omega_3 & \omega_2 \\ \omega_3 & 0 & -\omega_1 \\ -\omega_2 & \omega_1 & 0 \end{vmatrix} \begin{vmatrix} R_{c1} \\ R_{c2} \\ R_{c3} \end{vmatrix}. \quad (6.30)$$

Now, the next step is to solve the Eqs.(6.26) – (6.30), to update the position and velocities of the moving sphere with time advancement. Crank – Nicolson – type method with implicit time discretisation is used for Eqs.(6.26) – (6.27) and (6.29) – (6.30). This can be written in matrix form as,

$$\frac{\mathbf{Y}^{n+1} - \mathbf{Y}^n}{\Delta t} = \frac{1}{2} \{ \boldsymbol{\xi}^{n+1} + \boldsymbol{\xi}^n \}, \quad (6.31)$$

where $\mathbf{Y} = [\mathbf{X}_R(t), R_c(t), \mathbf{L}_T(t), \mathbf{L}_A(t)]^T$ and

$\boldsymbol{\xi} = [\mathbf{v}(t), \boldsymbol{\omega}(t) \times R_c(t), \mathbf{F}_i^{net}, \mathbf{T}_i^{net}]^T$. n is the time step. Following a

predictor-corrector (Patankar et al. (2000)) approach, Eq.(6.31) is iteratively solved.

The other fluid variables: density, pressure and kinematic viscosity are calculated using Eq.(6.32).

$$\rho = \sum_{\alpha=0}^N f_{\alpha}, \quad P = \rho c_s^2, \quad \nu = \left(\tau - \frac{1}{2} \right) c_s^2 \delta t. \quad (6.32)$$

In summary, the solution procedure of the proposed numerical scheme is outlined below.

1. Set the initial flow field and calculate $f_{\alpha}(\mathbf{x}, t)$ and $f_{\alpha}^{eq}(\mathbf{x}, t)$.
2. Perform streaming using Eq.(6.5) with initial setting $F_{\alpha}, \delta \mathbf{u} = 0$ and calculate intermediate velocity $\mathbf{u}^* = \sum_{\alpha} \mathbf{e}_{\alpha} f_{\alpha} / \rho$.
3. From the desired boundary velocity, calculate Lagrangian velocity correction $\delta \mathbf{U}_B^p(\mathbf{X}_B^p, t) \Big|^{m=0}$.
4. Update Eulerian velocity \mathbf{u} as in Eq.(11) with updated $\delta \mathbf{u}$ and calculate the new $\delta \mathbf{U}_B^p(\mathbf{X}_B^p, t) \Big|^{m=1}$ using both the Eqs.(6.19) and (6.21).
Repeat this step with a sub-iteration loop until the CC in Eq.(6.21) is satisfied.
5. Calculate the new \mathbf{f} and $f_{\alpha}^{eq}(\mathbf{x}, t)$ using Eqs.(6.22) and (6.8). Update the net force and torque acting on the moving sphere as shown in

Eqs.(6.23) and (6.25). Then the new position and velocity of the sphere can be calculated using Eq.(6.31).

6. Repeat the above steps (2) – (5) for time evolution.

6.2 Numerical validations

The numerical accuracy of the proposed flexible forcing IB – LBM scheme was evaluated by performing a set simulations on three dimensional stationary (laminar flow past sphere) and moving boundary (freely falling spheres) flow problems. In the followings, we compare the results obtained from the flexible forcing IB – LBM scheme with those reported in the literature.

6.2.1 Flow past a stationary sphere

This problem has been extensively studied by researchers (Gilmanov et al. (2003); Wu and Shu (2010)) to validate new three dimension algorithms. In our first validation test case, we considered the flow over a stationary sphere in the laminar flow regime ($Re < 300$). The Re is defined as,

$$Re = \frac{U_{\infty} D}{\nu}, \quad (6.33)$$

where U_{∞} is the free stream velocity, and D is the diameter of the sphere. The flow regime of this problem is Re dependent. The flow pattern is found steady axisymmetric when $Re < 200$, and becomes steady non-axisymmetric when $210 < Re < 270$. For higher Re , the flow exhibits an unsteady behaviour.

In the present simulation, the computational domain is selected as $25D \times 20D \times 20D$, along the X, Y and Z coordinate axis, respectively. The sphere centre is located at $(10D, 10D, 10D)$. Grid independence study is performed to ensure the results are independent of mesh resolutions as shown in Table 6.1. Based on the results in Table 6.1, we have adopted a non-uniform Cartesian mesh of size, $141 \times 121 \times 121$, which is sufficient to ensure the mesh independent results. A Lagrangian interpolation based LBM (Wu and Shu (2010)) is utilised to solve the fluid flow evolution in the non-uniform Cartesian mesh.

Table 6.1 Grid independence test of flow past a stationary sphere at $Re = 100$.

Mesh size	C_d	% Error = $\left \frac{C_d^{Newgrid} - C_d^{Oldgrid}}{C_d^{Oldgrid}} \right \times 100$
99×85×85	1.162	--
113×97×97	1.151	0.94
141×121×121	1.147	0.34
161×139×139	1.145	0.17

To simulate the steady axisymmetric flow, Re is selected between 50 to 200. The fluid density ρ and the free stream velocity U_∞ are used as, $\rho = 1.0$ and $U_\infty = 0.1$. To change the Re , only the kinematic viscosity ν is changed. The surface of the sphere is discretised with 915 triangular elements. Since the flow is axisymmetric, only the streamlines on XY symmetric plane is shown in Fig.6.2. A recirculation region is formed behind the sphere. The length of

the recirculation zone (L_s) is found to increase with Re and is compared in Fig.6.3. We also compare the drag coefficient (C_d) as shown in Table 6.2. The C_d is defined as,

$$C_d = \frac{8F_D}{\rho U_\infty \pi D^2}, \quad (6.34)$$

$$F_D = \int_{\Gamma} f_x^B d\Gamma, \quad (6.35)$$

where f_x^B is the X component of the boundary force on the sphere (from Eq.(6.22)). The numerical results from the present scheme agree very well with the published data.

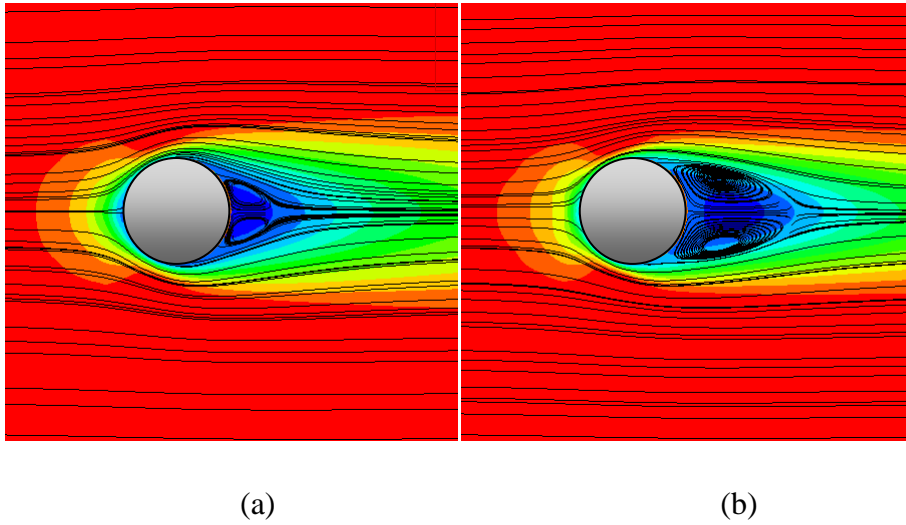


Fig.6.2 Streamlines and velocity contours for the steady axis-symmetric flow past the sphere on XY plane at (a) $Re = 50$, (b) $Re = 150$.

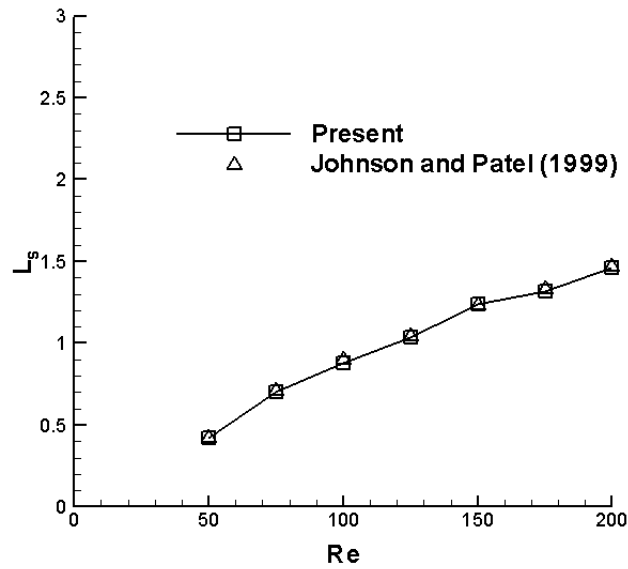


Fig.6.3 Recirculation region (L_s) behind the sphere at different Re .

In the previous section, we have mentioned that the number of sub-iteration/forcing (NF) to achieve the no-slip boundary condition is CC dependent and the NF values can be reduced by suitably selecting SRP. In Table 6.3, effects of CC and SRP selection on the NF and C_d are shown at $Re = 100$. It can be observed that NF requirement increases with decreasing CC value. Again, minimum NF is observed when SRP value lies between 0.6 – 0.8. So, it can be concluded that higher accuracy (i.e. lower CC and better C_d values) demands higher number of forcing (NF), and use of SRP can significantly reduce the overall computational time. In the rest of our simulations, CC is selected as 10^{-6} and SRP as 0.6.

Table 6.2 Comparison of drag coefficient (C_d) at $Re = 100, 200$.

Flow Case	Co-efficient of Drag C_d			
	Gilmanov, Sotiropoulos et al. (2003)	Wu and Shu (2010)	Johnson and Patel (1999)	Present
Re = 100	1.153	1.128	1.16	1.147
Re = 200	--	0.8	0.85	0.82

Table 6.3 Variation of number of forcing (NF) with CC and SRP at $Re = 100$.

SRP \ CC	10^{-4}		10^{-5}		10^{-6}	
	NF	C_d	NF	C_d	NF	C_d
0.2	25	1.152	29	1.149	34	1.146
0.4	23	1.151	28	1.148	32	1.147
0.6	16	1.152	21	1.148	26	1.147
0.8	17	1.153	22	1.148	28	1.147
1.0	21	1.154	25	1.149	31	1.147

We have also simulated the steady non-axisymmetric flow case by increasing Re to 250. The streamlines plotted in Fig.6.4 that clearly indicates the loss of symmetry in the XZ plane and the flow is no longer axisymmetric. Similar results are also observed in the literature (Gilmanov et al. (2003); Wu and Shu (2010)) and they are found to be in good agreement.

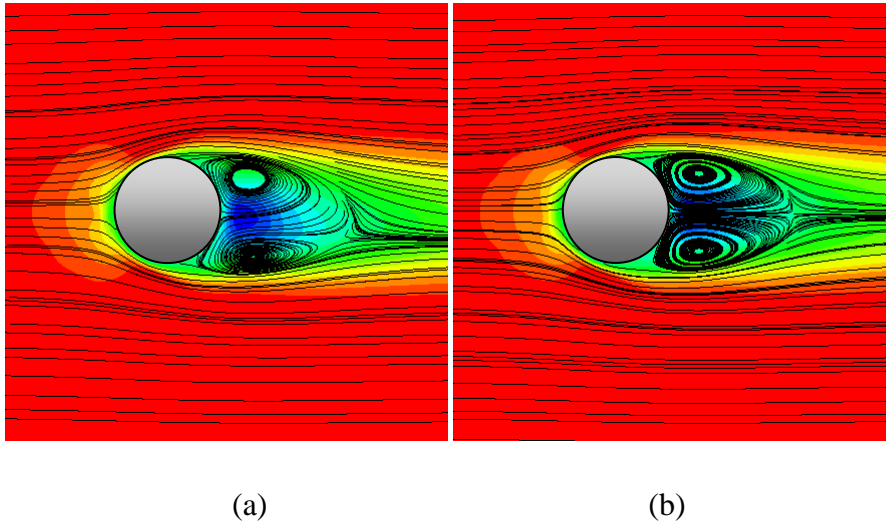


Fig.6.4 Streamlines and velocity contours for the steady non axis-symmetric flow past the sphere at $Re = 250$ on (a) XZ and (b) XY plane.

6.2.2 Single sphere sedimentation

Next, we have considered the settling of a sphere under the effects of gravity in a fluid filled rectangular box. The schematic of the problem is shown in Fig.6.5. This problem was experimentally studied by Ten Cate et al. (2002) for different fluid density ρ_f and viscosity μ_f as shown in Table 6.4. The falling sphere initially accelerates and later moves with a uniform/terminal velocity as the force (Weight, Drag and Buoyancy) balance condition is attained. The terminal Reynolds number (Re_T) of the falling sphere was derived from its terminal velocity U_T .

$$Re_T = \frac{\rho_f U_T d_p}{\mu_f}, \quad (6.36)$$

where $d_p = 15$ mm is the diameter of the sphere and its density is $\rho_b = 1120$ kg/m³.

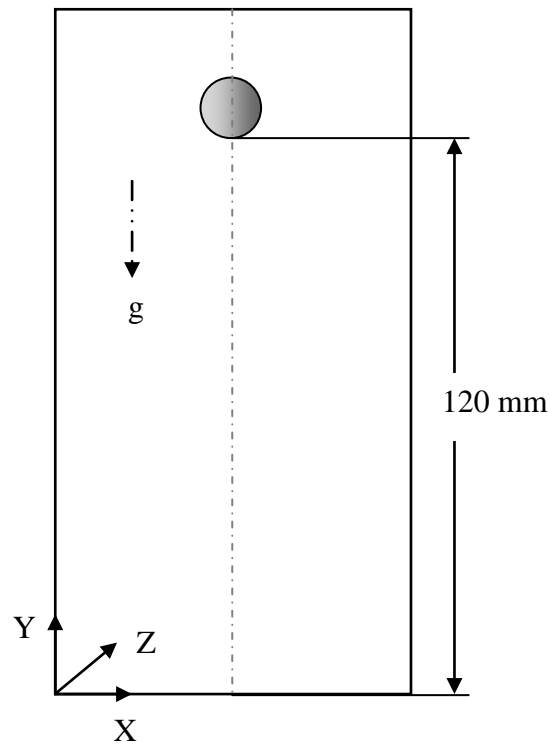


Fig.6.5 Schematic diagram of the computational domain ($100 \times 160 \times 100 \text{ mm}^3$) followed for the single sphere sedimentation.

In the present numerical simulation, we set the fluid and solid sphere parameters as those used by Ten Cate et al. (2002) in order to compare the accuracy/capabilities of the proposed flexible forcing scheme.

Table 6.4 Fluid properties used in the experiments by Ten Cate et al. (2002), and parameters used in the present simulations.

	Re_T	$\rho_f (\text{Kg/m}^3)$	$\mu_f (10^{-3} \text{Ns/m}^2)$	τ	$\Delta t (10^{-4} \text{s})$
Case E1	11.6	962	113	0.8	8.51
Case E2	32.2	960	58	0.65	8.28

Similar to the experimental set up, the size of the computational domain is chosen as $100 \times 160 \times 100 \text{ mm}^3$. We have performed grid independence study to ensure that the results are independent of the mesh resolutions as shown in Table 6.5. A sufficiently resolved uniform mesh of size $101 \times 161 \times 101$ is adopted for this study. The sphere was initially kept at rest at an initial height of 120 mm from the bottom of the box. The sphere starts falling under the effects of gravity, $g = 9.8 \text{ m}^2/\text{s}$. The force and torque acting on the moving sphere is calculated after the no-slip boundary condition is accurately satisfied. Here, it is worth noting that the use of proposed flexible forcing IB – LBM scheme alters the number of forcing/sub-iteration at each time step such that the exact no-slip condition on the moving sphere is satisfied. Also, the no-slip boundary conditions prescribed on the walls of the rectangular box are attained using bounce back scheme (Suzuki and Inamuro (2013)).

Table 6.5 Grid independence test of single sphere sedimentation at $Re_T = 11.6$.

Mesh size	U_T (m/s)	% Error = $\left \frac{U_T^{Newgrid} - U_T^{Oldgrid}}{U_T^{Oldgrid}} \right \times 100$
61×97×61	0.087	--
81×129×81	0.089	2.3
101×161×101	0.090	1.1
121×193×121	0.0902	0.2

We have compared the trajectory and vertical velocity evolution of the moving sphere at two distinct Re_T , i.e. 11.6 and 32.2. The results are plotted in Fig.6.6.

and found to be in excellent agreement with the experimental data of Ten Cate et al. (2002).

In addition, we have fabricated an apparatus to perform in-house experiments on single sphere sedimentation with Derlin spheres of different diameters. The details about the experimental setup will be discussed in the next chapter. The sphere is allowed to fall freely in a mixture of glycerine-water. The time evolution of sphere trajectories is shown in Fig.6.7. The parameters used in the experiments are provided in Table 6.6. A set up numerical simulations are also performed with parameters similar to the experimental conditions. A quantitative comparison of the terminal velocities obtained from the experiments and flexible forcing IB-LBM schemes are shown in Table 6.6, and they are in good agreement. This further implicates that the proposed IB – LBM scheme is capable of simulating unsteady, moving boundary problems.

Table 6.6 Parameters used in the present experimental studies along with the comparisons of data from experiments and flexible forcing IB-LBM scheme

(U_T is terminal velocity, Re_T is corresponding Reynolds number).

	Sphere diameter (m)	ρ_b (Kg/m ³)	ρ_f (Kg/m ³)	μ_f (10 ⁻³ Ns/m ²)	U_T (Exp) (m/s)	U_T (IB-LBM) (m/s)	Re_T (Exp)	Re_T (IB-LBM)
Case 1	0.0127	1350	1195	30.5	0.101	0.098	50.25	48.76
Case 2	0.0095	1350	1195	30.5	0.083	0.084	30.89	31.26
Case 3	0.0079	1350	1195	30.5	0.073	0.072	22.59	22.28
Case 4	0.0063	1350	1195	30.5	0.061	0.060	15.06	14.81

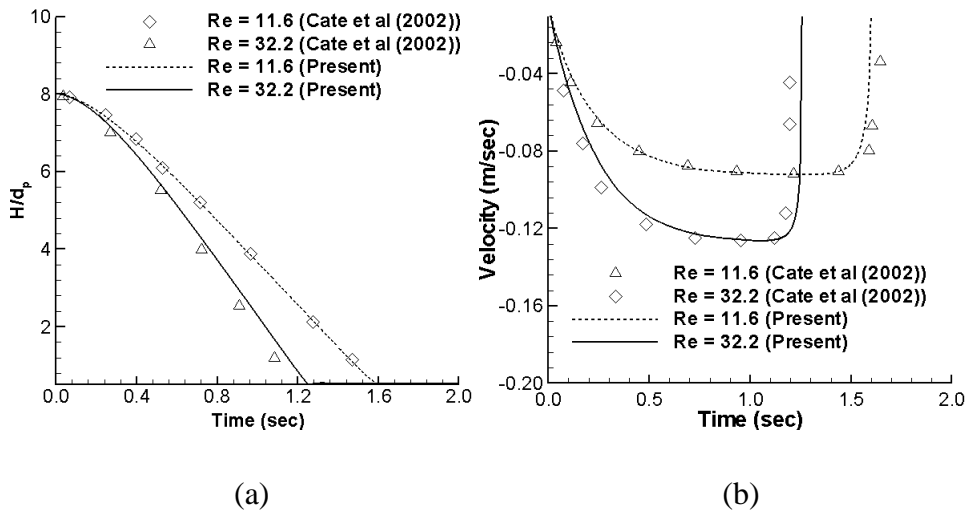


Fig.6.6 Comparison of the settling spheres' (a) trajectories and (b) vertical velocities at different terminal Re , where H is the instantaneous vertical sphere centre height and d_p is the diameter of sphere.

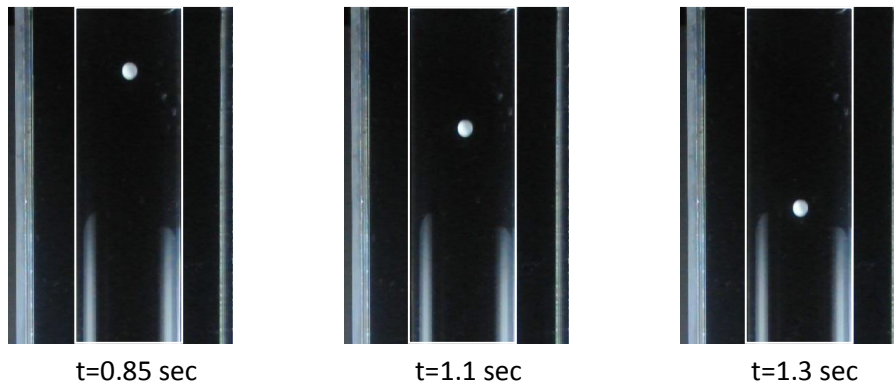


Fig.6.7 Experiment performed on single sphere sedimentation in glycerine-water mixture with the Derlin sphere of diameter, 12.7 mm and $Re_T = 50.25$.

The instantaneous positions of falling sphere are shown.

6.2.3 Two sphere sedimentation

Finally, we have considered the sedimentation of two spheres of same size and density in a fluid filled rectangular box. This is a classical fluid-solid interaction problem that involves a unique DKT (Fortes et al. (1987); Qi (1999)) phenomenon. When two inline spherical particles are allowed to fall freely; the leading sphere leaves a wake behind and the trailing sphere gets trap in the wake. The trailing one accelerated in the wake/low pressure region (otherwise known as Drafting) and touches the leading sphere (otherwise known as Kissing). This long body formation by two kissing spheres (with long axis parallel to the streamlines of the flow) is an unstable equilibrium situation. With inception of slight angular displacement, a destabilising couple is created that breaks the unstable equilibrium state and brings the sphere to a stable cross stream configuration (otherwise known as Tumbling). The tumbling mechanism is basically the cross stream rearrangement of the sphere centres, which is again similar to the settling of a long body in a Newtonian fluid, where its broad side becomes perpendicular to the stream in action of a turning couple. The generation of turning couple for the long body is related to the pressure distribution, stagnation and separation points (Hu et al. (1992)).

From the literature, we found that the experiments on the two sphere sedimentation were only done by Fortes et al. (1987). To further check the validity of their findings we have also conducted in-house experiments and studied the DKT phenomenon for two same diameter Derlin spheres, settling in the glycerine-water mixture. The sphere and fluid parameters are tabulated

in Table 6.6. We observed that irrespective of the change in diameters (that alters the Re_T), the spheres undergo DKT phenomenon. In Fig.6.8, visualisation of the trajectory of the spheres while exhibiting DKT is shown. Also, a set of numerical simulations are performed to check the capabilities of the proposed IB – LBM scheme with parameters similar to those in the experiments. In Fig.6.9, the numerical simulation results are shown that qualitatively match our experimental visualisation.

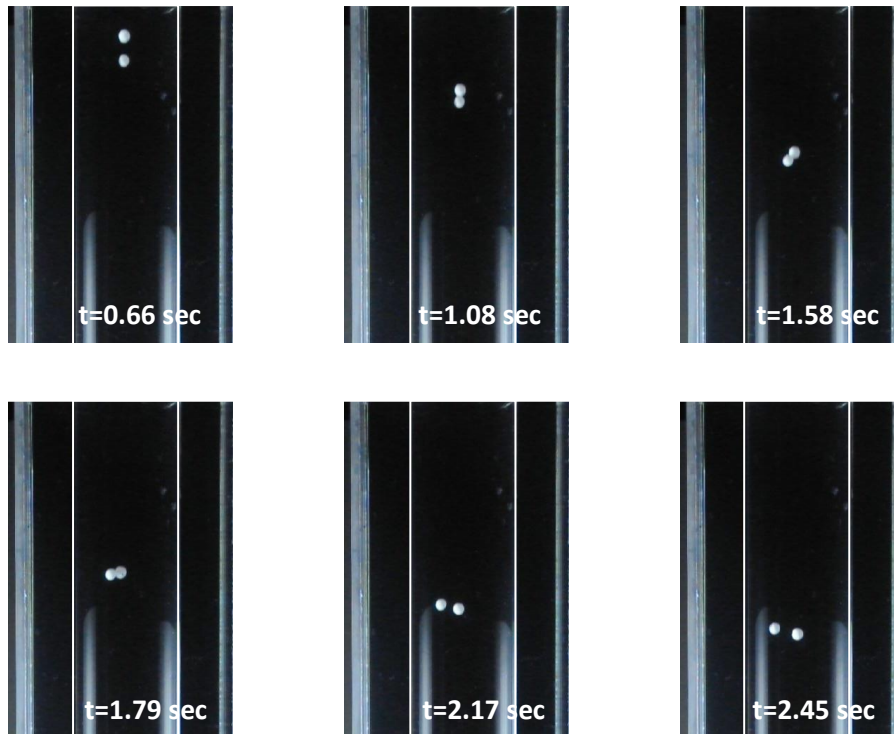
Table 6.7 Grid independence test for two equal spheres sedimentation case, by comparing the terminal velocity when only one sphere is released in the computational domain.

Mesh size	U_T (m/s)	% Error = $\left \frac{U_T^{Newgrid} - U_T^{Oldgrid}}{U_T^{Oldgrid}} \right \times 100$
63×252×63	0.0498	--
81×324×81	0.0511	2.6
90×360×90	0.0521	1.9
99×396×99	0.0524	0.5

To make quantitative comparison, the computational domain and other parameters are set from the previous simulation study by Glowinski et al. (2001). The computational domain shown in Fig.6.10 is selected as, $10 \times 40 \times 10$ mm³. Two spheres of same size 1.67 mm, are initially positioned at (5.0, 35.0, 5.0) (sphere-1 or trailing sphere) and (5.0, 31.6, 5.0) (sphere-2 or leading sphere). The initial translational and angular velocity of the sphere and fluid are set to zero. The numerical simulations are performed for density ratio of

solid sphere to fluid as $\rho_b/\rho_f = 1.14/1.0$ and the kinematic viscosity set as, $\nu = 0.01 \text{ cm}^2/\text{s}$. After conducting the mesh independence test as shown in Table 6.7, a uniform Cartesian mesh of size $90 \times 360 \times 90$ is adopted for the Eulerian domain. Lagrangian spheres surface is discretised with 303 triangular boundary elements. The comparisons are made for temporal evolution of X, Y, Z centre coordinates and the vertical velocity of the spheres with that of Glowinski et al. (2001). The results obtained from the present scheme are found to be in excellent agreement and shown in Fig.6.11.

The above set of simulations verify the capabilities of the proposed numerical scheme that can suitably capture the flow physics of complex three dimension fluid-solid interactions.



(Continued.....)

Fig.6.8 Experiments performed on two spheres sedimentation in glycerine-water mixture with the Derlin spheres of same diameter, 9.5 mm. The instantaneous positions of the falling spheres are shown while they exhibits Drafting – Kissing – Tumbling (DKT) phenomenon.

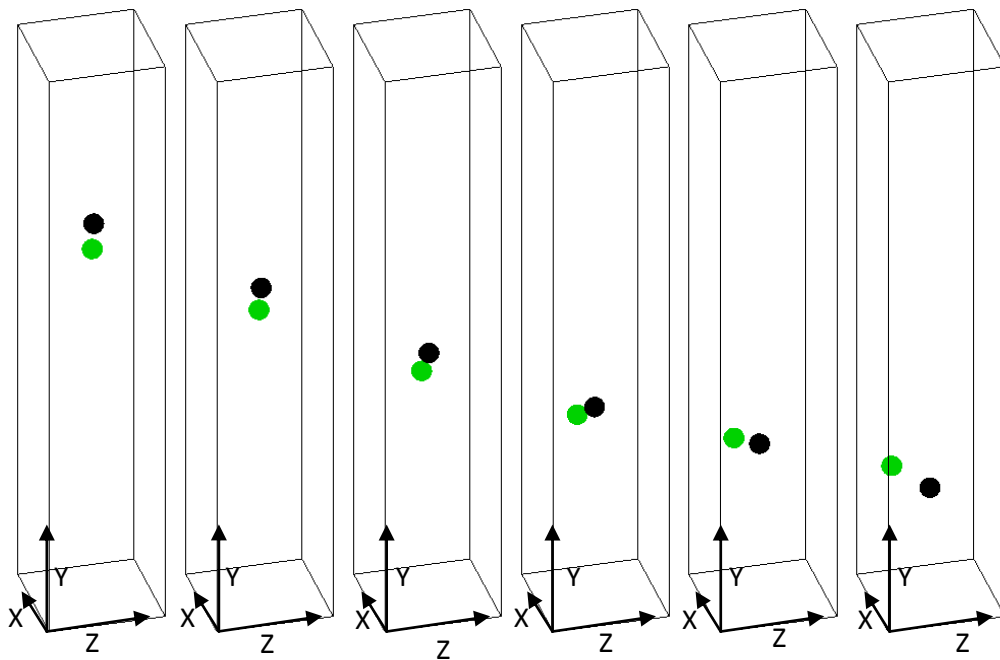


Fig.6.9 Instantaneous positions of the spheres undergoing Drafting – Kissing – Tumbling (DKT) phenomenon as obtained from flexible forcing IB – LBM simulation.

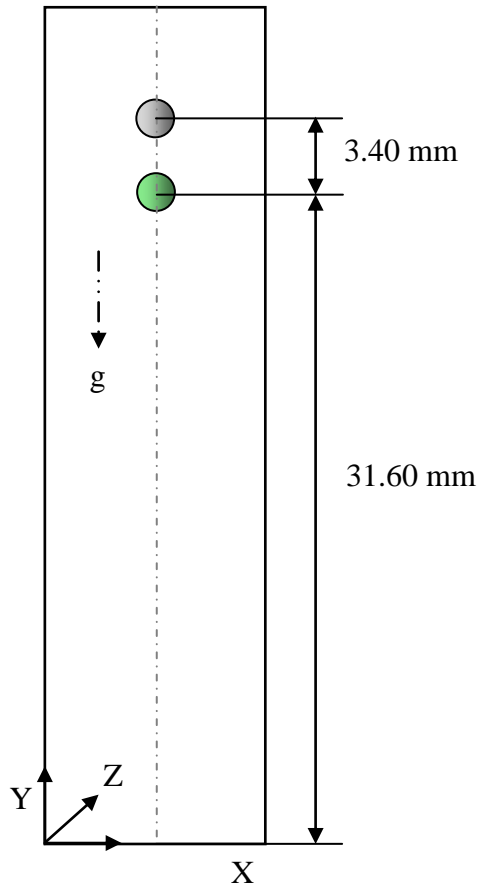
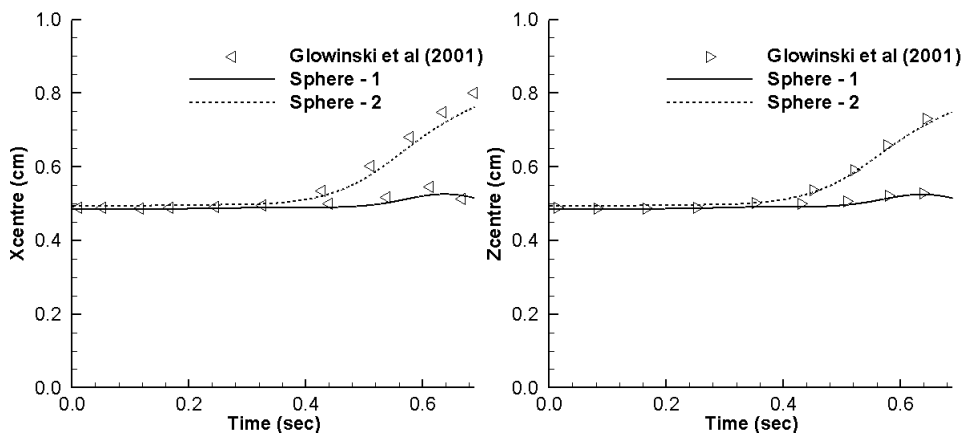


Fig.6.10 Schematic diagram of the computational domain ($10 \times 40 \times 10 \text{ mm}^3$)

followed for the two sphere sedimentation mechanisms.



(a)

(b)

(Continued...)

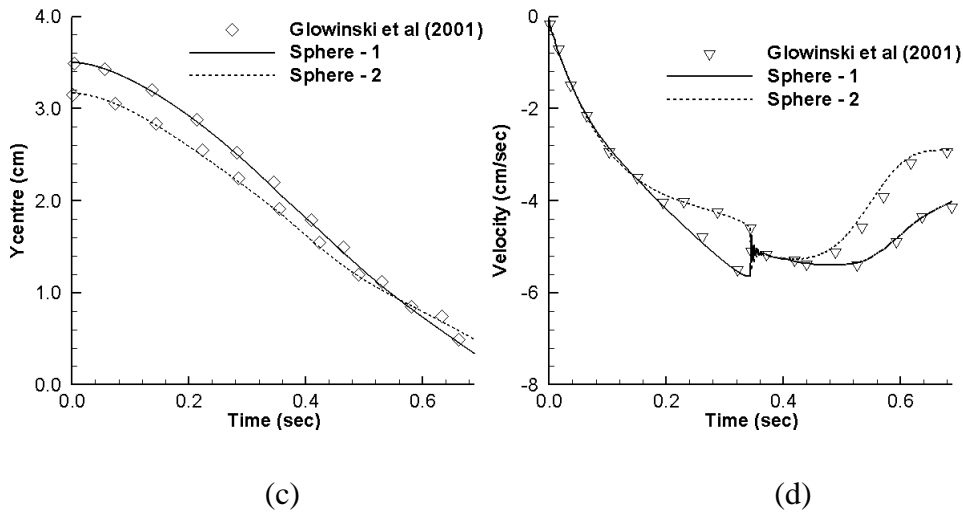


Fig.6.11 Comparison of the two settling spheres trajectories along (a) X, (b) Z and (c) Y directions as well as their (d) vertical velocities.

6.3 Concluding remarks

In this chapter, we have discussed a flexible forcing IB – LBM scheme to simulate three dimensional flow problems. Following an implicit type forcing term calculation, a single Lagrangian velocity correction term is introduced to satisfy the boundary condition within a convergence limit. The proposed flexible forcing concept not only avoids the complex mathematics involved in the matrix inversion, but also satisfy the boundary condition consistently at every time step with same order of convergence. This formulation is particularly advantageous for unsteady and moving boundary flow problems. Additionally, the algorithm proposed here is simple for computational code development.

The proposed algorithm is validated against a number benchmark three dimensional flows such as, flow past a stationary sphere, settling of a single

sphere and DKT phenomenon of two sphere sedimentation. The obtained results from flexible forcing IB-LBM scheme are in excellent agreement with literatures and with our in-house experimental data.

Chapter 7

Two Sphere Sedimentation Dynamics in a Viscous Liquid Column⁶

In this chapter results of three-dimensional numerical simulation and limited experimental study on the sedimentation of two inline spheres in a Newtonian fluid at a Reynolds number (Re) range of 10 to 60 are presented. Experiments were conducted in a vertical tank containing glycerine-water mixture of a predetermined viscosity and numerical study was carried out using the proposed 3D flexible forcing immersed boundary – lattice Boltzmann numerical scheme. This study is motivated by the earlier experiment of Fortes, Joseph et al. (1987), which shows that two settling spheres uniquely experience a non-linear wake interaction that captures the trailing sphere in the low pressure wake of the leading one and accelerates its motion to form a pair of kissing spheres. The spheres subsequently tumble before splitting and travel with the same velocity. The present study aims to take the investigation

⁶ Part of this work has been published as:

Dash SM, Lee TS, Lim TT and Huang H. (2014). "A flexible forcing three dimensional IB-LBM scheme for flow past stationary and moving sphere." *Computers and Fluids* **95**(0): 159-170
Dash SM, Lim TT and Lee TS. (2014). "Two spheres sedimentation dynamics in a viscous liquid column." *Physics of Fluids*: (Under Review)

further and examine the influence of hydrodynamic forces and induced turning couples acting on the settling spheres during the process of Drafting – Kissing – Tumbling (henceforth refer to as DKT). Our numerical results indicate that the tumbling mechanism is influenced by the turning couple, which together with repulsive hydrodynamic forces causes vertical and lateral migrations of the spheres until they acquire a steady state alignment. The sense of the turning couple dictates whether the spheres would exhibit normal or inverse tumbling mechanism. Our result further show that normalised trajectories, velocity and the hydrodynamics force coefficients of the falling spheres are independent of the Reynolds number, at least for the range of values considered here.

In the following, at first we have presented the experimental setup utilised in this research work. Subsequently, we have shown validation of the solver by performing a set of experiments. The details of the numerical model won't be discussed here as those are reported in Chapter 6. Lastly, results and discussions are outlined at the end of the chapter.

7.1 Experimental setup and Procedure

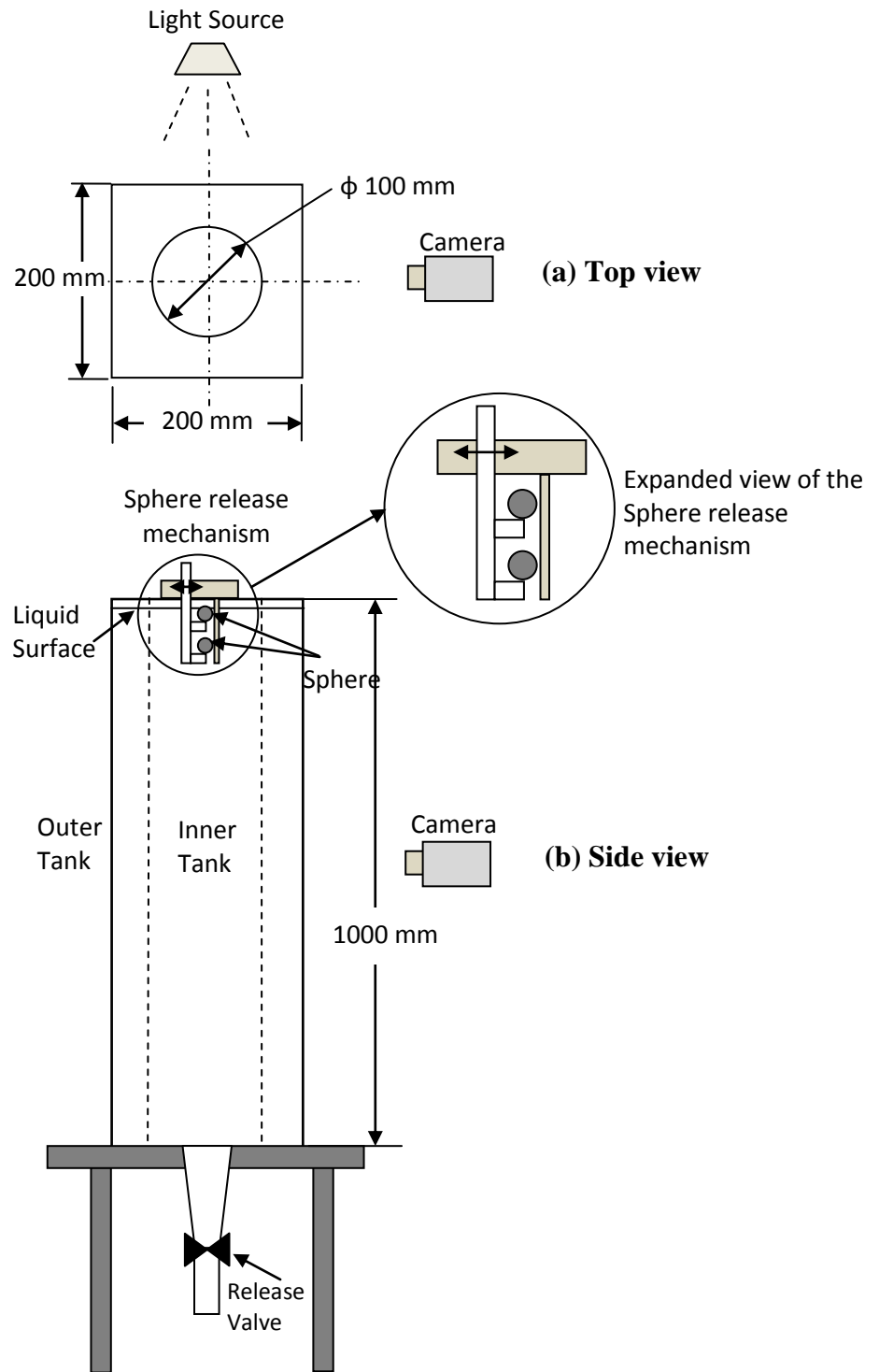
The experiments were conducted in a vertical plexi-glass cylindrical tank with dimensions 100 mm (diameter) \times 1000 mm (high). The cylindrical tank is surrounded by a rectangular tank of the same height but with the cross-section of 200 mm \times 200 mm (see schematic drawing of the setup in Fig.7.1). The outer rectangular tank is filled with water while the inner cylindrical tank contains the working fluid which is a homogenous mixture of glycerine and

water with predetermined density (ρ_f) 1195 kg/m³ and dynamic viscosity (μ_f) 0.0305 Ns/m². The purpose of the rectangular is to prevent distortion of the captured flow images due to the curvature of the cylinder. The fluid density was determined using specific gravity bottle and the viscosity was measured using *HAAKE MARS* rheometer with the measurement uncertainties estimated to be of less than $\pm 0.1\%$.

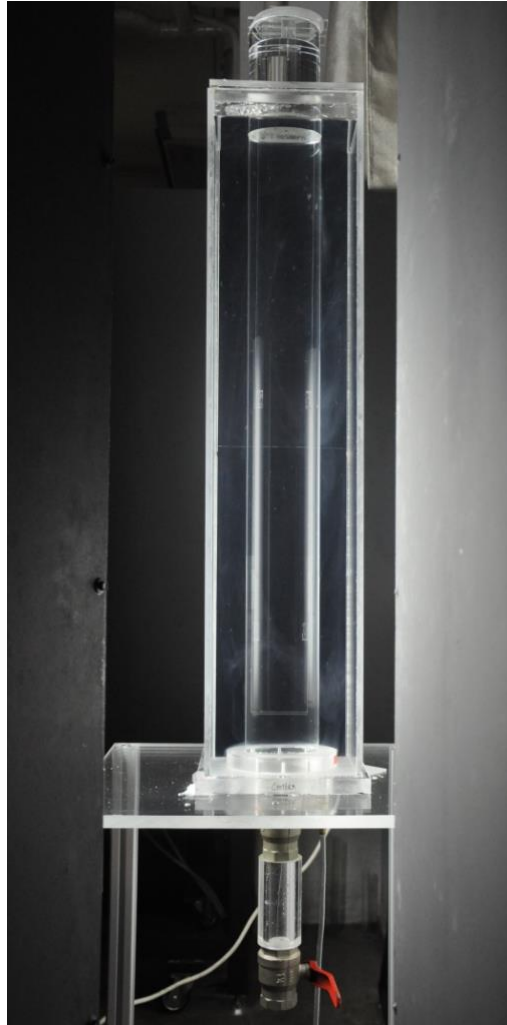
The settling spheres used in the present study were precision Delrin bearing balls of constant density ρ_b . Table 7.1 shows the diameter of the four different sized spheres along with other physical parameters used in the present experiments. Mounted on the top of the tank is a release mechanism that allows the sphere to be released into the centre of the tank. The mechanism is designed such as it allows multiple spheres to be held on top of each other with predefined centre distances. Here, we focus on a single and two spheres sedimentation only.

The sphere(s), upon released from the mechanism, travelled vertically in the working fluid and their visual images were captured (in video mode) using a Nikon D90 at framing rate of 48 fps for subsequent analysis. The sphere was illuminated using a diffused fluorescent light source located perpendicular to camera lens axis. Each experimental condition was repeated 20 times to check for repeatability of the results. A release valve located at the bottom of the tank was used to remove the settled spheres from the tank (see Fig.7.1(b)). In all cases, the cross-section of the tank is significantly larger than the diameter of the sphere such that the wall effects are negligible. A MATLAB code was written for image processing and to analyse the trajectories, sedimentation

speeds and steady state alignment of the spheres. The experimental results are used to further validate the solver.



(Continued...)



(c) Real time image



(d) Releasing mechanism

Fig.7.1. Schematic drawing of the experimental setup (a) Top view, (b) Side view, (c) Real time image of the setup and (d) releasing mechanism.

Table 7.1 Parameters used in the present experiments (U_T is terminal velocity,

$Re_T = \rho_f U_T d_p / \mu_f$ is the corresponding Reynolds number).

	d_p (m)	ρ_b (Kg/m ³)	ρ_f (Kg/m ³)	μ_f (x10 ⁻³) Ns/m ²)	U_T (Exp) (m/s)	Re_T (Exp)
Case 1	0.0127	1350	1195	30.5	0.101	50.25
Case 2	0.0095	1350	1195	30.5	0.083	30.89
Case 3	0.0079	1350	1195	30.5	0.073	22.59
Case 4	0.0063	1350	1195	30.5	0.061	15.06

7.2 Validation of the numerical solver

The numerical model is validated using the present experimental results of the single sphere. The selected computational domain size is $7.8d_p$ (wide; W) \times $7.8d_p$ (depth; D) \times $17.8d_p$ (height; H) that suitably mimics the experimental apparatus with negligible wall effects. A comparison study is made to determine the wall effect on the terminal velocity of the settling sphere and the results are presented in Fig.7.2. Here, the aspect ratio along the horizontal axis is defined as ratio of the cross section of the tank and the diameter of sphere. The results show that as long as the aspect ratio is greater than 7.0, the variation of the terminal velocity is negligible suggesting that the wall effect in the present setup is also negligible.

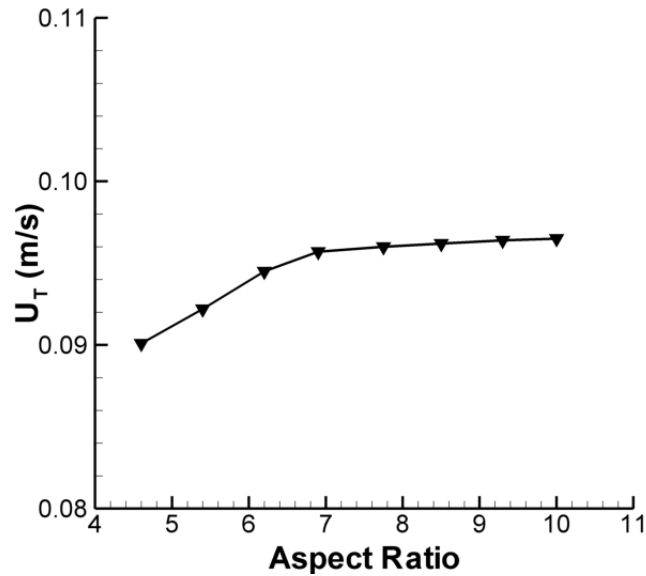


Fig.7.2. Wall effects study by comparing the terminal velocity of the sphere ($d_p = 12.7$ mm) with respect to varied aspect ratio (i.e. cross section width or depth of the computational domain to diameter of the sphere) of the fixed height computational domain.

The diameter d_p of the sphere and the physical properties of the fluid are selected from Table 7.1 and adopted in the numerical simulation. The computational domain is discretized with uniform physical mesh size of 1 mm along the three Cartesian coordinate directions after the grid independence check has been performed. The physical simulation time step is fixed as 0.00065 sec. When the proposed flexible forcing IB – LBM solver was used, the physical mesh size and time step are converted to lattice scales (Feng and Michaelides (2005)).

As the initial condition, the centre of the sphere was kept at $(3.9d_p, 3.9d_p, 16.15d_p)$ and the no-slip boundary condition was prescribed on the surface of the moving sphere by flexible forcing IB – LBM. The no-slip boundary conditions on the walls of the rectangular tank were satisfied using bounce

back rules of the lattice velocities (Wu and Shu (2010)). The initial flow field was kept stationary with zero Cartesian velocity components.

The sphere starts falling through the fluid due to gravity until it reaches the tank base. In all cases (i.e. $10 < \text{Re}_{\text{max}} < 60$) the sphere travelled along the vertical centreline of the tank as shown in Fig.7.3. Here, Re is defined as,

$$\text{Re} = \frac{\rho_f U d_p}{\mu_f}. \quad (7.1)$$

where U is the settling velocity of the sphere. Previous study by Jenny, Bouchet et al. (2003) has shown that for the Galileo number less than 156, the sphere fall or ascend in the Newtonian fluid along a straight vertical path due to the existence of an axisymmetric wake behind the sphere. The Galileo number G for our present experiments is defined as,

$$G = \frac{\sqrt{\left| \frac{\rho_b}{\rho_f} - 1 \right| g d_p^3}}{\nu}. \quad (7.2)$$

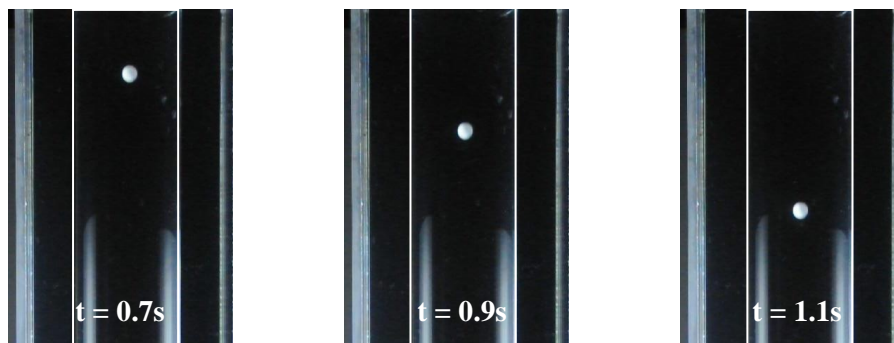


Fig.7.3. Experiments on single sphere sedimentation ($d_p = 12.7$ mm).

The maximum Galileo number encountered in the present study is 57, which is well below the critical Galileo number of 156. This is consistent with our experimental observation of a straight vertical trajectory of the sphere.

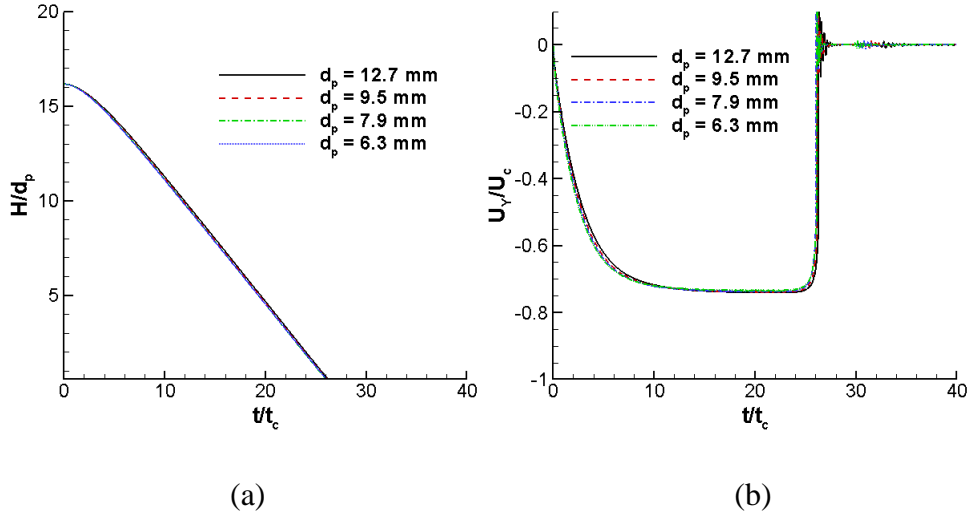


Fig.7.4. Single sphere sedimentation using flexible forcing IB – LBM for different diameters where (a) non-dimensional vertical centre trajectory and (b) non-dimensional vertical centre velocity of the spheres.

Before embarking on the simulation of two-sphere sedimentation, the numerical solver is first validated against the experimental results of single sphere sedimentation. Fig.7.4(a) shows the numerical results of the vertical centre trajectory of the spheres as a function of time for different sphere diameters and Fig.7.4(b) shows their corresponding vertical centre velocity. Note that time on the horizontal axis is normalised by t_c and settling velocity of the sphere is normalised by U_c ; they are defined as,

$$t_c = \sqrt{d_p / [|\rho_b / \rho_f - 1| g]} \quad , \quad U_c = \sqrt{|\rho_b / \rho_f - 1| g d_p} \quad (7.3)$$

where $a_c = \left| \rho_b / \rho_f - 1 \right| g$ within the square root is the characteristic acceleration after taking into consideration of the buoyancy effect.

The results clearly show that regardless of the spheres diameter, the normalised vertical trajectories of all the sphere collapse on a single curve. The same applies to the normalised settling velocity. It is obvious from Fig.7.4(b) that the sphere initially accelerated (only the magnitude is shown and the negative sign is due to sign convention) before settling to a steady/terminal velocity U_T .

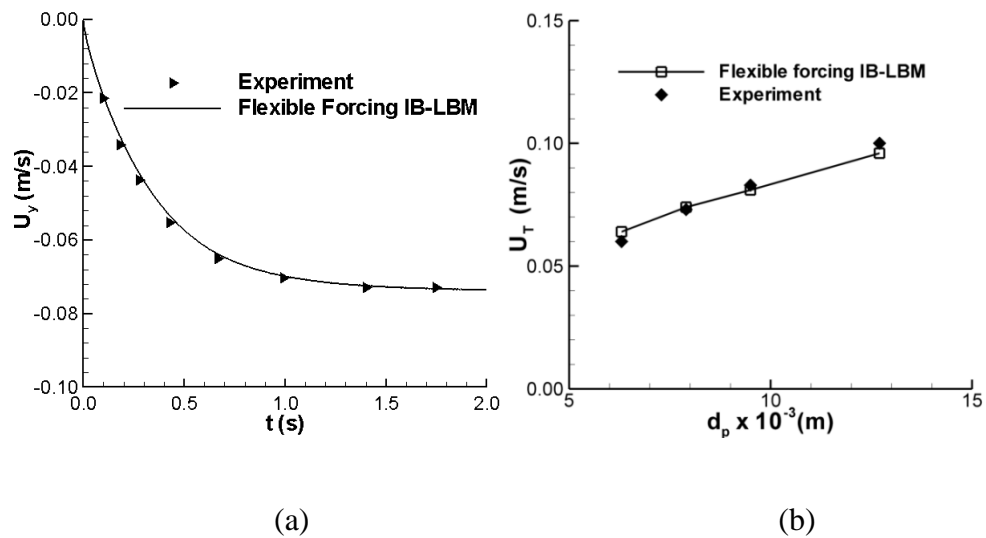


Fig.7.5. Comparisons of (a) instantaneous vertical settling velocity and (b) terminal velocity U_T as obtained from Experiments and IB – LBM observations.

To validate the numerical solver, computed terminal velocities U_T of the spheres are compared to the corresponding experimental results. Fig 7.5 clearly shows the numerical results are in good agreement with the experiment thus validating the accuracy of the numerical solver. It is worth noting that U_T

is determined experimentally using the MATLAB image processing code, where the uncertainty error in the measurement is ± 1 pixel.

Here, the conversion of the physical quantities to lattice scale has been followed from Feng et al (2005). In the followings an example of such conversion is shown,

$$\text{Lattice velocity } u^* = u \frac{\Delta t}{\Delta x}$$

$$\text{Lattice viscosity } \nu^* = \nu \cdot \frac{\Delta t}{\Delta x^2}$$

$$\text{Lattice gravity } g^* = g \cdot \frac{\Delta t^2}{\Delta x}$$

where u , ν , g , Δx and Δt are in respective physical units. For the physical mesh size of 1 mm, we have set time step size 0.00065 sec. The kinematic viscosity of the glycerine/water mixture used in the present study is $30.5 \times 10^{-3} / 1195 = 2.552 \times 10^{-5} \text{ m}^2/\text{s}$. Hence, $\Delta x = 0.001$, $\Delta t = 0.00065$, $\nu_r = 2.552 \times 10^{-5}$.

Using the scaling by Feng et al (2005), we can compute lattice scale viscosity and the corresponding relaxation time as,

$$\nu = \frac{(\Delta t \cdot \nu_r)}{(\Delta x)^2} = 0.01658, \quad \tau = \frac{6\nu + 1}{2} = 0.5497$$

7.3 Results and Discussions

The primary objective of the present research is to address the two questions raised in the introduction section regarding sedimentation phenomenon of the

two inline spheres. In the following, we first discuss the problem setup in experiment and in computation, followed by detail analyses of the results.

7.3.1 Problem setup descriptions

7.3.1.1 Experiment

The experimental studies were conducted using the same vertical tank discussed above (see Fig.7.1). Two spheres of identical weights and diameters d_p were initially placed in the release mechanism with their centres $2d_p$ apart. The uncertainties in the diameters and the weights of the settling spheres are $\pm 0.01\text{mm}$ and $\pm 0.01\text{gm}$, respectively. The spheres were released at the centre of the tank inside the working liquid column, and their motions were captured by Nikon D90 camera operating in video mode at 48 fps with the resolution of 720×1080 pixels. The captured images were subsequently analysed using MATLAB image processing code to determine the trajectories of the spheres, where the uncertainty in measurement is ± 1 pixel. In total, four different sized spheres with same centre spacing ($2d_p$). The working parameters can be referred from Table 7.1.

7.3.1.2 Numerical simulation

Here, a long enough computational domain is selected such that the drafting – kissing – tumbling actions of the two settling spheres are suitably captured. With reference to Fig.7.2, the computational domain size is fixed to $7.8d_p$ (wide; W) $\times 7.8d_p$ (depth; D) $\times 40d_p$ (height; H) such that the wall effects are negligible.

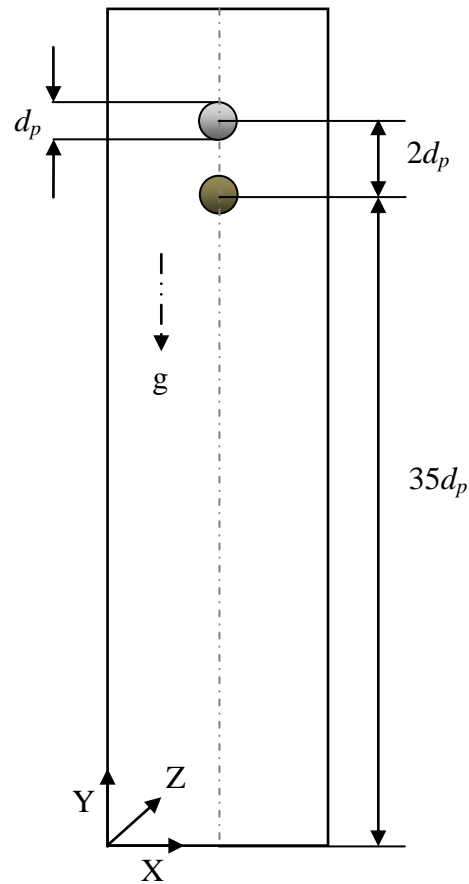


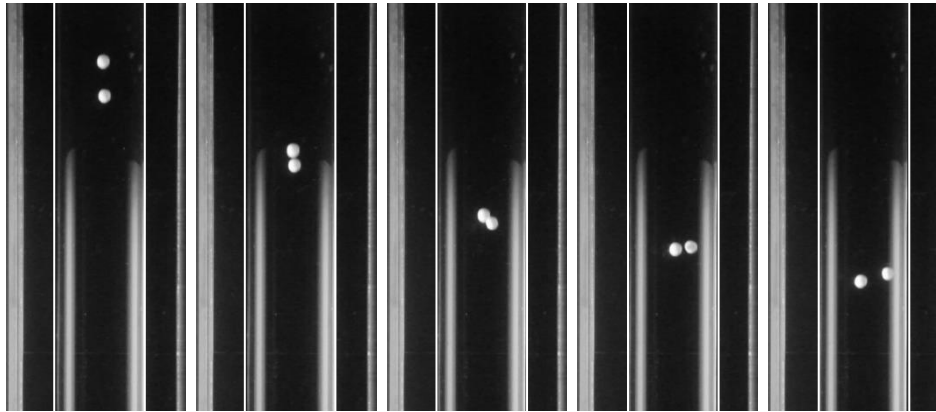
Fig.7.6. Two sphere sedimentation with their initial spacing $2d_p$. The box dimension is $(X, Z, Y) = (7.8d_p, 7.8d_p, 40d_p)$.

Similar to the experimental condition, the spheres are initially aligned along the vertical direction with their centre spacing $2d_p$ (ref. Fig.7.6). The initial sphere centre co-ordinates are respectively: (leading sphere) sphere-1 $(3.9d_p, 3.9d_p, 35d_p)$, (trailing sphere) sphere-2 $(3.9d_p, 3.9d_p, 37d_p)$. The computational mesh and time step size is followed the same as in section.7.2. The sphere surface is discretised with uniform triangular boundary elements where the number of elements varies between 591 – 1161, with respect to diameter of the spheres. At the beginning, the flow field and sphere velocities were initialised to zero along all Cartesian directions. The spheres start to move with gravity and its kinematics is calculated using the description provided in Chapter 6

(ref. section 6.1.1). The no-slip boundary conditions are prescribed on the walls of the computational domain with bounce back scheme (Wu and Shu (2010)) and on the moving sphere surface using flexible forcing IB – LBM. OPENMP principles are adhered to write the parallel computational code so as to perform faster computation.

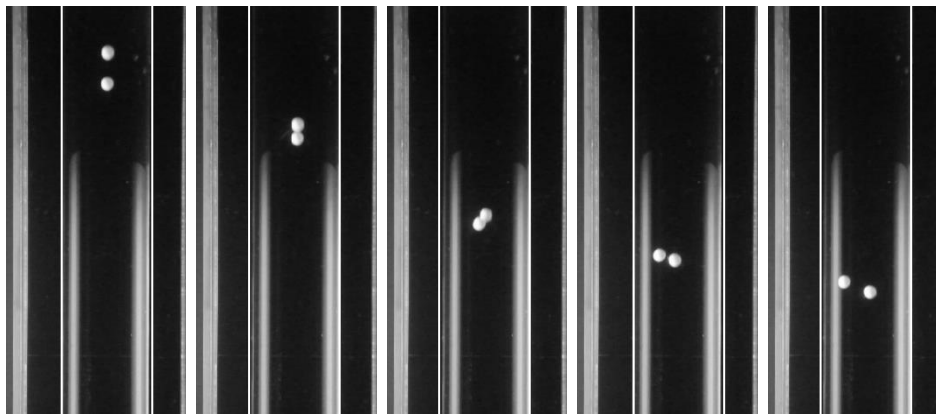
7.3.2 DKT and Inverse DKT

When two inline spheres were allowed to settle freely, the leading sphere leaves behind a low pressure wake. If the initial gap between the leading and trailing spheres is small enough ($<6d_p$) (Fortes et al. (1987)) the trailing sphere becomes trapped in the wake regime, and both the spheres subsequently display a unique DKT mechanism as discussed previously (see Chapter 1). The visualisation of this phenomenon from our own experiments is shown in Fig.7.7 where kissing spheres may experience either *tumbling* or *inverse tumbling* so as to break the unstable equilibrium state. As suggested by Joseph et al. (1992), the settling long-body always tries to put its broadside perpendicular to the oncoming stream to attain a stable configuration. The direction of rotation is determined by the sense of turning couple. In the same manner, the tumbling action of the kissing spheres depends on the sense of the destabilizing couple. Detailed discussion of the destabilizing couple will be presented in the next section.



t = 0.000 s t = 0.325 s t = 0.960 s t = 1.250 s t = 1.500 s

(a)



t = 0.000 s t = 0.325 s t = 0.960 s t = 1.250 s t = 1.500 s

(b)

Fig.7.7. Experimental visualization of two sphere sedimentation with (a) Drafting-Kissing-Tumbling and (b) Drafting – Kissing – Inverse Tumbling mechanism. ($d_p = 12.7$ mm)

In order to capture DKT and Inverse DKT (Drafting – Kissing – Inverse Tumbling) mechanism of the spheres in the present numerical simulations, we introduced a small spatial perturbation as a function of the rotational sense of the destabilizing couple. The centres of the two spheres were initially offset slightly from the vertical mid-plane of the computational domain such that the

direction of the offset will change the direction of moment arm and hence the rotational sense of the destabilizing couple. Thus, the initial offset centre coordinates are, (leading sphere) sphere-1 ($3.9d_p + \Delta x$, $3.9d_p + \Delta z$, $35d_p$), (trailing sphere) sphere-2 ($3.9d_p$, $3.9d_p$, $37d_p$) and sphere-1 ($3.9d_p - \Delta x$, $3.9d_p - \Delta z$, $35d_p$), sphere-2 ($3.9d_p$, $3.9d_p$, $37d_p$), respectively for DKT and Inverse DKT.

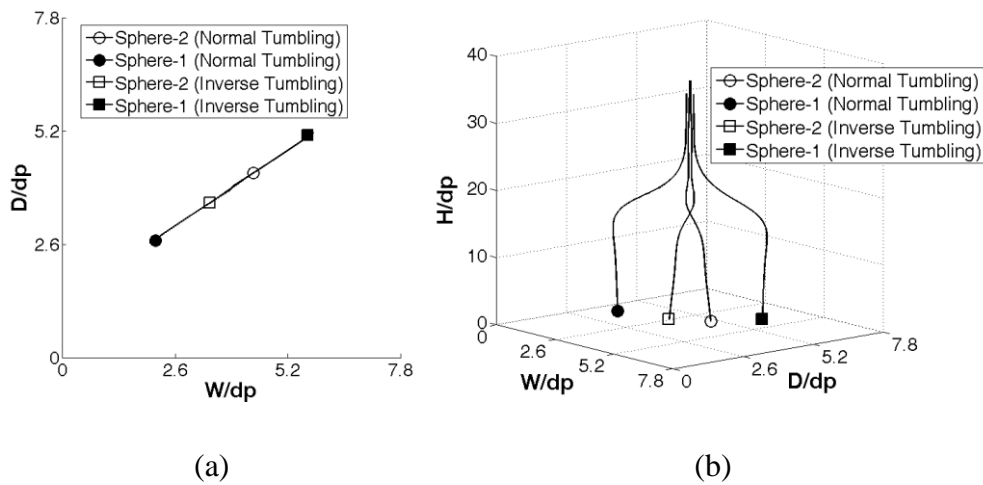


Fig.7.8. Numerical simulations on two sphere sedimentation using IB – LBM showing DKT and Inverse DKT. ($d_p = 12.7$ mm) where (a) Top view, (b) Front view of the 3D trajectory.

This technique has been formerly implemented (Uhlmann (2005) and Wang et al. (2008)) to study symmetry breakdown of two colliding particles. The selection of the offset distance also affects the time require to breakdown the equilibrium. Since we are focused only on the qualitative results for DKT and Inverse DKT, only one offset distance is used and equal to one mesh spacing along X and Z direction, i.e. Δx and Δz from the vertical centre plane.

Fig.7.8 shows the computed results of the sphere centre trajectories during DKT and Inverse DKT, and the results are in good agreement with the

experiments. Due to initial symmetric offsetting of the sphere centres along the vertical centre plane, the trajectories for DKT are the mirror image of Inverse DKT.

7.3.3 Forces acting on the settling spheres

The DKT mechanisms of two settling spheres were initially reported as wake induced anisotropy by Joseph et al. (1992), where they attributed the tumbling action as a competition between inertia and normal stress. The formation of the wake and boundary layer separation is a complex function of fluid viscosity and shear stress components, and to the date is still not fully understood. Although various attempts have been made to provide possible explanation on tumbling of the spheres, there were limitations in these studies (ref. Chapter 1) and much of the hydrodynamic forces during the interaction remain unclear.

In this research we adopt a convenient approach based on Newtonian dynamics to study the forces acting on the moving spheres. Following Newton's laws of motion, the state of the moving spheres and their interactions can be governed by determining the active hydrodynamic forces on them. The present numerical scheme using IBM has advantages in direct determination of the hydrodynamic force and torque exerted on the moving spheres. In Eq.(6.22), the force density term represents the hydrodynamic force exerted on the fluid by the moving sphere (Wu and Shu (2010)), and by applying Newton's third law of motion the reaction force acting on the moving sphere can be derived. Hence, the Cartesian force components on the moving

spheres are: F_X , F_Y , F_Z along X, Y and Z directions respectively. These forces are normalised with $1/2 \rho U_c^2 S$ as shown in Eq.(7.4),

$$C_{dX} = \frac{8F_X}{\pi\rho_f d_p^2 U_c^2}, \quad C_{dY} = \frac{8F_Y}{\pi\rho_f d_p^2 U_c^2}, \quad C_{dZ} = \frac{8F_Z}{\pi\rho_f d_p^2 U_c^2}, \quad (7.4)$$

where U_c is the characteristic velocity and S is the projected surface area of the sphere along the respective planes. In Fig.7.9, the non-dimensional hydrodynamic force coefficients (C_{dX} , C_{dY} and C_{dZ}) on the two settling spheres are plotted as a function of non-dimensional time. Outside the time-interval of $11.0 < t/t_c < 19.0$ where kissing and tumbling occur, the C_{dX} and C_{dZ} are zero and C_{dY} has negative value because of sign convention. This obviously suggests that the spheres experience only vertical downward force without X or Z direction force components. Thus, the spheres are restricted to move along Y direction only outside the time-interval indicated above. The C_{dY} plot in Fig. 7.10 indicates that while the trailing sphere (Sphere-2) drafts towards the leading sphere (Sphere-1), the vertical force on the sphere-2 increases in the low pressure wake regime, causing sphere-2 to accelerate towards sphere-1. Then after, the spheres momentarily kiss and tumble away according to the force profiles C_{dX} , C_{dY} and C_{dZ} as shown in the non-dimensional time region $11.0 < t/t_c < 19.0$, in Fig.7.9.

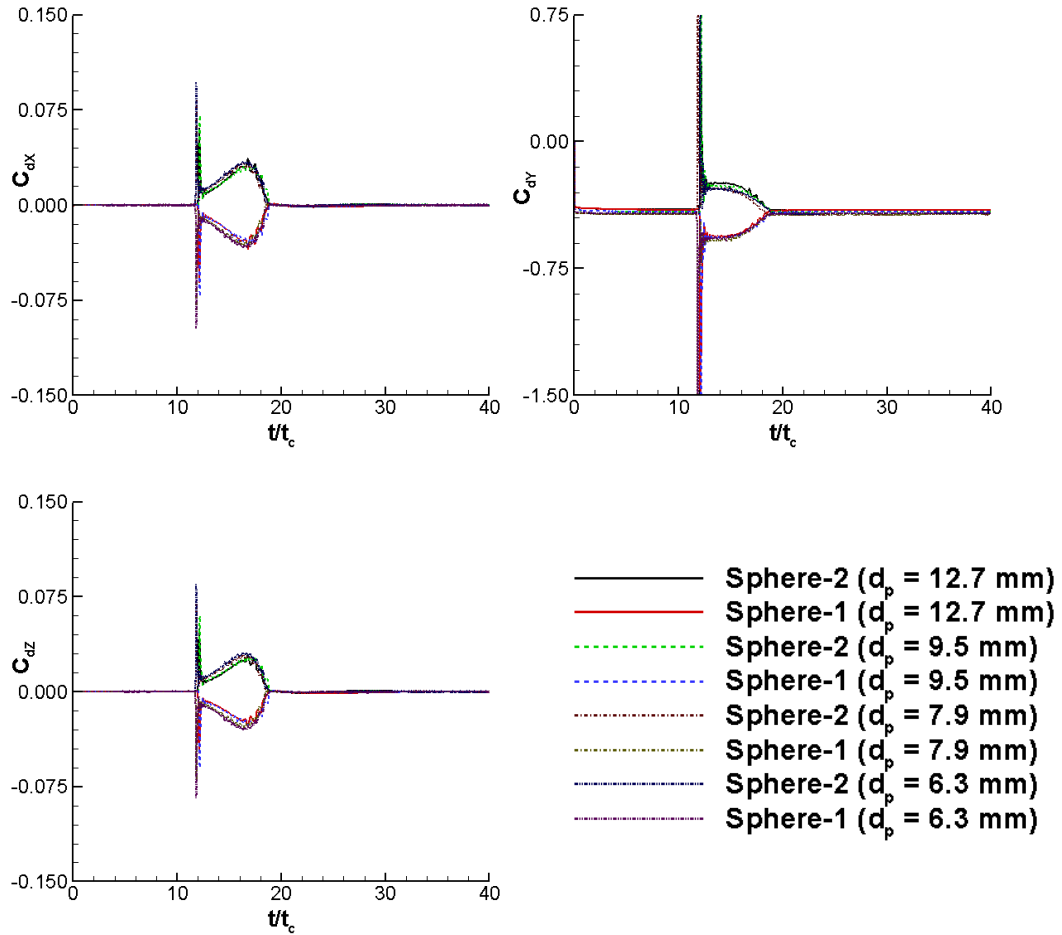


Fig.7.9. The hydrodynamic force coefficients C_{dX} , C_{dY} and C_{dZ} on the (trailing) sphere-1 and (leading) sphere-2.

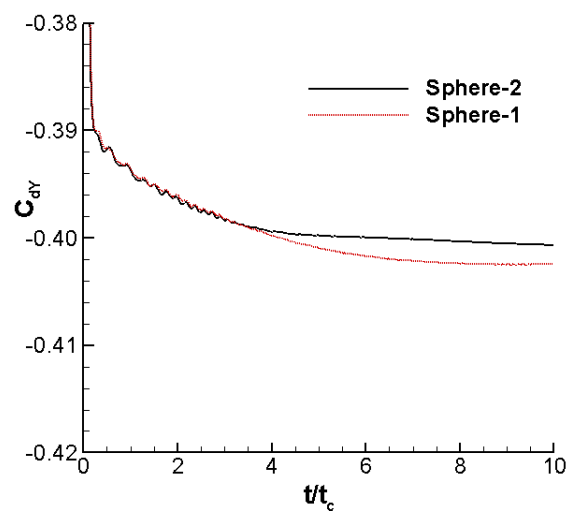


Fig.7.10. The C_{dY} variation on the (trailing) sphere-1 and (leading) sphere-2 while performing drafting ($d_p = 12.7$ mm).

The instantaneous spikes at $t/t_c = 11.0$, represent the instantaneous lubrication forcing (Glowinski et al. (1999)), that avoids the solid wall penetrations when the spheres collide among themselves. The equal and opposite variation of C_{dX} , C_{dY} and C_{dZ} on the two settling spheres produce corresponding repulsive sphere motions as they separates away.

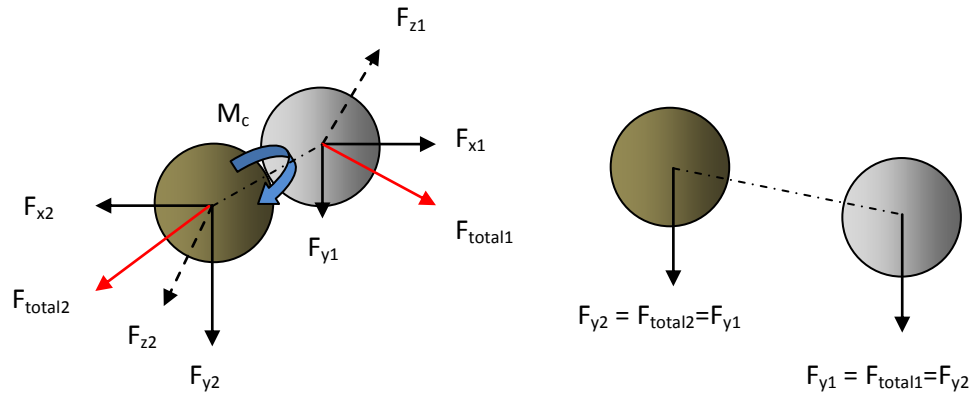


Fig.7.11. Schematic of the hydrodynamic forces acting on the spheres to generate vertical and lateral migrations.

A pictorial representation of such X, Y and Z direction forces are shown in Fig.7.11 at $t/t_c = 12.0$ and $t/t_c = 22.0$. The resultant forces F_{total1} , F_{total2} will act on the two kissing spheres whose line of action vector gives rise to a turning moment M_c (same as destabilizing couple in section 7.3.2). The spheres in action of the repulsive forces and turning moment tumble and migrate to align themselves such that their interactions stop and they attain a steady fall condition. Here, it is worth noting that the sense of the turning couple defines the direction of tumbling action and dictates whether the spheres will undergo *Tumbling* or *Inverse Tumbling*.

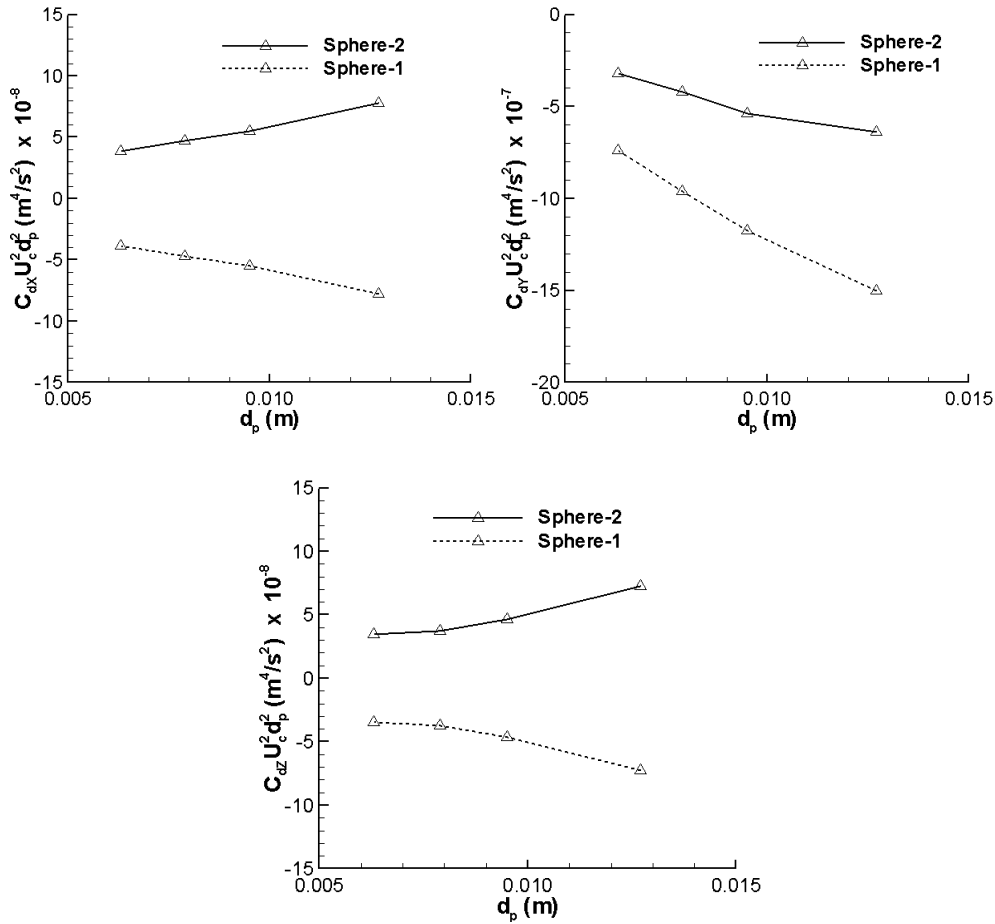


Fig.7.12 The functions of maximum force coefficient C_{dx} , C_{dy} and C_{dz} vs diameter of the spheres.

Further, the magnitudes of the resultant repulsive forces dictate the separation distance among the tumbling spheres. To quantify the maximum forces, we have plotted in Fig.7.12 $C_{dx} U_c^2 d_p^2$, $C_{dy} U_c^2 d_p^2$ and $C_{dz} U_c^2 d_p^2$ based on the maximum peak values in the C_{dx} , C_{dy} and C_{dz} profiles in Fig 7.9. Here, it can be seen that the force magnitude decreases with decreasing sphere diameter. Thus, smaller the repulsive force, the smaller will be the separation distance. This also agrees with our experimental observations as will discussed in the next section and shown in Fig.7.13.

7.3.4 Migration of the tumbling spheres

After DKT or Inverse DKT, as the tumbled spheres further settle down, a lateral and vertical migration is observed before they attain a steady fall alignment. The force calculation in section 7.3.3, clearly suggests that the settling spheres only experience limited zone of variation ($11.0 < t/t_c < 19.0$, ref. Fig.7.9) where the opposite varying parabolic-like trends are responsible for the generation of lateral and vertical migration of the tumbled spheres.

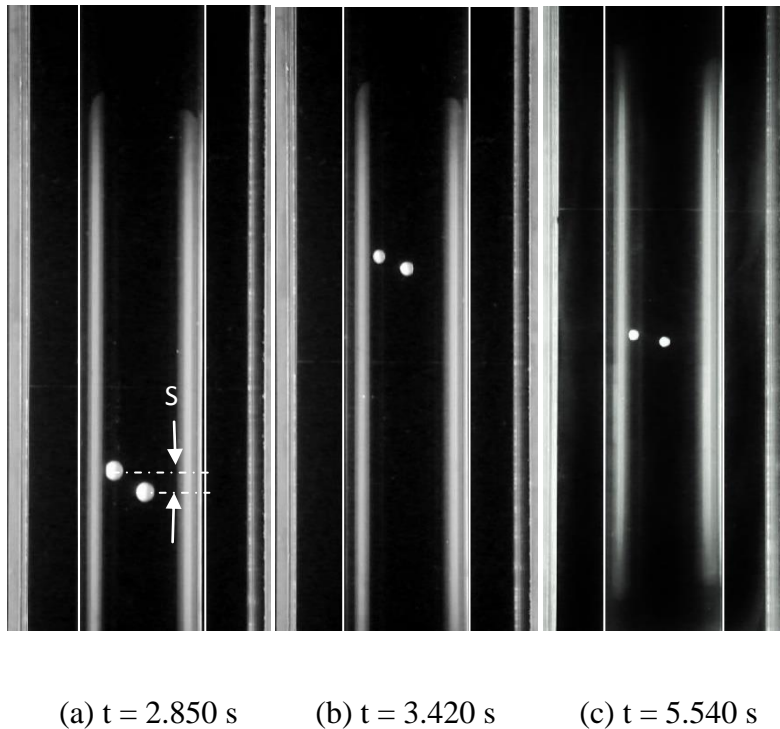
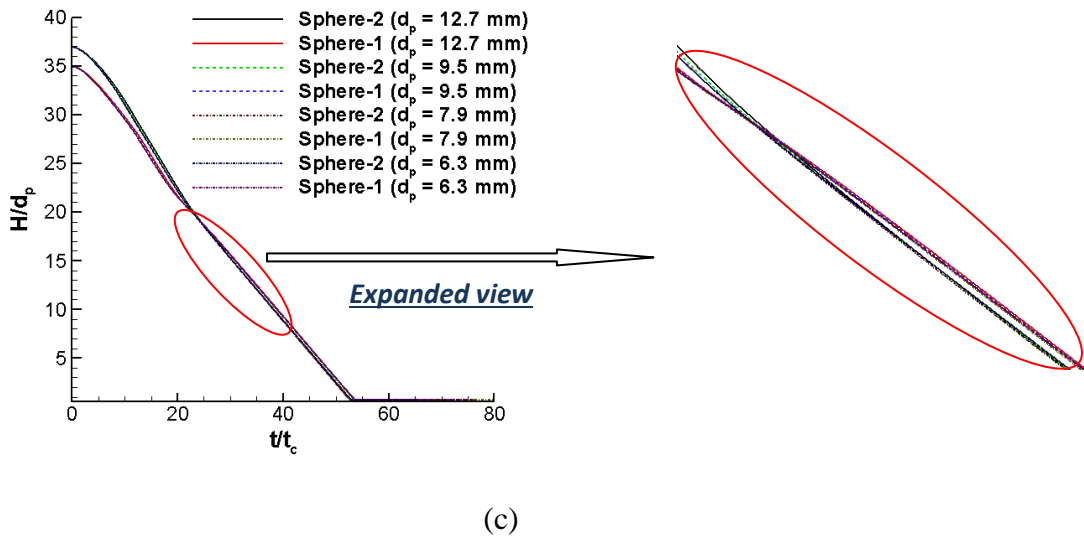
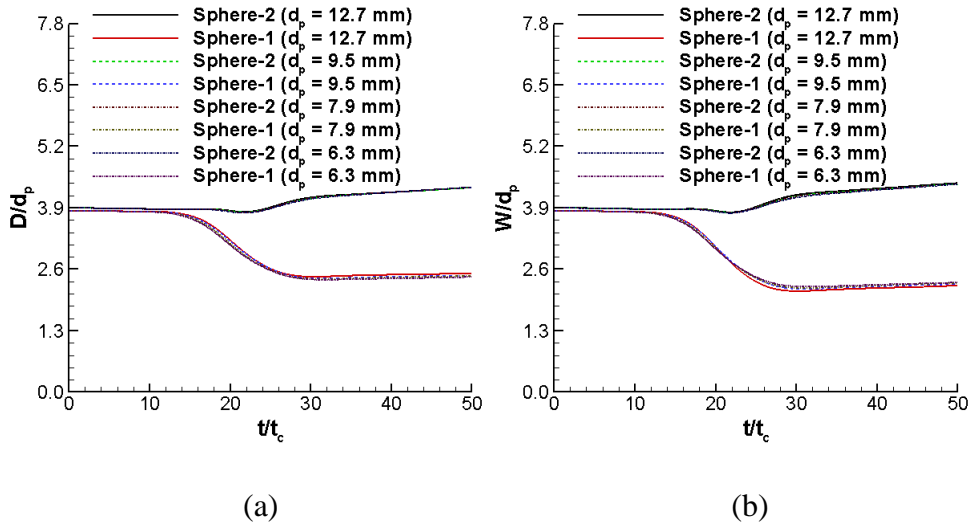
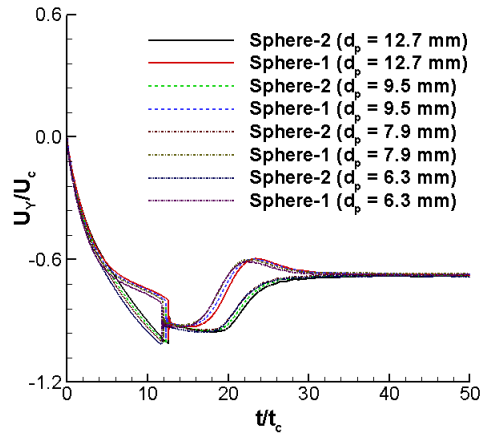


Fig.7.13. Steady state alignment of the settling spheres after DKT and migration. The sphere sizes are, (a) $d_p = 12.7$ mm, (b) $d_p = 9.5$ mm and (c) $d_p = 7.9$ mm.

Fig.7.13 shows the experimental observations of the steady fall alignment of the migrated spheres, where the same alignment continues until the spheres reach the bottom of the tank. We have also observed that the migrations of the

spheres during Inverse DKT mechanisms are equal and in opposite directions to the DKT mechanism.





(d)

Fig.7.14. Two spheres performing DKT mechanism with different diameters where Non-dimensional (a) X centre trajectories, (b) Z centre trajectories, (c) Y centre trajectory and (d) Vertical velocity of the spheres are shown.

Further, our numerical simulation in Fig 7.14 shows that the normalised lateral and vertical migrating distance, and the normalised vertical velocities are independent of Reynolds number of the settling spheres. The two spheres: leading sphere (sphere-1) and trailing sphere (sphere-2), initially move with same vertical velocities and closely follow their centre trajectories, until the trailing sphere interacts with the wake of leading one (see Fig.7.14(a)-(d)). In the wake, the trailing sphere accelerates faster and reduces the Y centre gap between them. This subsequently leads to collision (kissing mechanism) and follows by tumbling. These events cause the sphere trajectories and velocities to change. As shown in Fig.7.14(d), the two tumbled spheres experience different retardation in velocities, which are functions of the magnitude of the generated repulsive force and the diameter of the spheres. In the case of the larger spheres, the generated repulsive force is comparatively higher (ref. Fig.7.12) and produces higher migration among the tumbled spheres. This

observation is consistent with the experimental observation displayed in Fig 7.13.

We have further quantified the amount of vertical and lateral migration by comparing the Y, X and Z centre coordinates of the spheres. The centre differences: $(Y_{c1} - Y_{c2})$, $(X_{c1} - X_{c2})$ and $(Z_{c1} - Z_{c2})$ are normalised with the sphere diameter d_p and plotted in Fig.7.15, where the subscript C1 and C2 corresponds to centre coordinates of Sphere-1 and Sphere-2, respectively.

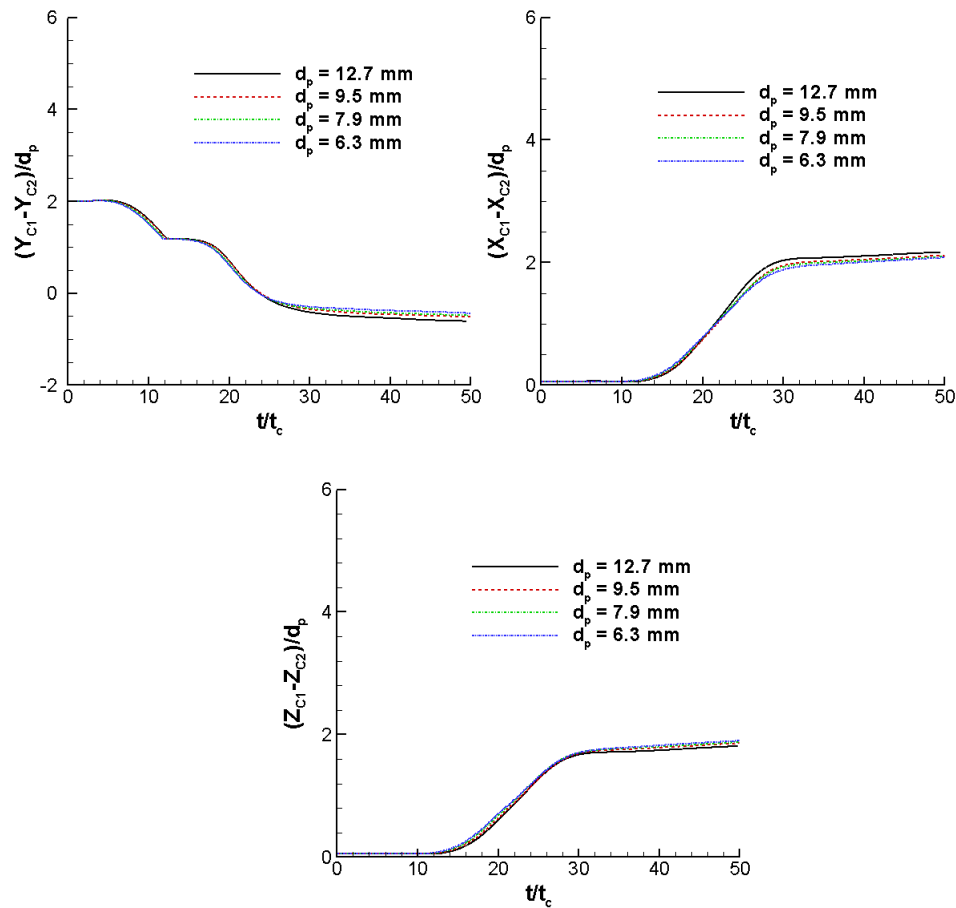


Fig.7.15. Y, X and Z centre migration of the two settling spheres with different diameter while undergoing DKT.

The results show that the initial centre gap ($2d_p$) along Y direction decreases overtime and attains a steady state negative migration. The negative gap

indicates that the spheres have altered their initial arrangement and the trailing sphere becomes the leading one and vice versa (see also Fig 7.14(c)). In all cases, the X and Z centres of the spheres were the same initially (starts with zero centre difference, ref. Fig.7.15), but proceeds to a near constant gap after the DKT actions.

The experimental observations on vertical migration of the spheres are post-processed and compared with numerical simulations as shown in Fig 7.16. They are found to be in good agreement. It should be stressed that we are comparing the vertical migration only because the camera axis is perpendicular to the sphere sedimentation direction (ref. Fig.7.1), which restrict our observation of the lateral migration.

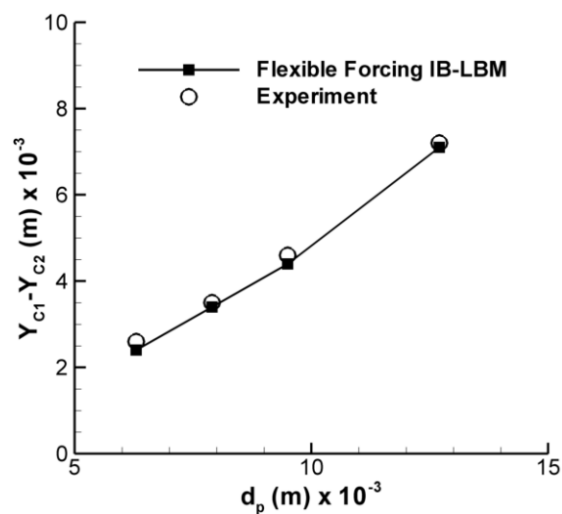


Fig.7.16. Experimental and IB – LBM comparisons of the vertical migration of different diameter spheres during steady fall after DKT actions.

On the DKT phenomenon in a broader and narrower channel, it was previously reported by Glowinski et al. (2008) that the two settling spheres in a narrow channel undergo multiple DKT before they reach the bottom of the

channel. However, we do not observe multiple DKT in our studies. Close examination shows that our numerical and experimental domain size is comparatively broader than that of Glowinski et al. (2008). It is most likely that the broader domain in our study allows the spheres to migrate more freely. Specifically, when the spheres fall steadily with certain spatial alignment between their centres, the wake interaction between them is minimal and this may have avoided multiple DKT observed in the narrower domain of Glowinski, Dean et al. (2008). The C_{dx} , C_{dy} and C_{dz} plots in Fig.7.9 further supports our claim.

7.4 Concluding remarks

In this chapter, 3D numerical simulations and experiments have been conducted to study the sedimentation dynamics of two in-line falling spheres in the Reynolds number (Re) range of 10 to 60. Our results show that the trajectories of the falling spheres are highly three-dimensional and not confined in a plane as was assumed in the previous studies. In all cases, the trailing sphere initially falls with the same velocity as the leading sphere, but subsequently increases due to the low pressure region created in the leeward side of the leading sphere. The ensuing interaction that leads to DKT produces complex sedimentation velocity profiles, before two spheres split and travel with the same velocity. On the hydrodynamic forces, our results indicate that the tumbling mechanism is influenced by the turning couple, which together with repulsive hydrodynamic forces causes vertical and lateral migrations of the spheres until they acquire a steady state alignment. The sense of the turning couple dictates whether the spheres would exhibit normal or inverse

tumbling mechanism. Regardless of the sphere size, the non-dimensionalised trajectories, velocity and hydrodynamics force coefficients are independent of the Reynolds number, at least for the range of values considered here. Further, we did not observe multiple DKT as was reported previously in a narrow channel.

Chapter 8

Conclusions and Future Recommendations

At first, conclusions are drawn for the present thesis work and thereafter, recommendations are made to extend this work in future.

8.1 Conclusions

In this thesis, a novel flexible forcing IB – LBM scheme is introduced for fluid – solid interaction in an incompressible, viscous flow domain with stationary and moving solid boundaries. The developed scheme uniquely combines the immersed boundary concept in the framework of the lattice Boltzmann method that removes the numerical defects often suffered by convectional IB – LBM schemes, such as non-physical streamline penetration into the solid boundary; improper hydrodynamic force and torque calculations. Afore identified defects may be avoided by an improved implicit velocity correction based IB – LBM (Wu and Shu (2009)) which demands a significant computational memory usage for formation/inversion of a complex matrix. In contrast, our proposed flexible forcing algorithm simplifies the formulation while keeping the

benefits of the implicit velocity corrections and at same time avoids the complicated matrix operations.

The numerical accuracy of the proposed IB – LBM scheme is assessed by performing simulation of Taylor-Green decaying vortex and lid-driven cavity flow. The obtained results show that the overall accuracy of the scheme is slightly less than second-order, which is attributed to utilisation of the first-order Dirac delta function interpolation near the boundary.

The proposed IB – LBM scheme is validated with a number of benchmark flow cases such as, steady/unsteady flow past a stationary circular cylinder, motion of a neutral buoyant circular particle in a linear shear flow, single and two particles sedimentation in a vertical channel. We observed that the quantitative numerical results obtained from our present scheme are in good agreement with data in literature. Unlike to the conventional IB – LBM scheme, the non-physical penetration of streamline into the solid boundary is absent in flexible forcing IB – LBM, where the no-slip velocity boundary condition is exactly satisfied.

After verifying the capabilities and accuracy of the proposed scheme, we have applied it to simulate particulate flow where the wall effects dominate. We have studied the settling of the circular particle in a semicircular constricted channel for the first time, to showcase the wall effects on the flow regime. Several flow configurations have been identified, also detail analysis of sedimentation process are presented as functions of density of the particle, constriction shape and size. We have also extended the study for multi particle

(two particles) case where interesting momentary upward movement of the trailing particle is observed at certain constriction gap size.

With suitable implication of the flexible forcing IB – LBM in 2D flows without accounting the temperature variations, we subsequently tried to explore the fluid-solid interaction problems that include the temperature effects. A new flexible forcing IB – thermal LBM numerical scheme is developed that satisfies the two Dirichlet boundary conditions (velocity, temperature) on the immersed solid surface accurately. Compare to the conventional IB – LBM scheme, the proposed scheme avoids the non-physical streamline and isotherm penetration into the solid boundary. The numerical accuracy is verified by performing a benchmark flow cases such as, natural and forced convection flow problems from a heat source.

The developed thermal IB – LBM model is then applied for studying the natural convection process in the complex cavity situations. Due to its practical applications, the natural convection has got lot of attentions over last decades, where only limited studies are found for the complex cavity scenarios. In our present study we have consider few complex cavity situations formed by an outer cold square enclosure and inner hot square heat source (cylinder). Here, for the first time we have discussed the flow regime and heat transfer pattern in the annulus of the enclosure, as functions of Ra, eccentricity and inclination of the inner square cylinder (heat source). The quantitative comparison of the heat transfer rates are also discussed by computing the local and average Nusselt number.

After successful implications of the 2D flexible forcing IB – LBM model, finally we have extended the study for 3D flow regime. Both presence of stationary and moving solid boundary in the flow domain is considered here. The scheme is validated with stationary flow past a sphere, single and two spherical particles sedimentation in a viscous liquid medium. We have investigated the unique mechanism Drafting – Kissing – Tumbling (DKT) of the two inline settling spheres. Active hydrodynamic force and turning couple experienced by the settling spheres are identified which will help to define the exact sphere movement over time. Further we have characterised the sedimentation process with Re of the flow.

8.2 Future recommendations

This thesis has demonstrated a unique way to combine the immersed boundary and lattice Boltzmann principle to simulate fluid-structure interaction problems including thermal effects in either 2D or 3D flow cases. Nevertheless, there are still scopes for future extensions for improvement of the algorithm as well as applications to complex flow scenarios. In the followings some recommendations and suggestions are highlighted.

1. The present simulations are either performed in uniform or non-uniform structured Cartesian mesh. For a high resolution solution in case of complex 3D problems this may require much finer grids and hence necessitate higher computational resources, which may also limits its applicability. Alternatively, an adaptive mesh refinement

technique may be developed that maintains a balance between the mesh resolutions and computational effort.

2. The developed thermal IB – LBM model with single relaxation time (SRT), may be extended to study the moving boundary and 3D flow cases using multi relaxation time (MRT) collision model where the numerical stability can be enhanced by removing the limitation of fixed ratio between kinematic and bulk viscosity.
3. The immersed solid material properties such as, elasticity, bending moment, stiffness may be included in the coupled flexible forcing IB – LBM scheme so as to model the fluid and deformable/flexible structure interactions.
4. The studied problem, particle sedimentation in the constricted channel may further extended to various shapes of particles and constrictions with inclusion of elasticity/deformable effects.
5. The developed 3D IB – LBM scheme may be extended to study more complex flow problems for example particle sedimentation in a 3D constricted channel, aerodynamics of flapping wings.

References

- Adhikari R, Stratford K, Cates M and Wagner A. (2005). "Fluctuating lattice boltzmann." EPL (Europhysics Letters) **71**: 473.
- Aidun C and Lu Y. (1995). "Lattice Boltzmann simulation of solid particles suspended in fluid." Journal of Statistical Physics **81**(2): 49-61.
- Ahlrichs P and Dünweg B. (1999). "Simulation of a single polymer chain in solution by combining lattice Boltzmann and molecular dynamics." The Journal of Chemical Physics **111**(17): 8225-8239.
- Alansary H, Zeitoun O and Ali M. (2012). "Numerical modeling of natural convection heat transfer around horizontal triangular cylinders." Numerical Heat Transfer, Part A: Applications **61**(3): 201-219.
- Ansumali S and Karlin IV. (2005). "Consistent lattice boltzmann method." Physical Review Letters **95**(26): 260605.
- Asan H. (2000). "Natural convection in an annulus between two isothermal concentric square ducts." International Communications in Heat and Mass Transfer **27**(3): 367-376.
- Bararnia H, Soleimani S and Ganji DD. (2011). "Lattice Boltzmann simulation of natural convection around a horizontal elliptic cylinder inside a square enclosure." International Communications in Heat and Mass Transfer **38**(10): 1436-1442.

- Behrend O. (1995). "Solid-fluid boundaries in particle suspension simulations via the lattice Boltzmann method." Physical Review E **52**(1): 1164-1175.
- Benzi R and Succi S. (1990). "Two-dimensional turbulence with the lattice Boltzmann equation." Journal of Physics A: Mathematical and General **23**(1): L1.
- Bhatnagar PL, Gross EP and Krook M. (1954). "A Model for Collision Processes in Gases. I. Small Amplitude Processes in Charged and Neutral One-Component Systems." Physical Review **94**(3): 511-525.
- Boger DV. (1987). "Viscoelastic flows through contractions." Annual Review of Fluid Mechanics **19**(1): 157-182.
- Braza M, Chassaing P and Minh HH. (1986). "Numerical study and physical analysis of the pressure and velocity fields in the near wake of a circular cylinder." Journal of Fluid Mechanics **165**: 79-130.
- Brownlee RA, Gorban AN and Levesley J. (2007). "Stability and stabilization of the lattice Boltzmann method." Physical Review E **75**(3): 036711.
- Cates M, Stratford K, Adhikari R, Stansell P, Desplat J and Pagonabarraga I. "Simulating colloid hydrodynamics with lattice Boltzmann methods." Journal of Physics: Condensed Matter **16**: S3903.
- Cesini G, Paroncini M, Cortella G and Manzan M. (1999). "Natural convection from a horizontal cylinder in a rectangular cavity." International Journal of Heat and Mass Transfer **42**(10): 1801-1811.

- Chatterjee D and Mondal B. (2011). "Effect of thermal buoyancy on vortex shedding behind a square cylinder in cross flow at low Reynolds numbers." International Journal of Heat and Mass Transfer **54**(26): 5262-5274.
- Chen DJ, Lin KH and Lin CA. (2007). "Immersed boundary method based lattice boltzmann method to simulate 2D and 3D complex geometry flows." International Journal of Modern Physics C **18**(4): 585-594.
- Chen S, Martínez D and Mei R. (1996). "On boundary conditions in lattice Boltzmann methods." Physics of Fluids **8**(9): 2527-2536.
- Chen S and Tian Z. (2009). "Simulation of microchannel flow using the lattice Boltzmann method." Physica A: Statistical Mechanics and its Applications **388**(23): 4803-4810.
- Chen XW and Shi BC. (2005). "A new lattice Boltzmann model for incompressible magnetohydrodynamics." Chinese Physics **14**(7): 1398-1406.
- Chen Y, Ohashi H and Akiyama M. (1994). "Thermal lattice Bhatnagar-Gross-Krook model without nonlinear deviations in macrodynamic equations." Physical Review E **50**(4): 2776-2783.
- Chen F, Xu AG, Zhang G and Wang Y. (2014). "Two-dimensional MRT LB model for compressible and incompressible flows." Frontiers of Physics **9**: 246-254.

- De Palma P, De Tullio MD, Pascazio G and Napolitano M. (2006). "An immersed-boundary method for compressible viscous flows." Computers & Fluids **35**(7): 693-702.
- De Vahl Davis G and Jones IP. (1983). "Natural convection in a square cavity: A comparison exercise." International Journal for Numerical Methods in Fluids **3**(3): 227-248.
- Deng QH. (2008). "Fluid flow and heat transfer characteristics of natural convection in square cavities due to discrete source–sink pairs." International Journal of Heat and Mass Transfer **51**(26): 5949-5957.
- Dennis SCR and Chang GZ. (1970). "Numerical solutions for steady flow past a circular cylinder at Reynolds numbers up to 100." Journal of Fluid Mechanics **42**(3): 471-489.
- Ding H, Shu C, Yeo KS and Xu D. (2004). "Simulation of incompressible viscous flows past a circular cylinder by hybrid FD scheme and meshless least square-based finite difference method." Computer Methods in Applied Mechanics and Engineering **193**(11): 727-744.
- Dupuis A, Chatelain P and Koumoutsakos P. (2008). "An immersed boundary–lattice-Boltzmann method for the simulation of the flow past an impulsively started cylinder." Journal of Computational Physics **227**(9): 4486-4498.
- Fadlun EA, Verzicco R, Orlandi P and Mohd-Yusof J. (2000). "Combined immersed-boundary finite-difference methods for three-dimensional

- complex flow simulations." Journal of Computational Physics **161**(1): 35-60.
- Fauci LJ and McDonald A. (1995). "Sperm motility in the presence of boundaries." Bulletin of Mathematical Biology **57**(5): 679-699.
- Fedkiw RP, Aslam T, Merriman B and Osher S. (1999). "A non-oscillatory eulerian approach to interfaces in multimaterial flows (the ghost fluid method)." Journal of Computational Physics **152**(2): 457-492.
- Feng J, Hu HH and Joseph DD. (1994). "Direct simulation of initial value problems for the motion of solid bodies in a Newtonian fluid. Part 2. Couette and Poiseuille flows." Journal of Fluid Mechanics **277**: 271-301.
- Feng ZG, Michaelides EE. (2004). "The immersed boundary-lattice Boltzmann method for solving fluid-particles interaction problems." Journal of Computational Physics **195**(2): 602-628.
- Feng ZG, Michaelides EE. (2005). "Proteus: a direct forcing method in the simulations of particulate flows." Journal of Computational Physics **202**(1): 20-51.
- Folkersma R, Stein HN and Vosse FN. (2000). "Hydrodynamic interactions between two identical spheres held fixed side by side against a uniform stream directed perpendicular to the line connecting the spheres' centres." International Journal of Multiphase Flow **26**: 877-887.

References

- Fornberg B. (1980). "Numerical study of steady viscous flow past a circular cylinder." Journal of Fluid Mechanics **98**(pt 4): 819-855.
- Fortes AF, Joseph DD and Lundgren TS. (1987). "Nonlinear mechanics of fluidization of beds of spherical particles." Journal of Fluid Mechanics **177**: 467-483.
- Frisch U, Hasslacher B and Pomeau Y. (1986). "Lattice gas automata for the Navier-Stokes equation." Physical Review Letters **56**(14): 1505-1508.
- Ghaddar NK. (1992). "Natural convection heat transfer between a uniformly heated cylindrical element and its rectangular enclosure." International Journal of Heat and Mass Transfer **35**(10): 2327-2334.
- Ghia U, Ghia KN and Shin CT. (1982). "High-Re solutions for incompressible flow using the Navier-Stokes equations and a multigrid method." Journal of Computational Physics **48**(3): 387-411.
- Ghias R, Mittal R and Dong H. (2007). "A sharp interface immersed boundary method for compressible viscous flows." Journal of Computational Physics **225**(1): 528-553.
- Gilmanov A and Sotiropoulos F. (2005). "A hybrid Cartesian/immersed boundary method for simulating flows with 3D, geometrically complex, moving bodies." Journal of Computational Physics **207**(2): 457-492.
- Gilmanov A, Sotiropoulos F and Balaras E. (2003). "A general reconstruction algorithm for simulating flows with complex 3D immersed boundaries

- on Cartesian grids." Journal of Computational Physics **191**(2): 660-669.
- Ginzburg I. (2008). "Consistent lattice Boltzmann schemes for the Brinkman model of porous flow and infinite Chapman-Enskog expansion." Physical Review E **77**(6): 066704-066712.
- Glowinski R, Pan TW and Periaux J. (1994). "A fictitious domain method for Dirichlet problem and applications." Computer Methods in Applied Mechanics and Engineering **111**(3-4): 283-303.
- Glowinski R, Pan TW, Hesla TI and Joseph DD. (1999). "A distributed Lagrange multiplier/fictitious domain method for particulate flows." International Journal of Multiphase Flow **25**(5): 755-794.
- Glowinski R, Pan TW, Hesla TI, Joseph DD and Périaux J. (2001). "A fictitious domain approach to the direct numerical simulation of incompressible viscous flow past moving rigid bodies: application to particulate flow." Journal of Computational Physics **169**(2): 363-426.
- Glowinski R, Dean EJ, Guidoboni G, Juarez LH and Pan TW. (2008). "Applications of Operator-Splitting Methods to the Direct Numerical Simulation of Particulate and Free-Surface Flows and to the Numerical Solution of the Two-Dimensional Elliptic Monge-Ampère Equation." Japan Journal of Industrial and Applied Mathematics **25**(1): 1-63.
- Goldstein D, Handler R and Sirovich L. (1993). "Modeling a no-slip flow boundary with an external force field." Journal of Computational Physics **105**(2): 354-366.

- Guo Z, Shi B and Zheng C. (2002). "A coupled lattice BGK model for the Boussinesq equations." International Journal for Numerical Methods in Fluids **39**(4): 325-342.
- Guo Z, Zheng C and Shi B. (2002). "Discrete lattice effects on the forcing term in the lattice Boltzmann method." Physical Review E **65**(4): 046308.
- Ha MY, Kim IK, Yoon HS, Yoon KS, Lee JR and Balachandar S. (2002). "Two dimensional and unsteady natural convection in a horizontal enclosure with a square body." Numerical Heat Transfer, Part A: Applications **41**(2): 183-210.
- He X, Chen S and Doolen GD. (1998). "A novel thermal model for the lattice boltzmann method in incompressible limit." Journal of Computational Physics **146**(1): 282-300.
- He X, Chen S and Zhang R. (1999). "A lattice boltzmann scheme for incompressible multiphase flow and its application in simulation of rayleigh-taylor instability." Journal of Computational Physics **152**(2): 642-663.
- He X, Luo LS and Dembo M. (1996). "Some progress in lattice Boltzmann method. Part I. Nonuniform mesh grids." Journal of Computational Physics **129**(2): 357-363.
- Higuera FJ and Jiménez J. (1989). "Boltzmann approach to lattice gas simulations." EPL(Europhysics Letters) **9**(7): 663-668.

- Hinton FL, Rosenbluth MN, Wong SK, Lin-Liu YR and Miller RL. (2001). "Modified lattice Boltzmann method for compressible fluid simulations." Physical Review E **63**(6 D): 061212/061211-061212/061219.
- Hou S, Zou Q, Chen S, Doolen G and Cogley AC. (1995). "Simulation of cavity flow by the lattice Boltzmann method." Journal of Computational Physics **118**(2): 329-347.
- Hu HH. (1996). "Direct simulation of flows of solid-liquid mixtures." International Journal of Multiphase Flow **22**(2): 335-352.
- Hu HH, Joseph DD and Fortes AF. (1992). "Experiments and direct simulation of fluid particle motions." International Video Journal in Engineering Research **2**: 17-24.
- Hu HH, Patankar NA and Zhu MY. (2001). "Direct numerical simulations of fluid–solid Systems using the arbitrary Lagrangian–Eulerian technique." Journal of Computational Physics **169**(2): 427-462.
- Hu Y, Yuan H, Shu S, Niu X and Li M. (2014). " An improved momentum exchange-based immersed boundary-lattice Boltzmann method by using an iterative technique." Computer & Mathematics with Applications **68**(03): 140-155.
- Huang H, Huang JJ and Lu XY. (2014). "A mass-conserving axisymmetric multiphase lattice Boltzmann method and its application in simulation of bubble rising." Journal of Computational Physics **269**: 386-402.

- Huang H, Krafczyk M and Lu X. (2011). "Forcing term in single-phase and Shan-Chen-type multiphase lattice Boltzmann models." Physical Review E **84**(4): 046710.
- Hussain SH and Hussein AK. (2010). "Numerical investigation of natural convection phenomena in a uniformly heated circular cylinder immersed in square enclosure filled with air at different vertical locations." International Communications in Heat and Mass Transfer **37**(8): 1115-1126.
- Ingram DM, Causon DM and Mingham CG. (2003). "Developments in Cartesian cut cell methods." Mathematics and Computers in Simulation **61**(3-6): 561-572.
- Jayaweera KOLF, Mason BJ and Slack GW. (1964). "The behaviour of clusters of spheres falling in a viscous fluid Part 1. Experiment." Journal of Fluid Mechanics **20**(01): 121-128.
- Jehring L, Chapman S and Cowling TG. (1992). "The Mathematical Theory of Non-Uniform Gases. 3rd edition. Cambridge etc., Cambridge University Press 1990. XXIV, 422 pp., £ 19.50 P/b. ISBN 0-521-40844-X." ZAMM - Journal of Applied Mathematics and Mechanics / Zeitschrift für Angewandte Mathematik und Mechanik **72**(11): 610-610.
- Jenny M, Bouchet G and Dusek J. (2003). "Nonvertical ascension or fall of a free sphere in a Newtonian fluid." Physics of Fluids **15**(1): L9-L12.

- Jeong HK, Yoon HS and Ha MY. (2010). "An immersed boundary-thermal lattice Boltzmann method using an equilibrium internal energy density approach for the simulation of flows with heat transfer." Journal of Computational Physics **229**(7): 2526-2543.
- Johnson TA and Patel VC. (1999). "Flow Past a Sphere up to a Reynolds Number of 300." Journal of Fluid Mechanics **378**: 19-70.
- Joseph DD, Liu YJ, Poletto M and Feng J. (1994). "Aggregation and dispersion of spheres falling in viscoelastic liquids." Journal of Non-Newtonian Fluid Mechanics **54**(0): 45-86.
- Joseph DD, Nelson J, Hu HH and Liu Y. (1992). "Competition between inertial pressure and normal stresses in the flow induced anisotropy of solid particles." Theoretical and Applied Rheology Elsevier: 60-65.
- Kalyana Raman S, Arul Prakash K and Vengadesan S. (2012). "Natural convection from a Heated Elliptic Cylinder with a Different Axis Ratio in a Square Enclosure." Numerical Heat Transfer, Part A: Applications **62**(8): 639-658.
- Kang SK and Hassan YA. (2011). "A comparative study of direct-forcing immersed boundary-lattice Boltzmann methods for stationary complex boundaries." International Journal for Numerical Methods in Fluids **66**(9): 1132-1158.
- Kang SK and Hassan YA. (2011). "A direct-forcing immersed boundary method for the thermal lattice Boltzmann method." Computers & Fluids **49**(1): 36-45.

- Kempe T and Fröhlich J. (2012). "Collision modelling for the interface-resolved simulation of spherical particles in viscous fluids." Journal of Fluid Mechanics **709**: 445-489.
- Kempe T and Fröhlich J. (2012). "An Improved Immersed Boundary Method with Direct Forcing for the Simulation of Particle Laden Flows." Journal of Computational Physics **231**: 3663-3684.
- Kim BS, Lee DS, Ha MY and Yoon HS. (2008). "A numerical study of natural convection in a square enclosure with a circular cylinder at different vertical locations." International Journal of Heat and Mass Transfer **51**(7–8): 1888-1906.
- Kim I, Elghobashi S and Sirignano WA. (1993). "Three-dimensional flow over two spheres placed side by side." Journal of Fluid Mechanics **246**: 465-488.
- Kim J, Kim D and Choi H. (2001). "An immersed-boundary finite-volume method for simulations of flow in complex geometries." Journal of Computational Physics **171**(1): 132-150.
- Koelman J. (2007). "A simple lattice Boltzmann scheme for Navier-Stokes fluid flow." EPL (Europhysics Letters)**15**(6): 603.
- Kumar De A and Dalal A. (2006). "A numerical study of natural convection around a square, horizontal, heated cylinder placed in an enclosure." International Journal of Heat and Mass Transfer **49**(23–24): 4608-4623.

- Ladd AJC. (1993). "Short-time motion of colloidal particles: Numerical simulation via a fluctuating lattice-Boltzmann equation." Physical Review Letters **70**(9): 1339-1342.
- Ladd AJC. (1994a). "Numerical simulations of particulate suspensions via a discretized Boltzmann equation. Part 1. Theoretical foundation." Journal of Fluid Mechanics **271**: 285-309.
- Ladd AJC. (1994b). "Numerical simulations of particulate suspensions via a discretized Boltzmann equation. Part 2. Numerical results." Journal of Fluid Mechanics **271**: 311-339.
- Ladd AJC and Verberg R. (2001). "Lattice-Boltzmann simulations of particle-fluid suspensions." Journal of Statistical Physics **104**(5-6): 1191-1251.
- Lai MC and Peskin CS. (2000). "An immersed boundary method with formal second-order accuracy and reduced numerical viscosity." Journal of Computational Physics **160**(2): 705-719.
- Le DV, Khoo BC and Peraire J. (2006). "An immersed interface method for viscous incompressible flows involving rigid and flexible boundaries." Journal of Computational Physics **220**(1): 109-138.
- Lee JM, Ha MY and Yoon HS. (2010). "Natural convection in a square enclosure with a circular cylinder at different horizontal and diagonal locations." International Journal of Heat and Mass Transfer **53**(25-26): 5905-5919.

- Lee L and Leveque RJ. (2003). "An immersed interface method for incompressible Navier-Stokes equations." SIAM Journal on Scientific Computing **25**(3): 832-856.
- Lee T and Lin CL. (2005). "A stable discretization of the lattice Boltzmann equation for simulation of incompressible two-phase flows at high density ratio." Journal of Computational Physics **206**(1): 16-47.
- Leveque RJ and Li Z. (1997). "Immersed interface methods for Stokes flow with elastic boundaries or surface tension." SIAM Journal on Scientific Computing **18**(3): 709-735.
- Li Q, He YL, Wang Y and Tang GH. (2008). "An improved thermal lattice Boltzmann model for flows without viscous heat dissipation and compression work." International Journal of Modern Physics C **19**(01): 125-150.
- Li Y, Jung E, Lee W, Lee HG and Kim J. (2012). "Volume preserving immersed boundary methods for two-phase fluid flows." International Journal for Numerical Methods in Fluids **69**(4): 842-858.
- Lim CY, Shu C, Niu XD and Chew YT. (2002). "Application of lattice Boltzmann method to simulate microchannel flows." Physics of Fluids **14**(7): 2299-2308.
- Liu TG and Khoo BC. (2007). "The accuracy of the modified ghost fluid method for gas-gas Riemann problem." Applied Numerical Mathematics **57**(5-7 SPEC. ISS.): 721-733.

- Liu XD, Fedkiw RP and Kang M. (2000). "A boundary condition capturing method for poisson's equation on irregular domains." Journal of Computational Physics **160**(1): 151-178.
- Luo K, Wang Z, Fan J and Cen K. (2007). "Full-scale solutions to particle-laden flows: Multidirect forcing and immersed boundary method." Physical Review E **76**(6): 066709.
- Luo XS and Girimaji SS. (2002). "Lattice Boltzmann model for binary mixtures." Physical Review E **66**(3): 035301/035301-035301/035304.
- Luo LS. (1998). "Unified Theory of Lattice Boltzmann Models for Nonideal Gases." Physical Review Letters**81**(8): 1618-1621.
- Mahapatra PS, De S, Ghosh K, Manna NK and Mukhopadhyay A. (2013). "Heat transfer enhancement and entropy generation in a square enclosure in the presence of adiabatic and isothermal blocks." Numerical Heat Transfer, Part A: Applications **64**(7): 577-596.
- Malaspinas O, Fiétier N and Deville M. (2010). "Lattice Boltzmann method for the simulation of viscoelastic fluid flows." Journal of Non-Newtonian Fluid Mechanics **165**(23–24): 1637-1653.
- Mark A, Svenning E and Edlevik F. (2013). "An Immersed Boundary Method for Simulation of Flow with Heat Transfer." International Journal of Heat and Mass Transfer **56**(1-2):424-435.
- Mavriplis DJ. (1997). "Unstructured grid techniques." Annual Review of Fluid Mechanics**29**(1): 473-514.

- McNamara G, Garcia A and Alder B. (1995). "Stabilization of thermal lattice Boltzmann models." Journal of Statistical Physics **81**(1-2): 395-408.
- McNamara GR and Zanetti G. (1988). "Use of the Boltzmann equation to simulate lattice-gas automata." Physical Review Letters **61**(20): 2332-2335.
- Mei R, Shyy W, Yu D and Luo LS. (2000). "Lattice Boltzmann method for 3D flows with curved boundary." Journal of Computational Physics **161**(2): 680-699.
- Mittal R and Iaccarino G. (2005). "Immersed boundary methods." Annual Review of Fluid Mechanics **37**(1): 239-261.
- Mohamad AA and Kuzmin A. (2010). "A critical evaluation of force term in lattice Boltzmann method, natural convection problem." International Journal of Heat and Mass Transfer **53**(5-6): 990-996.
- Mohd-Yusof J. (1997). "Combined immersed boundary/B-spline methods for simulations of flow in complex geometries." Annual Research Brief, Centre for Turbulence Research: 317-327.
- Nabavizadeh SA, Talebi S and Sefid M. (2012). "Natural convection in a square cavity containing a sinusoidal cylinder." International Journal of Thermal Sciences **51**(0): 112-120.
- Nash RW, Adhikari R and Cates ME. (2008). "Singular forces and pointlike colloids in lattice Boltzmann hydrodynamics." Physical Review E **77**(2): 026709.

- Niu XD, Shu C, Chew YT and Peng Y. (2006). "A momentum exchange-based immersed boundary-lattice Boltzmann method for simulating incompressible viscous flows." Physics Letters A **354**(3): 173-182.
- Pacheco JR, Pacheco-Vega A, Rodic T and Peck RE. (2005). "Numerical Simulations of Heat Transfer and Fluid Flow Problems Using an Immersed-Boundary Finite-Volume Method on NonStaggered Grids." Numerical Heat Transfer, Part B: Fundamentals **48**(1): 1-24.
- Pan C, Hilpert M and Miller CT. (2004). "Lattice-Boltzmann simulation of two-phase flow in porous media." Water Resources Research **40**(1): W01501.
- Patankar NA, Singh P, Joseph DD, Glowinski R and Pan TW. (2000). "A new formulation of the distributed Lagrange multiplier/fictitious domain method for particulate flows." International Journal of Multiphase Flow **26**(9): 1509-1524.
- Pattison MJ, Premnath KN, Morley NB and Abdou MA. (2008). "Progress in lattice Boltzmann methods for magnetohydrodynamic flows relevant to fusion applications." Fusion Engineering and Design **83**(4): 557-572.
- Pavlo P, Vahala G, Vahala L and Soe M. (1998). "Linear stability analysis of thermo-lattice Boltzmann models." Journal of Computational Physics **139**(1): 079-091.
- Peng Y, Shu C and Chew YT. (2003). "Simplified thermal lattice Boltzmann model for incompressible thermal flows." Physical Review E **68**(2): 026701.

- Peng Y, Shu C, Chew YT, Niu X and Lu XY. (2006). "Application of multi-block approach in the immersed boundary–lattice Boltzmann method for viscous fluid flows." Journal of Computational Physics **218**(2): 460-478.
- Perry AE and Chong MS. (1987). "A Description of Eddying Motions and Flow Patterns Using Critical-Point Concepts." Annual Review of Fluid Mechanics **19**(1): 125-155.
- Peskin CS. (1977). "Numerical analysis of blood flow in the heart." Journal of Computational Physics **25**(3): 220-252.
- Prosperetti A and Oğuz HN. (2001). "Physalis: a new O(N) method for the numerical simulation of disperse systems: potential flow of spheres." Journal of Computational Physics **167**(1): 196-216.
- Qi D. (1999). "Lattice-Boltzmann simulations of particles in non-zero-Reynolds-number flows." Journal of Fluid Mechanics **385**: 41-62.
- Qian YH, D'Humières D and Lallemand P. (1992). "Lattice BGK models for Navier-Stokes equation." EPL (Europhysics Letters) **17**(6): 479-484.
- Raji A, Hasnaoui M, Firdaouss M and Ouardi C. (2013). "Natural convection heat transfer enhancement in a square cavity periodically cooled from above." Numerical Heat Transfer, Part A: Applications **63**(7): 511-533.
- Ren WW, Shu C, Wu J and Yang WM. (2012). "Boundary condition-enforced immersed boundary method for thermal flow problems with Dirichlet

- temperature condition and its applications." Computers & Fluids **57**(0): 40-51.
- Saiki EM and Biringen S. (1996). "Numerical simulation of a cylinder in uniform flow: application of a virtual boundary method." Journal of Computational Physics **123**(2): 450-465.
- Schouveiler L, Brydon A, Leweke T and Thompson MC. (2004). "Interactions of the wakes of two spheres placed side by side." European Journal of Mechanics - B/Fluids **23**(1): 137-145.
- Seta T. (2013). "Implicit temperature-correction-based immersed-boundary thermal lattice Boltzmann method for the simulation of natural convection." Physical Review E **87**(6): 063304.
- Seta T, Rojas R, Hayashi K and Tomiyama A. (2014). "Implicit-correction-based immersed boundary-lattice Boltzmann method with two relaxation times." Physical Review E **89**(02): 023307.
- Sharma A and Eswaran V. (2004). "Heat and fluid flow across a square cylinder in the two-dimensional laminar flow regime." Numerical Heat Transfer, Part A: Applications **45**(3): 247-269.
- Shao JY, Shu C and Chew YT. (2013). "Development of an immersed boundary-phase field-lattice Boltzmann method for Neumann boundary condition to study contact line dynamics." Journal of Computational Physics **234**: 8-32.

- Shi Y, Tang GH and Xia HH. (2014). "Lattice Boltzmann simulation of droplet formation in T-junction and flow focusing devices." Computers & Fluids **90**: 155-163.
- Shim JW and Gagniol R. (2011). "Thermal lattice Boltzmann method based on a theoretically simple derivation of the Taylor expansion." Physical Review E **83**(4): 046710.
- Shirokoff D and Nave JC. (2014). "A Sharp-Interface Active Penalty Method for the Incompressible Navier–Stokes Equations." Journal of Scientific Computing Article in Press .
- Shu C, Liu N and Chew YT. (2007). "A novel immersed boundary velocity correction–lattice Boltzmann method and its application to simulate flow past a circular cylinder." Journal of Computational Physics **226**(2): 1607-1622.
- Shu C, Niu XD and Chew YT. (2003). "Taylor series expansion and least squares-based lattice Boltzmann method: three-dimensional formulation and its applications." International Journal of Modern Physics C **14**(07): 925-944.
- Shu C, Xue H and Zhu YD. (2001). "Numerical study of natural convection in an eccentric annulus between a square outer cylinder and a circular inner cylinder using DQ method." International Journal of Heat and Mass Transfer **44**(17): 3321-3333.
- Shukla RK, Tatineni M and Zhong X. (2007). "Very high-order compact finite difference schemes on non-uniform grids for incompressible Navier–

- Stokes equations." Journal of Computational Physics **224**(2): 1064-1094.
- Singh P, Caussignac P, Fortes A, Joseph DD and Lundgren T. (1989). "Stability of periodic arrays of cylinders across the stream by direct simulation." Journal of Fluid Mechanics **205**: 553-571.
- Singh P, Joseph DD, Hesla TI, Glowinski R and Pan TW. (2000). "A distributed Lagrange multiplier/fictitious domain method for viscoelastic particulate flows." Journal of Non-Newtonian Fluid Mechanics **91**(3): 165-188.
- Smoluchowski MS. (1911). "O oddziaływaniu wzajemnem kul, poruszających się w cieczy lepkiej. – Über die Wechselwirkung von Kugeln, die sich in einer zähen Flüssigkeit bewegen." Bulletin International de l'Academie des Sciences de Cracovie (1): 28-39.
- Smoluchowski MS. (1912). On the practical applicability of Stokes' law of resistance, and the modifications of it required in certain cases. Fifth International Congress of Mathematicians, Cambridge, Cambridge: at the University Press.
- Sohankar A, Norberg C and Davidson L. (1998). "Low-Reynolds-number flow around a square cylinder at incidence: Study of blockage, onset of vortex shedding and outlet boundary condition." International Journal for Numerical Methods in Fluids **26**(1): 39-56.

- Succi S, Benzi R and Higuera F. (1991). "The lattice Boltzmann equation: A new tool for computational fluid-dynamics." Physica D: Nonlinear Phenomena **47**(1–2): 219-230.
- Sui Y, Chew YT, Roy P and Low HT. (2007). "A hybrid immersed-boundary and multi-block lattice Boltzmann method for simulating fluid and moving-boundaries interactions." International Journal for Numerical Methods in Fluids **53**(11): 1727-1754.
- Sumner D, Price SJ and Paidoussis MP. (1999). "Tandem cylinders in impulsively started flow." Journal of Fluids and Structures **13**(7): 955-965.
- Sun C. (2000). "Simulations of compressible flows with strong shocks by an adaptive lattice Boltzmann model." Journal of Computational Physics **161**(1): 70-84.
- Suzuki K and Inamuro T. (2013). "A higher-order immersed boundary-lattice Boltzmann method using a smooth velocity field near boundaries." Computers & Fluids **76**(0): 105-115.
- Taghilou M and Rahimian MH. (2014). "Investigation of two-phase flow in porous media using lattice Boltzmann method." Computers and Mathematics with Applications **67**: 424-436.
- Ten Cate A, Nieuwstad CH, Derkesen JJ and Van den Akker HEA. (2002). "Particle imaging velocimetry experiments and lattice-Boltzmann simulations on a single sphere settling under gravity." Physics of Fluids **14**(11): 4012-4025.

- Teixeira CM. (1998). "Incorporating turbulence models into the lattice-Boltzmann method." International Journal of Modern Physics C **09**(08): 1159-1175.
- Tezduyar T. (2001). "Finite element methods for flow problems with moving boundaries and interfaces." Archives of Computational Methods in Engineering **8**(2): 83-130.
- Tölke J, Krafczyk M, Schulz M and Rank E. (2002). "Lattice Boltzmann simulations of binary fluid flow through porous media." Philosophical Transactions of the Royal Society A: Mathematical, Physical and Engineering Sciences **360**(1792): 535-545.
- Touil H, Ricot D, Leveque E. (2014). "Direct and large-eddy simulation of turbulent flows on composite multi-resolution grids by the lattice Boltzmann method." Journal of Computational Physics **256**: 220-233.
- Tran PH and Plourde F. (2014). "Computing Compressible Internal Flows by Means of an Immersed Boundary Method." Computers & Fluids **97**(1): 21-30.
- Tseng YH and Huang H. (2014). "An Immersed Boundary Method for Endocytosis." Journal of Computational Physics **273**(1): 143-159.
- Tucker PG and Pan Z. (2000). "A Cartesian cut cell method for incompressible viscous flow." Applied Mathematical Modelling **24**(8-9): 591-606.

- Udaykumar HS, Kan HC, Shyy W and TranSonTay R. (1997). "Multiphase dynamics in arbitrary geometries on fixed cartesian grids." Journal of Computational Physics **137**(2): 366-405.
- Uhlmann M. (2005). "An immersed boundary method with direct forcing for the simulation of particulate flows." Journal of Computational Physics **209**(2): 448-476.
- Usman RA. (2009). "The Lattice-Boltzmann Method on Optimal Sampling Lattices." IEEE Transactions on Visualization and Computer Graphics **15**(4): 630-641.
- Verhaeghe F, Luo LS and Blanpain B. (2009). "Lattice Boltzmann modeling of microchannel flow in slip flow regime." Journal of Computational Physics **228**(1): 147-157.
- Verzicco R, Yusof M, Orlandi P and Haworth D. (1998). LES in complex geometries using boundary body forces. CTR Proc. 1998 Summer Program, Center for Turbulence Research, Stanford University and NASA Ames Research Center.
- Wan D and Turek S. (2006). "Direct numerical simulation of particulate flow via multigrid FEM techniques and the fictitious boundary method." International Journal for Numerical Methods in Fluids **51**(5): 531-566.
- Wang X and Liu WK. (2004). "Extended immersed boundary method using FEM and RKPM." Computer Methods in Applied Mechanics and Engineering **193**(12-14): 1305-1321.

- Wang Z, Fan J and Luo K. (2008). "Combined multi-direct forcing and immersed boundary method for simulating flows with moving particles." International Journal of Multiphase Flow **34**(3): 283-302.
- Wang Z, Fan J and Luo K. (2009). "Immersed boundary method for the simulation of flows with heat transfer." International Journal of Heat and Mass Transfer **52**(19–20): 4510-4518.
- Wang L, Guo Z, Baochang S and Chuguang Z. (2013). "Evaluation of three lattice Boltzmann models for particulate flows." Communications in Computational Physics **13**(4): 1151-1171.
- Wang Y, Shu C and Teo CJ. (2014). "Development of LBGK and incompressible LBGK-based lattice Boltzmann flux solvers for simulation of incompressible flows." International Journal for Numerical Methods in Fluids **75**: 344-364.
- Wang Y, Shu C and Teo CJ. (2014). "Thermal Lattice Boltzmann Flux Solver and Its Application for Simulation of Incompressible Thermal Flows." Computers and Fluids **94**: 98-111.
- Watari M and Tsutahara M. (2004). "Possibility of constructing a multispeed Bhatnagar-Gross-Krook thermal model of the lattice Boltzmann method." Physical Review E **70**(1): 016703.
- Williamson CHK. (1996). Vortex dynamics in the cylinder wake. **28**: 477-539.

- Wu J and Shu C. (2009). "Implicit velocity correction-based immersed boundary-lattice Boltzmann method and its applications." Journal of Computational Physics **228**(6): 1963-1979.
- Wu J and Shu C. (2010). "An improved immersed boundary-lattice Boltzmann method for simulating three-dimensional incompressible flows." Journal of Computational Physics **229**(13): 5022-5042.
- Wu J and Shu C. (2010). "Particulate flow simulation via a boundary condition-enforced immersed boundary-lattice Boltzmann scheme." Communications in Computational Physics **7**(4): 793-812.
- Wu J and Shu C. (2012). "Simulation of three-dimensional flows over moving objects by an improved immersed boundary-lattice Boltzmann method." International Journal for Numerical Methods in Fluids **68**(8): 977-1004.
- Yan G, Dong Y and Liu Y. (2006). "An implicit Lagrangian lattice Boltzmann method for the compressible flows." International Journal for Numerical Methods in Fluids **51**(12): 1407-1418.
- Yu H, Luo LS and Girimaji SS. (2006). "LES of turbulent square jet flow using an MRT lattice Boltzmann model." Computers & Fluids **35**(8-9): 957-965.
- Zheng HW, Shu C and Chew YT. (2006). "A lattice Boltzmann model for multiphase flows with large density ratio." Journal of Computational Physics **218**(1): 353-371.

References

Zhu L and Peskin CS. (2002). "Simulation of a flapping flexible filament in a flowing soap film by the immersed boundary method." Journal of Computational Physics **179**(2): 452-468.

Zhu L and Peskin CS. (2003). "Interaction of two flapping filaments in a flowing soap film." Physics of Fluids **15**(7): 1954-1960.

List of Publications

Dash SM, Lim TT and Lee TS. (2014). "Two sphere sedimentation dynamics in a viscous liquid column." Physics of Fluids (Under Review).

Dash SM, Lee TS, Lim TT and Huang H. (2014). "A flexible forcing three dimension IB-LBM scheme for flow past stationary and moving spheres." Computers & Fluids **95**(0): 159-170.

Dash SM, Lee TS and Huang H. (2014). "Particle sedimentation in a constricted passage using a novel flexible forcing IB-LBM scheme." International Journal of Computational Methods **11**(05): 1350095.

Dash SM, Lee TS and Huang H. (2014). "A novel flexible forcing hybrid IB-LBM scheme to simulate flow past circular cylinder." International Journal of Modern Physics C **25**(01): 1340014.

Dash SM, Lee TS and Huang H. (2014). "Natural convection from an eccentric square cylinder using a novel flexible forcing IB-LBM method." Numerical Heat Transfer, Part A: Applications **65**(6): 531-555.

Dash SM, Lee TS and Huang H. (2014). "Natural convection from an inclined square cylinder using novel flexible forcing IB-LBM approach." Engineering Applications of Computational Fluid Mechanics **8**(1): 91-103.

Dash SM, Lee TS and Huang H. (2013). "A novel flexible forcing hybrid IB-thermal LB model for natural convection from a circular cylinder." International Journal of Dynamics of Fluids **9**(1): 1-15.

Dash SM, Lee TS and Huang H. (2012). "A new flexible forcing hybrid IB-LBM scheme – Application to particle sedimentation in a constricted passage." 3rd Thermo-Fluid seminar, NUS Singapore, 17th December 2012.

Dash SM, Lee TS and Huang H. (2012). "Efficient hybrid IB-LBM scheme to simulate flow past circular cylinder." Proceedings of the 21st International Conference on Discrete Simulation of Fluid Dynamics (DSFD-2012), 23rd-27th July 2012, Bangalore, India.